

ABSTRACT

MEASUREMENTS OF THE TOP QUARK PAIR PRODUCTION CROSS SECTION AND BRANCHING RATIO TO A W -BOSON AND BOTTOM QUARK USING THE SEMI-LEPTONIC AND DILEPTON FINAL STATES WITH THE ATLAS DETECTOR AT THE LHC

Robert E. Calkins, Ph.D.
Department of Physics
Northern Illinois University, 2012
Dhiman Chakraborty, Director

In the Standard Model, the top quark plays a unique role as the heaviest known fundamental particle and as a quark that decays before it is able to hadronize. Top quarks are expected to decay to a W -boson and a b -quark nearly 100% of the time. If the branching ratio of $t \rightarrow Wb$ is lower than one, the distribution of the number of b -tagged jets will shift to lower multiplicities. A simultaneous likelihood fit to the number of b -tagged jets distributions in the lepton+jets and dilepton channels is performed on 4.7 fb^{-1} of data collected by the ATLAS detector to extract both the branching ratio and the $t\bar{t}$ cross section. The branching ratio of $t \rightarrow Wb$, R , is measured to be 1.06 ± 0.11 , which is consistent with the Standard Model value. This is the first measurement of the $t \rightarrow Wb$ branching ratio performed with the ATLAS detector using both the lepton+jets and dilepton channels at the LHC. The $t\bar{t}$ cross section is measured to be $167^{+27}_{-26} \text{ pb}$, which agrees with NNLO predictions.



NORTHERN ILLINOIS UNIVERSITY
DE KALB, ILLINOIS

DECEMBER 2012

MEASUREMENTS OF THE TOP QUARK PAIR
PRODUCTION CROSS SECTION AND BRANCHING RATIO
TO A W -BOSON AND BOTTOM QUARK USING THE
SEMI-LEPTONIC AND DILEPTON FINAL STATES WITH
THE ATLAS DETECTOR AT THE LHC

BY

ROBERT E. CALKINS
© 2012 Robert E. Calkins

A DISSERTATION SUBMITTED TO THE GRADUATE SCHOOL
IN PARTIAL FULFILLMENT OF THE REQUIREMENTS
FOR THE DEGREE
DOCTOR OF PHILOSOPHY

DEPARTMENT OF PHYSICS

Dissertation Director:
Dhiman Chakraborty

ACKNOWLEDGEMENTS

I would like to first and foremost thank my parents for supporting me all of these years and providing me with the opportunities to pursue my interests. I would like to thank my adviser, Dhiman Chakraborty, for his guidance and supervision over the past years and without whom this thesis would not have been possible. Additionally I would like to thank Jean-Francois Arguin for suggesting the topic after supervising the b -tagging calibration analysis and pointing out the similarities in technique, as well as acting as a second adviser since the days when we were expecting a 14 TeV collider. I would like to thank Noemi Ochoa for her encouragement.

I am very grateful for the support I received from my NIU colleagues Chad Suhr and Gui Lima over the years. I would like to thank Sergey Uzunyan for his technical support with the NICADD cluster, which was used to produce the majority of the results found in this thesis. I would also like to thank Philippe Piot and the NIU beam physics group for allowing me to use some of their CPU resources.

The ALPGEN parameter studies would not have been possible without the guidance of Beate Heinemann and I would like to thank Michelangelo L. Mangano for taking the time to go over the results with me.

The foundation for the tag counting method in ATLAS was laid down by Bin Guo and Jie Yu, which made the task much easier. I would like to thank Gvantsa Mchedlidze for bringing the analysis in the dilepton channel to completion despite graduating and moving onto a new job. I would like to thank my fellow $t\bar{t}$ b -tagging calibrators, Martin zur Nedden, Agnieszka Leyko, Lukas Heinrich and Dominik Duda, for their support.

Much of this work was performed at the Argonne ATLAS Analysis Support Center and I would like to thank them for their support over the years. In particular, I would like to thank Rik Yoshida for introducing me to ROOT, Jimmy Proudfoot for his expertise on all things related with TileCal, Sasha Paramonov for his advice and Tom LeCompte for his guidance on analysis.

I would like to thank all of the people I worked with while I was based at CERN. In particular, Esteban Fullana and Belen Salvachua for all of their support over the years. Denis Fellmann for helping me to understand the ATLAS trigger system and his family for their hospitality. Ana Henriques for giving me the opportunity to serve as DQ coordinator for Tile. Peter Onysis for making that role easier to fill. Luca Fiorini and Irene Vichou for their supervision and guidance. Carlos Solans for helping me to understand the TileCal DAQ system and for livening up the Geneva area. The entire TileCal community for providing a great environment to work in.

My 2.5 years stationed at CERN would not have been possible without the financial support I received from the NSF, specifically the US LHC Graduate Student Support Award, in addition to the support the NSF has provided NICADD. This work was also supported by the NIU graduate school through the Dissertation Completion Fellowship.

Finally, I would like to thank all of my fellow ATLAS collaborators, in particular the ATLAS Top group, which made this work possible and anyone who responded to the various questions I posted to mailing lists.

DEDICATION

To my friends and family.

TABLE OF CONTENTS

	Page
List of Tables	ix
List of Figures	xv
List of Appendices	xxiv
Chapter	
1 The Standard Model	1
1.1 Generations	2
1.2 Interactions	3
1.3 Gauge theories	5
1.3.1 Electroweak Symmetry Breaking and the Higgs Mechanism .	7
1.3.2 Weinberg, Salam, Glashow model	9
1.4 Quantum Chromodynamics	11
1.4.1 Jets	11
1.5 Top Quarks within the Standard Model	13
1.5.1 Top Quark Production and Decay	14
1.6 Beyond the Standard Model	19
1.6.1 Supersymmetry	19
2 The Large Hadron Collider	23
2.1 Injection Chain	24
3 The ATLAS Detector	26
3.1 Magnets	28

Chapter	Page
3.2 Tracking	28
3.2.1 Inner Detector	29
3.2.2 Pixel Layers	30
3.2.3 Silicon Layers	32
3.2.4 Transition Radiation Tracker	32
3.2.5 Muon Spectrometer	34
3.2.6 Cathode Strip Chambers	36
3.2.7 Monitored Drift Tubes	37
3.2.8 Resistive Plate Chambers	39
3.2.9 Thin Gap Chambers	39
3.3 Calorimetry	40
3.3.1 Liquid Argon Calorimeter	40
3.3.2 Tile Calorimeter	43
3.4 Trigger and DAQ	45
3.4.1 Level 1	45
3.4.2 Level 2 and Event Filter	47
3.5 ATLAS's Luminosity Detectors	48
4 Luminosity	50
4.1 Luminosity Determination and Uncertainty	51
5 Physics Object Reconstruction and Event Selection	53
5.1 Trigger	54
5.1.1 Electron Triggers	55
5.1.2 Muon Triggers	55

Chapter	Page
5.2 Electron Identification	56
5.2.1 Determination QCD Fake Electron Contributions to Signal . .	57
5.3 Muon Identification	58
5.3.1 Determination QCD Fake Muon Contributions to Signal . . .	59
5.4 Jet Reconstruction	59
5.4.1 Determination of the Jet Energy Scale	61
5.5 Missing Energy Reconstruction.	63
5.6 Event Selection	64
6 Monte Carlo Simulation	68
6.1 $t\bar{t}$ samples.	72
6.2 Vector Boson + Jets modeling	73
6.2.1 ALPGEN parameters	75
6.2.1.1 ptjmin and etclu.	76
6.2.1.2 ktfac.	77
6.2.1.3 qfac.	83
6.2.1.4 iqopt.	83
6.2.1.5 PYTHIA tunes	88
6.2.1.6 Overall effects	91
6.2.1.7 Conclusions	91
6.2.2 Vector Boson + Heavy Flavor Production	94
6.3 Other Processes	94
6.4 Detector Simulation	95
7 Extraction of R	97
7.1 Introduction	98

Chapter	Page
7.2 Method	99
7.3 Systematic Uncertainties	104
7.4 Results.	105
8 Conclusions	114
8.1 Remarks for the future	116
References.	118
Appendices	136

LIST OF TABLES

Table	Page
1.1 Strength of coupling constants	5
1.2 Summary of Electroweak Bosons	10
2.1 Table of the LHC machine parameters for a typical late 2011 proton-proton run [1]. The machine parameters evolved rapidly during the 2011 running period.	23
3.1 Summary of trigger level input/output rates [2].	26
3.2 Summary of the ATLAS inner detector hit position resolution for the three inner detectors [3].. . . .	29
5.1 Summary table listing the event selection cuts applied for the five decay channels, e , μ , ee , $e\mu$ and $\mu\mu$	67
6.1 Listing of ALPGEN parameters varied.. . . .	75
6.2 Listing of available ALPGEN renormalization/factorization scale (Q) forms for W+jets production. The <code>qfac</code> parameter is described in Sec. 6.2.1.3 and m_W is the mass of the W -boson. The sums over p_T treat p_T as a scalar term.	86
7.1 Table of relative uncertainties in % for the simultaneous measurement of R and $\sigma_{t\bar{t}}$	106
7.2 Table of relative uncertainties in % for the measurements of R and $\sigma_{t\bar{t}}$, with $\sigma_{t\bar{t}}$ being fixed at 166.8 pb in the fit for the measurement of R and R fixed at 0.999 for the measurement of $\sigma_{t\bar{t}}$	107

Table	Page
A.1 The five largest F_{ijk} terms for jets with p_T above 25 GeV for the e channel (top) and μ channel (bottom) [4]. The largest $t\bar{t}$ term is F_{202} , which are events with two b -jets and two light jets. The background is dominated by the F_{004} term, which are events with four light jets. Uncertainties are statistical only.	145
A.2 The five largest F_{ijk} contributions for the 30-40 GeV p_T bin. Most $t\bar{t}$ events don't have any jets with p_T in the 30-40 GeV range and about 25% have one light jet that falls within the p_T acceptance. The background event terms are dominated by the case where no jets are contributed and the case where just one light jet falls within the p_T bin acceptance.	145
B.1 ($\mu+e$ combined). Systematic and statistical uncertainties for the IP3D+SV1 tagger at a working point corresponding to a 80% b -tagging efficiency.	165
B.2 ($\mu+e$ combined). Systematic and statistical uncertainties for the IP3D+SV1 tagger at a working point corresponding to a 70% b -tagging efficiency.	166
B.3 ($\mu+e$ combined). Systematic and statistical uncertainties for the IP3D+SV1 tagger at a working point corresponding to a 60% b -tagging efficiency.	167
B.4 ($\mu+e$ combined). Systematic and statistical uncertainties for the JetFitterCOMBNN tagger at a working point corresponding to a 70% b -tagging efficiency.	168
B.5 ($\mu+e$ combined). Systematic and statistical uncertainties for the JetFitterCOMBNN tagger at a working point corresponding to a 80% b -tagging efficiency.	169
B.6 ($\mu+e$ combined). Systematic and statistical uncertainties for the JetFitterCOMBNN tagger at a working point corresponding to a 60% b -tagging efficiency.	170
B.7 ($\mu+e$ combined). Systematic and statistical uncertainties for the JetFitterCOMBNN tagger at a working point corresponding to a 57% b -tagging efficiency.	171

Table	Page
B.8 ($\mu+e$ combined). Systematic and statistical uncertainties for the MV1 tagger at a working point corresponding to a 85% b -tagging efficiency.	172
B.9 ($\mu+e$ combined). Systematic and statistical uncertainties for the MV1 tagger at a working point corresponding to a 75% b -tagging efficiency.	173
B.10 ($\mu+e$ combined). Systematic and statistical uncertainties for the MV1 tagger at a working point corresponding to a 70% b -tagging efficiency.	174
B.11 ($\mu+e$ combined). Systematic and statistical uncertainties for the MV1 tagger at a working point corresponding to a 60% b -tagging efficiency.	175
B.12 ($\mu+e$ combined). Systematic and statistical uncertainties for the SV0 tagger at a working point corresponding to a 50% b -tagging efficiency.	176
B.13 (e +jets). Systematic and statistical uncertainties for the IP3D+SV1 tagger at a working point corresponding to a 80% b -tagging efficiency.	177
B.14 (e +jets). Systematic and statistical uncertainties for the IP3D+SV1 tagger at a working point corresponding to a 70% b -tagging efficiency.	178
B.15 (e +jets). Systematic and statistical uncertainties for the IP3D+SV1 tagger at a working point corresponding to a 60% b -tagging efficiency.	179
B.16 (e +jets). Systematic and statistical uncertainties for the JetFitterCOMBNN tagger at a working point corresponding to a 70% b -tagging efficiency.	180
B.17 (e +jets). Systematic and statistical uncertainties for the JetFitterCOMBNN tagger at a working point corresponding to a 80% b -tagging efficiency.	181
B.18 (e +jets). Systematic and statistical uncertainties for the JetFitterCOMBNN tagger at a working point corresponding to a 60% b -tagging efficiency.	182

Table	Page
B.19 (e +jets). Systematic and statistical uncertainties for the JetFitterCOMBNN tagger at a working point corresponding to a 57% b -tagging efficiency.	183
B.20 (e +jets). Systematic and statistical uncertainties for the MV1 tagger at a working point corresponding to a 85% b -tagging efficiency. 184	
B.21 (e +jets). Systematic and statistical uncertainties for the MV1 tagger at a working point corresponding to a 75% b -tagging efficiency. 185	
B.22 (e +jets). Systematic and statistical uncertainties for the MV1 tagger at a working point corresponding to a 70% b -tagging efficiency. 186	
B.23 (e +jets). Systematic and statistical uncertainties for the MV1 tagger at a working point corresponding to a 60% b -tagging efficiency. 187	
B.24 (e +jets). Systematic and statistical uncertainties for the SV0 tagger at a working point corresponding to a 50% b -tagging efficiency.	188
B.25 (μ +jets). Systematic and statistical uncertainties for the IP3D+SV1 tagger at a working point corresponding to a 80% b -tagging efficiency.	189
B.26 (μ +jets). Systematic and statistical uncertainties for the IP3D+SV1 tagger at a working point corresponding to a 70% b -tagging efficiency.	190
B.27 (μ +jets). Systematic and statistical uncertainties for the IP3D+SV1 tagger at a working point corresponding to a 60% b -tagging efficiency.	191
B.28 (μ +jets). Systematic and statistical uncertainties for the JetFitterCOMBNN tagger at a working point corresponding to a 70% b -tagging efficiency.	192
B.29 (μ +jets). Systematic and statistical uncertainties for the JetFitterCOMBNN tagger at a working point corresponding to a 80% b -tagging efficiency.	193

Table	Page
B.30 (μ +jets). Systematic and statistical uncertainties for the JetFitterCOMBNN tagger at a working point corresponding to a 60% b -tagging efficiency.	194
B.31 (μ +jets). Systematic and statistical uncertainties for the JetFitterCOMBNN tagger at a working point corresponding to a 57% b -tagging efficiency.	195
B.32 (μ +jets). Systematic and statistical uncertainties for the MV1 tagger at a working point corresponding to a 85% b -tagging efficiency. 196	
B.33 (μ +jets). Systematic and statistical uncertainties for the MV1 tagger at a working point corresponding to a 75% b -tagging efficiency. 197	
B.34 (μ +jets). Systematic and statistical uncertainties for the MV1 tagger at a working point corresponding to a 70% b -tagging efficiency. 198	
B.35 (μ +jets). Systematic and statistical uncertainties for the MV1 tagger at a working point corresponding to a 60% b -tagging efficiency. 199	
B.36 (μ +jets). Systematic and statistical uncertainties for the SV0 tagger at a working point corresponding to a 50% b -tagging efficiency.	200
C.1 Table of relative uncertainties in % for the measurement of R and $\sigma_{t\bar{t}}$ using the 2-D method.	205
D.1 Event yields for the five analysis channels. Uncertainties include both systematic and statistical uncertainties. Total uncertainties account for correlated systematics across samples such as jet energy scale and fragmentation.	207
E.1 Table of relative uncertainties in % for the measurement of R and $\sigma_{t\bar{t}}$ in the electron channel.	212
E.2 Table of relative uncertainties in % for the measurement of R and $\sigma_{t\bar{t}}$ in the muon channel.	213

Table	Page
E.3 Table of relative uncertainties in % for the measurement of R and $\sigma_{t\bar{t}}$ in the lepton+jets channel.	214
E.4 Table of relative uncertainties in % for the measurement of R and $\sigma_{t\bar{t}}$ in the ee channel.	215
E.5 Table of relative uncertainties in % for the measurement of R and $\sigma_{t\bar{t}}$ in the $e\mu$ channel.	216
E.6 Table of relative uncertainties in % for the measurement of R and $\sigma_{t\bar{t}}$ in the $\mu\mu$ channel.	217
E.7 Table of relative uncertainties in % for the measurement of R and $\sigma_{t\bar{t}}$ in the dilepton channel.	218
E.8 Table of results for all of the channels.	219

LIST OF FIGURES

Figure	Page
1.1 The W -fermion interaction vertex.	2
1.2 The Cabibbo-Kobayashi-Maskawa (CKM) matrix.	3
1.3 Electron-positron scattering	4
1.4 The self-interaction vertex for the scalar field ϕ	8
1.5 Hadronization of a pair of quarks	12
1.6 Constraints on the Higgs mass from measurements of the top and W boson mass [5].	13
1.7 SM tree level $t\bar{t}$ production mechanisms	15
1.8 SM $t\bar{t}$ decay to a W -boson and a b -quark.	16
1.9 Approximate branching ratios for $t\bar{t}$ events.	17
1.10 A tree level Feynman diagram showing production of a $t\bar{t}$ event through gluon-gluon fusion which then decays through the lepton+jets channel.	18
1.11 A top quark decaying into a b -quark and a charged Higgs boson . . .	20
1.12 Branching ratios for $t \rightarrow H^+b$ and H^+ as a function of $\tan(\beta)$ for a charged Higgs with a mass of 100 GeV [6].	21
2.1 The CERN Accelerator Complex showing the LHC and the injection chain [7]. Other CERN physics programs are also included such as the neutrino beam to the Gran Sasso laboratory.	24
3.1 Cutaway diagram of the ATLAS detector with the major sub-detector systems labeled [8]. Note the people included in the figure for a sense of scale.	27

Figure	Page
3.2 Overview of the ATLAS tracker system providing coverage of $ \eta < 2.5$ [8]. The geometry for the inner tracking detectors consists mainly of cylinders and disks.	30
3.3 Track reconstruction efficiency for tracks with $p_T > 400$ MeV as a function of η in pile-up conditions ranging from one primary vertex to 41 vertices. “Robust” tracks have at least nine hits between the the SCT and pixel layers and no missing hits in the pixel layers where an expected hit is derived from the reconstructed track trajectory [9].	31
3.4 Discriminating variable based upon TRT hit information used for pion-electron identification for data and Monte Carlo simulations [10]. The figure shows difference between the relativistic γ factor and high threshold hit probability for pions and electrons with the same momentum. By looking at the number of hits in the TRT that pass the high threshold criteria, discrimination between electrons and charged hadrons can be achieved.	34
3.5 The ATLAS Muon spectrometer showing the position and arrangement of the various detector technologies [8]. Like the inner detector, the geometry of the muon spectrometer also consists of cylinders and disks or wheels.	35
3.6 Reconstructed muon p_T resolution for central muons reconstructed in the inner detector (left) and the muon spectrometer (right) [11]. .	36
3.7 Geometry for the barrel Muon spectrometer showing the arrangement of inner and outer chambers which allows for overlapping coverage [8].	37
3.8 Muon reconstruction efficiency for $Z \rightarrow \mu\mu$ events as measured in Monte Carlo simulation and in the 2011 dataset using a “tag-and-probe” technique [12].	38
3.9 The combined ATLAS calorimeter system showing the various sub-detectors and cylindrical geometry [8]. The liquid argon calorimeter is encased within a precision controlled cryostat (not labeled).	41
3.10 Accordion geometry and segmentation of the central barrel LArg calorimeter [8]. The three layers of longitudinal segmentation allows for reconstruction of incident photon direction.	42

Figure	Page
3.11 Diagram of a TileCal module showing the orientation of the steel and scintillating plates with respect to the beam direction [8]. The PMTs are located in the girder on top of each Tile module and light is collected from the scintillator tiles through WLS fibers that run along the edges of the module.	44
3.12 Overview of the ATLAS trigger system and data flow from detector electronics to events on tape [8].	46
5.1 The '4-2-0' scheme for TopoCluster seeding shown in 2D. The "seed" cell in the center is colored in red, with an energy greater than $4\sigma_{noise}$. The surrounding cells, in green, must have $E > 2\sigma_{noise}$	60
5.2 Summary of event selection efficiencies for $t\bar{t}$ events including branching ratios.	66
6.1 A Feynman diagram of $gg \rightarrow q\bar{q}$ illustrating the hard scattering region handled by the matrix element calculation in black and the regions handled by parton shower modeling in red.	70
6.2 The process in the left would contribute to the total cross section from the matrix element generator while the one of the right would arise from the parton shower as the final state gluon appears from initial-state radiation.	71
6.3 Reconstructed jet multiplicity in candidate $t\bar{t}$ events compared with MC predictions. Uncertainties are derived using AcerMC and the relative uncertainty is applied to nominal MC@NLO samples [13].	73
6.4 Jet multiplicity and p_T of the leading jet for W+jet events in data and as described by the ATLAS MC chain [14]. The ALPGEN W+jet Monte Carlo jet multiplicity agrees with the data quite well as deviations are less than 10% and covered by the uncertainties. The event kinematics are also well modeled as the leading jet p_T as predicted by ALPGEN agrees with the data.	74

Figure		Page
6.5	Effect of varying <code>ptjmin</code> on leading jet p_T for <code>ptjmin</code> values between 10 and 30 GeV for final W+jets states with at least four high- p_T jets. The top plot shows the leading jet p_T spectrum. The bottom plot shows the leading jet p_T spectrum normalized to the leading jet p_T spectrum derived from the nominal <code>ptjmin</code> =15 GeV sample. At low p_T , there is a turn on curve for <code>ptjmin</code> >20 GeV.	78
6.6	Effect of varying <code>ptjmin</code> on jet multiplicity for <code>ptjmin</code> values between 10 and 30 GeV for final W+jets states with at least one high- p_T jet. The top plot shows the jet multiplicity for the various <code>ptjmin</code> variations. The bottom plots shows the same distribution normalized to the <code>ptjmin</code> =15 GeV. The <code>ptjmin</code> =10 GeV jet multiplicity distribution closely matches the <code>ptjmin</code> = 15 GeV but higher values of <code>ptjmin</code> > 20 GeV have lower cross sections.	79
6.7	The top plot shows the leading jet p_T distribution for <code>ktfac</code> values between 0.5 and 2 for final W+jets states with at least one high- p_T jet. The bottom plot is the ratio of the above distributions to the nominal <code>ktfac</code> =1 value and shows a systematic dependence.	80
6.8	Effect of varying <code>ktfac</code> on leading jet p_T for <code>ktfac</code> values between 0.5 and 2 for final W+jets states with at least four high- p_T jets. Like Fig. 6.7, the top plot is the leading jet p_T and the lower plot has been normalized to the nominal <code>ktfac</code> . The bottom plots shows that while the normalization is affected by <code>ktfac</code> , the shape of the distribution is unaffected.. . . .	81
6.9	Effect of varying <code>ktfac</code> on jet multiplicity for <code>ktfac</code> values between 0.5 and 2 for final W+jets states with at least one high- p_T jet. The top plot shows the jet multiplicity while the bottom plot shows the jet multiplicities normalized to the nominal distribution. Since <code>ktfac</code> affects the value of α_s , the jet multiplicity is very sensitive to the <code>ktfac</code> setting.	82
6.10	Effect of varying <code>qfac</code> on leading jet p_T for <code>qfac</code> values between 0.5 and 2 for final W+jets states with at least one high- p_T jet. The leading jet p_T is shown in the top plot while the distribution normalized to the default <code>qfac</code> parameter is shown below, which illustrates some dependence on the value of <code>qfac</code>	84

Figure	Page
6.11 Effect of varying qfac on jet multiplicity for qfac values between 0.5 and 2 for final W+jets states with at least one high- p_T jet. The top plot shows the jet multiplicity distribution while the bottom plot shows the distributions normalized to the nominal distribution showing the shape dependence on qfac	85
6.12 Effect of different iqopt models on H_T (muon, selected jets) for final W+jets states with at least one high- p_T jet. The top plot shows the distribution of H_T (muon, selected jets) while the bottom plot is normalized to the nominal distribution. At low H_T , where the scales are dominated by the m_W terms, the three distributions are approximately equal but as H_T increases, the scales start to diverge.	87
6.13 Effect of different HERWIG/JIMMY and several PYTHIA underlying event tunes on jet multiplicity for final W+jets states with at least one high- p_T jet. The jet multiplicity distributions are shown in the top plot and the distributions normalized to the HERWIG/JIMMY distribution is shown in the bottom plot. The three Perugia tunes show an overall different jet multiplicity with respect to the HERWIG/JIMMY distribution.	89
6.14 The same plots as are shown in Fig. 6.13 but omitting the HERWIG/JIMMY distribution and the bottom plot is normalized to the nominal Perugia distribution instead. The “cross over” around six jets is due to the matrix element-parton shower matching and is explained in more detail in Sec. 6.2.1.5.	90
6.15 The effect of varying the ALPGEN parameters on the complete analysis described in Ref. [15]. Each point is the result when using samples produced with that particular variation normalized to the baseline result. The large variations in the results for H_T originate from the effects noted in earlier sections. The deviations from one can be interpreted as the systematic uncertainty due to the parameter variation.	92
7.1 The n -tag distribution template for the electron + jets channel. The 0-tag bin is shown for illustrative purposes only.	100
7.2 The n -tag distribution template for the muon + jets channel. The 0-tag bin is shown for illustrative purposes only.	101
7.3 The n -tag distribution template for the electron-electron channel.	101

Figure	Page
7.4 The n -tag distribution template for the electron-muon channel. . . .	102
7.5 The n -tag distribution template for the muon-muon channel.	102
7.6 Linearity test of the fit response to varying R values. The fit to a linear function returns a slope consistent with one and zero y -intercept.	104
7.7 Linearity test of the fit response to re-scaling the $t\bar{t}$ cross section. The resulting fit to a line is consistent with a zero y -intercept and a slope equal to one.	105
7.8 Contour from the likelihood fit. The $1\text{-}\sigma$ (green) and $2\text{-}\sigma$ (yellow) bands corresponding to the statistical error of the fit are shown. . .	108
7.9 The n -tag distribution for the electron + jets channel after fitting showing the statistical uncertainty. The 0-tag bin is shown for illustrative purposes only.	109
7.10 The n -tag distribution for the muon + jets channel after fitting showing the statistical uncertainty. The 0-tag bin is shown for illustrative purposes only.	110
7.11 The n -tag distribution for the electron-electron channel after fitting showing the statistical uncertainty.	111
7.12 The n -tag distribution for the electron-muon channel after fitting showing the statistical uncertainty.	112
7.13 The n -tag distribution for the muon-muon channel after fitting showing the statistical uncertainty.	113
8.1 The result of the measurement of R presented in this thesis is shown along with the latest results from CDF [16], D0 [17] and CMS [18].	115
A.1 Figure illustrating key parameters in b -tagging algorithms [19]. Since b -hadrons travel some distances before decaying, there is often a secondary vertex in the event. Tracks coming from such a vertex will have large impact parameters with respect to the primary vertex. . .	138

Figure	Page
A.2 B-jet efficiency and light jet rejection curves for a variety of ATLAS b -tagging algorithms based on simulated $t\bar{t}$ events. The MV1 tagging algorithm performs well across the entire range of efficiency working points [20].	141
A.3 The n -tag distributions for the electron (left) and muon (right) channels for data and Monte Carlo [4]. The MV1 tagger at a 70% efficiency working point was used in these particular figures. The uncertainty band shows the normalization uncertainties for the QCD fake lepton background.	142
A.4 The n -tag distributions for the electron-electron, muon-muon and electron-muon channels for data and Monte Carlo [4]. The statistical uncertainty is shown on the data points while the QCD multijet normalization uncertainty is the uncertainty band attached to the Monte Carlo distribution.	143
A.5 Comparison of the overall uncertainties for the analysis when fixing the normalization as opposed to letting them float. For the majority of the p_T bins, the uncertainty is lower when allowing both the $t\bar{t}$ normalization and the backgrounds float.	147
A.6 The linearity of the fit is shown for the MV1 tagger for several p_T bins. The top left plots shows the linearity for the 30-40 GeV bin, followed by the the 75-90 GeV bin on the top right. The bottom row shows the linearity plot for the 90-110 GeV p_T bin on the left and the 200-300 GeV p_T bin on the right. The deviations from linearity are typically small.	148
A.7 This figure shows the n -tag distribution for the electron channel for the nominal MC sample and the JES systematic varied up and down by 1σ	150
A.8 The $t\bar{t}$ cross section results as extracted from the numerous fits to data. Each entry corresponds to an individual p_T bin, tagger and working point. The peak around 165pb is due to the Gaussian constraint on the $t\bar{t}$ cross section fit, which makes this a preferred value.	

Figure	Page
A.9 The b -tagging efficiency in MC and as measured in data for the JetFitterCombNN tagger at the 57%, 60%, 70% and 80% average efficiency working points(left) for the lepton+jets channel. The plots on the right show the scale factor (data/MC) needed to scale the MC b -tagging efficiency to the data [4].	158
A.10 The b -tagging efficiency in MC and as measured in data for the MV1 tagger at the 60%, 70%, 75% and 85% average efficiency working points(left) for the lepton+jets channel. The plots on the right show the scale factor (data/MC) needed to scale the MC b -tagging efficiency to the data [4].	159
A.11 The b -tagging efficiency in MC and as measured in data for the IP3D+SV1 tagger at the 60%, 70% and 80% average efficiency working points(left) for the lepton+jets channel. The plots on the right show the scale factor (data/MC) needed to scale the MC b -tagging efficiency to the data [4].	160
A.12 The b -tagging efficiency in MC and as measured in data for the SV0 tagger at a 50% average efficiency working point(left) for the lepton+jets channel. The plot on the right shows the scale factor (data/MC) needed to scale the MC b -tagging efficiency to the data [4].	161
A.13 Distribution of the p_T^{rel} variable for b , c and light jets with p_T between 40 and 50 GeV before any b -tagging selection has been applied for data and Monte Carlo simulation [20].. . . .	161
A.14 Scale factors for the muon and $t\bar{t}$ based calibrations as a function of jet p_T [4]. For all methods, the results are consistent with unity and all methods agree within the uncertainties. The muon based calibrations are only valid up to 200 GeV whereas the $t\bar{t}$ based calibrations extend up to 300 GeV.	162
C.1 The distributions of $ \eta \times \text{Charge}$ for the electron (left) and muon (right) channel before any tagging requirement is applied.	203
C.2 The 2-dimensional templates for the electron channel for $t\bar{t}$ (top) and the backgrounds(bottom).	204

Figure	Page
D.1 The W transverse mass distributions for the electron + jets and muon+jets channels.	208
D.2 The E_T^{miss} distributions for the electron + jets and muon+jets channels.	208
D.3 The dilepton invariant mass distributions for the electron-electron and muon-muon channels.	209
D.4 The H_T distribution for the electron-muon channel.	209
E.1 The likelihood function for each of the channels evaluated at the combined fitted value for the $t\bar{t}$ cross section.	219

LIST OF APPENDICES

Appendix	Page
A B-tagging Calibration	136
A.1 B-tagging Algorithms	138
A.2 Tag Counting Method	140
A.2.1 p_T binning	147
A.2.2 Systematic uncertainties	149
A.2.3 Results	150
A.3 Other Calibration Methods	151
A.3.1 other $t\bar{t}$ -based methods	152
A.3.2 p_T^{rel} method	153
A.3.3 <i>System8</i> method	155
A.4 Results.	156
B Tables of systematic uncertainties for the tag counting method.	163
C Two dimensional likelihood fit to extract R	201
D Event yields and control plots	206
E Measurements of R and the top pair cross section in the individual channels	210

CHAPTER 1

THE STANDARD MODEL

Ever since its advent in the late 1960s [21] and early 70s [22, 23], the Standard Model (SM) of particle physics has served as the theoretical backbone of phenomenology. The model consists of two sets of matter particles or “fermions”: quarks and leptons. It also contains a class of particles called bosons which carry the four forces (electromagnetism, weak nuclear, strong nuclear and gravity) between the quarks and leptons. As of today, three “generations” of fermions, each comprised of a pair of quark types and a pair of leptons, are known to exist, although the number of generations is not specified in the model. The SM has been an incredibly successful theory at explaining the majority of measured phenomena in particle physics. It is an exact theory but to use it practically requires solving it as a series of perturbative expansions or using other techniques such as lattice calculations [24].

In this Chapter, the structure of the Standard Model is presented starting with the generations of particles. The various interactions are described. An overview of gauge theories is presented as a build up to the description of electroweak symmetry breaking and the Higgs mechanism. The Weinberg-Salam-Glashow model of leptons is presented, showing the generation of electroweak boson masses. Quantum Chromodynamics is discussed with an overview of jet clustering. Top quarks are introduced with an emphasis on the production and decay mechanisms. Finally, physics scenarios beyond the Standard Model are presented with a focus on ways they could reveal themselves through the top quark sector.

1.1 Generations

The three fermion generations are labeled in increasing order of mass. The first generation is composed of particles that make up most of the matter we encounter in our daily lives : the electron, down and up-type quarks. There is also a weakly interacting electron neutrino. The second generation is composed of the muon, charm and strange-type quarks and the muon-neutrino. The third and the heaviest generation contains the tau lepton, tau neutrino, top and bottom-type quarks.

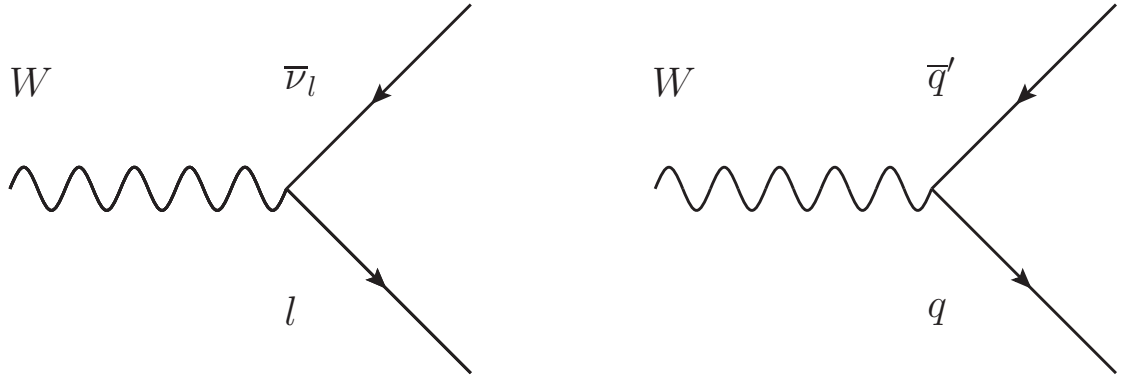


Figure 1.1: The W -fermion interaction vertex.

Different kinds of particles can be referred to as being of a different flavor. The particle's flavor can be distinguished from other similar types of particles by its mass and quantum numbers. Changes in flavor occur at tree level through emission or absorption of W -bosons as show in Fig. 1.1. In the lepton sector, tau and muon decays are mediated by virtual W -bosons. Lepton number violation occurring between electrons, taus and muons has not been observed but neutrino oscillations suggest that there is mixing between neutrino flavors. For quarks, mixing between generations is allowed and described by the Cabibbo-Kobayashi-Maskawa (CKM) matrix shown in Fig. 1.2 [25].

$$V = \begin{pmatrix} V_{ud} & V_{us} & V_{ub} \\ V_{cd} & V_{cs} & V_{cb} \\ V_{td} & V_{ts} & V_{tb} \end{pmatrix}$$

Figure 1.2: The Cabibbo-Kobayashi-Maskawa (CKM) matrix.

The CKM matrix is essentially a rotation matrix between the weak interaction states to which the W -bosons couple and the physical mass states. The SM allows for more than three generations but additional ones have not been discovered yet so the CKM matrix remains a 3×3 matrix. Elements of the CKM matrix have to be measured experimentally since they are fundamental constants of nature.

The CKM elements corresponding to light quarks are usually measured using various meson decays. The $|V_{tb}|$ element has been constrained to be greater than 0.89 at the 95% confidence level (C.L.) by the D0 collaboration by measuring the top quark branching fractions and assuming three generations [26]. Single top production rates can provide a direct measurement of $|V_{tb}|$ without any assumptions on the number of generations and this was measured at the Tevatron as $|V_{tb}| = 0.88 \pm 0.07$ [27]. This indicates that the majority of the time a top quark will decay into W -boson and a b -quark since the coupling is nearly unity.

1.2 Interactions

There are four known fundamental forces; gravity, electromagnetism, the strong force and the weak force. The Standard Model describes most of them with the exception of gravity. Within the Standard Model, all forces are mediated by boson exchange between particles as illustrated in Fig. 1.3. Photons are the mediators of

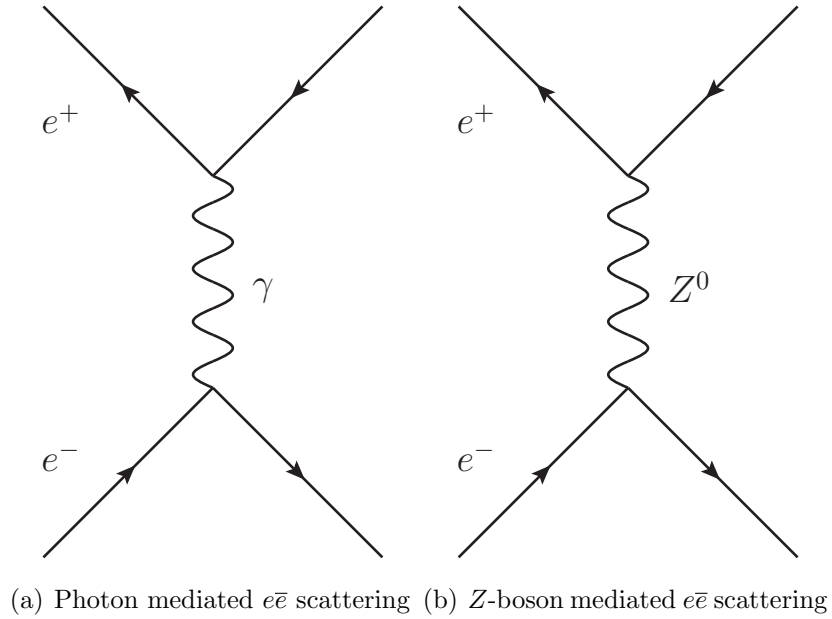


Figure 1.3: Electron-positron scattering

the electromagnetic force and couple to any charged particle. The W and Z bosons are exchanged under weak interactions. Gluons are the carriers of the strong force and couple to anything carrying color charge, even themselves.

The basic calculation of the rate of some transition from a particular initial state to a final state can be generalized as :

$$\text{rate} \propto (\text{amplitude})^2 \times (\text{Lorentz invariant phase space}). \quad (1.1)$$

[28] The Lorentz invariant phase space available to the process is determined by kinematics and the amplitude for the process is derived from theory. For perturbative calculations, we can expand the equation by its coupling constant for the interaction taking place. For coupling constants of the electroweak processes, the constants are much less than one so the first few terms of the expansion give a good approximation. For the strong force, the coupling constant is larger and more

Electrodynamics	$\alpha = \frac{e^2}{4\pi\hbar c} \approx \frac{1}{137}$
Electroweak	$\alpha_W = \frac{g^2}{4\pi} \approx 0.035$ but $G_F \approx 10^{-5}$
Strong	$\alpha_s(M_Z) \approx 0.1$

Table 1.1: Strength of coupling constants

terms have to be summed in the perturbative series to reach an acceptable level of accuracy. Fortunately the strong coupling constant is a running constant that decreases as the scale of the interaction increases, making perturbative calculations more accurate for high energy interactions [29]. The strength of the couplings for the three forces described by the SM are summarized in Tab. 1.1.

1.3 Gauge theories

Gauge theories form the backbone of the SM framework. A gauge theory is one that is invariant under gauge transformations. Starting with the Dirac equation,

$$(i\gamma^\mu\partial_\mu - m)\psi(x) = 0, \quad (1.2)$$

it is possible to write down a Lagrangian for a free spin- $\frac{1}{2}$ particle with mass m :

$$\mathcal{L} = \bar{\psi}(x)(i\gamma^\mu\partial_\mu - m)\psi(x) = i\bar{\psi}(x)\gamma^\mu\partial_\mu\psi(x) - m\bar{\psi}(x)\psi(x), \quad (1.3)$$

where γ are the Dirac or gamma matrices. The solution(ψ) to these equations(1.2,1.3) are 4-dimensional spinor fields that can be decomposed into left and right handed components.

If we apply a global phase transformation to a field,

$$\psi \rightarrow e^{i\theta}\psi, \quad (1.4)$$

terms in the Lagrangian(1.3) that contain $\bar{\psi}\psi$ are invariant under this transformation [30]. The difficulty arises if we want to apply a local phase transformation instead,

$$\psi \rightarrow e^{i\theta(x)}\psi, \quad (1.5)$$

then all terms in the Lagrangian with a derivative will pick up additional terms from $\theta(x)$ and the Lagrangian is no longer invariant. The solution to preserve invariance is to add a massless gauge field into the mix to absorb the extra terms. Adding a mass term,

$$\frac{1}{8\pi}\left(\frac{mc}{\hbar}\right)^2 A^\nu A_\nu, \quad (1.6)$$

for the new field (A) into the Lagrangian also causes it to lose local gauge invariance. In particular, this new gauge field must transform under a gauge transformation as:

$$A_\mu \rightarrow A_\mu - \frac{1}{e}\partial_\mu\alpha \quad (1.7)$$

and all derivatives must be replaced with the covariant derivative:

$$D_\mu\psi = \partial_\mu\psi + ieA_\mu\psi. \quad (1.8)$$

As a consequence, there is now a term like :

$$- q \bar{\psi} \gamma^\mu \psi A_\mu \quad (1.9)$$

in the Lagrangian which corresponds to a current. The original fields couple to the gauge field with strength q , which is simply e in the case of electrodynamics. The transformation $e^{i\theta}$ can be thought of as a rotation preserving $U(1)$ symmetry. Noether's theorem states that where there is a symmetry present in the Lagrangian there is also an associated conserved current.

In the 1950's, Yang and Mills generalized this to apply to field doublets (Eq. 1.10) in a $SU(2)$ symmetry as well [31].

$$\psi = \begin{pmatrix} \psi_1 \\ \psi_2 \end{pmatrix} \quad (1.10)$$

The procedure is similar to the field singlets procedure. The gauge fields must be massless and are defined to absorb the terms that originate from the transformation. The covariant derivative is also redefined. The symmetry is no longer just $U(1)$ but now has a $SU(2)$ symmetry as well. This adds three new gauge fields, B_μ , to the Lagrangian in addition to the gauge field, A , corresponding to the $U(1)$ symmetry.

1.3.1 Electroweak Symmetry Breaking and the Higgs

Mechanism

At this stage, there are a total of four massless gauge bosons corresponding to the various symmetries. Breaking the symmetry will allow us to generate masses for

some of the massless gauge bosons. We start by looking at a complex scalar field that has a complex mass term and a four self-interaction vertex (Fig. 1.4).

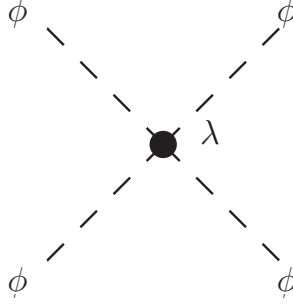


Figure 1.4: The self-interaction vertex for the scalar field ϕ

This scalar field contributes a potential to the Lagrangian:

$$V = \frac{1}{2}m^2\phi^*\phi + \frac{\lambda}{4}(\phi^*\phi)^2. \quad (1.11)$$

This potential has a local minimum at $\phi = 0$ and global minimums at $|\phi| = \sqrt{-\frac{m^2}{\lambda}} \equiv v$. The ground state for this scalar field is the vacuum expectation value. The scalar field can be expanded around the vacuum expectation value and decomposed into real and complex components ($\phi_1(x)$ and $\phi_2(x)$ respectively) as shown in Eq. 1.12.

$$\phi = \frac{1}{\sqrt{2}}(\phi_1(x) + i\phi_2(x)) \quad (1.12)$$

With this parameterization of the scalar field, it is possible to utilize the symmetry and perform a transformation such that the vacuum expectation value of ϕ_2 is 0. After substituting this into the Lagrangian for a scalar field and doing the usual covariant derivative trick :

$$\mathcal{L} = \frac{1}{2}(\partial_\mu + \frac{ie}{\hbar c}A_\mu)\phi^*(\partial^\mu + \frac{ie}{\hbar c}A^\mu)\phi + \frac{1}{2}m^2(\phi^*\phi) - \frac{1}{4}\lambda^2(\phi^*\phi)^2 - \frac{1}{16\pi}F^{\mu\nu}F_{\mu\nu}, \quad (1.13)$$

the Lagrangian is invariant under local gauge transformations. Since ϕ is a scalar field, we can redefine a new field that is shifted by a constant term:

$$\phi(x)' = v + \phi(x). \quad (1.14)$$

If we change variables in Eq. 1.13 with Eq. 1.14, a Goldstone boson will remain as the ϕ_2 field and a mass term for the gauge field, A^μ , is created. The trick here is to now pick a particular gauge. By applying a transformation of $\phi' \rightarrow \phi'' = e^{-i\theta} \phi'$ where $\theta = -\tan^{-1} \frac{\phi_1}{\phi_2}$, the ϕ_2 terms will disappear from the Lagrangian. The mass term for the gauge field remains and the Lagrangian now only contains physical fields including the scalar field which is now massive ¹.

1.3.2 Weinberg, Salam, Glashow model

Weinberg, Salam and Glashow unified electrodynamics with the weak force into a single theory [21]. Leptons are grouped into weak isospin doublets or singlets based on flavor and handedness,

$$\psi_L = \begin{pmatrix} \nu_{eL} \\ e_L \end{pmatrix}; \quad \psi_R = e_R, \quad (1.15)$$

where L and R stand for left and right handedness corresponding to the orientation of the particle's spin axis with respect to its direction of motion. If neutrinos are massless, only left-handed ones exist leaving the right-handed component as a singlet. It is useful to add gauge invariance to the Lagrangian in the form of a $SU(2) \times U(1)$ symmetry with weak isospin (T) charge corresponding to the $SU(2)$ gauge fields

¹For a more complete explanation, consult [28], [30], [32] or [33].

(A^μ) and hypercharge (Y) for the $U(1)$ (B^μ field) symmetry. These are related to electrodynamic charge through

$$Q = T^3 + \frac{Y}{2}. \quad (1.16)$$

These gauge fields are still massless but by introducing them as a doublet,

$$\phi = \begin{pmatrix} \phi^+ \\ \phi_0 \end{pmatrix} \quad (1.17)$$

and applying the Higgs mechanism such that

$$\langle \phi \rangle = \begin{pmatrix} 0 \\ v \end{pmatrix}, \quad (1.18)$$

the three fields associated with the $SU(2)$ invariance gain mass terms but the $U(1)$ field remains massless. Due to the Higgs field, mass terms for the leptons appear in the Lagrangian. The four electroweak vector bosons are built out of the four gauge fields (Tab. 1.2). The coupling constants, g and g' , corresponding to the $SU(2)$ and

	construction	Mass
W_μ^\pm	$\frac{1}{\sqrt{2}}(A_\mu^1 \mp iA_\mu^2)$	$\frac{gv}{2}$
Z_μ^0	$\frac{1}{\sqrt{g^2 + g'^2}}(gA_\mu^3 - g'B_\mu)$	$\sqrt{g^2 + g'^2}\frac{v}{2}$
A_μ	$\frac{1}{\sqrt{g^2 + g'^2}}(g'A_\mu^3 + gB_\mu)$	0

Table 1.2: Summary of Electroweak Bosons

$U(1)$ currents respectively, are related to the electron charge by

$$e = \frac{gg'}{\sqrt{g^2 + g'^2}}. \quad (1.19)$$

1.4 Quantum Chromodynamics

The Weinberg-Glashow-Salam model unifies the electroweak interactions but there are still the interactions corresponding to the strong force remaining. Quantum Chromodynamics (QCD) takes its name from the name given to the charges involved in the interaction. In addition to hypercharge and weak isospin, quarks carry “color” charge. There are three kinds of color charge and corresponding anti-charges. QCD is built around a $SU(3)$ symmetry with local invariance. This gives rise to eight gauge bosons that mediate the strong force. These are the gluons and they carry one unit of color and one unit of anti-color charge. Since gluons carry color charge, they have self-interactions. This causes a sort of charge screening effect similar to electric charge screening that occurs in atoms. QCD exhibits “asymptotic freedom” which means the force becomes weaker at short distances and at higher momentum scales [34]. In nature, only colorless states are observed which means quarks only exist in bound states.

1.4.1 Jets

Since quarks and gluons only exist in bound states, we don’t really observe isolated bare quarks except the top quark, which decays before it has time to form a bound state. As two quarks are separated, the strong force between them increases which is equivalent to the potential energy increasing. This energy transforms into quark-anti-quark pairs. This process of hadronization results in a collimated “jet” of particles (Fig. 1.5).

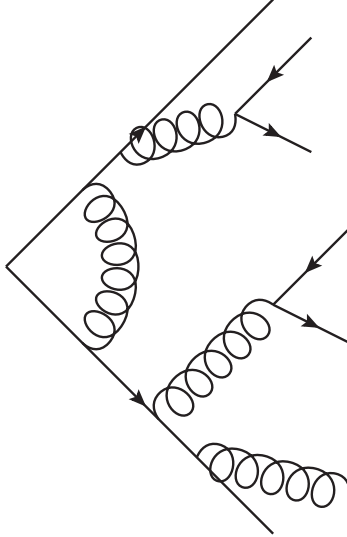


Figure 1.5: Hadronization of a pair of quarks

There is no natural definition of what is a “jet”. A jet definition consists of two parts, a clustering algorithm and a set of algorithm parameters. At the Tevatron, cone-based algorithms were used for a variety of measurements. These take high p_T clusters of energy and sum the energy in a cone around them with a fixed radius [35]. This type of clustering has some parameters that must be defined such as cone radius and an arbitrary split/merge fraction that comes into play when two nearby cones overlap each other. At the LHC, k_T based algorithms [36] are the defaults for the CMS and ATLAS experiments. The clustering is based around a parameter,

$$d_{ij} = \min(p_{T,i}^{2k_T}, p_{T,j}^{2k_T}) \frac{\Delta R_{ij}^2}{D^2} \quad (1.20)$$

where ΔR is the angular separation between the constituents, D is a parameter and k_T is a multiplier that is 1 for the k_T algorithm, 0 for Cambridge [37] and -1 for the anti- k_T algorithm [38]. The anti- k_T algorithm produces circular shaped jets, like the cone algorithms, but has desirable features such as infra-red and colinear safety [35].

A typical input to jet building is calorimeter cells (above an energy threshold), but any collection of 4-vectors can be used. Most analyses in ATLAS use jets built from “TopoClusters” (defined in Sec. 5.4), but some use calorimeter towers or even jets built from tracks.

1.5 Top Quarks within the Standard Model

The top quark is the most massive fundamental particle known. Currently the best measurements of its mass come from the Tevatron: $m_t = 173.5 \pm 0.6 \pm 0.8$ GeV [39]. Using the top mass and W boson mass, constraints can be placed on the mass of the SM Higgs boson as illustrated in Fig. 1.6.

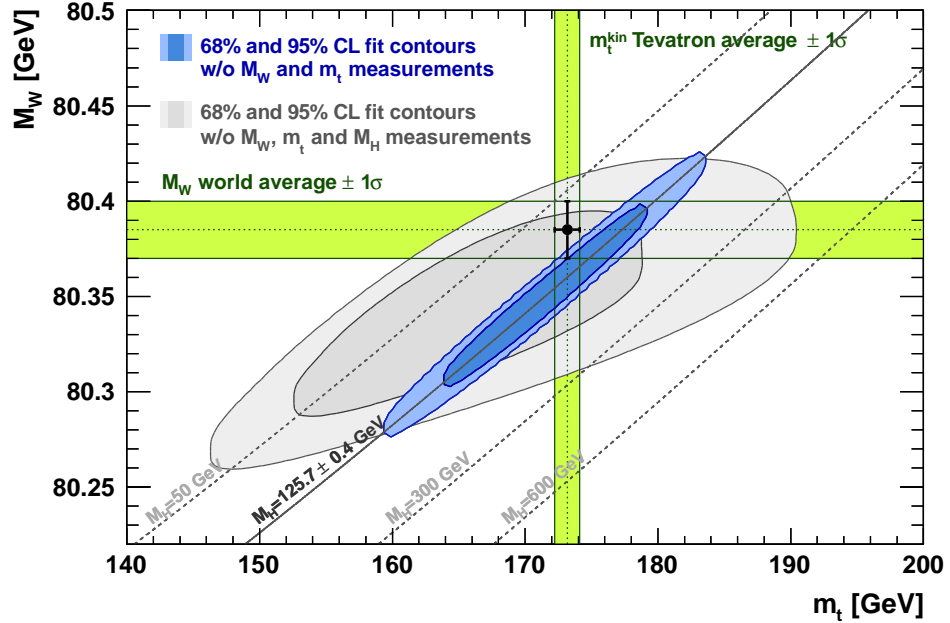


Figure 1.6: Constraints on the Higgs mass from measurements of the top and W boson mass [5].

The top quark was discovered experimentally in 1995 by the CDF [40] and D0 [41] collaborations at Fermilab and has been recently observed at the Large Hadron Collider (LHC) [42, 43]. Its lifetime predicted in the SM is on the order of 0.5×10^{-24} s so it decays nearly instantly. Because it decays so quickly, it never hadronizes unlike lighter quarks [44].

1.5.1 Top Quark Production and Decay

Production. At the LHC, the majority of top quarks are produced in top-antitop ($t\bar{t}$) pairs through gluon fusion as illustrated in Fig. 1.7 (b) and (c) but a small fraction are produced through the $q\bar{q}$ annihilation process (Fig. 1.7 (a)). The gg -fusion process contributes the majority of $t\bar{t}$ pairs produced at the LHC operating at $\sqrt{s} = 7$ TeV, while $q\bar{q}$ annihilation and a much less significant contribution from gg account for the rest [45]. The predicted cross section for $t\bar{t}$ production at the LHC operating at $\sqrt{s} = 7$ TeV from NNLO calculations is $166.8^{+16.5}_{-17.8}$ pb [46]. The $t\bar{t}$ production at the LHC is quite different from $t\bar{t}$ production at the Tevatron, which is mostly from $q\bar{q}$, due to the fact that the Tevatron collides protons and anti-protons at a significantly lower energy than the LHC. The LHC is a proton-proton collider that can really be thought of as a gluon-gluon collider. Recently the differences in collider design have been crucial as the Fermilab collaborations have reported slight deviations in the top quark forward-backwards asymmetry with respect to SM predictions [47, 48]. Unfortunately this is more difficult to measure at the LHC due to the symmetric collider design, pp versus $p\bar{p}$, but progress has been made to repeat the measurement with the ATLAS [49] and CMS [50] detectors.

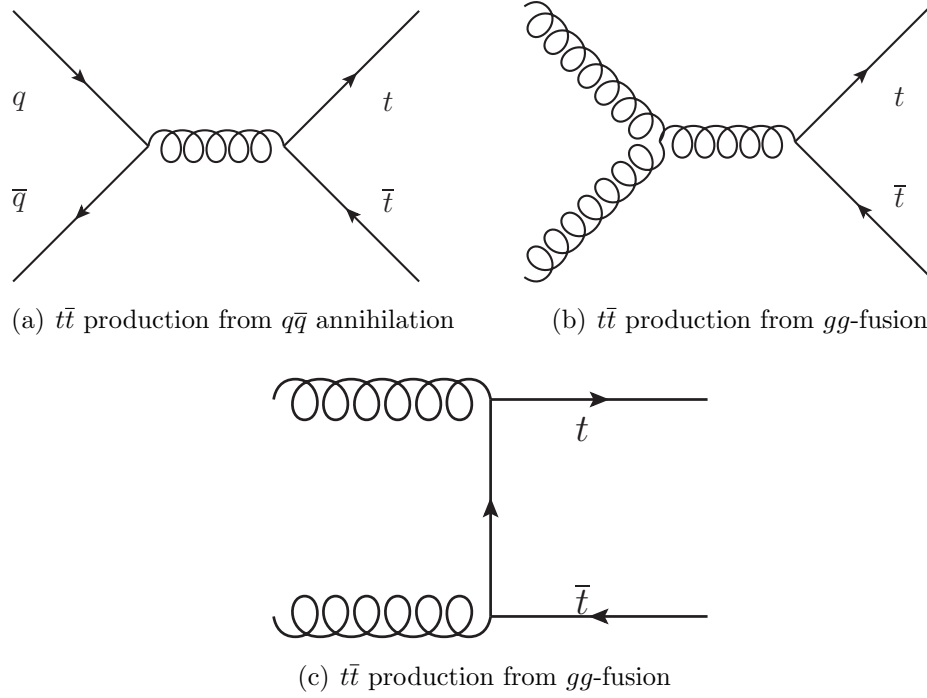


Figure 1.7: SM tree level $t\bar{t}$ production mechanisms. At the LHC, the gg -fusion process (b) is the dominant production channel while at the Tevatron, the $q\bar{q}$ -annihilation is dominant.

Single top quarks can be produced through electroweak processes. The smaller coupling strength of the EW vertex suppresses the production rate but the additional phase space available (since only one top quark is produced) partially balances this out so the rate at the LHC is comparable to top pair production to about a factor of two. Additionally the production rate is proportional to the V_{tb} vertex which makes a direct measurement possible [51,52]. Experimentally it is very difficult to disentangle single top events from W +jets events and it was not until 2008 that D0 [53] and CDF [54] had selected enough signal events to claim evidence (3σ significance) of production. The latest t -channel single top results from the Tevatron have reached 5σ significance [55]. The LHC single top program is very active, and both ATLAS and CMS observed t -channel production at the 3σ significance level in 2011 [56,57].

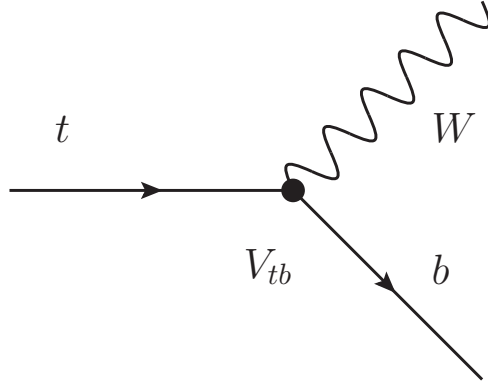


Figure 1.8: SM $t\bar{t}$ decay to a W -boson and a b -quark.

Decay. Due to the large V_{tb} term of the CKM matrix, top quarks decay into a W -boson and a b -quark nearly 100% of the time (Fig. 1.8). The branching ratio of the top to Wb is given by:

$$R = \frac{\text{BR}(t \rightarrow Wb)}{\text{BR}(t \rightarrow Wq)} = \frac{|V_{tb}|^2}{|V_{tb}|^2 + |V_{ts}|^2 + |V_{td}|^2}, \quad (1.21)$$

which assumes that the top always decays to a W -boson and a quark. Assuming three generations of quarks, the denominator of Eq. 1.21 is equal to one and $R = |V_{tb}|^2$. The branching ratio, R , has been measured by CMS [18], CDF [16] and D0 [17]. The CDF and CMS measurements agree with the Standard Model value but the D0 measurement is inconsistent by about 2.5σ . The measurement of R performed with the ATLAS detector presented in this thesis is in Chapter 7.

The final states of a $t\bar{t}$ event, shown in Fig. 1.9, are determined by how the two W -bosons decay. These are referred to as the all-hadronic, lepton+jets and dilepton channels respectively, although the lepton+jets channel is also often referred to as the semi-leptonic channel. The majority of the time, a W -boson will decay into a quark-antiquark pair but about $\frac{1}{3}$ of the time, it will decay into an $e\nu_e$, $\mu\nu_\mu$ or $\tau\nu_\tau$ pair. The W 's preference for hadronic decays means that $\approx 44\%$ of the time,

$t\bar{t}$ decay branching fractions

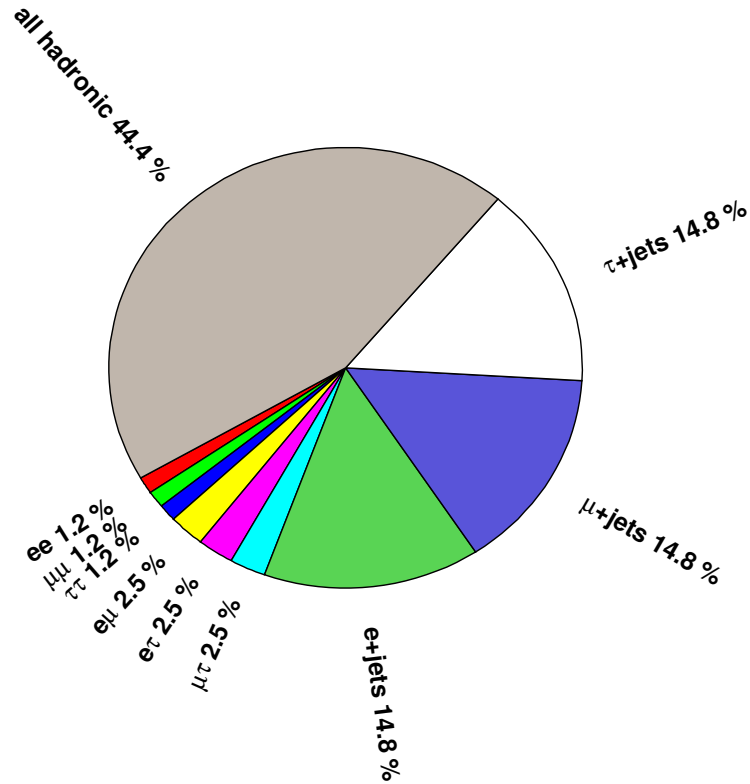


Figure 1.9: Approximate branching ratios for $t\bar{t}$ events.

the $t\bar{t}$ final state will consist of six partons (at lowest order). At hadron colliders, the QCD production rate for six jets is enormous, which makes this decay channel very difficult to study despite having the largest branching ratio. The next most common decay is for one W -boson to decay hadronically while the other decays into a lepton-neutrino pair, including taus which may then decay leptonically or hadronically. This final state has a lepton (e or μ , ignoring hadronically decaying taus), four partons plus an imbalance of transverse momentum (E_T^{miss}) that is due to momentum that is carried away by the undetected neutrino. This channel has a

sizable branching fraction but the main advantage is the final state lepton, which is a rare signature at a hadron collider. In addition, these kinds of $t\bar{t}$ events typically have substantial E_T^{miss} present, which can be used to reject the QCD multijet background. The E_T^{miss} in QCD multijet events usually comes from the finite detector resolution or from neutrinos in heavy flavor decays. The rarest SM decay channel is the dilepton channel where both W -bosons decay leptonically. This has the cleanest signature (especially different flavored leptons) but only occurs 6.5% of the time when excluding hadronically decaying taus [58]. A $gg \rightarrow t\bar{t} \rightarrow b\bar{b}l\bar{\nu}q\bar{q}$ lepton+jets event is illustrated in Fig. 1.10.

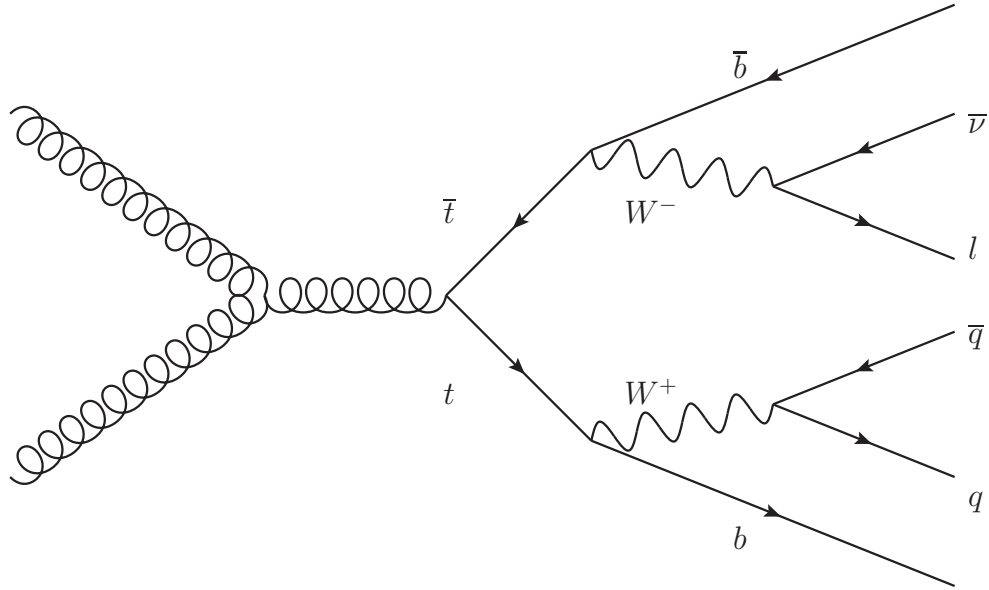


Figure 1.10: A tree level Feynman diagram showing production of a $t\bar{t}$ event through gluon-gluon fusion which then decays through the lepton+jets channel.

1.6 Beyond the Standard Model

Being the heaviest known fundamental particle, the top quark often plays a role in many physics scenarios beyond the Standard Model (BSM). Due to its large mass, the top quark should be sensitive to models that include mass-dependent couplings. In particular, new particles heavier than the top might decay into top pairs at the LHC. This would first manifest itself as an observed excess of measured $t\bar{t}$ events with respect to SM predictions due to the additional production mechanism. It could also be observed as a bump in the invariant mass spectrum of $t\bar{t}$ pairs. This type of search has been performed at the Tevatron [59,60] and at the LHC [61,62]. In general, the event signatures for top events involve leptons, jets, and E_T^{miss} , which are common signatures for many BSM physics scenarios. $t\bar{t}$ production will be an important background for these BSM processes and will need to be understood at a high level of precision.

1.6.1 Supersymmetry

One popular BSM scenario is Supersymmetry (SUSY). In SUSY models, there is a symmetry between fermionic and bosonic states. There is an operator that transforms a particle into its super-partner, which is in the opposite fermionic/bosonic state of the original particle and vice versa [63]. That means for the electron, a spin- $\frac{1}{2}$ particle, there exists another particle, the selectron, which is a spin-0 particle. In the Minimal Supersymmetric Standard Model (MSSM), each SM particle has a super-partner.

Charged Higgs. The SUSY Higgs sector is slightly more complicated than the SM due to the extra degrees of freedom. The MSSM requires two Higgs doublets to break electroweak symmetry which introduces three neutral Higgs bosons and a charged Higgs boson and its charge conjugate. The two vacuum expectation values for the doublets are related to the SM vacuum expectation value through the relation $v_1^2 + v_2^2 = v_{\text{SM}}^2$. The relationship between v_1 and v_2 is often parameterized as:

$$\tan(\beta) = \frac{v_2}{v_1} \quad (1.22)$$

The singly charged Higgs bosons can replace the W -boson in many physics processes, especially those involving high-mass states. Single top production occurs through interactions with W -bosons so this is affected by charged Higgs scenarios. In top quark decays, a charged Higgs boson (H^+ will also refer to the charge conjugate) can replace the W -boson in the decay chain as shown in Fig. 1.11.

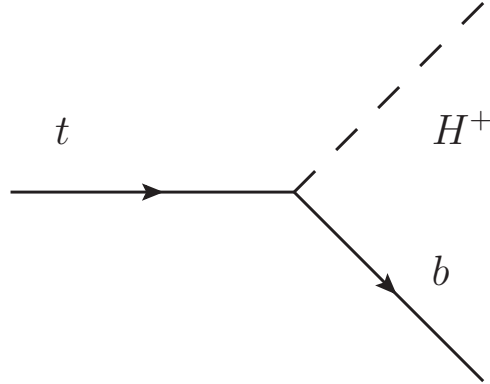


Figure 1.11: A top quark decaying into a b -quark and a charged Higgs boson

This scenario really only applies when $m(H^+) \lesssim 140$ GeV. Lower limits on the charged Higgs mass have been set at 78.6 GeV by the LEP experiments, which is well below the top mass [64]. As the mass of the H^+ approaches the top mass, the decay of a top quark to H^+b becomes kinematically suppressed. For a charged Higgs

mass greater than the top quark mass, it is possible to decay into a top and bottom quark.

The branching ratio of $t \rightarrow H^+ b$ for a given value of $m(H^+)$ as a function of $\tan(\beta)$, as well as the branching ratios of $H^+ \rightarrow X$ are shown in Fig. 1.12. The

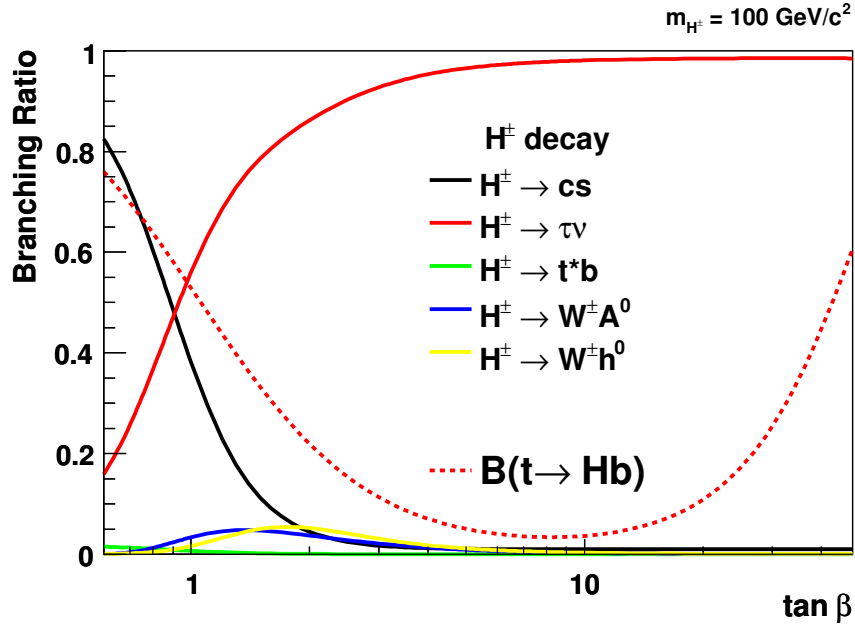


Figure 1.12: Branching ratios for $t \rightarrow H^+ b$ and H^+ as a function of $\tan(\beta)$ for a charged Higgs with a mass of 100 GeV [6].

dominant decays of H^+ are to tau final states and jet final states through $c\bar{s}$ for different values of $\tan(\beta)$. The charged Higgs tends to couple to massive particles which is why it prefers to decay to $\tau\nu_\tau$ rather than electrons or to $c\bar{s}$ rather than $u\bar{d}$ (the decay to $t\bar{b}$ being kinematically suppressed for low charged Higgs mass).

The branching ratios of H^+ are very different from the branching ratios of the W -boson which is exploited for searches. ATLAS, CMS, CDF and D0 have searched for excess taus in $t\bar{t}$ events to probe the limits of $\tan(\beta)$ [65–68]. ATLAS and CDF have looked for H^+ in the low $\tan(\beta)$ region by looking at the kinematics of jets in the final state of lepton+jet $t\bar{t}$ events [69, 70]. If there is a charged Higgs that

decays to cs (as is predicted for low values of $\tan(\beta)$), then it should be possible to reconstruct the two jets coming from the H^+ decay and observe a bump in the di-jet invariant mass spectrum. The D0 collaboration has taken a different approach for this type of analysis. As the branching ratio of $t \rightarrow H^+b \rightarrow bc\bar{s}$ increases, the total number of $t\bar{t}$ events with final state leptons should decrease and the ratio of lepton+jets to dilepton $t\bar{t}$ events changes [6]. This method has an advantage for a charged Higgs mass near the W -boson's mass since it does not rely on reconstructing the invariant mass but as the branching ratio of $t \rightarrow H^+b$ goes to zero, the number of expected “missing” dilepton $t\bar{t}$ events decreases rapidly and the method loses sensitivity quickly. Deviations from the predicted SM $t\bar{t}$ cross section in the dilepton or lepton+jets channel can be an early indicator of such a scenario.

CHAPTER 2

THE LARGE HADRON COLLIDER

The Large Hadron Collider (LHC), shown schematically in Fig. 2.1, is a proton-proton collider located just outside of Geneva, Switzerland at CERN. The entire complex consists of several linear accelerators (linacs) connected to circular boosters which accelerate protons to 450 GeV before they are injected into the LHC. The LHC is designed to accelerate particles up to 7 TeV for collisions. There are several experiments installed along the LHC ring. At Point 1 between the two injection lines is ATLAS [8], which is a general purpose detector. Across the ring from ATLAS at Point 5 is another general purpose detector, CMS [71]. A particle detector optimized for heavy ion collisions, ALICE [72], is located at Point 2 and LHCb [73], a detector designed for B -physics, is located at Point 7. The highlights of the LHC complex are shown in Fig. 2.1 and the typical machine parameters are listed in Tab. 2.1.

E_{beam}	3.5 TeV
$E_{\text{injection}}$	0.45 TeV
protons per bunch	1.5×10^{11}
number of bunches	1380
bunch spacing	50 ns
emittance	1.9-2.3 μ m rad
β^*	1 m
max. instantaneous luminosity	$3.6 \times 10^{33} \text{ cm}^{-2} \text{ s}^{-1}$

Table 2.1: Table of the LHC machine parameters for a typical late 2011 proton-proton run [1]. The machine parameters evolved rapidly during the 2011 running period.

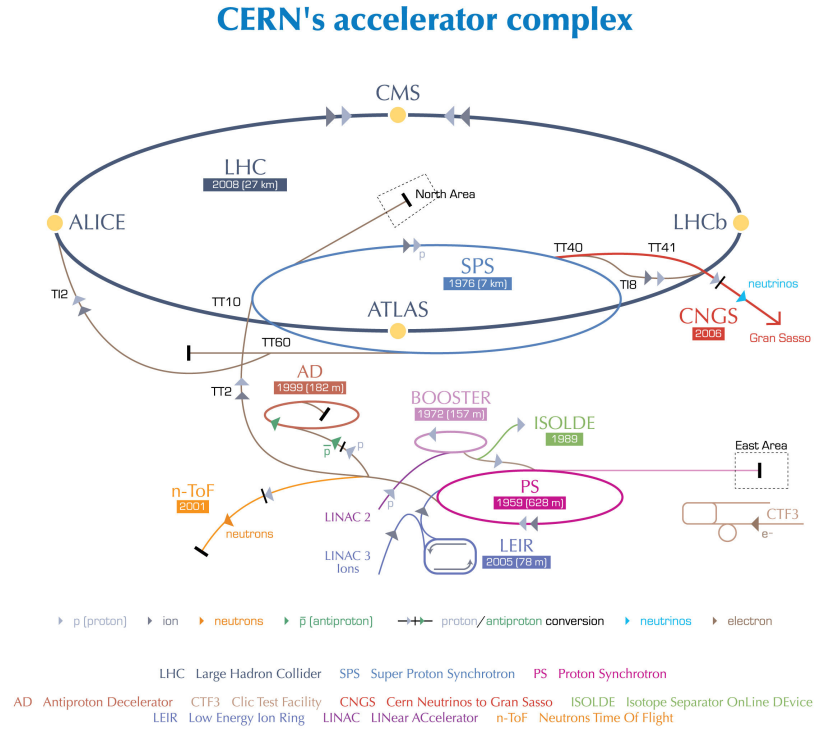


Figure 2.1: The CERN Accelerator Complex showing the LHC and the injection chain [7]. Other CERN physics programs are also included such as the neutrino beam to the Gran Sasso laboratory.

2.1 Injection Chain

Protons in the LHC start out as hydrogen atoms stripped of their electrons. The first accelerating stage the protons are subjected to is a linear accelerator, Linac2, which accelerates them up to 50 MeV [74]. The protons are then sent into the Proton Synchrotron Booster which accelerates them up to 1.4 GeV before sending them to the Proton Synchrotron (PS). The protons leave the PS at 25 GeV before entering the Super Proton Synchrotron (SPS), which accelerates them to the LHC

injection energy of 450 GeV. After this stage, the beam is ready to be injected into the LHC through one of two injection lines.

CHAPTER 3

THE ATLAS DETECTOR

ATLAS is a general purpose particle detector at the LHC designed to provide as much solid angle coverage around the interaction point as possible. It is located about 90 meters underground in between the two SPS injection points. The scale of the detector is enormous as illustrated in Fig. 3.1. The detector itself is actually comprised of many smaller sub-detector systems (typically cylinders) nested inside one another. The inner most layers consists of tracking detectors to determine vertex positions and to measure the momenta of charged particles. Beyond this are the calorimeters to measure energy of both charged and neutral particles. Calorimetry is a destructive process so very few particles exit the calorimeters with the exception of muons and neutrinos. Muons are measured using the muon spectrometer located outside of the calorimeters. ATLAS also has forward detectors along the beam pipe to measure beam conditions and luminosity. Triggering is done using a three tier system summarized in Tab. 3.1, designed to reduce a 40 MHz bunch crossing rate down to a 200-400Hz recorded event rate. The first trigger level is hardware based and the other two are software based.

	incoming rate	output rate
Level 1	40 MHz	100 kHz
Level 2	100 kHz	3 kHz
Level 3 (HLT)	3 kHz	200-400 Hz

Table 3.1: Summary of trigger level input/output rates [2].

For angular measurements, ATLAS uses a $\eta - \phi$ coordinate system where η is the pseudo-rapidity¹ and ϕ is the azimuthal angle. The distance along the beamline, z , is taken with respect to the center of the detector and the positive z direction corresponds with $\eta = +\infty$. ATLAS uses a right handed coordinate system where $\phi = 0$ lies in the horizontal plane of the detector, pointing to the center of the LHC ring. For practical purposes, the side of ATLAS within $+\eta$ is referred to as the A-side and the opposite side is referred to as the C-side.

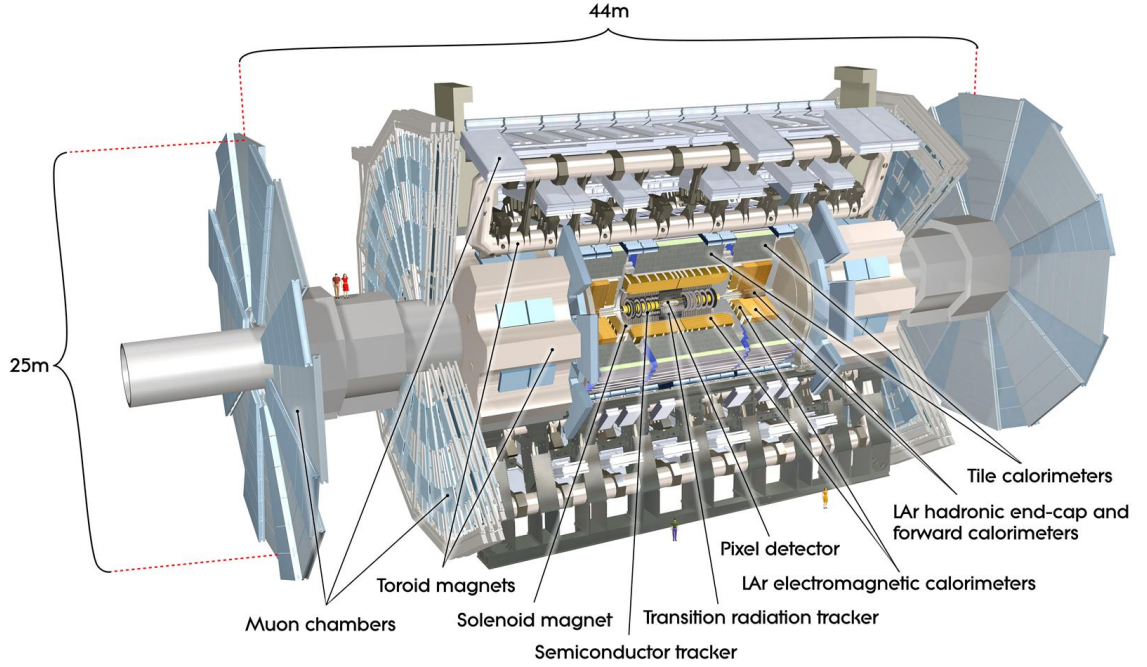


Figure 3.1: Cutaway diagram of the ATLAS detector with the major sub-detector systems labeled [8]. Note the people included in the figure for a sense of scale.

This Chapter presents an overview of the ATLAS detector and its sub-systems. The magnet system is crucial for charged particle momentum measurements and is presented first. The tracking systems, the inner detector and muon spectrometer,

¹Pseudo-rapidity is defined as $\eta = -\ln(\tan(\frac{\theta}{2}))$ where θ is the angle with respect to the beamline.

are both summarized and sections are devoted to individual sub-detectors. Next, the tile and liquid argon calorimeters are described in detail. ATLAS's three tier trigger system is described along with readout system. The chapter concludes with a description of the luminosity detectors used for the determination of the integrated luminosity of the dataset collected during the 2011 run.

3.1 Magnets

Magnetic fields are essential for performing momentum measurements using tracks. The most visible magnetic system in ATLAS is the barrel toroid system. This is the outermost magnetic system and consist of eight air-core superconducting toroid magnets. These magnets provide a ≈ 0.5 T field for the barrel muon spectrometer [8]. Two smaller toroid magnets are located within the barrel toroid that provide a ≈ 1.0 T field for the end cap muon spectrometer. For the inner detector, a superconducting solenoid magnet is used which provides a 2.0 T field.

3.2 Tracking

For most of the physics done at ATLAS, measuring the momentum of charged particles accurately is essential. To accomplish this, ATLAS has several tracking detectors located around the interaction point that are designed to maximize coverage. Tracking is divided into two sections, the inner detector (ID) and the muon spectrometer which is located outside the rest of ATLAS. Tracking relies on measuring the ionization energy of particles as they move through a medium. Neutral particles such as neutrons and photons don't leave ionization trails so they are in-

visible to the tracker and are only detected with calorimeters. One can exploit this fact to aid particle identification. For tracking systems, material budget is an issue since material distorts the trajectory of the particle. It is also possible for a particle to interact with an atom in the detector and convert into an electron-positron pair. Since tracking relies on measuring the position of “hits”, knowledge of the detector’s position is crucial as well as any distortions in the detector geometry.

3.2.1 Inner Detector

The inner tracking detector, shown in Fig. 3.2, is the innermost detector system in ATLAS with respect to the interaction point before the calorimeters. Coverage extends out to $|\eta| \approx 2.5$ with a high reconstructed track efficiency as illustrated by Fig. 3.3 [8]. The general geometry of the the ID consists of concentric cylinders and discs centered around the beam line. As a particle travels outward from the interaction point, the detector technology changes. The inner most layers are the pixel layers, followed by the silicon tracker layers and the final ID layers are the transition radiation tracker. Table 3.2 summarizes the hit position resolution capability of these three tracking detectors. During the 2010 commissioning period, the momentum resolution of the combined ID tracking system was measured to be $\sigma_p/p = 4.83 \pm 0.16 \times 10^{-4} \text{GeV}^{-1} \times p_T$ [75].

Detector	resolution (direction)
Pixel	10 μm (z for barrel strips, R for the end caps), 115 μm ($R\phi$)
SCT	17 μm ($R\phi$)
TRT	130 μm ($R\phi$)

Table 3.2: Summary of the ATLAS inner detector hit position resolution for the three inner detectors [3].

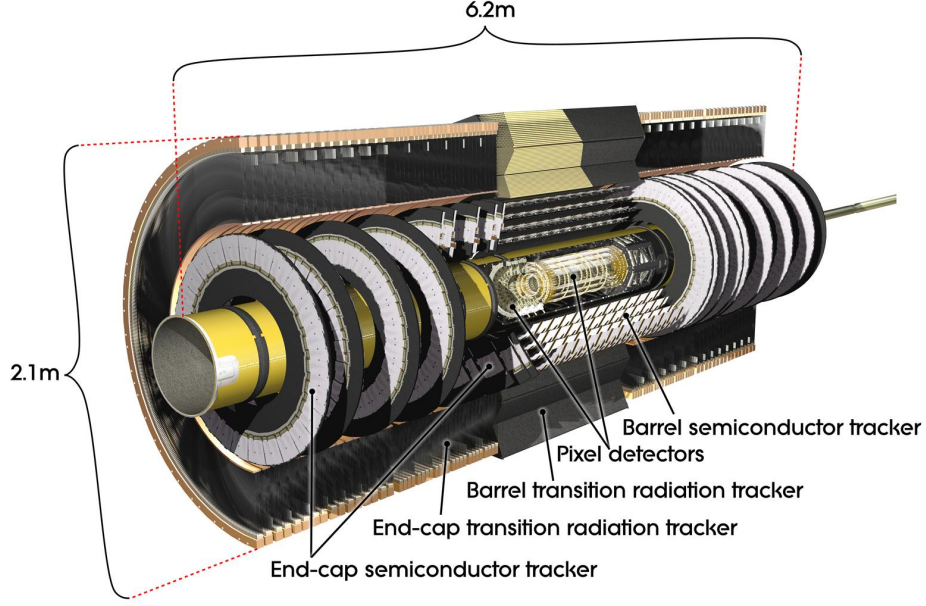


Figure 3.2: Overview of the ATLAS tracker system providing coverage of $|\eta| < 2.5$ [8]. The geometry for the inner tracking detectors consists mainly of cylinders and disks.

3.2.2 Pixel Layers

The pixel detector is made from 1744 pixel sensors in an arrangement of disks and cylinders. Each sensor contains 47232 pixels located on the n^+ side of the semiconducting wafer [8]. A bias voltage is applied to create a depletion layer in the center of the wafer so that charges drift to the sides [76]. On one side, tiny drops of solder have been applied to create little beads that are used to connect the pixels to a front end electronics board.

The innermost layer is located at a radius of just 5.05 cm away from the interaction point. This layer is often referred to as the b -layer due to its important role in b -tagging. Many b -tagging algorithms rely on reconstructing a secondary vertex that is displaced from the primary vertex. Hits in the b -layer are crucial for good

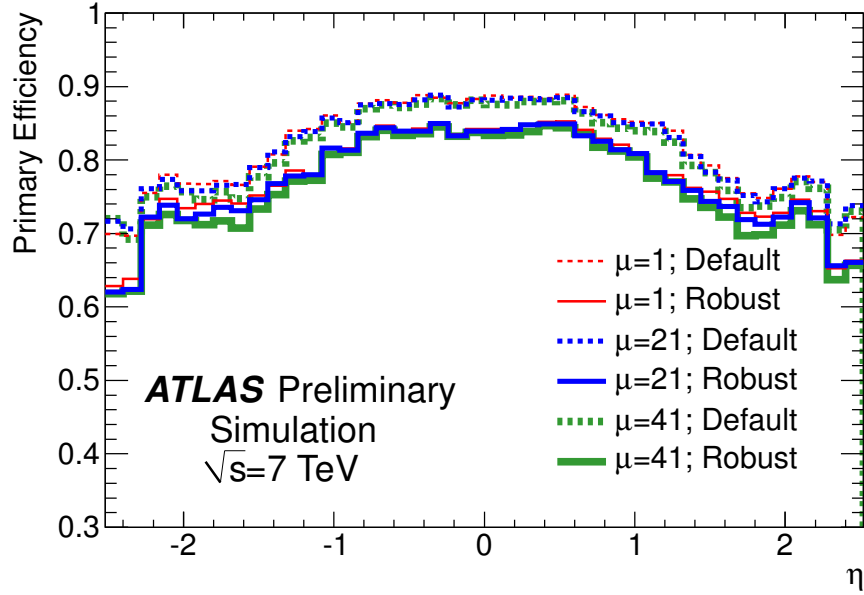


Figure 3.3: Track reconstruction efficiency for tracks with $p_T > 400$ MeV as a function of η in pile-up conditions ranging from one primary vertex to 41 vertices. “Robust” tracks have at least nine hits between the SCT and pixel layers and no missing hits in the pixel layers where an expected hit is derived from the reconstructed track trajectory [9].

vertex resolution. Since it is impractical to put tracking in the interaction area, tracks have to be measured at greater radii and extrapolated back to the interaction vertex. The closer the b -layer is to the interaction, the smaller the uncertainty on the reconstruction of the origin of the tracks. Correct assignment of tracks to vertices is a challenge as the number of pile-up vertices in a bunch crossing increases as the instantaneous luminosity of the LHC improves. The resolution of vertexing is measured to be $22.1 \pm 0.9 \mu\text{m}$ in the transverse plane and $112 \pm 4 \mu\text{m}$ along the beamline [75].

The other two layers of the pixel barrel have radii 8.85 and 12.25 cm respectively. All three layers of the pixel barrel terminate at $z=40.05$ cm, which is long enough

for the inner most layer to provide coverage past $|\eta| = 2.5$. The pixel also has six disks (three per side) that cover $2.0 < |\eta| < 2.5$ located at $z=49.5, 58$ and 65 cm.

3.2.3 Silicon Layers

The silicon layer tracker (SCT) uses a simpler technology than the pixel detector. Like the pixel, it is built out of sensor plates but the active detector material consist of many strips on top of a semiconducting wafer. Sensors plates are positioned on top of each other and angled slightly (40 mrad) for 3-dimensional measurements of hit positions [75]. The position resolution for hits in the SCT is $17 \mu\text{m}$ along the $R\theta$ direction [3]. A simple threshold is applied to the collected signal to define a hit. The read out electronics are located at the edge of each sensor plate.

The sensors are arranged into a barrel section that has four layers of double sided strips and two end caps with nine disks each. The barrel layers are located much farther from the interaction point with the innermost at a radius 29.9 cm and the furthest is at 51.4 cm. Barrel coverage extends slightly past $|\eta|$ of 1.5 but end cap disks continue SCT coverage out to $|\eta|$ of 2.5 . The innermost SCT disk is located at $z=85.38$ cm and the outermost is at the far edge of the inner detector at $z=272.02$ cm.

3.2.4 Transition Radiation Tracker

The Transition Radiation Tracker (TRT) is a drift tube-based detector located outside the SCT but inside the magnetic field solenoid. The basic detector element design consists of a $30 \mu\text{m}$ diameter gold-plated tungsten wire anode located in a

4 mm diameter cathode tube [77]. The tubes (also referred to as straws) are constructed from several layers of material. The bulk of the material is a polyurethane layer surrounded by an aluminum layer to enhance conductivity and a layer of graphite polyimide to protect the aluminum [8]. The assembly is reinforced with carbon rods for structural stability. The gas mixture filling the tubes is 70% Xe, 27% CO₂ and 3%O₂ [77]. Readout electronics are attached at the ends of the modules.

The TRT barrel is divided radially into three modules extending from R=56.3 cm to 106.6 cm and out to $z=71.2$ cm along the beamline. The straws are aligned parallel to the beamline and supported at their ends by the TRT support structure. The arrangement of tubes is non-projective in ϕ to allow for continuous coverage with an average spacing of 7 mm [8]. The space between the tubes is filled with polypropylene fibers.

The end caps are built out of many wheels. The TRT wheels consist of tubes arranged radially like spokes on a bike. In the detector assembly the wheels are rotated slightly with respect to each other to improve coverage. Twelve wheels are spaced 15 cm apart for the inner TRT end cap and eight wheels spaced 37 cm apart constitute the outer end cap. The z range for each TRT end cap extends from $z=84.8$ cm to 271.0 cm which translates into coverage in $|\eta|$ up to 2.0.

One of the main purposes of the TRT is to provide particle identification based upon the transition radiation that is produced as charged particles travel through the polypropylene fibers. Substantial differences in transition radiation between electrons and pions are expected for similar momentum ranges. By applying thresholds, it is possible to utilize the TRT for particle identification as illustrated in Fig. 3.4.

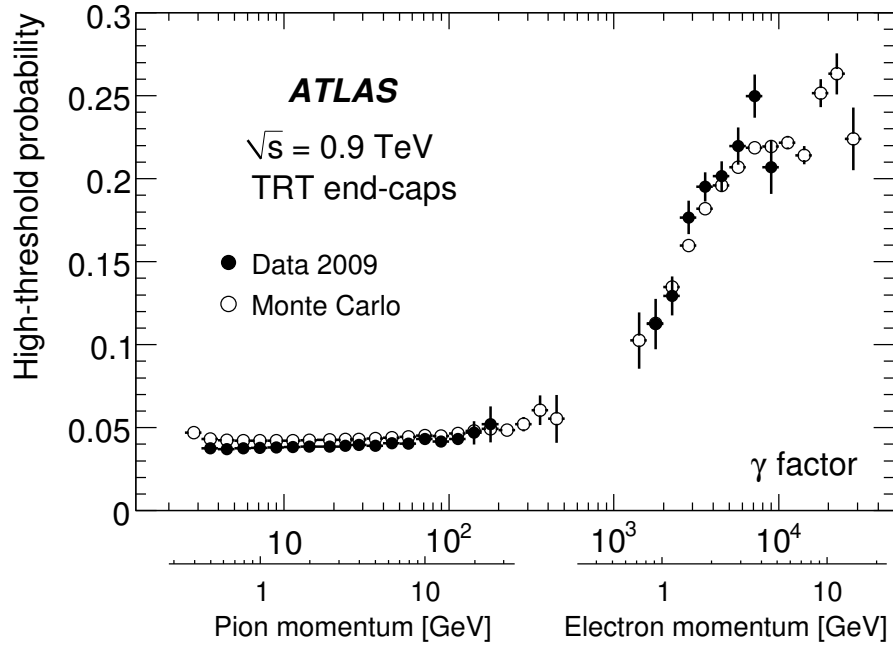


Figure 3.4: Discriminating variable based upon TRT hit information used for pion-electron identification for data and Monte Carlo simulations [10]. The figure shows difference between the relativistic γ factor and high threshold hit probability for pions and electrons with the same momentum. By looking at the number of hits in the TRT that pass the high threshold criteria, discrimination between electrons and charged hadrons can be achieved.

3.2.5 Muon Spectrometer

The ATLAS muon spectrometer, shown in Fig. 3.5, is the outermost detector system and takes up nearly the entire experimental cavern. Muons are relatively long lived so at relativistic velocities they decay well outside the detector. They also don't interact with material much so they are able travel through the calorimeters leaving behind just ionization energy before escaping. The muon spectrometer is composed of several sub-detectors that utilize different technologies in different regions. The resistive plate chambers, cathode strip chambers, thin gap chambers and

monitored drift tubes are all named after the detector technology each one utilizes. The combined muon system provides good muon p_T resolution for muons with $p_T > 25$ GeV as shown in Fig. 3.6.

The geometry of the barrel uses three concentric cylinders with sixteen subdivisions. The divisions are divided into eight small and eight large detector segments. The smaller segments are placed aligned radially with the toroid magnets. The larger segments are placed between the magnets and at a slightly smaller radius than the small segments to allow for overlapping coverage, as shown in Fig. 3.7. This configuration allows the ATLAS muon system to have excellent muon reconstruction efficiency, which is above 95% for most regions in η as shown in Fig. 3.8 [11].

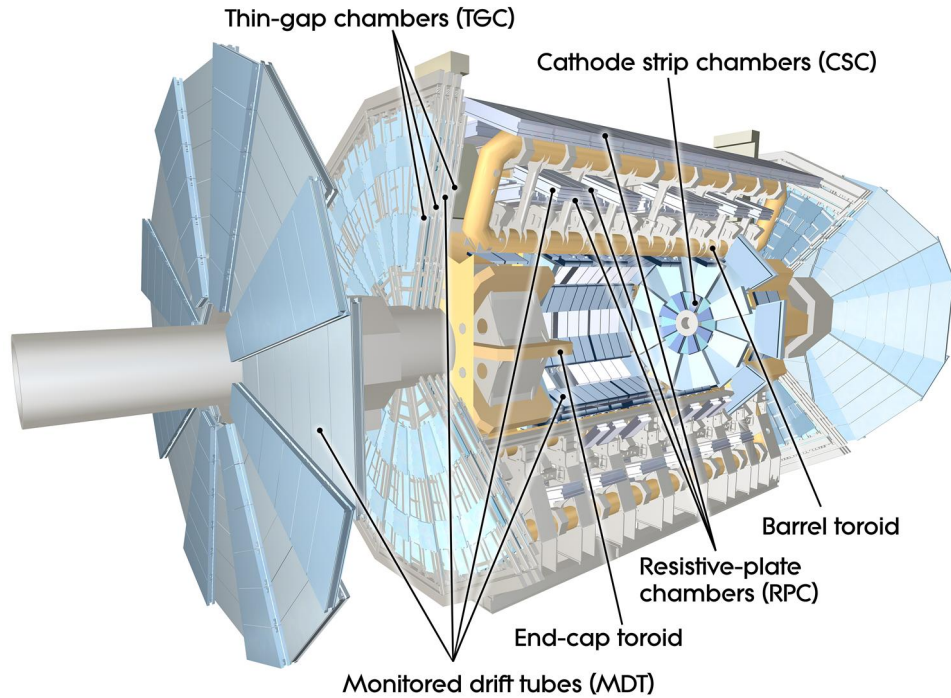


Figure 3.5: The ATLAS Muon spectrometer showing the position and arrangement of the various detector technologies [8]. Like the inner detector, the geometry of the muon spectrometer also consists of cylinders and disks or wheels.

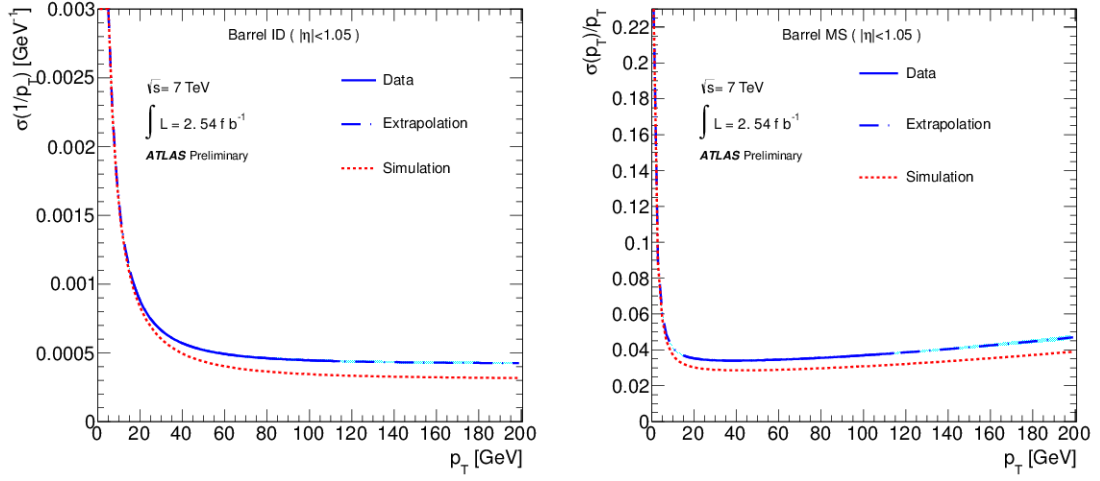


Figure 3.6: Reconstructed muon p_T resolution for central muons reconstructed in the inner detector (left) and the muon spectrometer (right) [11]

3.2.6 Cathode Strip Chambers

The cathode strip chambers (CSC) wire chamber detector provide coverage in the forward regions between $2 < |\eta| < 2.7$. The chambers contain gold-plated tungsten anode wires at a 2.5 mm spacing which is also the distance between the wire and the plane of cathode strips. The $17 \mu\text{m}$ thick copper cathode strips are orientated perpendicularly to the anode wires and are read out at the inner edge of the detector. The gap between the 5.308 mm (or 5.567 mm in the eight larger chambers) strips is 0.25 mm [8]. The position of a hit is determined using several adjacent strips to better reconstruct the avalanche pulse.

The CSC is arranged as a disk and follows the eight larger plus eight smaller scheme employed in the barrel spectrometer for complete ϕ coverage. A CSC chamber is four wire planes deep and contains either 250 or 402 wires depending on

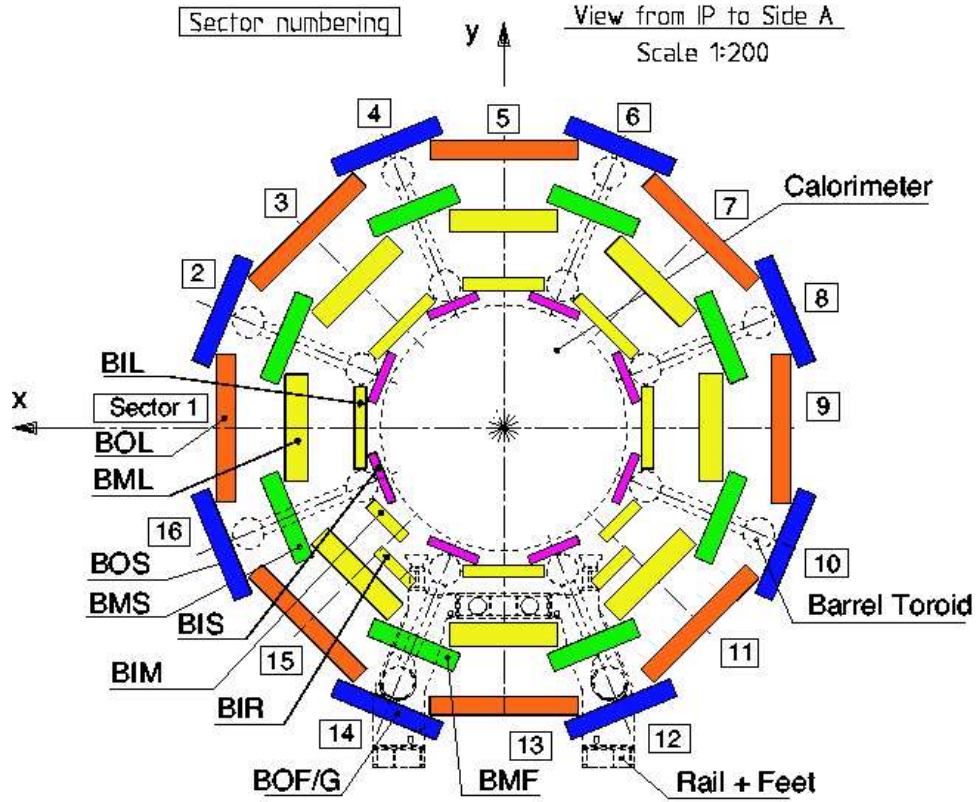


Figure 3.7: Geometry for the barrel Muon spectrometer showing the arrangement of inner and outer chambers which allows for overlapping coverage [8].

whether it is a large or small chamber. To reduce the effects of inclined tracks, the CSC chambers are oriented at 83° with respect to the z direction.

3.2.7 Monitored Drift Tubes

The monitored drift tubes (MDT) are used throughout much of the muon system to provide precision position measurements. MDT detectors are used in the barrel as well as in the forward muon wheels. The basic detector element consists of an Ar/CO₂ gas filled tube with a 50 μm diameter tungsten-rhenium wire running down the center. The tubes themselves have a diameter just under 3 cm and are

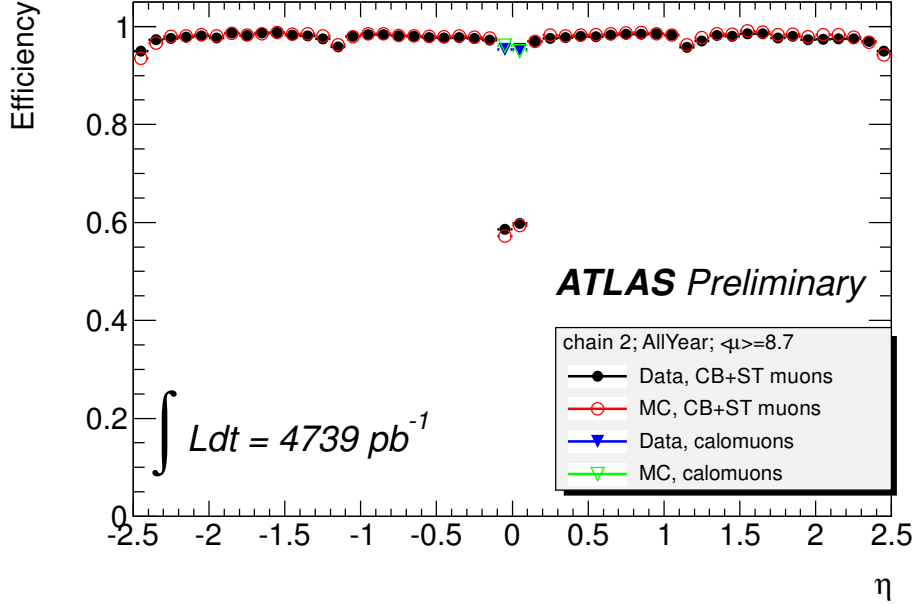


Figure 3.8: Muon reconstruction efficiency for $Z \rightarrow \mu\mu$ events as measured in Monte Carlo simulation and in the 2011 dataset using a “tag-and-probe” technique [12].

constructed out of aluminum [78]. Readout electronics are attached to one end of the tube while the high voltage for the anode and cathode is delivered from the other side.

Tubes are arranged in chambers such that the tube axis aligns with ϕ in both the barrel and end cap. The chamber structure has an alignment support structure in the center and an arrangement of 3-4 tubes on each side. End caps hold the tubes in place and glue is applied in between the tubes to add rigidity to the structure. The barrel consists of three concentric cylindrical arrangements of chambers. The inner set of chambers are typically located around $R=4.55$ m but some special cases exist for services and support structures. The middle barrel layer is around 8.1 m and the outer most layer of chambers is around 10m and extends the farthest in z out to 5.11 m. For the end caps, trapezoid-shaped chambers are used and a wheel geometry is used. There are a total for four wheels located around 7 m, 11 m, 14 m,

21 m. The number of radial segments increases as the distance from the interaction point increases from just two chambers to six in the outermost wheel.

3.2.8 Resistive Plate Chambers

The main function of the resistive plate chambers (RPCs) is to provide triggering information. The detector element of the RPC consists of two electrode plates separated by a thin 2 mm gas filled gap. This provides a fast response to charged particles compared with other drift methods but has no spacial measurement within the plate area. RPC “units” are built out of two gap chambers separated by 6 mm, which have their own resistive and readout plates. Structurally the RPC units are supported by thin aluminum plates and frames. The RPC system covers the central barrel region of the ATLAS detector up to $|\eta|$ of 1.05. Adjacent RPC units are staggered slightly in the radial direction to allow for overlap ensuring continuous coverage along the ϕ direction.

3.2.9 Thin Gap Chambers

The thin gap chambers (TGC) perform a similar role to the RPCs but in the forward direction but also provide precision positioning measurements. The TGC $|\eta|$ coverage starts at 1.05 and extends out to 2.4. Like the CSC, the TGCs are a gas filled multi-wire chamber with gold-plated tungsten anode wires and graphite cathode walls with a wire spacing of 1.8 mm and a wire-cathode spacing of 1.4 mm. One cathode wall is connected to the ground of the electronics while there is pickup

strip layer behind the other. The copper pickup strips are orientated orthogonal to the wires.

Chambers are arranged into triplet and doublet units of three and two chambers separated by a 20 mm honeycomb paper mesh. The units are arranged into four wheels on each side. The inner most wheel consists of a two disks of doublet TGC units between $z=7$ m and $z=7.4$ m. The external wheel consists of two wheels containing doublet units segmented into three radial disks and one triplet wheel similarly segmented. In between the two doublet wheels and the triplet wheel is a MDT wheel. The outer wheel starts at $z=13.4$ m and extends to $z=15.1$ m. The innermost radius is 1.9 m and the outer radius of the wheels reaches 11.9 m.

3.3 Calorimetry

The ATLAS calorimeter system consists of electromagnetic (EM) and hadronic calorimeters (Fig. 3.9). The active material in the electromagnetic and forward hadronic calorimeters is liquid argon. The material used for the absorber depends on the pseudo-rapidity but is steel in the central regions and copper-tungsten in the forward regions. The central hadronic calorimeter utilizes scintillating tiles instead of liquid argon as its active material.

3.3.1 Liquid Argon Calorimeter

The Liquid Argon Calorimeter (LArg) consists of an EM and a hadronic portion depending on position in η . It is enclosed in a precisely controlled cryostat that maintains the temperature uniformity to better than 100 mK precision in all LArg

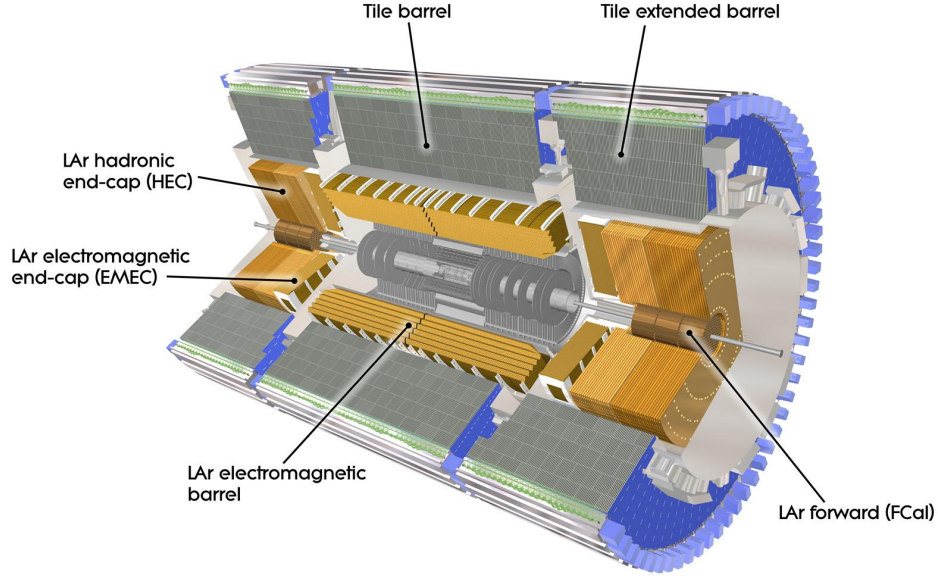


Figure 3.9: The combined ATLAS calorimeter system showing the various sub-detectors and cylindrical geometry [8]. The liquid argon calorimeter is encased within a precision controlled cryostat (not labeled).

barrels [79]. The EM calorimeter is essential for the identification of electrons and photons as well as measuring a significant portion of hadronic jet energies. Beyond $|\eta| \sim 1.7$, the expected radiation damage to scintillating tiles would be too great for the planned luminosity and lifetime of the experiment which justifies the need for another solution. One of the unique features of the LArg is its “accordion” geometry as illustrated in Fig. 3.10, which provides complete coverage in ϕ . Alternating accordion layers of absorber material and electrodes are stacked on top of each other to build the calorimeter barrels. Electrode boards contain the readout electronics which sum up the analogue signals from nearby regions before being readout through electronics located at the inner or outer radius of the barrel [8].

Electromagnetic Calorimeter. The barrel EM calorimeter is cylindrically symmetric in ϕ and extends out to $|\eta| < 1.475$, at which point the end caps coverage

Figure 3.10: Accordion geometry and segmentation of the central barrel LArg calorimeter [8]. The three layers of longitudinal segmentation allows for reconstruction of incident photon direction.

Hadronic Calorimeter. The hadronic end cap covers $1.5 < |\eta| < 3.2$, which overlaps slightly with the end of the Tile calorimeter, and consists of copper ab-

sorbers instead of lead. There are a total of four wheels which contain 32 ϕ wedges each. The granularity for the region covered by the tracker is 0.1×0.1 in $\eta - \phi$ but increases to 0.2×0.2 for $|\eta| > 2.5$. For higher $|\eta|$ regions, the forward calorimeters (FCal) cover $3.1 < |\eta| < 4.9$. This forward coverage is essential for increasing the hermeticity of the ATLAS detector which improves the missing energy resolution. The FCal is divided into three layers. The first layer is an EM calorimeter which uses copper absorbers. The other two layers are hadronic calorimeters and use tungsten instead [8]. The geometry of the FCal is quite different from the rest of the LArg. Instead of layers of accordion shaped sheets, the FCal is built up of a matrix of tubes containing a LArg gap that are held in place by absorber plates.

3.3.2 Tile Calorimeter

The Tile Calorimeter (TileCal) is a sampling calorimeter providing ϕ -symmetric coverage from $-1.7 < |\eta| < 1.7$ [80]. Located radially outside the LArg, TileCal predominately measures the energy of hadrons that aren't measured in the LArg. Muons traveling through TileCal deposit energy which is also measured. The calorimeter cell construction consists of a steel-and-scintillator structure illustrated in Fig. 3.11. A wavelength-shifting-fiber runs along the side of each scintillating tile to transport light signal from the scintillator to the photo-multiplier tubes (PMT) located in a steel girder that runs along the top of each module. The wavelength-shifting-fibers absorb the light from the scintillator and reemit photons at a wavelength suitable for the PMTs.

There are four barrels consisting of 64 modules each for a total of 256 modules in ATLAS. In the central region ($|\eta| < 1$), the two barrels are linked together to

form a single long barrel (LB). Each long barrel module contains 45 channels which correspond to about 22 cells. On each side of the LB, there is an extended barrel (EB) which extends the coverage out to $|\eta| = 1.7$. Each EB has 26 channels and typically 17 or 18 cells depending on whether or not a read-out channel has been dedicated to a Minimum Bias Trigger Scintillator.

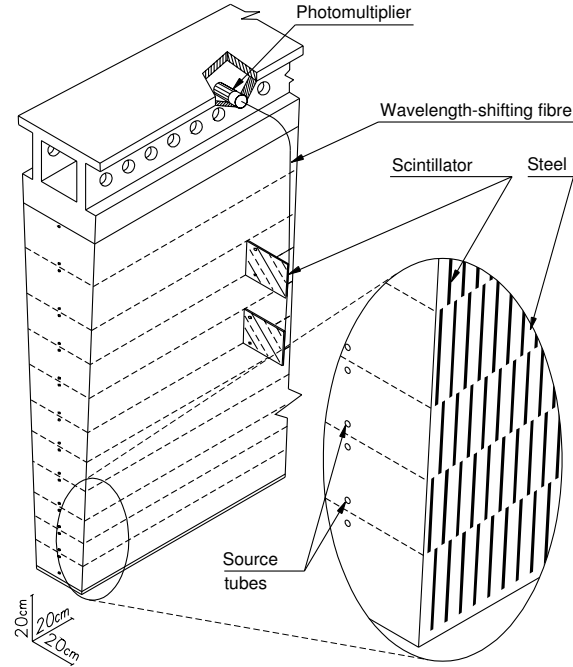


Figure 3.11: Diagram of a TileCal module showing the orientation of the steel and scintillating plates with respect to the beam direction [8]. The PMTs are located in the girder on top of each Tile module and light is collected from the scintillator tiles through WLS fibers that run along the edges of the module.

TileCal has calibration systems for each link in the read-out chain. The gain of the electronics is calibrated using a charge injection system which injects a known pulse that mimics the pulse coming from a PMT. The stability of the optics of the PMT is measured using a laser system. The laser is located outside of the detector and the light is distributed to the PMTs by optical fibers. To calibrate cell response, a cesium source is routinely sent through the detector through a series of tubes that

pass through the center of most cells. Before the assembly of TileCal in the ATLAS detector, several modules were subjected to test beam testing. Electron beams were used to define the electromagnetic scale of the first layer of cells. The cesium sources were used to normalize the response of the rest of the cells to this calibration. After assembly in the ATLAS cavern, the results of the electromagnetic scale calibration were confirmed using cosmic muons with an uncertainty of 4% [80].

3.4 Trigger and DAQ

With bunch crossing times of 25 ns possible, it is essential to have a trigger and readout system that can cope with the demand. The ATLAS detector uses a three tier trigger system with the lowest level being hardware based while the other two are performed on CPU farms located off the detector. The design goal for the complete trigger and DAQ system (Fig. 3.12) is to provide an event rate of 200-400 Hz at the final level [81]. The sub-detectors utilizes pipeline memory that is able to hold data for several events. The trigger and DAQ systems retrieve this data for triggered events and the rest are discarded to make room for more data in a “First In, First Out” (FIFO) scheme.

3.4.1 Level 1

The level 1 trigger relies on analogue signals from the calorimeters and muon spectrometer for its trigger decision process. The level 1 calorimeter trigger (L1Calo) is based around “trigger towers” objects. A trigger tower is the sum of energies from a 0.1×0.1 projection of calorimeter cells in the $\eta - \phi$ plane. This summing

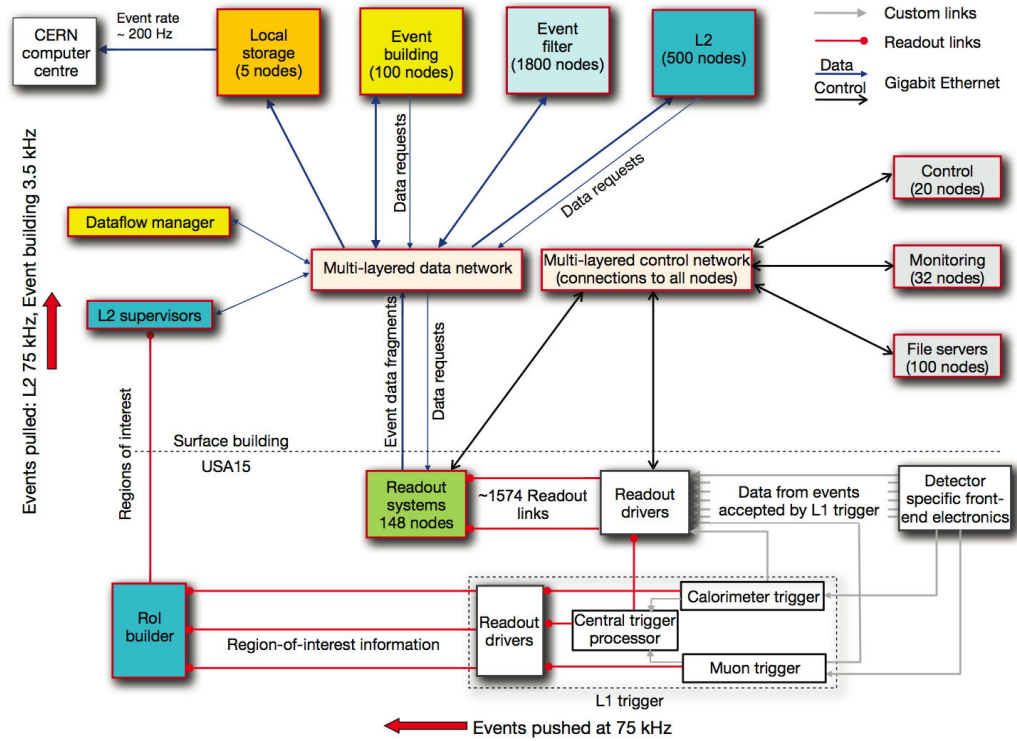


Figure 3.12: Overview of the ATLAS trigger system and data flow from detector electronics to events on tape [8].

is performed by the calorimeter electronics and the analogue signal is transmitted through dedicated trigger cables to the processing room USA15 that is adjacent to the detector. At this stage, simple cluster finding is performed to identify electron, tau and photon candidates as well as simple jet finding based on 0.2×0.2 calorimeter tower sums and windows. The entire L1 system is based upon counting objects above thresholds and this information is sent to the central trigger processor(CTP).

The level 1 muon trigger (L1Muon) uses information from the RPC in the barrel and TGC for the forward regions. As the momentum of a particle increases, it is bent less by the magnetic field. By looking at hits in several detector layers and

defining a window around the inner hits projected onto the outer detectors, it is possible to adjust the p_T threshold of the trigger by changing the width of the window. To reject fake tracks, coincidence hits on several layers within a window is required. The RPC trigger signals are sent to coincidence matrix boards which perform this search in either a 0.1×0.2 or 0.2×0.1 $\eta - \phi$ window. Information from two coincidence matrix boards are combined on a “PAD” card to create a 0.2×0.2 window. For the TGC, the role of the coincidence matrix boards is performed by a “patch panel and slave” board. These signals are sent through VMEbus crates before being sent to the CTP.

3.4.2 Level 2 and Event Filter

The higher level trigger decisions are performed on a CPU farm so more sophisticated techniques can be used than the ones implemented in the L1 trigger decision. The basis for the trigger decision comes from “regions of interest” (RoI) rather than analogue signals. Information about trigger objects is sent from the readout drivers and CTP to a RoI builder which builds a data fragment containing $\eta - \phi$ information about the particular L1 trigger object that passed the event [82]. These data fragments are sent to L2 “supervisors” which distribute them among the CPU farm where the data corresponding to a particular RoI is retrieved from readout buffers. The RoI size corresponds to only a few percent of that of the full detector [8]. Using this information it is possible to crudely reconstruct some objects that rely on multiple detector systems like electrons and jets.

The event filter (EF) is the highest trigger level and has the smallest output. Events that pass L2 are sent to the event builder which reconstructs the event using

the full information from the detector readout. The reconstructed events are then passed through the ATLAS analysis software which applies the actual event filtering and separates the events into output trigger streams. Events passing this final step are written to tape and eventually distributed to the worldwide computing grid for analysis.

3.5 ATLAS's Luminosity Detectors

ATLAS currently has three luminosity detectors but only two were installed in time for the 2010 LHC run. The Beam Conditions Monitor (BCM) is located 1.838m from the interaction point at a radius of 55 mm from the beam [83]. Its primary purpose is to signal the LHC to dump the beams if the conditions become too dangerous for the sensitive tracking electronics in ATLAS, but it has been utilized as a hit counter. The BCM consists of eight diamond detectors, four on each side of ATLAS, that detect minimum ionizing particles (MIPs). LUCID is a dedicated luminosity detector that is based on a different technology than the BCM. It uses Cerenkov light to determine the number of particles passing through since the number of tracks is proportional to the amount of light received [84]. Like the BCM, it was installed very close to the beam pipe but much farther away (17 m) from the interaction point. Each LUCID detector (one on each side) has 200 tubular Cerenkov counters arranged in a series of concentric circles. The most recent luminosity detector is the ALFA detector which was installed during the 2010-2011 winter shutdown. ALFA is a series of Roman pot detectors located on each side of ATLAS, 240m from the IP [85]. The active area consists of scintillating fibers connected to PMTs. These are arranged in sets of titanium stereo plates and stacked

ten plates deep in each Roman pot. The stereo arrangement and stacking allows for tracking of charged particles very close to the beam.

CHAPTER 4

LUMINOSITY

For any absolute cross section measurement, it is necessary to know the integrated luminosity ($\int \mathcal{L} dt$).

$$\sigma = \frac{N_{signal}}{A \cdot \epsilon \cdot \int \mathcal{L} dt} \quad (4.1)$$

In this simplified cross section formula (Eq. 4.1), A and ϵ are the acceptance and efficiency terms which are typically derived from Monte Carlo (MC) simulations and N_{signal} is the number of signal events for the process being measured. Determining the instantaneous luminosity, \mathcal{L} , accurately requires very good knowledge of the beam parameters. At the LHC, each individual experiment is responsible for measuring the luminosity at their interaction points (IP).

Since the LHC beam structure is composed of several bunches that continuously revolve around the ring, the luminosity can be expressed as:

$$\mathcal{L} = \frac{\mu_{visible} \cdot n_b \cdot f}{\sigma_{visible}}. \quad (4.2)$$

[86] The $\mu_{visible}$ term is the average number of interactions during each bunch crossing that pass a certain set of selection criteria. The next term, n_b , stands for the number of bunches in the machine and f is the frequency of revolution. This is normalized to the total pp cross section that has been corrected for the efficiency of the event selection, $\sigma_{visible}$. To understand how Eq. 4.2 was derived, it is best to start thinking about how one would calculate the number of expected interactions

and work backwards. This method to measure luminosity is referred to as event counting.

Luminosity can also be measured using a different method relying on beam profile measurements [86] as shown in Eq. 4.3.

$$\mathcal{L} = \frac{n_b \cdot f \cdot n_1 \cdot n_2}{2\pi \cdot \Sigma_x \Sigma_y} \quad (4.3)$$

Now n_1 and n_2 are the numbers of protons in each colliding bunch and the Σ terms are parameters related to the beam width. During a van der Meer scan [87], the two beams are gradually passed through each other and Σ_x and Σ_y are extracted from fits of the number of interactions as a function of beam displacement. This method trades off the requirement of knowledge of the pp cross section for knowledge of the number of protons per beam.

4.1 Luminosity Determination and Uncertainty

By combining Eq. 4.2 and 4.3, it is possible to solve for $\sigma_{visible}$ as a function of the machine parameters and quantities that are measured during a van der Meer scan as shown by :

$$\sigma_{visible} = \mu_{visible}^{max} \frac{2\pi \cdot \Sigma_x \Sigma_y}{n_1 n_2} \quad (4.4)$$

. For each of ATLAS's luminosity sub-detectors, $\sigma_{visible}$ has to be measured separately since each luminosity detector has different acceptances. Since the luminosity detectors are symmetric about the interaction point, the definition of a “hit” can require either one side or both sides to record a signal. Requiring both sides virtually removes all beam background events but extracting $\mu_{visible}$ is slightly more

difficult [88]. Assuming the number of interactions (μ) follows a Poisson distribution, $\mu_{visible}$ can be expressed as a function of number of hits (N_{hits}) and the number of bunch crossings ($N_{\text{bunch crossings}}$) when requiring either side to record a hit, as illustrated by Eq. 4.5.

$$\mu_{visible} = -\ln\left(1 - \frac{N_{\text{hits}}}{N_{\text{bunch crossings}}}\right) \quad (4.5)$$

Ultimately it was decided to use the horizontal BCM detector (see Sec. 3.5) results to determine the luminosity in 2011.

Uncertainty. There are several effects that contribute to the uncertainty in the luminosity measurement. The dominant one comes from the measurement of the beam currents which contribute 3.4% to the total uncertainty [88]. Stability of the detectors can be determined by comparing stability with each other, including luminosity measurements performed by the ATLAS calorimeters. This contributes another 1% to the uncertainty. There is a small dependence on μ which is taken as a 1% systematic uncertainty. As the beam travels and collides in the experimental cavern, surrounding materials can become activated. This contributes a small amount (2 orders of magnitude less than beam) to the luminosity detector activity. The corrections and uncertainty due to this afterglow contribute 0.2% to the total luminosity uncertainty. The total luminosity uncertainty for the 2011 run is 3.7% [88].

CHAPTER 5

PHYSICS OBJECT RECONSTRUCTION AND EVENT SELECTION

Identifying physics objects, such as jets and electrons, in the LHC environment is no trivial task. It requires an excellent understanding of the detector response and performance to make the most of the data. For a top quark analysis, the entire detector is utilized whereas a $Z \rightarrow e\bar{e}$ analysis will primarily make use of just the LArg calorimeter and tracker. Jets are essential for any $t\bar{t}$ decay channel since there are at least two b -quarks in the final state. Sophisticated algorithms are run which can “tag” these jets a fraction of the time (see Appendix A). When either W -boson decays into leptons there is an associated neutrino carrying off momentum that only can be inferred by examining E_T^{miss} . About 66% of the time, W -bosons will decay to light jets but can also decay into electrons($\approx 11\%$), muons ($\approx 11\%$) and taus ($\approx 11\%$), which can then decay hadronically($\approx 65\%$) or leptonically($\approx 35\%$).

We start this Chapter by describing the first stage of the event selection, the trigger, and describe the details of the efficiency calibration. Next, lepton reconstruction and identification are discussed for electrons and muons separately with sections describing the measurement of the QCD multijet background contributions to the background. There is a description of jet reconstruction in ATLAS and a section is devoted to the measurement of the jet energy scale and its uncertainty, which is often a large systematic uncertainty in $t\bar{t}$ measurements. The reconstruction of E_T^{miss} is discussed, which relies on reconstruction of the previously mentioned ob-

jects. Finally, this Chapter concludes by putting all of the components together by summarizing the event selection.

5.1 Trigger

Since ATLAS has limited bandwidth to read out events, the trigger system is used to minimize dead time and select interesting events (see Sec. 3.4). For the lepton+jets and dilepton $t\bar{t}$ decay channels, the final state leptons are a very clean signature for rejecting the QCD multijet background. This prompts the use of lepton triggers for these analyses. The rate for jet production is extremely high, which forces us to “pre-scale” low p_T jet triggers. The pre-scale trigger condition means that only a fraction of events satisfying the trigger requirements will be accepted. The p_T thresholds for the unpre-scaled triggers are high and this reduces the trigger efficiency for $t\bar{t}$ events. This makes triggering on jets undesirable for a $t\bar{t}$ analysis (except in the all-hadronic case when there is no alternative).

For lepton triggers, the main selection criteria for trigger choice was the lowest p_T unpre-scaled lepton trigger available. The efficiency as a function of p_T of a trigger will have a turn-on curve around the trigger p_T cut that is difficult to parameterize. Offline lepton p_T cuts are placed sufficiently above the trigger p_T cut to avoid this region. The Monte Carlo simulations are produced with a mix of the several trigger menus used over the course of the 2011 run. These samples are reweighted to the corresponding portions in data.

5.1.1 Electron Triggers

As the LHC luminosity increased over the course of running, an increasing number of triggers were pre-scaled, had criteria tightened or were removed completely from the trigger menu to ensure that ATLAS was able to run at a 400Hz EF trigger rate. For the first part of the 2011 run, the *EF_e20_medium* trigger was used which is an EventFilter level trigger with a p_T threshold of 20 GeV and a medium electron identification requirement applied. As the luminosity of the LHC increased, the lowest unpre-scaled electron trigger was *EF_e22_medium1* which had a 22 GeV p_T threshold. This proved to be insufficient as the luminosity increased and the trigger was changed to *EF_e22vh_medium1* which has even more stringent electron identification cuts.

5.1.2 Muon Triggers

The trigger rates for muons are lower, allowing for looser selection criteria than electron triggers. The *mu_20 trigger* was used for the early periods of 2011 data taking. This trigger has a 20 GeV p_T requirement but very few quality requirements on the muon. It later became necessary to use the *mu_20_medium* trigger. Both the electron and muon triggers are calibrated with data using a “tag and probe” method. Events where at least one trigger has fired (the “tag”) and have two leptons that reconstruct into a Z -boson are selected. The efficiency is derived from the efficiency of the “probe” lepton trigger to fire using the leptons reconstructed offline.

5.2 Electron Identification

Electrons can be reconstructed either starting from a track in the inner detectors or a cluster of energy in the EM calorimeter. In either case, a pair must be formed between a track and a cluster by requiring that the ΔR ¹ between the track and the center of the cluster be below a threshold. For tracks, several quality cuts are applied such as number of hits in the various tracking detectors. Cuts are also applied on TRT hit information to utilize its pion/electron discrimination capabilities. For EM calorimeter showers, cuts on a variety of shower shape variables, such as width at the second sampling layer, and energy fractions between the EM and hadronic calorimeters are also applied. The results of identification cuts are summarized as an “EgammaPID” status word. Due to the high QCD multijet background, rejection of jets faking isolated electrons is the driving factor in choice and only electron candidates passing the “tight++” EgammaPID selection criteria are accepted [89].

The kinematic selection requires that electrons have $p_T > 25$ GeV and $|\eta| < 2.47$. The η cut goes up to slightly before tracking coverage ends and the efficiency drops rapidly. Electrons with clusters within the transition region between two LArg barrels, $1.37 < |\eta| < 1.52$, are rejected. The 25 GeV cut is well above any of the electron trigger turn-on curves. During the 2011 run, portions of the LArg calorimeter were disabled due to hardware failures. Electrons in these regions are excluded from the selection. Signal electrons are expected to be prompt and isolated from both charged tracks and calorimeter energy. Calorimeter isolation cones add up all the energy surrounding the electron cluster (excluding the electron cluster energy) within a certain radius. Similarly, track isolation cones are constructed by

¹ $(\Delta R)^2 = (\Delta\eta)^2 + (\Delta\phi)^2$

adding the scalar p_T of tracks within a cone surrounding the electron track. Cuts are applied to both simultaneously so that the efficiency for true electrons is maintained at 90% [90].

5.2.1 Determination QCD Fake Electron Contributions to Signal

Since Monte Carlo simulation typically does a poor job of describing jets faking leptons, data-driven methods are used for estimating the QCD multijet contamination in the signal selection. The “matrix method” is one such method [42]. A loose selection is created that contains the tighter selection as a subset. For loose electrons, the isolation criteria was loosened, as well as only requiring electrons to pass the “medium++” EgammaPID cuts rather than the “tight++” criteria. By counting the number of events passing the loose or tight selections and using the efficiency of going from loose to tight, a system of equations (Eq. 5.1) can be written down and solved for the number of fake electrons in the signal region. This is done completely inclusively without any lepton p_T dependence.

$$\begin{aligned} N_{\text{loose}} &= N^{\text{signal}} + N^{\text{fake}} \\ N_{\text{tight}} &= \epsilon^{\text{signal}} N^{\text{signal}} + \epsilon^{\text{fake}} N^{\text{fake}} \end{aligned} \tag{5.1}$$

In Eq. 5.1, $N_{\text{loose,tight}}$ is the number of leptons passing the loose/tight selection criteria, N^{signal} is the number of real signal leptons, N^{fake} is the number of fake leptons which is the parameter we want to solve for. To measure ϵ^{fake} , the efficiency for a fake lepton to pass the tight lepton selection criteria, a QCD multijet

control region was selected by selecting events with $E_T^{miss} < 20$ GeV and requiring $\Delta R(e, \text{leading jet}) > 0.7$. Contributions from prompt electrons coming from W and Z decays is subtracted based on estimates from Monte Carlo simulation. The ϵ^{fake} term is the ratio of candidate electrons passing the tight criteria to the total number of loose electrons. For the measurement of ϵ^{signal} , the signal lepton efficiency, $Z \rightarrow ee$ events were used in a “tag and probe” method in a similar fashion. Events are required to have at least one electron passing the tight requirements to serve as the “tag” and ϵ^{signal} is determined by the fraction of loose “probe” electrons also passing the tight criteria.

5.3 Muon Identification

Muon identification starts from tracks in the muon spectrometer. Like electrons, there are varying levels of quality cuts applied and muons passing the tight criteria are used. These muons must also be matched to an inner detector track based on a χ^2 refit of the track (see Sec. 3.3 of Ref. [81] for details), accounting for energy loss and multiple scattering. Additional criteria on the inner track quality are applied, such as requiring a minimum number of hits in the various tracking detectors [91]. Muons are required to have $|\eta| < 2.5$ and $p_T > 25$ GeV, which puts them in the same kinematic region as electrons. For dilepton analyses there is the additional background of cosmic rays. Pairs of oppositely charged muons with large and oppositely signed impact parameters are rejected to remove this background. Non-prompt muons are also produced in heavy flavor decays in which case they are typically close to a jet. Muons that are within $\Delta R < 0.4$ of a jet that has $p_T > 25$ GeV are rejected. Further rejection of non-prompt muons is achieved by applying

isolation cuts on both tracks and calorimeter energy surrounding the projected muon track.

5.3.1 Determination QCD Fake Muon Contributions to Signal

Fake rates are determined using the matrix method as described in the electron fakes section (Sec. 5.2.1). For the loose selection, the tight criteria is still applied but the isolation requirements are dropped completely. The fake efficiency is estimated in a QCD enriched region that is defined by $E_T^{miss} < 20$ GeV and $E_T^{miss} + M_T(W) < 60$ GeV, where $M_T(W)$ is the W transverse mass ². The real efficiency is estimated using $Z \rightarrow \mu\mu$ events with the “tag and probe” method described earlier. Data events are reweighted based on the results to give an estimate for the QCD background for all channels involving muons.

5.4 Jet Reconstruction

Jets reconstruction relies on the ATLAS calorimeter information although there are also types of jet reconstructed from tracks [92]. Calorimeter objects undergo clustering before being fed through a jet algorithm. The simplest of these is 2-D calorimeter towers. These are built by superimposing an $\eta - \phi$ grid over the calorimeter cells and adding up the energy in each section. A scheme exists to distribute energy from larger cells among the multiple towers it may cover. This

² $M_T(W) = \sqrt{2p_T^l E_T^{miss} (1 - \cos(\Delta\phi_{E_T^{miss}, l}))}$

clustering takes all of the cell energies but there is no suppression of calorimeter noise. The typically used clustering object is TopoClusters which utilizes 3-D cell position information. Noise is suppressed through a “4-2-0” scheme as illustrated in Fig. 5.1. The seed for a TopoCluster must have energy that is 4σ above the average noise level. The cells surrounding the seed must have energy that is at least 2σ above the noise level. No other requirement is applied.

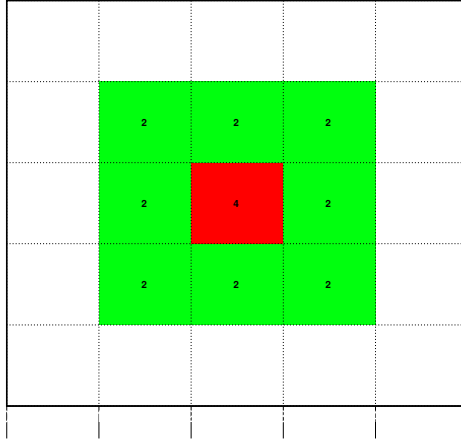


Figure 5.1: The ‘4-2-0’ scheme for TopoCluster seeding shown in 2D. The “seed” cell in the center is colored in red, with an energy greater than $4\sigma_{noise}$. The surrounding cells, in green, must have $E > 2\sigma_{noise}$.

TopoCluster 4-vectors are fed through **FastJet**, which runs the anti- k_T jet algorithm with a distance parameter of 0.4 [38, 93]. This algorithm clusters by sequentially taking small pieces and merging them together to form larger objects until everything has been merged. Since the calorimeters are non-compensating, raw jets (EM-scale) require corrections for the hadronic component of the shower. These corrections contribute to the overall jet energy scale (JES) which sets the scale of the jet to that of truth jets, which are defined by running the jet algorithm over

final state stable Monte Carlo particles. After the jets have been corrected, a $p_T > 25$ GeV cut and a cut on $|\eta| < 2.5$ is applied.

Since the LHC typically operates at high luminosity, especially for the 2011 run, there are a significant number of interactions in a single bunch crossing. This is referred to as “pile-up”. To further enhance jet purity, a jet vertex fraction(JVF) cut on $|\text{JVF}| > 0.75$ is applied [4]. This quantity characterizes the probability that a jet originated from a primary vertex rather than a pile-up vertex, . Jets can be faked by several sources such as cosmic rays, beam backgrounds and hardware flare-ups. Discrimination against cosmic rays is done using timing information. Detector-induced backgrounds, such as electronic noise bursts or hot cells, are identified based on signal pulse shapes and large isolated energy deposits. Events with an identified fake jet are discarded.

5.4.1 Determination of the Jet Energy Scale

Jets are a manifestation of final state partons which have undergone the hadronization process. Reconstruction of jets relies on complex algorithms, which makes calibration non-trivial. Monte Carlo truth jets are reconstructed from stable truth particles excluding muons and neutrinos. Detector-level jet kinematics at EM-scale are scaled to match the truth level jets.

The additional interactions due to pile-up deposit additional energy into the calorimeters that is unrelated to the hard interaction of interest. The pile-up contribution is parameterized as a function of jet η , number of primary vertices in the event and the timing between bunches. The correction, which is typically on the order of a few GeV, is subtracted from the EM-scale jet transverse energy [94].

The bunches in the LHC have a non-zero length along the Z coordinate, which spaces interactions out along the Z axis rather than always occurring in the center of the detector. Jets are reconstructed assuming they originate from the center of the detector. The four-momentum is recalculated using the primary vertex and a correction is applied. The final correction applied, which is derived using Monte Carlo simulations, is based on the ratio of detector-level EM-scale jets to truth-level jets, which is parameterized as a function of jet energy and η [94].

Understanding the calorimeter response to single particles is an important component since jets consist of multiple particles. Pion test beam data exists, but the environment differs with respect to the assembled detector in the experimental cavern. In particular, dead material distributions and geometries are different between the two setups. The uncertainty from mis-modeling of dead material is evaluated from Monte Carlo samples generated with a detector simulation containing additional dead material. Similar measurements were performed with collision data using isolated charged hadrons with the full ATLAS detector [95]. The test beam data covers the energy range above 20 GeV while the isolated hadron analysis is valid from 0.5 GeV to 20 GeV based on the track p_T . Ultimately the uncertainties from single particle response translates into a 1.5-4% uncertainty on the JES [94].

Since inputs to the jet algorithm are TopoClusters, correct modeling of detector noise in Monte Carlo simulations is essential to accurately reproduce data. Uncertainties are evaluated by shifting the noise thresholds and examining the difference, which is only significant for low p_T jets. For anti- k_T jets below 45 GeV, this is a 1% effect. The systematic uncertainty stemming from the choice of the Monte Carlo generator is evaluated by comparing results between `Pythia`-generated and `ALPGEN`-generated samples. The JES is also inter-calibrated using dijet data samples.

The determination of the JES ultimately comes from the Monte Carlo simulation. So, it is susceptible to the modeling uncertainties, as well as uncertainties in the various corrections used in the method itself. Closure of the method is defined as having both the reconstructed energy as well as the reconstructed transverse energy match the truth jet values, which requires that the jet masses be nearly equal [94]. The effects of non-closure are taken as a systematic uncertainty. The size of the JES corrections range from 1.2 for high p_T jets to 2 for jets with p_T around 20 GeV. For the jets entering this analysis, the JES uncertainty ranges from 2.2% to 6.5%, depending on jet p_T and η . For a central jet ($|\eta| < 0.3$) with $p_T = 20$ GeV, the JES uncertainty is 4.1%. For a jet in the same $|\eta|$ region with $p_T=200$ GeV, the JES uncertainty is around 2.3% [94].

5.5 Missing Energy Reconstruction

Missing momentum is used to infer the presence of a neutrino since they escape the detector without interacting. Colliding protons have no momentum in the transverse plane and since they are composite objects, the initial momentum of the constituents along the beamline direction is unknown. Imbalances in p_T are used to derive the “ E_T^{miss} ” vector. Since the variety of different physics object types have different calibration schemes from each other, cells belonging to each object are calibrated according to that particular scheme before the calculation of E_T^{miss} . The reconstructed objects entering the calculation are electrons, muons, taus, pho-

tons and jets as well as some additional objects through Eq. 5.2 as the $\sum_{\text{Electrons}} \vec{E}_T$, $\sum_{\text{Muons}} \vec{p}_T$, $\sum_{\text{Taus}} \vec{E}_T$, $\sum_{\text{Photons}} \vec{E}_T$, $\sum_{\text{Jets}} \vec{E}_T$ terms respectively [81].

$$\begin{aligned} \vec{E}_T^{miss} = & - \sum_{\text{Jets}} \vec{E}_T - \sum_{\text{Electrons}} \vec{E}_T - \sum_{\text{Taus}} \vec{E}_T - \sum_{\text{Photons}} \vec{E}_T \\ & - \sum_{\text{SoftJets}} \vec{E}_T - \sum_{\text{Cellout}} \vec{E}_T - \sum_{\text{Muons}} \vec{p}_T - \sum_{\text{Calo},\mu} \vec{E}_T \quad (5.2) \end{aligned}$$

Jets are split into two categories based on p_T . Jets with p_T above 20 GeV are calibrated using the JES scheme described in the previous section and enter into the calculation through the $\sum_{\text{Jets}} \vec{E}_T$ term. Jets with p_T between 7 and 20 GeV are considered “softjets” and calibrated by individual clusters and are handled separately as the $\sum_{\text{SoftJets}} \vec{E}_T$ term in Eq. 5.2 [96]. Energy that does not belong to any object, but does belong to a TopoCluster, contributes to the “cellout” term, $\sum_{\text{Cellout}} \vec{E}_T$, in the E_T^{miss} calculation [97]. Muons don’t shower in the calorimeters, but deposit energy through ionization. The corresponding cells are also included in the E_T^{miss} calculation as the $\sum_{\text{Calo},\mu} \vec{E}_T$ term. Central muons are required to have a matching ID track to reduce the contributions from fake muons.

5.6 Event Selection

Due to the variety of possible decay channels for $t\bar{t}$ events (Fig. 1.9), most types of reconstructed objects are required to observe the $t\bar{t}$ signal. W -bosons can decay into jets and all flavors of leptons. The leptonic decays of W -bosons have a final state neutrino which can only be inferred through the presence of E_T^{miss} in the event. Regardless of how the W -bosons decay, we expect to have two final state

b -quarks in the event which are reconstructed as jets. There are many processes that can mimic the $t\bar{t}$ event signatures, such as W +jets in the single lepton channel and Z +jets events in dilepton channels, so event selection cuts are applied that are designed to minimize the contributions from backgrounds while preserving $t\bar{t}$ signal events. The event selection cuts are summarized in Tab. 5.1 and the efficiencies for $t\bar{t}$ events are shown in Fig. 5.2 taking branching ratios into account.

The lepton+jets event selection requires exactly one good electron or muon that matches the trigger lepton. The appropriate single lepton trigger is required to have been fired. Non-collision background events are rejected by the requirement of a good reconstructed primary vertex with at least four tracks. Due to the multitude of detector requirements due to the complicated final states of $t\bar{t}$ events, only data with the majority of the detector functional is used. For the muon channel, events are required to have $E_T^{miss} > 20$ GeV and transverse W mass + $E_T^{miss} > 60$ GeV. Electrons suffer from a larger QCD multijet background so the E_T^{miss} and transverse W mass cuts are both raised to 30 GeV. Single lepton events must have at least four jets.

For the dilepton channel, exactly two oppositely charged leptons are required. Single lepton triggers are used and at least one of the leptons must match the trigger lepton. Non-collision background events are mostly rejected by requiring a good vertex but there is an additional background in the dilepton channel from cosmic rays. Muon events with back-to-back oppositely charged muons that have a large impact parameter ($> 0.5\text{mm}$) are rejected. Two neutrinos are expected in the final state so a threshold of 60 GeV is made on the E_T^{miss} for the ee and $\mu\mu$ channels. There is very little SM background the $e\mu$ channel so a cut on the minimum scalar p_T sum of objects, H_T , is applied at 130 GeV and the E_T^{miss} requirement is dropped.

cut	e	μ	cut	ee	$e\mu$	$\mu\mu$
Trigger	14.4	15.5	Trigger	1.32	2.65	1.31
one lepton	7.9	10.4	cosmic rej.	1.17	2.43	1.24
four jets	3.4	4.5	two leptons	0.39	1.03	0.65
E_T^{miss}	2.7	4.1	E_T^{miss} or H_T	0.21	0.96	0.36
$M_T(W)$	2.3	3.9	two jets	0.18	0.81	0.28
b -tag	2.1	3.4	$M(l\bar{l}) > 15$ GeV	0.17	0.80	0.28
(a) Selection efficiencies for the leptoni+jets channels in %.			Z -mass veto	0.15	0.80	0.23
			(b) Selection efficiencies for the dilepton channels in %.			

Figure 5.2: Summary of event selection efficiencies for $t\bar{t}$ events including branching ratios.

The dominant background for the same flavor-channels (ee and $\mu\mu$) is Z +jets events. The Z +jets contamination is suppressed by removing a 20 GeV wide window centered on m_Z for the invariant mass of the two leptons. There are additional low-mass resonances that can contribute. These are removed by requiring the invariant mass of the two leptons to be greater than 15 GeV. The jet multiplicity for dilepton events is typically lower than that of lepton+jets events, so only two jets are required.

cut	e	μ	ee	$e\mu$	$\mu\mu$
triggers	<i>EF_e20_medium</i>	<i>mu_20</i>	<i>EF_e20_medium</i>	<i>EF_e20_medium</i>	<i>mu_20</i>
used	<i>EF_e22_medium</i>	<i>mu_20_medium</i>	<i>EF_e22_medium</i>	<i>EF_e22_medium</i>	<i>mu_20_medium</i>
	<i>EF_e22vh_medium1</i>		<i>EF_e22vh_medium1</i>	<i>EF_e22vh_medium1</i>	
				<i>mu_20</i>	
				<i>mu_20_medium</i>	
exact # of leptons	1	1	2	2	2
min. lepton p_T [GeV]	25	25	25	25	25
min. # of jets	4	4	2	2	2
min. jet p_T [GeV]	25	25	25	25	25
min. E_T^{miss} [GeV]	30	20	60	-	60
min. $M_T(W)$ [GeV]	30	$E_T^{miss} + M_T(W) > 60$	-	-	-
min. H_T [GeV]	-	-	-	130	-
min. $m(l\bar{l})$ [GeV]	-	-	15	-	15
Z mass cut [GeV]	-	-	81-101	-	81-101
min. # b -tags	1	1	0	0	0

Table 5.1: Summary table listing the event selection cuts applied for the five decay channels, e , μ , ee , $e\mu$ and $\mu\mu$.

CHAPTER 6

MONTE CARLO SIMULATION

Monte Carlo (MC) modeling methods are indispensable tools in the HEP experimenter's trade. The procedure is typically divided into several steps. There is a hard scattering portion which generates events corresponding to a particular matrix element (ME) in some region of phase space. As mentioned in Chapter 1, processes in the Standard Model are calculated using a perturbative expansion in the coupling constant evaluated to a fixed order. The lowest order of the expansion is the leading order (LO). One order higher is the next-to-leading order (NLO) contribution to the calculation, followed by the next-to-next-to-leading order (NNLO). For many physics processes, the matrix element is calculated at LO precision, but in recent years there has been significant progress in calculating processes at the next-to-leading order (NLO). The events from the matrix element process are then fed through other MC generators to handle decays of unstable particles, radiation, and parton showering (PS). Most of these processes occur in the beam pipe at short distances before anything can interact with the detector but there can also be long-lived particles produced. The large ensemble of final state particles is run through a detector simulation which consists of two parts, energy deposition modeling and response modeling or digitization. The simulated detector output is reconstructed as if it was actual data. In most of these steps, there is modeling present which has adjustable parameters.

This Chapter aims to give an overview of the Monte Carlo simulations used in this analysis and address some of the issues associated with them. The first section

describes the general procedure for producing matrix element Monte Carlo samples and then proceeds to describe the procedures and issues associated with matching these processes with parton showers. The next section describes the $t\bar{t}$ Monte Carlo samples used, comparisons to data and some of the associated systematic uncertainties. The bulk of this Chapter is devoted to the modeling of the W +jets background and detailed studies are performed to assess the possible systematics associated with choice of generator parameters. The Monte Carlo samples for smaller backgrounds such as single top and dibosons are discussed briefly. The chapter concludes with a description of the ATLAS detector simulation.

Matrix Element Generation. The general procedure for MC generation in high energy physics is to start with the process at the highest energy scale, which is described by the matrix element, and work down. The matrix element is often referred to as the “hard” process while processes such as radiation and minimum bias are referred to as being “soft”. The matrix element calculation for many processes can be performed by hand. For others, numerical methods have been developed [98–100]. For generating single events, probability distribution functions are employed and random number generators are used to sample the phase space. An example of one popular program used to generate events is PYTHIA [101].

Matrix Element-Parton Shower Matching. Matrix element calculations don’t perform well with low scale interactions (infrared divergences) and small angles (collinear divergences) like soft radiation and showering so a different procedure must be used to model those effects. The perturbative regions where matrix element calculations are utilized are where the scale of the interaction is much larger than the scale of parton hadronization (see Fig. 6.1) which is typically of the order of a few hundred MeV [39]. Furthermore, final state parton hadronization and decay

have to be taken into account. Evolution of a hadronic shower can be calculated using the DGLAP equations [102–104] and this is implemented in many programs as a parton shower (PS) [101, 105–108]. The generated showers are usually clustered as jets at truth level and matched to partons by momenta. **HERWIG** [105, 106] is a popular generator that often used to produce parton showers. Both **HERWIG** and **PYTHIA** have the ability to perform matrix element calculations, as well as parton shower modeling.

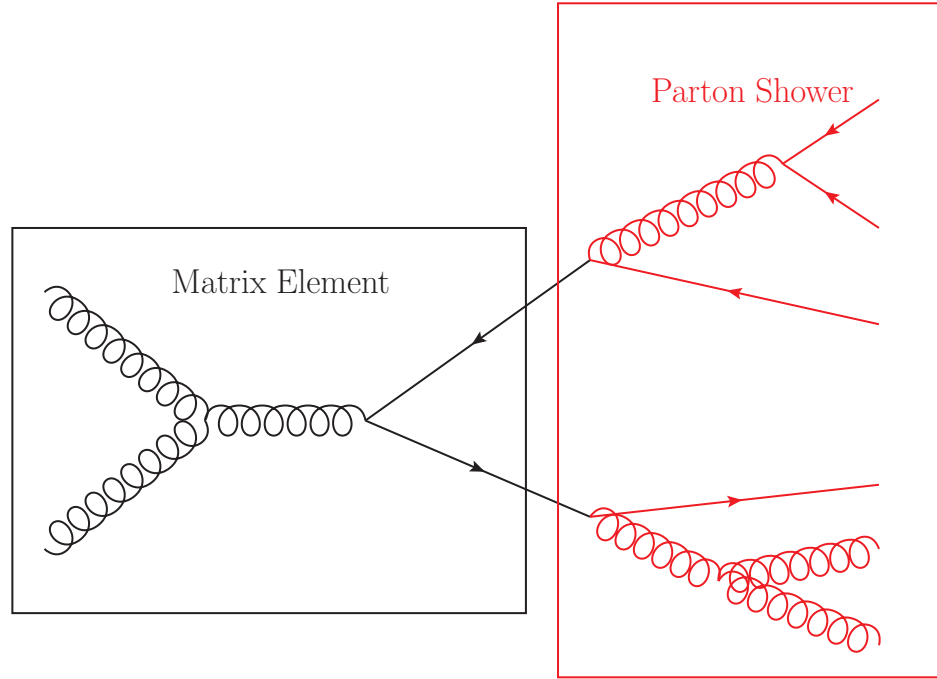


Figure 6.1: A Feynman diagram of $gg \rightarrow q\bar{q}$ illustrating the hard scattering region handled by the matrix element calculation in black and the regions handled by parton shower modeling in red.

There is also a double counting issue to be resolved since different arrangements of Feynman diagrams can produce identical final states for both matrix element generators and parton shower models as illustrated in Fig. 6.2. This can be avoided by restricting the matrix element and parton shower to handle different regions of phase space. Matrix element calculations diverge at small angles and low relative

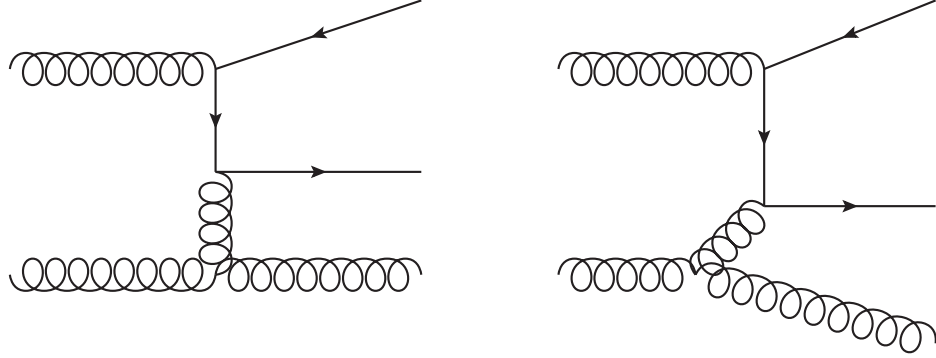


Figure 6.2: The process in the left would contribute to the total cross section from the matrix element generator while the one of the right would arise from the parton shower as the final state gluon appears from initial-state radiation.

p_T between particles so below some cut-off angle, parton shower are used instead. Similarly a p_T scale is used for the boundary between a “hard” and “soft” process.

In a pp collision, it is possible to have multiple interactions among partons within the proton. Simulation of this phenomenon is provided by the **JIMMY** program [109–111] which is interfaced through the **HERWIG** program or **PYTHIA** which contains this process. Both **HERWIG** and **JIMMY** have some tunable parameters which were compared with data. By selecting some observables, the parameters of **HERWIG** and **JIMMY** were modified to reproduce the distributions seen in data [112]. The **PYTHIA** generator is capable of doing matrix element calculations as well as parton shower modeling. The parameters of the the parton shower model have been tuned to data in what is referred to as **AMBT2** and **AUET2** which stand for **ATLAS Minimum Bias Tune 2** and **ATLAS Underlying Event Tune 2**, respectively [113]. The underlying event (UE) can be defined as everything occurring in the collision, such as radiation and multiple parton interactions, excluding the hard scattering.

6.1 $t\bar{t}$ samples

For generating $t\bar{t}$ samples, the **MC@NLO** [114, 115] generator was used. This is a NLO matrix element generator which was interfaced with the **HERWIG** and **JIMMY** programs to provide the parton shower and underlying event modeling. The samples were generated in two orthogonal sets with one set restricting both W -bosons to decay hadronically and the other requiring at least one to decay leptonically (which can include hadronically decaying tau final states). The default top mass used was 172.5 GeV [116] which is consistent with the PDG value of $173.5 \pm 0.6 \pm 0.8$ GeV [39]. The cross section was not taken from the **MC@NLO** generator as there are more precise predictions available at NNLO from the **HATHOR** [117] program. **HATHOR** is not capable of generating events so the **MC@NLO** $t\bar{t}$ sample cross sections were scaled to the 166.8 pb reference cross section predicted by **HATHOR** [118].

For Monte Carlo systematic studies, alternative $t\bar{t}$ samples are used. To assess the dependence on the MC generator used, analyses are repeated using **POWHEG** [107, 108] produced $t\bar{t}$ samples and compared with the baseline **MC@NLO** results. Shower modeling dependence is estimated by a comparison between **POWHEG** samples showered with **HERWIG** against the same samples showered with **PYTHIA**. Initial and final state radiation (ISR/FSR) modeling dependence is assessed by producing $t\bar{t}$ samples with **AcerMC** [119] and varying the parameters. Comparisons are made between the variations and nominal **AcerMC** samples to avoid adding in generator dependence into the systematic uncertainties. The preliminary systematic ISR variations were conservative as the data falls well within the range of ISR uncertainties as illustrated by the colored bars in Fig. 6.3 [13]. The systematic ISR/FSR prescriptions have been updated by allowing the data to constrain the reasonable range of variations.

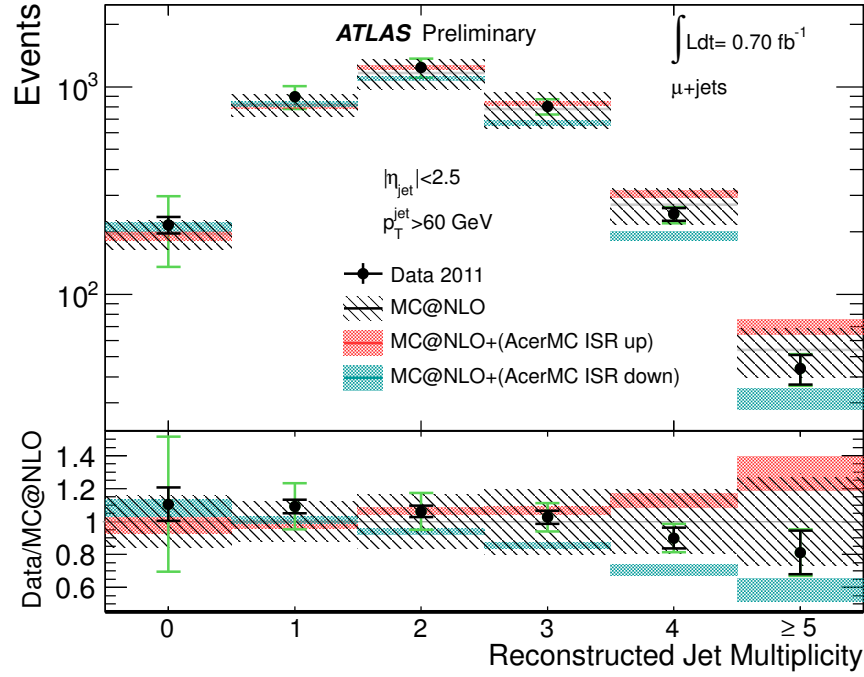


Figure 6.3: Reconstructed jet multiplicity in candidate $t\bar{t}$ events compared with MC predictions. Uncertainties are derived using **AcerMC** and the relative uncertainty is applied to nominal **MC@NLO** samples [13].

6.2 Vector Boson + Jets modeling

For both W and Z boson production, the **ALPGEN** [120] generator is used. **ALPGEN** is a LO generator that can provide matrix element calculations for a large variety of processes. Events are generated with a fixed number of final state partons which can go up to five. Since **ALPGEN** is a matrix element generator, it must be interfaced with either **PYTHIA** or **HERWIG** to provide the parton shower model. **ALPGEN** runs a simple jet finding algorithm to identify jets in the parton shower which it then matches to matrix element partons. The matching between matrix element and parton shower elements can be performed either inclusively or exclusively. For exclusive matching, each parton must be matched to a parton shower jet. If there

are extra jets in an event, that event is rejected. Inclusive matching also requires that each parton match to a shower jet but does not veto events with additional jets. For the ATLAS MC production, W and Z events with up to four additional partons are matched exclusively and the five parton sample is matched inclusively which effectively extends the jet multiplicity even higher by allowing additional jets from the parton shower. Each N -parton production is weighed to its generator calculated cross section and all parton multiplicities are combined to cover the full phase space. ALPGEN is quite successful in describing W +jet events in data as illustrated in Fig.

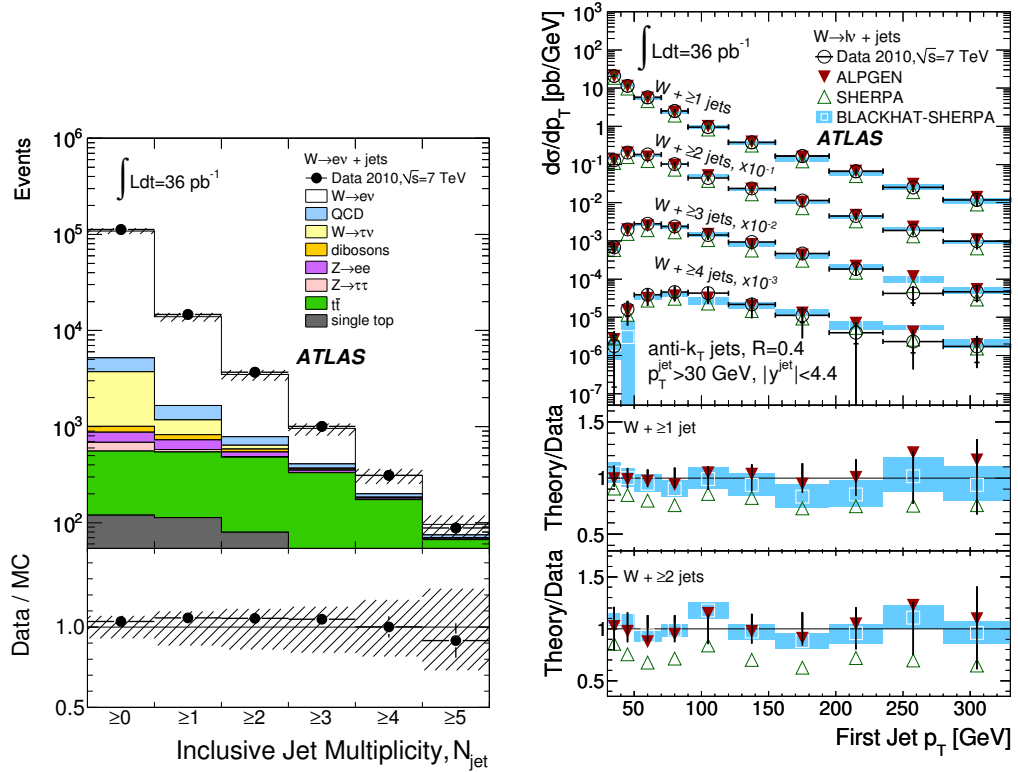


Figure 6.4: Jet multiplicity and p_T of the leading jet for W +jet events in data and as described by the ATLAS MC chain [14]. The ALPGEN W +jet Monte Carlo jet multiplicity agrees with the data quite well as deviations are less than 10% and covered by the uncertainties. The event kinematics are also well modeled as the leading jet p_T as predicted by ALPGEN agrees with the data.

Parameter	Function	default value	variations
<code>ptjmin</code>	min. jet p_T	15 GeV	10,20,25,30
<code>etclu</code>	min. cluster p_T	20 GeV	15,25,30,35 (<code>etclu</code> = <code>ptjmin</code> +5 GeV)
<code>ktfac</code>	re-scaling of α_s at vertices	x1.0	x0.5,x2.0
<code>qfac</code>	re-scaling of factorization/renorm. scale	x1.0	x0.5,x2.0
<code>iqopt</code>	factorization/renorm. scale form	<code>iqopt</code> =1	see Tab. 6.2
UE tune	underlying event tune	HERWIG	PYTHIA Perugia “hard”, “nominal”, “soft”

Table 6.1: Listing of ALPGEN parameters varied.

6.4. This dictated the choice of ALPGEN over the SHERPA generator [121] for these processes.

6.2.1 ALPGEN parameters

For the ALPGEN parameter studies, the parameters are chosen to be consistent with the centrally produced ATLAS MC samples, as well as giving reasonable values for physical observables. The list of parameters being studied is presented in Tab. 6.1. The top mass is set to 172.5 GeV to be consistent with top MC production while the W and Z boson masses are set to their PDG values [44]. Phase space cuts are applied to remove objects that wouldn’t pass the fiducial selection applied by the detector geometry. Final state partons are required to have $|\eta|$ less than 6, which is safely beyond the reach of the forward calorimeters. For the choice of parton distribution functions (PDFs), CTEQ6L1 tables are used [122].

Studies were performed to judge the sensitivity of W+jets modeling as a background process to a $t\bar{t}$ measurement by varying the parameters and analyzing their effects on numerous observables [123]. Since full simulation of the ATLAS detector is extremely CPU intensive, these studies were performed at MC generator level only. Jets are reconstructed from final state interacting particles using the anti- k_T algorithm provided with the **FastJet** program [124]. The charged leptons from the W decay are removed from the collection of particles used to form jets. To simulate E_T^{miss} , the neutrino p_T is used. The kinematic and event selection cuts that are applied in the $t\bar{t}$ analysis are applied to the MC objects.

6.2.1.1 ptjmin and etclu

The **ptjmin** parameter within ALPGEN specifies the minimum p_T that a light parton must have in order to be matched to a shower jet. In broad terms, this separates hard from soft processes since anything below this p_T threshold will come from the parton shower instead of the matrix element. The value chosen by ATLAS is 15 GeV which is below the typical top analysis jet p_T threshold. Additionally there is a threshold placed on the minimum E_T that a parton shower jet must have to be matched to a parton. The ALPGEN manual specifies that **etclu** should be set 5 GeV higher than **ptjmin** [120].

To study the effect varying **ptjmin** had on observables, it was varied in 5 GeV increments while all other parameters were kept at their nominal values except **etclu**, which was varied according as **etclu**=**ptjmin**+5 GeV. Figure 6.5 shows the leading jet p_T for final states passing the top analysis selection with four jets with p_T greater than 20 GeV. When normalized to the cross section for a nominal value

of 15 GeV, it is clear that lower `ptjmin` makes no difference when the jet p_T cut is much higher, but effects start appearing once `ptjmin` becomes comparable to the jet p_T cut. At a `ptjmin` setting of 20 GeV, `etclu` is now 5 GeV higher than the jet p_T cut and an overall drop in cross section is observed as shown in Fig. 6.5. In terms of shape of the distribution, there is a turn-on curve where low- p_T jets are affected but at substantially high- p_T the distribution, the shape returns to the nominal form, indicated by the zero slope for the ratio shown in Fig. 6.5. The effects on jet kinematics also affects the jet multiplicity as shown by Fig. 6.6. For `ptjmin` = 10 GeV, there is no noticeable effect on the jet multiplicity, but for higher `ptjmin` values the cross section and the shape of the distribution change with respect to the nominal `ptjmin`=15 GeV samples. As long as `ptjmin` is set below the jet p_T cut, the effects of `ptjmin` choice are minimal.

6.2.1.2 ktfac

In ALPGEN, it is possible to re-scale the α_s terms at the vertices of the Feynman diagrams by modifying the `ktfac` parameter, which rescales λ_{QCD} according to Eq. 6.1, where μ is the factorization/renormalization scale [125].

$$\alpha_s(\mu^2, \text{ktfac}) \propto \frac{1}{\ln(\mu^2 / (\frac{1}{\text{ktfac}} \lambda_{QCD}^2))} \quad (6.1)$$

By default, `ktfac` is set to unity but in principle, it can take any value. For assessing sensitivity to this parameter, variations of a factor of two (and sometimes four) are typically used although there is no particularly strong physical motivation for this range.

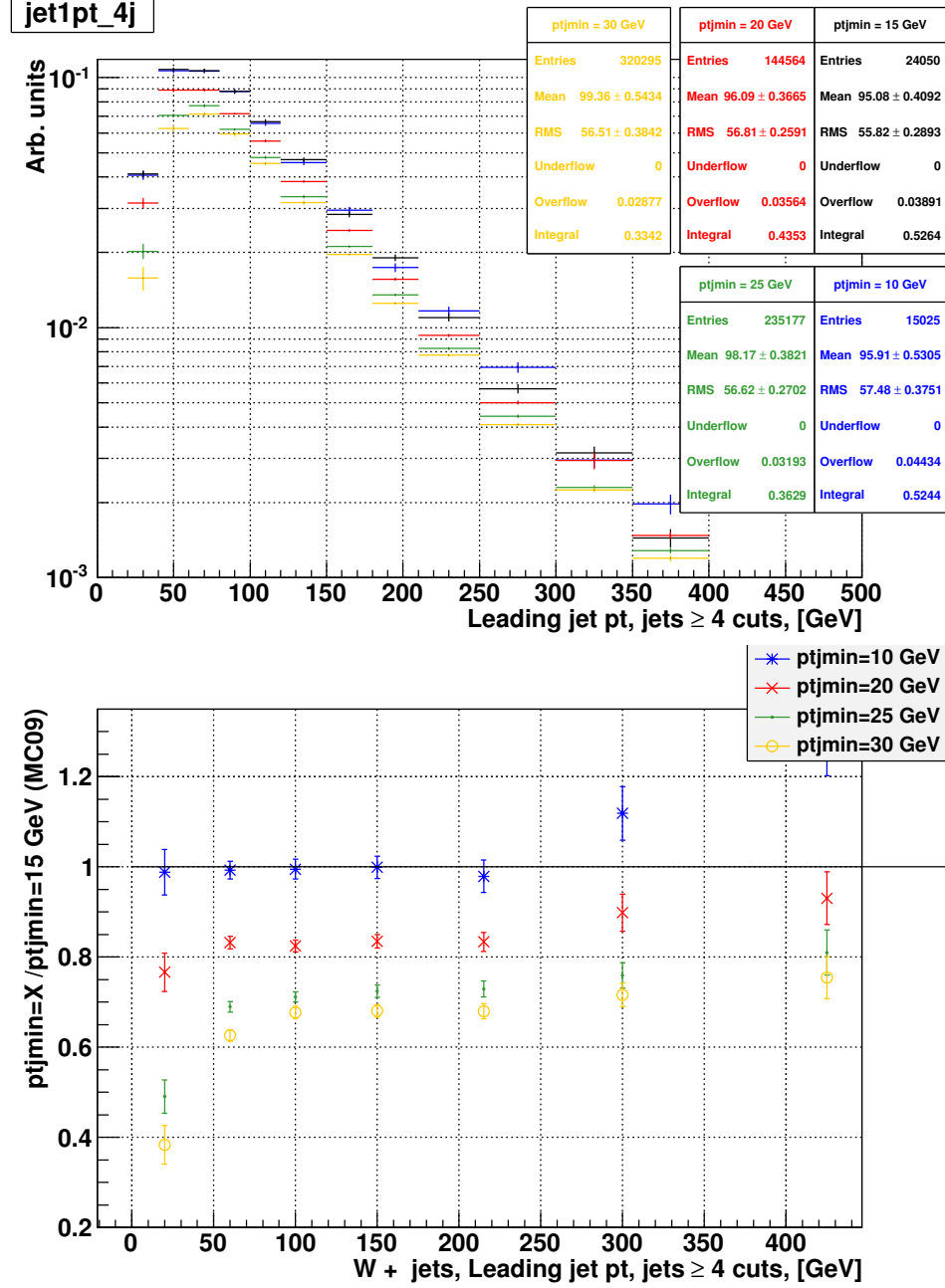


Figure 6.5: Effect of varying ptjmin on leading jet p_T for ptjmin values between 10 and 30 GeV for final W+jets states with at least four high- p_T jets. The top plot shows the leading jet p_T spectrum. The bottom plot shows the leading jet p_T spectrum normalized to the leading jet p_T spectrum derived from the nominal $\text{ptjmin} = 15$ GeV sample. At low p_T , there is a turn on curve for $\text{ptjmin} > 20$ GeV.

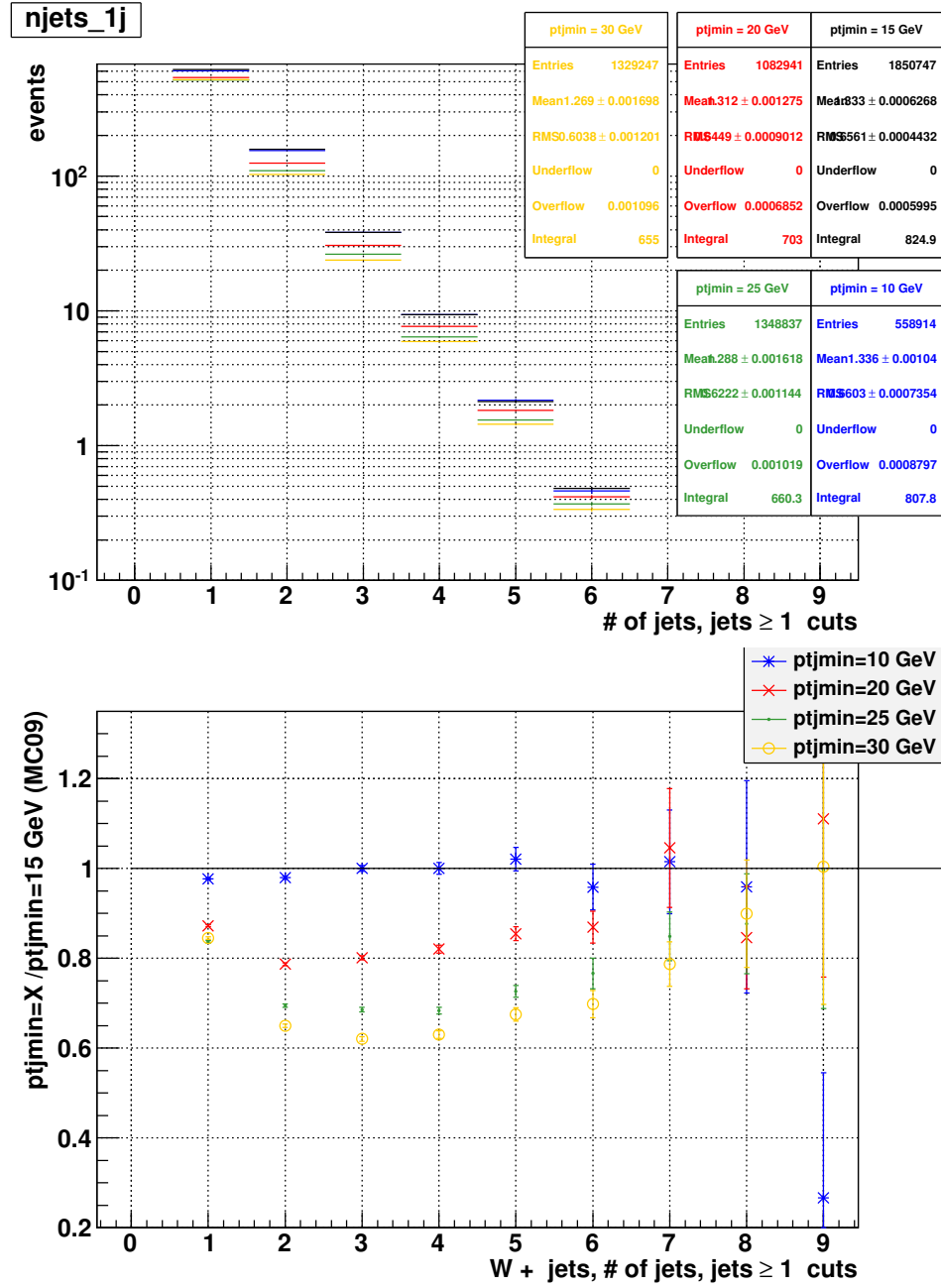


Figure 6.6: Effect of varying pt_{jmin} on jet multiplicity for pt_{jmin} values between 10 and 30 GeV for final W+jets states with at least one high- p_T jet. The top plot shows the jet multiplicity for the various pt_{jmin} variations. The bottom plots shows the same distribution normalized to the $pt_{jmin}=15$ GeV. The $pt_{jmin}=10$ GeV jet multiplicity distribution closely matches the $pt_{jmin}=15$ GeV but higher values of $pt_{jmin} > 20$ GeV have lower cross sections.

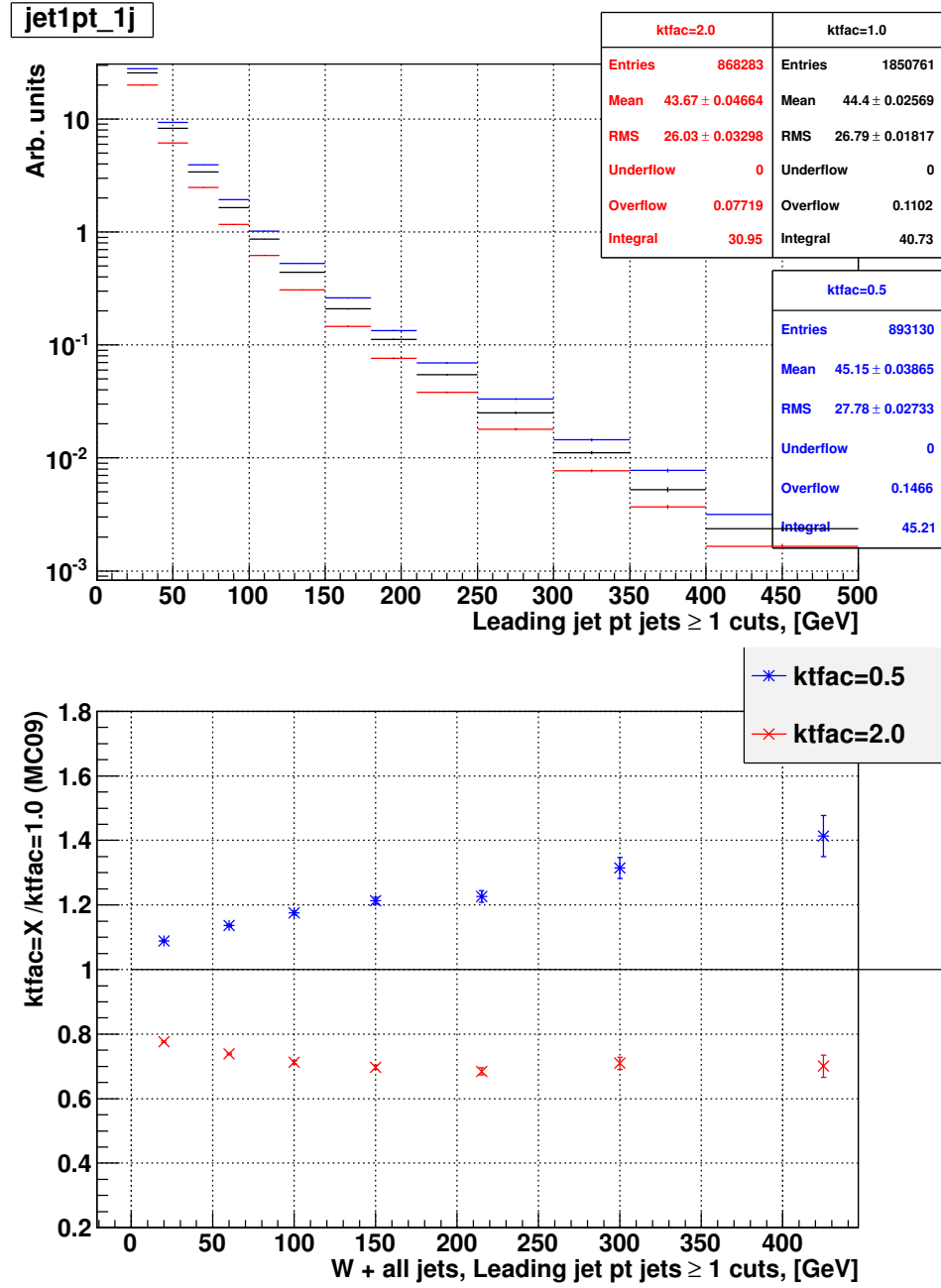


Figure 6.7: The top plot shows the leading jet p_T distribution for ktfac values between 0.5 and 2 for final W+jets states with at least one high- p_T jet. The bottom plot is the ratio of the above distributions to the nominal $\text{ktfac}=1$ value and shows a systematic dependence.

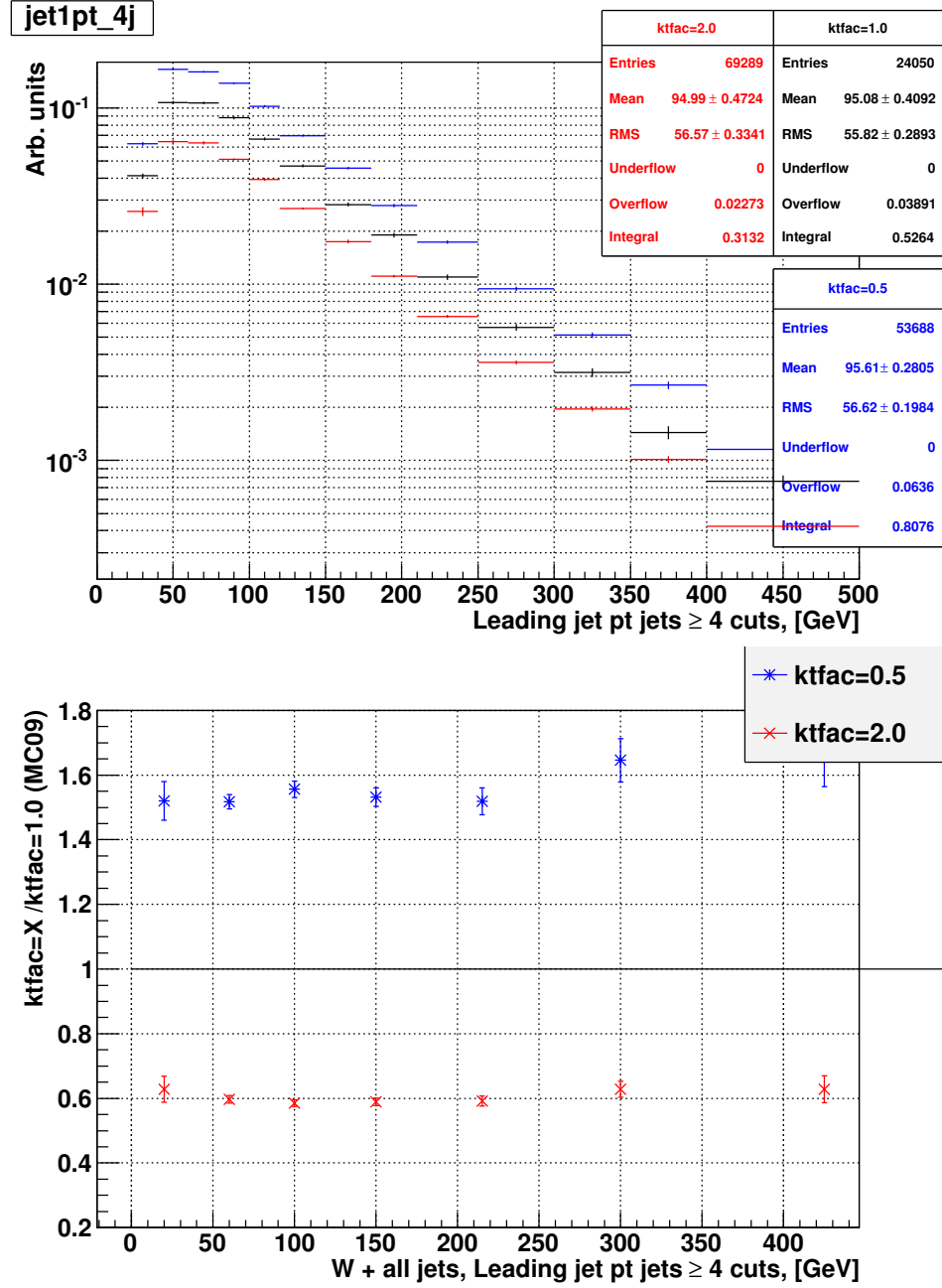


Figure 6.8: Effect of varying ktfac on leading jet p_T for ktfac values between 0.5 and 2 for final W+jets states with at least four high- p_T jets. Like Fig. 6.7, the top plot is the leading jet p_T and the lower plot has been normalized to the nominal ktfac . The bottom plots shows that while the normalization is affected by ktfac , the shape of the distribution is unaffected.

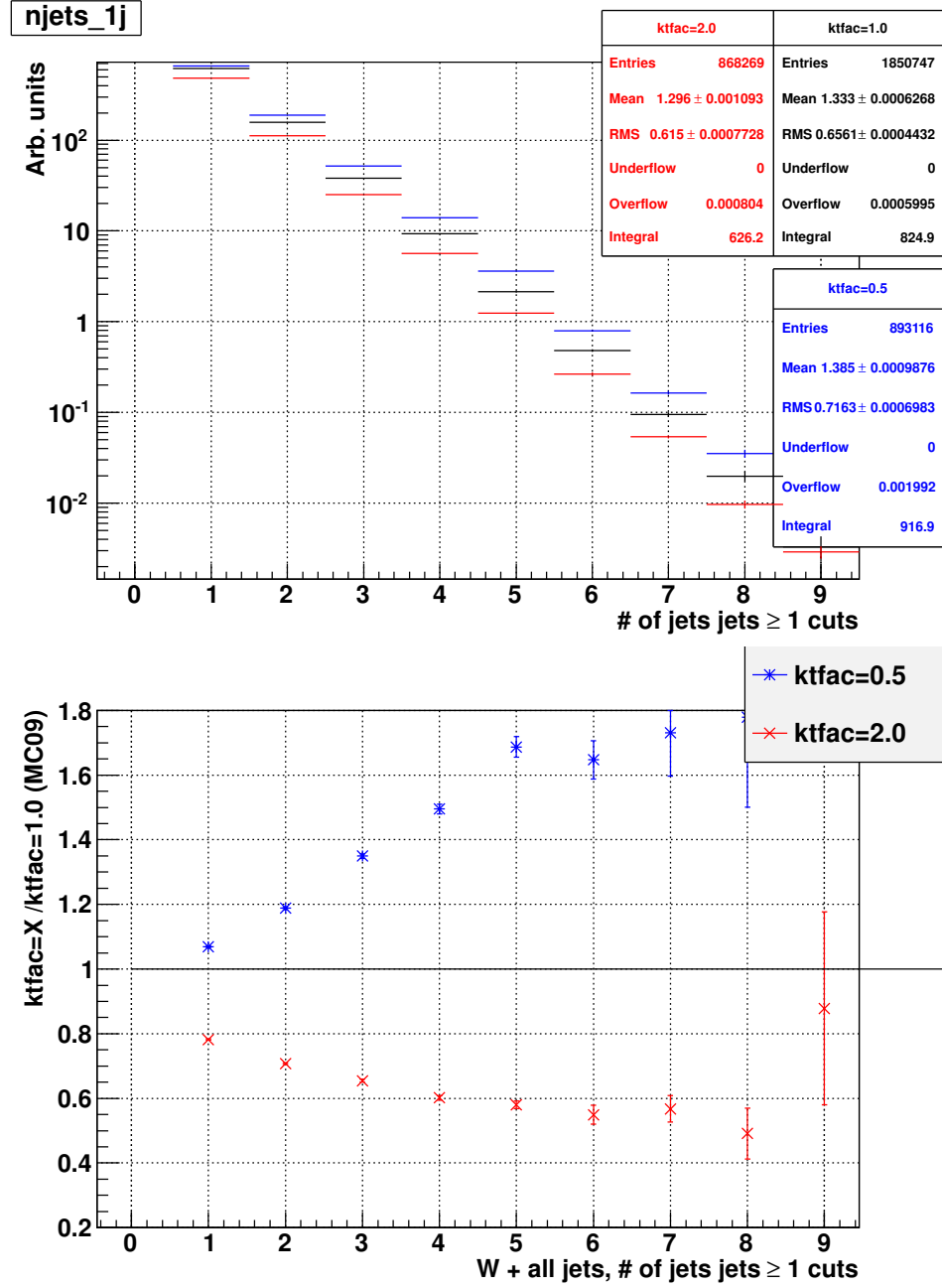


Figure 6.9: Effect of varying $ktfac$ on jet multiplicity for $ktfac$ values between 0.5 and 2 for final W+jets states with at least one high- p_T jet. The top plot shows the jet multiplicity while the bottom plot shows the jet multiplicities normalized to the nominal distribution. Since $ktfac$ affects the value of α_s , the jet multiplicity is very sensitive to the $ktfac$ setting.

Modifying `ktfac` not only changes the overall cross section after cuts are applied, but also changes the distribution of several observables. The leading jet p_T shape is affected by `ktfac` variations when only one jet is required but when this cut is raised to four jets, the difference in predicted cross sections increased while the shape of the distribution returns to its nominal value as illustrated in Fig. 6.7 and 6.8. Jet multiplicity is also strongly affected, as shown in Fig. 6.9. The predictions for the expected cross sections diverge as the number of jets increases.

6.2.1.3 qfac

This parameter rescales both the renormalization and factorization scales (μ) simultaneously by a common factor. Like `ktfac`, the range of variations is a factor of two by convention. The effect on jet p_T is similar to the case of `ktfac` with effects being seen in low jet multiplicity events (Fig. 6.10) that disappear as the jet multiplicity increases. The effect on normalization is not as dramatic as `ktfac`, but there are changes occurring in the jet multiplicity (Fig. 6.11).

6.2.1.4 iqopt

While `qfac` is a multiplicative factor for the scales, it is also possible to change the functional form of the scale within `ALPGEN` through the `iqopt` parameter. The available choices for W +jets production in `ALPGEN` are shown in Tab. 6.2. The default setting is `iqopt` = 1 which is a form that varies with H_T (the scalar sum of p_T) of the jets in the event. The choice of `iqopt` = 0 (`Q=qfac`) is provided so that users can set any fixed scale they choose. The other fixed scale choice is

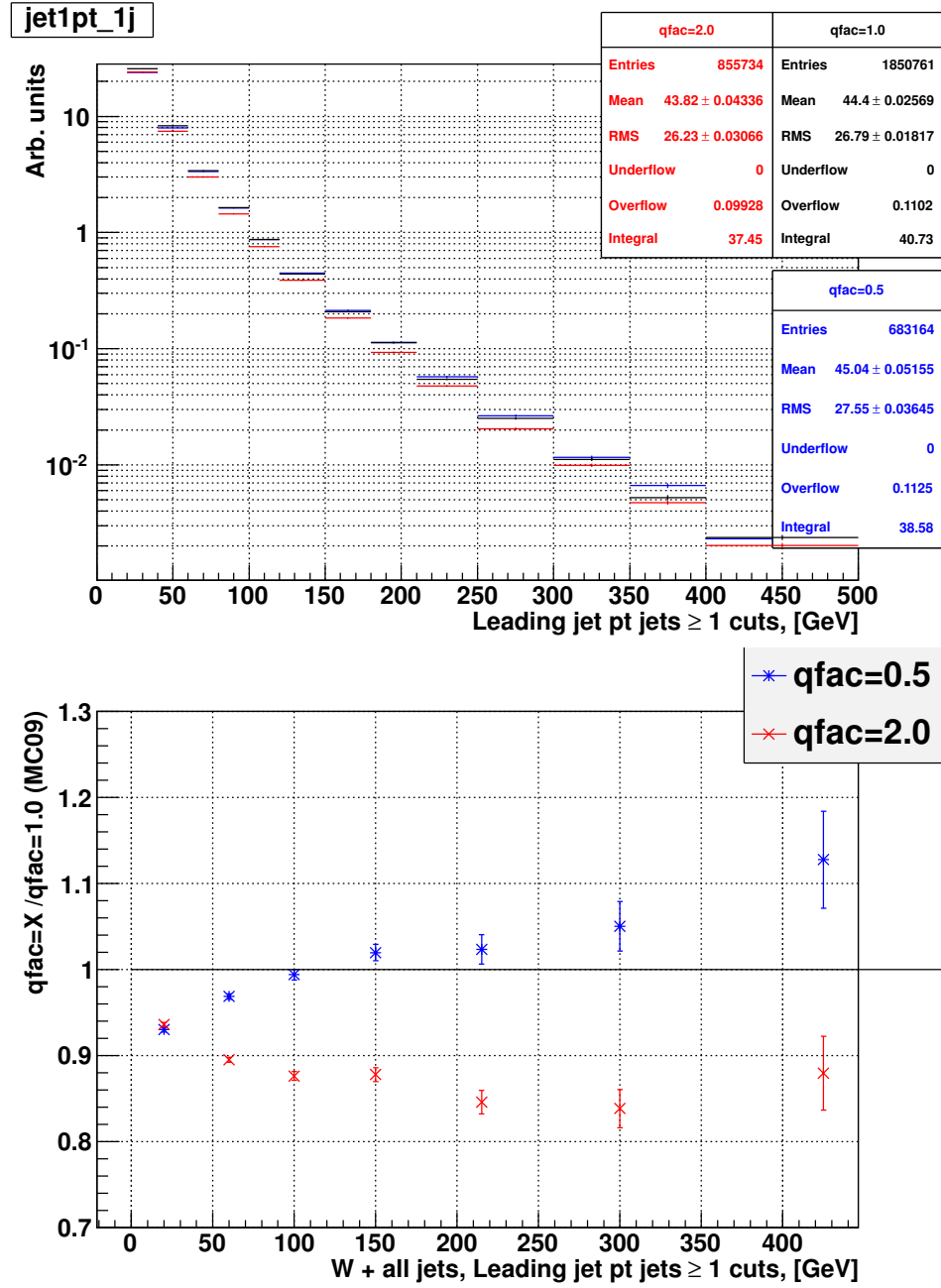


Figure 6.10: Effect of varying $qfac$ on leading jet p_T for $qfac$ values between 0.5 and 2 for final W+jets states with at least one high- p_T jet. The leading jet p_T is shown in the top plot while the distribution normalized to the default $qfac$ parameter is shown below, which illustrates some dependence on the value of $qfac$.

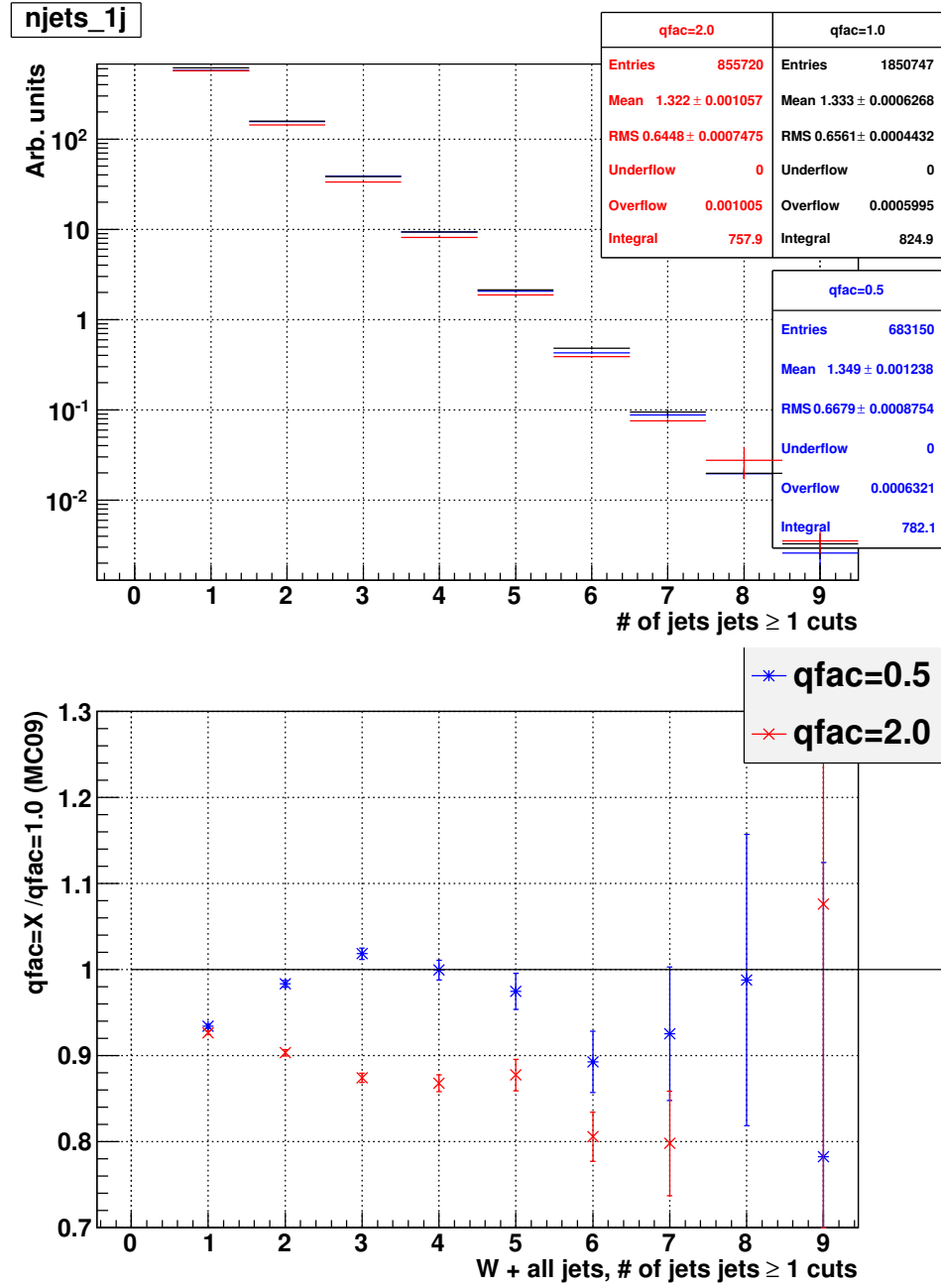


Figure 6.11: Effect of varying $qfac$ on jet multiplicity for $qfac$ values between 0.5 and 2 for final W +jets states with at least one high- p_T jet. The top plot shows the jet multiplicity distribution while the bottom plot shows the distributions normalized to the nominal distribution showing the shape dependence on $qfac$.

<code>iqopt</code>	Functional form
0	$Q = \text{qfac}$
1	$Q = \text{qfac} * \sqrt{m_W^2 + \sum_{\text{jets}} p_T^2}$
2	$Q = \text{qfac} * m_W$
3	$Q = \text{qfac} * \sqrt{m_W^2 + p_{T,W}^2}$
4	$Q = \text{qfac} * \sqrt{\sum_{\text{jets}} p_T^2}$

Table 6.2: Listing of available **ALPGEN** renormalization/factorization scale (Q) forms for W +jets production. The `qfac` parameter is described in Sec. 6.2.1.3 and m_W is the mass of the W -boson. The sums over p_T treat p_T as a scalar term.

`iqopt=2` ($Q=m_W$), which is one choice that was studied. Differences between the default `iqopt=1` setting and `iqopt=4` amounts only to an additive constant so this variation was not studied. The setting of `iqopt=3` was chosen as a variation of a dynamic scale that uses the p_T of the W rather than the jets it is recoiling against.

The most sensitive variable to `iqopt` selection was H_T , as shown in Fig. 6.12. This is not surprising. At low H_T , both the static and dynamic scales are all dominated by the m_W terms so there is general agreement between all three choices. As the H_T increases, the other terms become substantial and the three scales deviate from each other. The fixed scale deviates much more rapidly than `iqopt=3` since $p_{T,W}$ is correlated with the H_T term in `iqopt=1`.

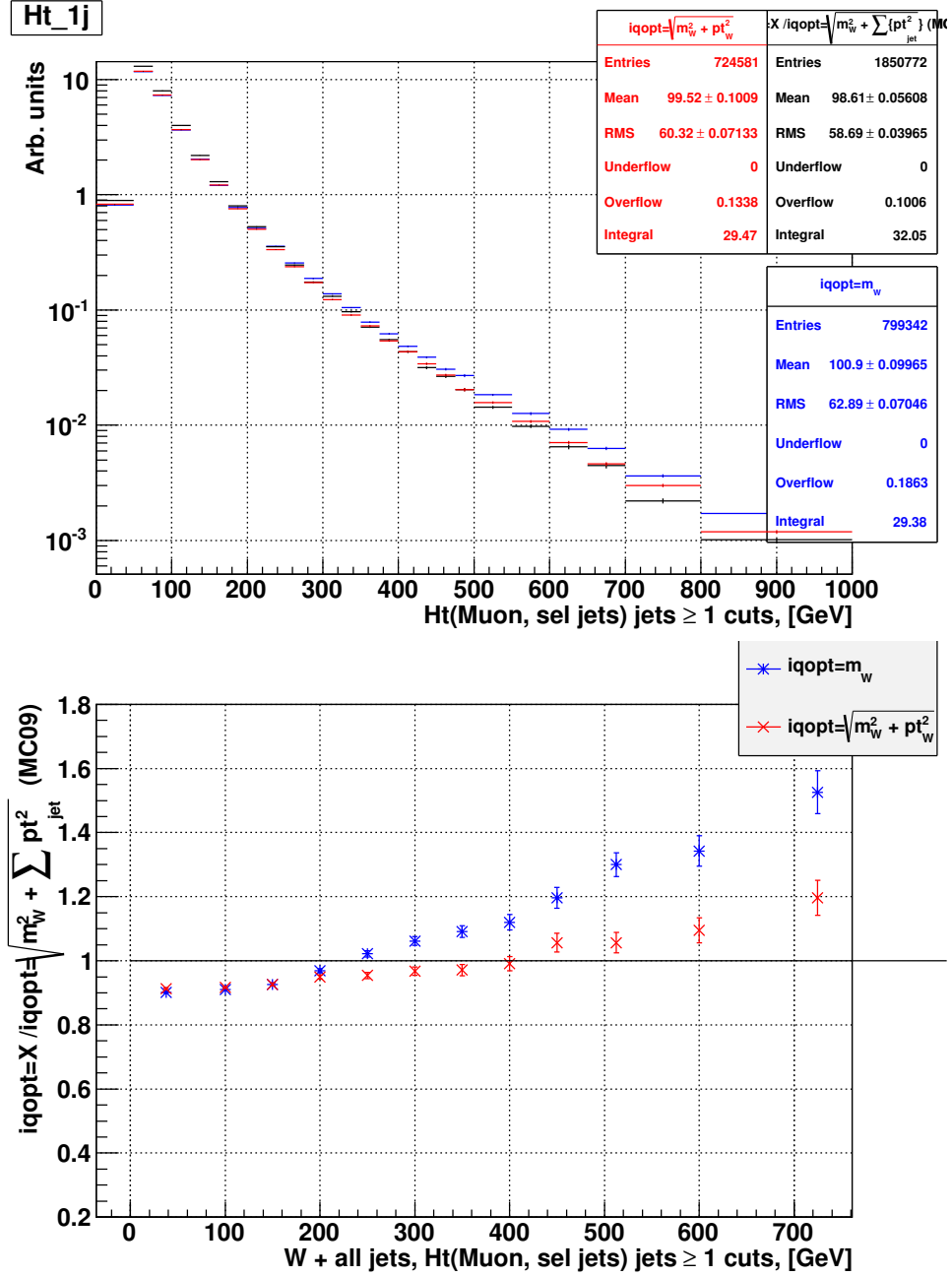


Figure 6.12: Effect of different iqopt models on H_T (muon, selected jets) for final W+jets states with at least one high- p_T jet. The top plot shows the distribution of H_T (muon, selected jets) while the bottom plot is normalized to the nominal distribution. At low H_T , where the scales are dominated by the m_W terms, the three distributions are approximately equal but as H_T increases, the scales start to diverge.

6.2.1.5 PYTHIA tunes

In addition to HERWIG, ALPGEN can also be interfaced with PYTHIA. PYTHIA has many more tunable parameters than HERWIG and JIMMY, which only have about three or four each. Since this modeling takes place in regions of low p_T and small angles, it is not particularly well described by theory and has to be tuned to match data. Tunes of this sort are typically valid at a particular center of mass energy. An effort was made to combine underlying event data across several experiments at different center of mass energies and extrapolate to LHC energies. The results are the “Perugia” tunes [126]. In addition to the central value, hard and soft systematic variations are also provided.

It is clear from Fig. 6.13 that there are intrinsic differences between PYTHIA and HERWIG/JIMMY as there is a common trend for all PYTHIA tunes to decrease in cross section around four jets with respect to HERWIG. The Perugia tunes can be compared against themselves to isolate the effects of the tunes and remove the parton shower generator dependency. There are strong effects on jet multiplicity as shown in Fig. 6.14. At low jet multiplicities, the soft tune has the highest cross section until $n_{jets} = 6$, when all three tunes converge before deviating again. This trend can be understood by examining the process for W+jets generation. For up five partons, there is exclusive matching between the parton and the parton shower jet so events with extra jets, which the hard tune is more likely to produce, are discarded. At five partons and above, the matching becomes inclusive and since ALPGEN can only generate up to five partons, everything from six jets and above comes exclusively from parton shower. Since the exclusive requirement no longer applies, the hard tune over takes the other tunes in this region.

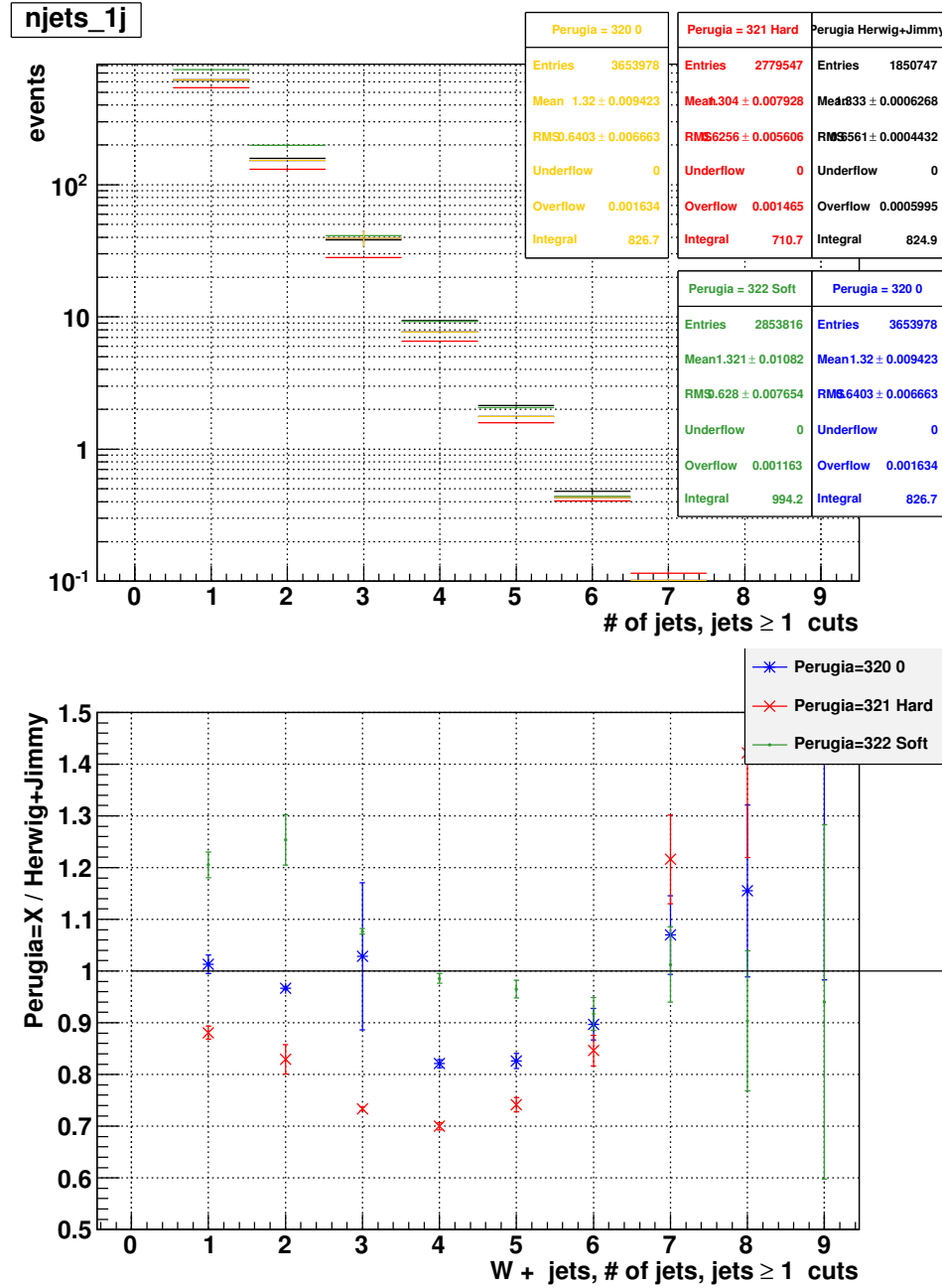


Figure 6.13: Effect of different HERWIG/JIMMY and several PYTHIA underlying event tunes on jet multiplicity for final W+jets states with at least one high- p_T jet. The jet multiplicity distributions are shown in the top plot and the distributions normalized to the HERWIG/JIMMY distribution is shown in the bottom plot. The three Perugia tunes show an overall different jet multiplicity with respect to the HERWIG/JIMMY distribution.

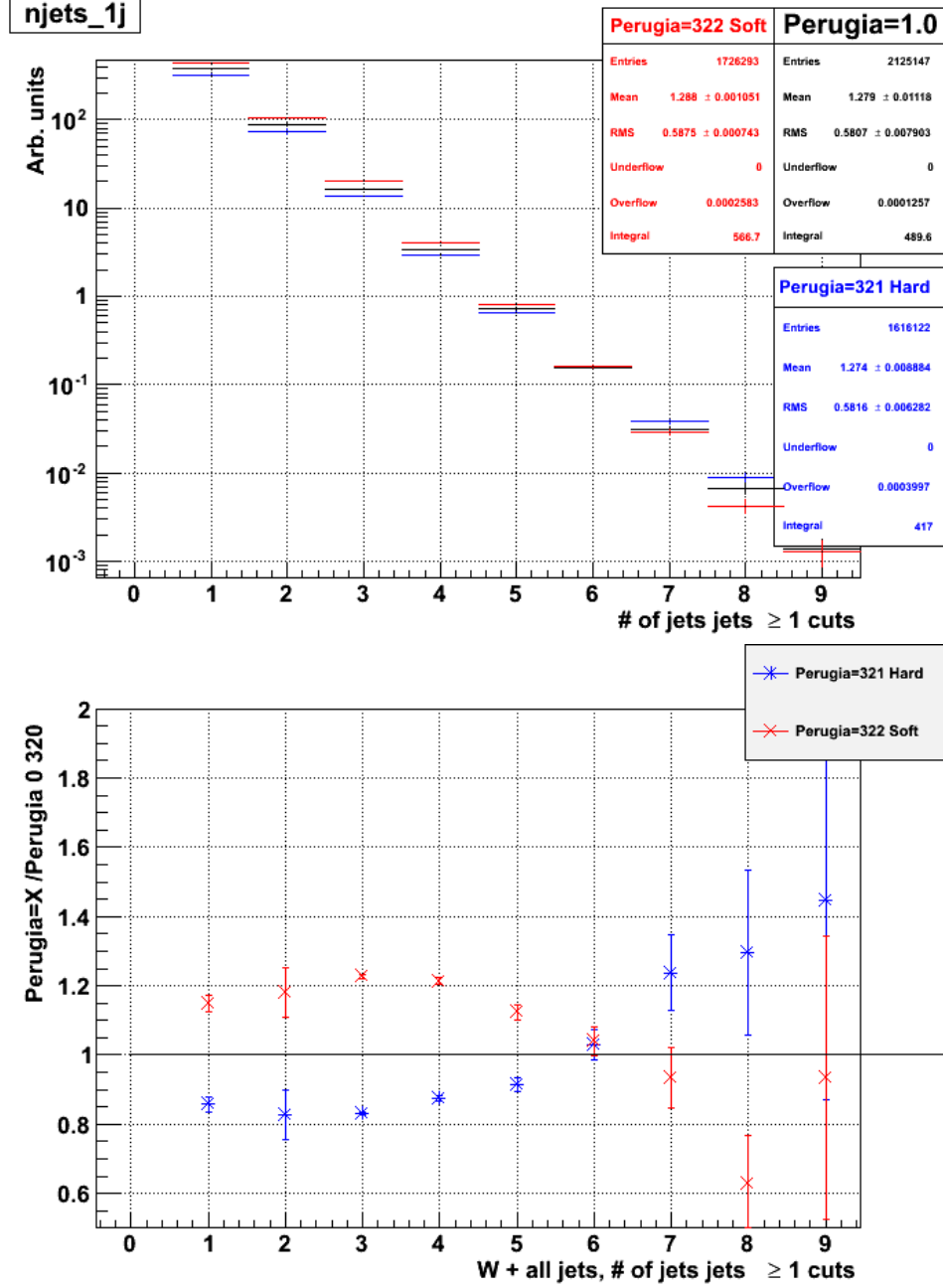


Figure 6.14: The same plots as are shown in Fig. 6.13 but omitting the HERWIG/JIMMY distribution and the bottom plot is normalized to the nominal Perugia distribution instead. The “cross over” around six jets is due to the matrix element-parton shower matching and is explained in more detail in Sec. 6.2.1.5.

6.2.1.6 Overall effects

To study how these parameters affect an actual physics analysis, they were studied in the context of the 1-D lepton η fit described in Ref. [15]. The analysis exploited the fact that leptons from $t\bar{t}$ decays tend to be more central in the detector than those originating from W +jets processes. The amount of $t\bar{t}$ and W +jets were allowed to float in a likelihood fit to the lepton $|\eta|$ distribution, with a fixed shape derived from Monte Carlo simulations, while all other backgrounds remained fixed. Since the samples with varied parameters are at truth level, the shape for the baseline W +jets sample was taken from MC truth as well with all other backgrounds and signal coming from full simulation MC. This is necessary to prevent detector effects from biasing the results and to isolate the effects of the MC variation. In addition to lepton η , H_T and sphericity were also studied as possible discriminating variables. It is clear from Fig. 6.15 that H_T performs the poorest while lepton η and sphericity are largely insensitive to the choice of MC parameters. This finding led to the choice of lepton η as the baseline variable for the early $t\bar{t}$ measurements at ATLAS [15, 127].

6.2.1.7 Conclusions

We've investigated the effects of varying the ALPGEN parameters within ranges appropriate for evaluating the systematic uncertainties associated with each parameter. For the `ptjmin` parameter, we can conclude that its value does not matter as long as it is well below the jet p_T cut. Since `ptjmin` is essentially a generator level parton p_T cut, it makes no physical sense to generate events constrained to a

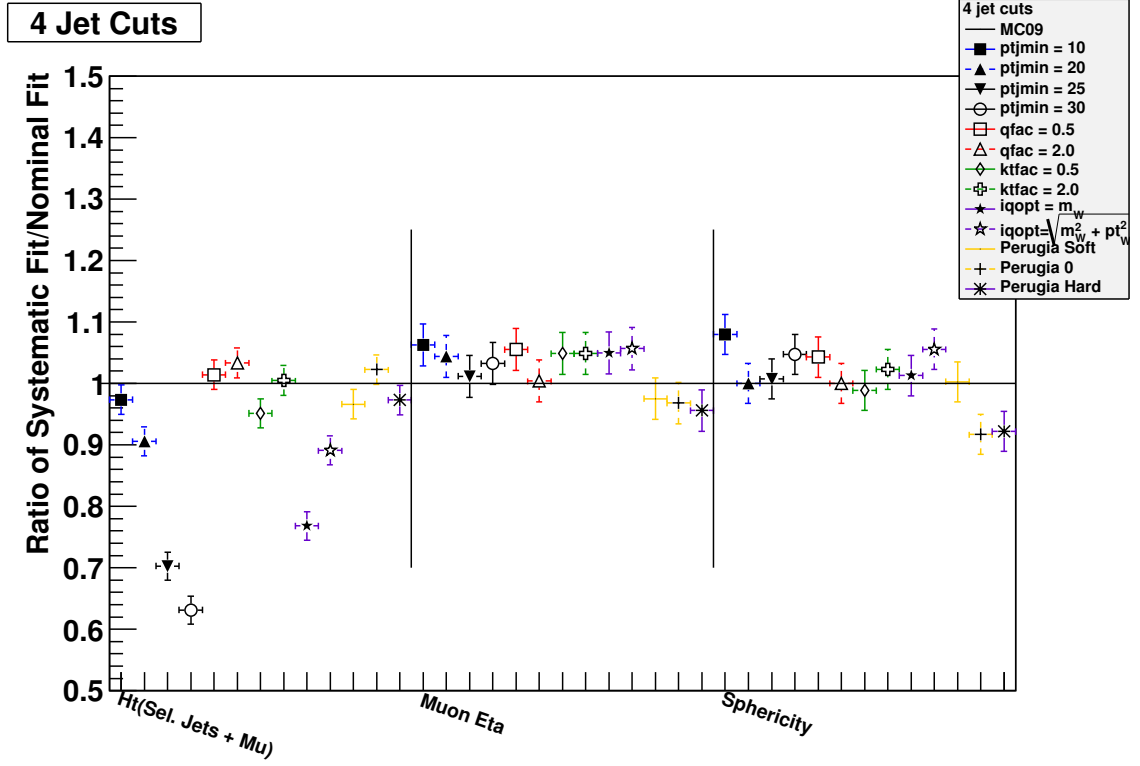


Figure 6.15: The effect of varying the ALPGEN parameters on the complete analysis described in Ref. [15]. Each point is the result when using samples produced with that particular variation normalized to the baseline result. The large variations in the results for H_T originate from the effects noted in earlier sections. The deviations from one can be interpreted as the systematic uncertainty due to the parameter variation.

different phase-space area than the one being studied. The **ktfac** parameter does not alter the kinematics of W +jet events much but has a significant effect on the jet multiplicity. Variations by factors of two seem to be too large judging from Fig. 6.4, where the Data/MC agreement has deviations smaller than 10%, whereas varying **ktfac** by factors of two typically causes variations between 10% and as much as 70% as shown in Fig. 6.9. Like **ktfac**, **qfac** affects the jet multiplicity of W +jet events. The variations shown in Fig. 6.11 are not as severe as the **ktfac** variations and are on the order of 10% effects, which is in agreement with the data within the uncertainties. The choice of scale (μ) functional form, **iqopt**, does not have a

significant effect at low H_T but deviations can be seen in the tail of the distribution (Fig. 6.12). This will be important for $t\bar{t}$ analyses using the H_T distribution as a variable. The results for the PYTHIA underlying event Perugia tunes are shown for completeness. Now that data has been delivered by the LHC, the underlying event parameters for HERWIG/JIMMY and PYTHIA have been tuned to reproduce various distributions in the data, resulting in the AMBT2 and AUET2 tunes [112,113].

In the context of an analysis, angular variables are much less sensitive to the parameter variations than p_T based ones such as H_T (Fig. 6.15). The $t\bar{t}$ dilepton $e\mu$ channel does utilize a cut on H_T but since this is a dilepton channel, contributions from W +jets events only enters through fake leptons, which are accounted for using the “Matrix Method” techniques described in Sec. 5.2.1. For the measurement of R and $\sigma_{t\bar{t}}$ presented in Chapter 7, only the W +jets normalization and fraction of W +heavy flavor quarks are important. Both of these quantities are derived from data-driven techniques, which reduces the dependence on Monte Carlo modeling. For more sophisticated analyses that rely on modeling of kinematic distributions, such as the one presented in Appendix D, ATLAS has developed a truth level reweighing scheme based on the leading truth jet p_T spectrum that reproduces the distribution for the various ALPGEN parameter variations. To evaluate systematic effects due to W +jets modeling, fully reconstructed events are re-weighted according to this scheme using the `iqopt = 2` ($Q = m_W$) and `ptjmin=10` GeV variations and compared against the nominal result.

6.2.2 Vector Boson + Heavy Flavor Production

The ALPGEN matching scheme does not take flavor into account when matching partons with showers. Since it is possible to produce the same flavor configurations in both the matrix element and parton shower, events can be double counted [128]. ALPGEN does not provide a solution for this problem internally, but schemes have been developed to address it. For soft colinear processes, parton shower typically perform better than matrix element. To avoid double counting of events, restrictions are applied on phase space. Events where the ΔR distance between two heavy quarks is greater than 0.4 are classified as Wbb or Wcc events otherwise the event is classified as a light jet event.

6.3 Other Processes

Although W +jets is the dominant source of background events to a lepton+jets final state $t\bar{t}$ events, it is not the only one. Single top production has a comparable cross section to $t\bar{t}$ with many of the same event characteristics, but lower jet multiplicities. There are three channels of single top production at the LHC, the t-channel, s-channel and associated W (Wt) channel. Like the baseline $t\bar{t}$ samples, single top processes are generated using the MC@NLO generator and showered with HERWIG and JIMMY.

An even smaller contribution comes from production of dibosons. HERWIG is used as matrix element and parton shower generator for WW , WZ and ZZ modeling. The MC samples are filtered so that they contain at least one lepton. The generator cross

section is multiplied by a corrective factor to account for selection cuts made at the MC generator level.

6.4 Detector Simulation

The interactions and processes generated by the matrix element and parton shower happen at extremely short scales in both time and space, well before any material is encountered. Once particles start passing through and interacting with physical material, additional interactions take place. The interaction of particles with the matter in the detector is simulated using the **GEANT4** program [129]. The **GEANT4** simulation consists of a model of ATLAS in a particular geometric configuration complete with material composition of the individual components [130]. Correct modeling of material is crucial for estimating the amount of energy lost by particles as they pass through active as well as passive areas of the detector. These models also include services and substructure such as read-out cables and detector supports. **GEANT4** provides several lists of physics processes that can be used and ATLAS utilizes the QGSP_BERT (quark gluon string model - Bertini model) physics list for the detector simulation [131, 132].

The ATLAS software framework (**ATHENA**) handles simulation of active detector areas. When particles pass through an active area, these are recorded as “hits” which contain position, time and energy deposition in each sub-detector [130]. The hits go through a process of digitization which converts the hit information into detector response data in terms of a signal shape or voltage. Detector noise taken from dedicated pedestal runs is introduced in this step as well as backgrounds such as cavern activity (typically spallation neutrons from particle interactions with shielding)

and out-of-time pileup interactions. The digitization step also requires specification of the detector conditions that describes which read-out channels are operating, as these change over time as hardware failures accumulate or are repaired over LHC shut down periods. The output of the digitization step goes through emulations of the algorithms run on the detector electronics before passing through an emulation of the Read Out Driver (ROD) electronics. The final step is full event reconstruction using the same software and reconstruction algorithms that are used for data processing.

CHAPTER 7

EXTRACTION OF R

A major underlying assumption in many top quark analyses is that the top quark decays to a W -boson and a b -quark 100% of the time. In the Standard Model, this is a valid assumption considering that the value of $|V_{tb}|$ from a global fit of the CKM matrix element is $0.999146^{+0.000021}_{-0.000046}$ but one that should be checked none the less as a test of the Standard Model [39]. This assumption is also present in the $t\bar{t}$ based calibration methods so it should be checked for accuracy of the results. The CKM unitarity constraint assumes three generations so deviations of V_{tb} from the Standard Model value can be indicative of new physics such as a fourth generation of quarks.

In this Chapter, the measurement of R and the $t\bar{t}$ cross section are presented. A brief review of the current measurements is provided. Next, the method to extract R and $\sigma_{t\bar{t}}$ from the data is described in detail and is followed by a section discussing the systematic uncertainties. The chapter concludes by presenting the main results of this thesis.

7.1 Introduction

The V_{tb} matrix element is not directly observable in $t\bar{t}$ decays but can be inferred from the top quark branching fraction to Wb :

$$R = \frac{\text{BR}(t \rightarrow Wb)}{\text{BR}(t \rightarrow Wq)} = \frac{|V_{tb}|^2}{|V_{tb}|^2 + |V_{ts}|^2 + |V_{td}|^2} \quad (7.1)$$

This has been measured at both the Tevatron and the LHC. The CDF collaboration measured a value greater than one but sets lower limits on $R > 0.62$ at the 95% confidence level (C.L.) [16]. On the other side of the Tevatron ring, the D0 collaboration has measured $R = 0.90 \pm 0.04$, which corresponds to $|V_{tb}| = 0.95 \pm 0.02$ [17]. This is over two standard deviations away from the Standard Model value. At the LHC, the CMS collaboration has measured $R = 0.98 \pm 0.04$ in the dilepton $t\bar{t}$ channel which agrees quite well with the Standard Model prediction [18].

In single top production, the cross sections are proportional to the value of $|V_{tb}|^2$, assuming that the branching ratio $t \rightarrow Wb$ is equal to one. By measuring the single top cross section, the value of $|V_{tb}|$ can be extracted. Both the CDF and D0 experiments have performed this measurement at the Tevatron. The D0 collaboration has constrained $|V_{tb}| > 0.81$ at the 95% C.L. using the t-channel production mode [133]. The CDF collaboration combines the t-channel with the s-channel and reports a measurement of $|V_{tb}| = 0.96 \pm 0.09(\text{stat.} + \text{syst.}) \pm 0.05(\text{theory})$ and sets lower bounds at the 95% C.L. of $|V_{tb}| > 0.78$ [134]. During the 2011 $\sqrt{s} = 7$ TeV LHC run, both CMS and ATLAS were able to measure t-channel single top production. From these measurements, ATLAS was able to measure $|V_{tb}| = 1.13^{+0.14}_{-0.13}(\text{stat.} + \text{syst.}) \pm 0.02(\text{theory})$ and set lower bounds at the 95% C.L. of $|V_{tb}| > 0.75$ [135]. Similarly, the

CMS collaboration measured $|V_{tb}| = 1.02 \pm 0.05(\text{stat.} + \text{syst.}) \pm 0.02(\text{theory})$ during the 2011 run and set stricter lower bounds of $|V_{tb}| > 0.92$ at the 95% C.L. [136]. For the 2012 LHC run, the center-of-mass energy was raised to 8 TeV which also increases the single top production cross sections. Single top results at $\sqrt{s}=8$ TeV have already been released by the ATLAS and CMS collaborations regarding $|V_{tb}|$. The ATLAS collaboration measured $|V_{tb}| = 1.04^{+0.10}_{-0.11}$ and sets a lower bound of $|V_{tb}| > 0.80$ at the 95% C.L. with the $\sqrt{s} = 8$ TeV data [137]. Across the ring, the CMS collaboration reports a result of $|V_{tb}| = 0.96 \pm 0.08(\text{stat.} + \text{syst.}) \pm 0.02(\text{theory})$ and sets a slightly stricter lower limit of $|V_{tb}| > 0.81$ at the 95% C.L. [138]. All of the measurements of $|V_{tb}|$ from single top cross section measurements at the Tevatron and the LHC are consistent with the Standard Model predictions within the uncertainties.

7.2 Method

The method applied here is very similar to the tag counting b -tagging calibration method described in Appendix A.2 except that the branching fraction is now the parameter of interest and the b -tagging efficiencies are fixed to the values measured in data with the p_T^{rel} and *System8* calibration methods that are described in Appendix A. If the top quark decays to a W -boson and a light flavor quark a substantial fraction of the time, there will be fewer real b -jets in the final state and the n -tag distributions will shift to lower tagged jet multiplicities as shown in figures 7.1 through 7.5. The number of $t\bar{t} \rightarrow WbWb$ are events proportion to R through the relationship $R^2 * N_{t\bar{t}}$ while the number of $t\bar{t} \rightarrow WbWq$ and $t\bar{t} \rightarrow WqWq$ events are proportional to R through $2 * R(1 - R) * N_{t\bar{t}}$ and $(1 - R)^2 * N_{t\bar{t}}$ respectively. The

branching ratio of $t \rightarrow Wb$ is extracted from the data by performing a likelihood fit to the n -tag templates.

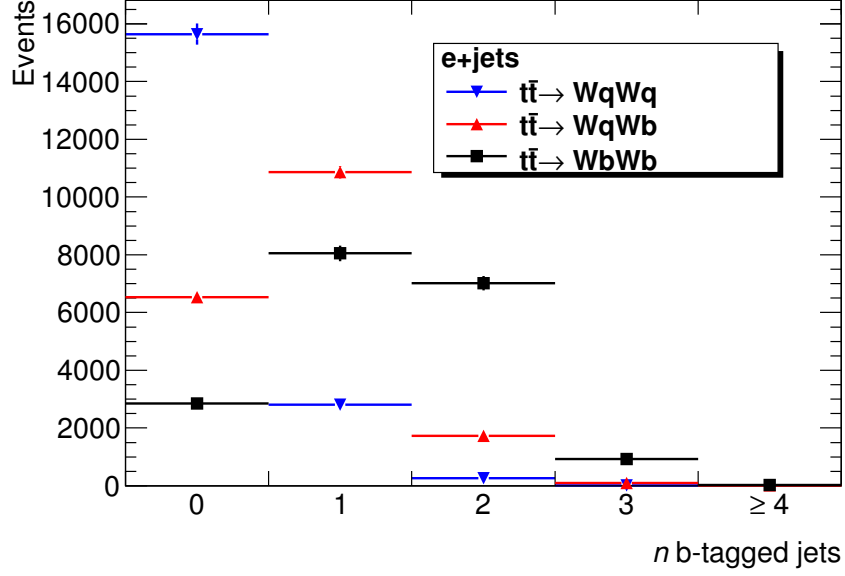


Figure 7.1: The n -tag distribution template for the electron + jets channel. The 0-tag bin is shown for illustrative purposes only.

The baseline $t\bar{t}$ samples were produced with `MC@NLO`, but due to technical difficulties, it was not possible to produce `MC@NLO` samples with modified $|V_{tb}|$ values. The `PROTOS` generator was used instead to produce the $WqWb$ and $WqWq$ final state templates. To eliminate generator effects, the modified $|V_{tb}|$ templates are re-scaled by an acceptance correction factor calculated from the ratio of the number of events in the $WbWb$ samples produced with `MC@NLO` to the number of events in the $WbWb$ sample produced using `PROTOS` for each channel separately. There exist schemes to reweigh $WbWb$ Monte Carlo samples to imitate $WbWq$ and $WqWq$ samples by relabeling jets, but these schemes often neglect kinematic differences between massless light partons and heavy b -quarks which have a mass around 5 GeV.

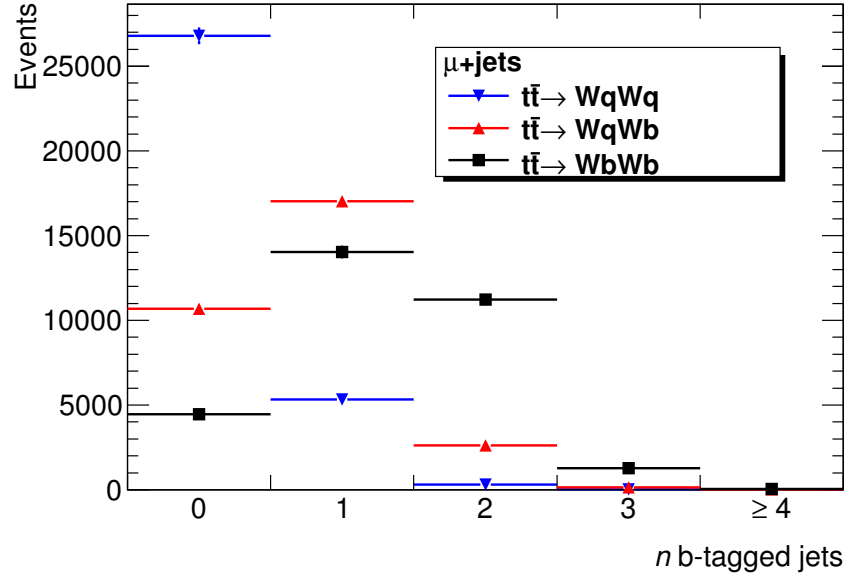


Figure 7.2: The n -tag distribution template for the muon + jets channel. The 0-tag bin is shown for illustrative purposes only.

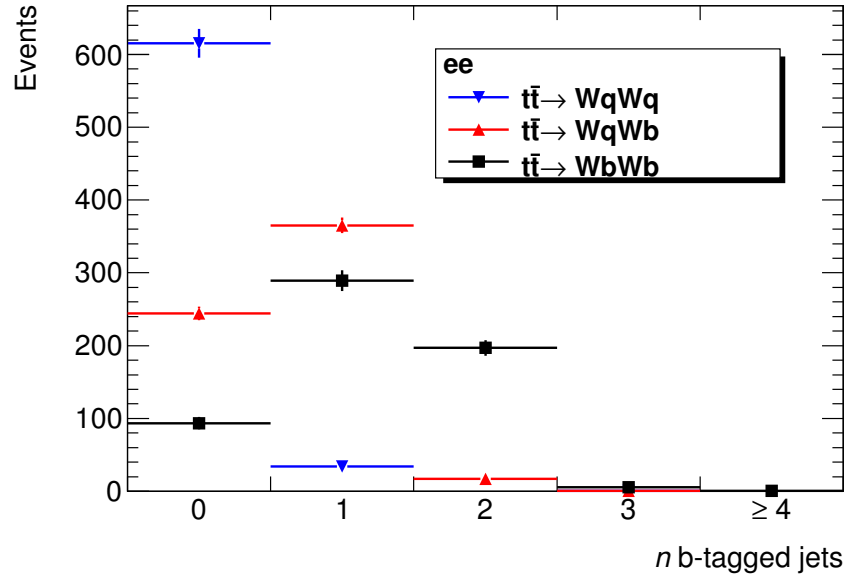


Figure 7.3: The n -tag distribution template for the electron-electron channel.

The MV1 tagger was used at a 70% efficiency working point for the baseline analysis. A 60% working point was also examined but the overall uncertainties in

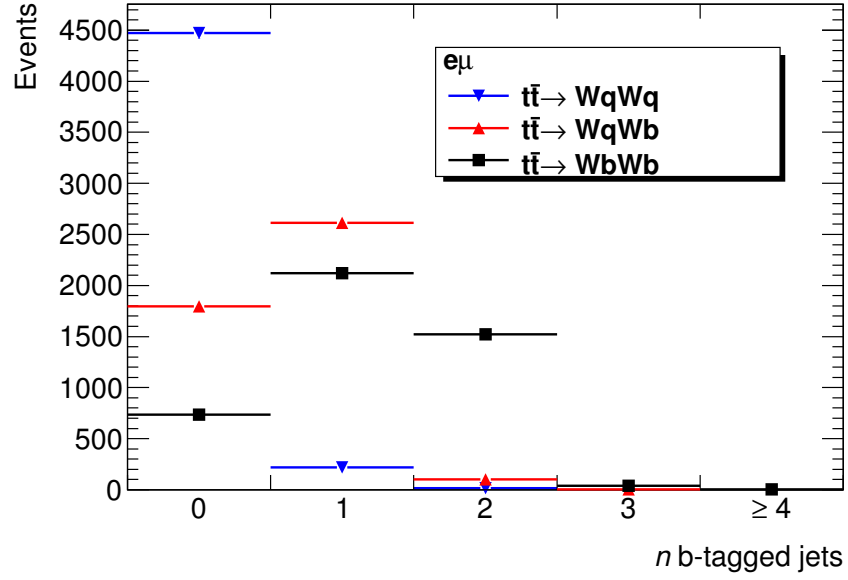


Figure 7.4: The n -tag distribution template for the electron-muon channel.

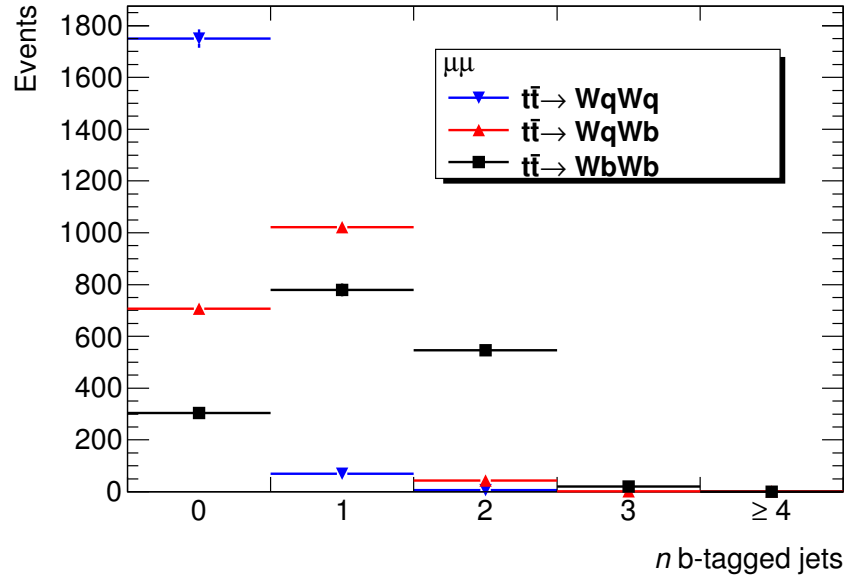


Figure 7.5: The n -tag distribution template for the muon-muon channel.

the measurement of R were about 1% higher. The uncertainties at both b -tagging working points are shown in Table 7.1. Since top quarks are assumed to decay into Wb 100% of the time in the $t\bar{t}$ based b -tagging calibration methods, only calibrations

and uncertainties from the p_T^{rel} and *System8* results are applied to avoid biasing the result. For the lepton+jets channel, the 0-tag bins are omitted from the fit due to the poor signal-to-background ratio and large systematic uncertainties.

The likelihood fit is performed using MINUIT while letting R and $\sigma_{t\bar{t}}$ float. The analysis was also studied with fixing the $\sigma_{t\bar{t}}$ value to its nominal MC value and only allowing R to float in the fit. The overall uncertainties are higher when fixing $\sigma_{t\bar{t}}$ largely due to the contribution of the $\sigma_{t\bar{t}}$ systematic uncertainty, shown in Tab. 7.2, that is not present when simultaneously measuring $\sigma_{t\bar{t}}$.

The number of expected events with n tagged jets is given by:

$$\langle N_n \rangle = N_{\text{background},n} + R^2 * N_{t\bar{t} \rightarrow WbWb,n} + 2R(1-R) * N_{t\bar{t} \rightarrow WqWb,n} + (1-R)^2 * N_{t\bar{t} \rightarrow WqWq,n} \quad (7.2)$$

where $N_{\text{background},n}$ is the number of background events with n b -tagged jets including contributions from the QCD multijet background. The $N_{t\bar{t} \rightarrow WxWx,n}$ terms are the number of $t\bar{t}$ events decaying to a $WxWx$ final state with n b -tagged jets. The number of expected events follows Poisson statistics. The likelihood function (L) being maximized is given by :

$$L = \prod_{\text{channel}} \left(\prod_{n\text{-tag bin}} \text{Poisson}(N_{\text{channel},n} | \langle N_{\text{channel},n} \rangle) \right), \quad (7.3)$$

where channel refers to the decay channel ($e,\mu,ee,e\mu$, and $\mu\mu$), n is the number of b -tagged jets in the event, N is the number of events in that decay channel with n b -tagged jets and $\langle N_{\text{channel},n} \rangle$ is the number of expected events as described by Eq. 7.2 evaluated per channel. The linearity of the fit has been confirmed by performing ensemble tests with pseudo-experiments with varied parameters. The

results of the linearity test for R are shown in Figs 7.6 and 7.7 for the $t\bar{t}$ cross section measurement. Deviations from linearity are negligible.

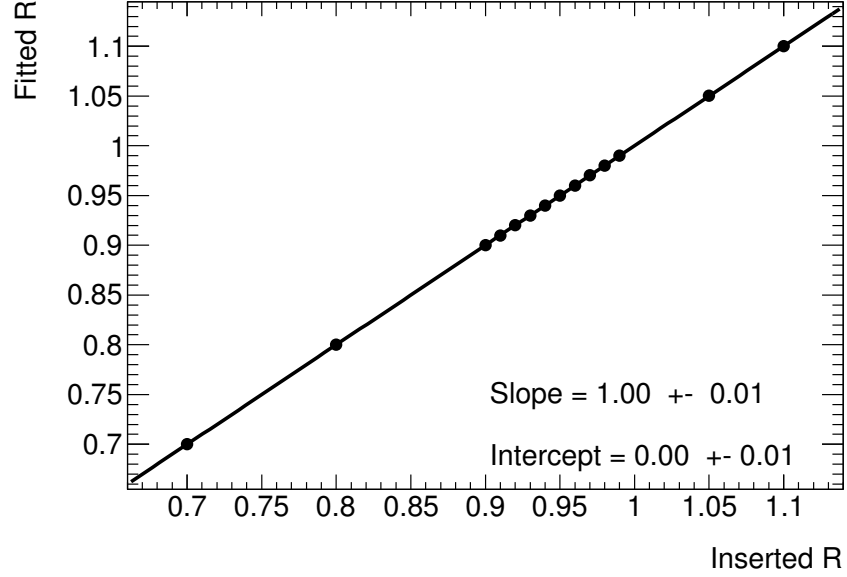


Figure 7.6: Linearity test of the fit response to varying R values. The fit to a linear function returns a slope consistent with one and zero y -intercept.

7.3 Systematic Uncertainties

The measurement of R is sensitive to most of the uncertainties present in the b -tagging calibration method with the notable addition of b -tagging efficiency uncertainties. Descriptions of the various uncertainties are present in previous chapters. For the b -tagging calibrations and uncertainties, only the combined $p_T^{\text{rel}}\text{-}System8$ values are used to avoid biasing the result. The full set of uncertainties is shown in Table 7.1.

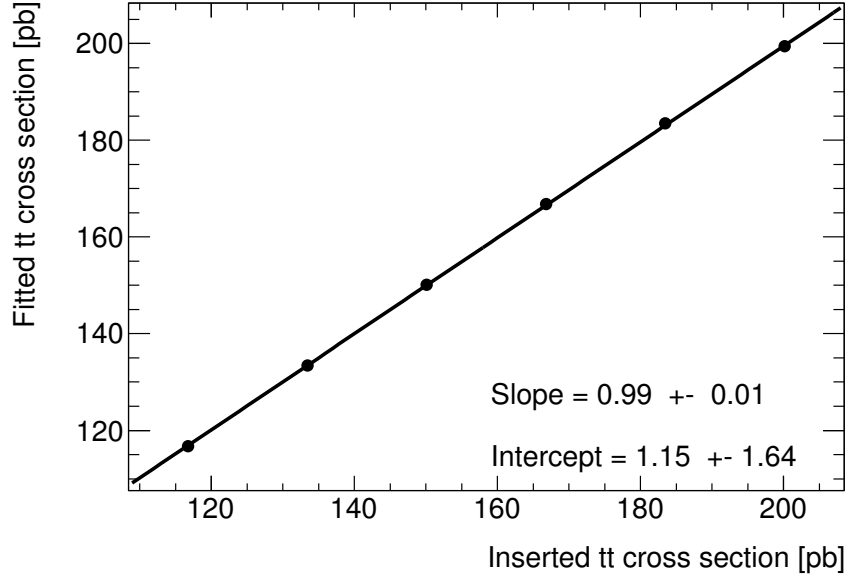


Figure 7.7: Linearity test of the fit response to re-scaling the $t\bar{t}$ cross section. The resulting fit to a line is consistent with a zero y -intercept and a slope equal to one.

7.4 Results

The fit was performed to a dataset consisting of 4.7 fb^{-1} of integrated luminosity. The value for R was measured to be 1.06 ± 0.11 , which is consistent with the Standard Model expectation but cannot strictly be interpreted as a branching ratio since the value is greater than one. As a cross check, the same fit is performed to the data while keeping the value of $\sigma_{t\bar{t}}$ fixed returns $R = 1.06 \pm 0.12$. A fit for just the cross section while keeping R fixed measured $\sigma_{t\bar{t}} = 172 \pm 28 \text{ pb}$.

The $t\bar{t}$ cross section was measured to be $167_{-26}^{+27} \text{ pb}$ at $\sqrt{s} = 7 \text{ TeV}$, which is consistent the Standard Model value of $166.8_{-17.8}^{+16.5} \text{ pb}$ and previous ATLAS measurements [42, 46, 58]. The results of the likelihood fit are shown in Fig. 7.8, with uncertainty bands that illustrate the statistical fit uncertainty. The fit results have

	R MV1 60%	R MV1 70%	$\sigma_{t\bar{t}}$ MV1 60%	$\sigma_{t\bar{t}}$ MV1 70%
ISR/FSR	± 7.6	± 6.5	± 6.8	± 7.3
Generator	± 0.8	± 0.5	± 1.4	± 1.6
Fragmentation	± 1.0	± 0.1	± 1.4	± 1.8
Diboson	± 0.0	± 0.0	± 0.0	± 0.0
single top	$+0.1$ -0.1	$+0.1$ -0.1	$+0.2$ -0.3	$+0.2$ -0.3
Z + jets	± 1.0	± 1.0	± 1.5	± 1.6
W + jets	± 0.3	± 0.6	± 1.0	± 1.4
Multijets	± 1.0	± 1.1	± 2.5	± 2.7
JES	$+1.2$ -1.3	$+1.9$ -2.0	$+11.2$ -10.4	$+12.7$ -11.6
JER	± 0.8	± 0.9	± 1.3	± 1.6
JRE	± 0.0	± 0.0	± 0.1	± 0.1
JVF	± 0.0	± 0.1	± 1.6	± 1.7
W+HF SF	$+0.2$ -0.1	$+0.2$ -0.2	$+0.5$ -0.5	$+0.5$ -0.5
ε_b	± 9.2	± 8.3	± 0.5	± 0.4
ε_c	± 0.9	± 0.7	± 0.9	± 1.1
ε_{light}	± 0.4	± 0.5	± 0.7	± 0.1
E_T^{miss} cellout	$+0.0$ -0.0	$+0.0$ -0.0	$+0.1$ -0.0	$+0.1$ -0.0
E_T^{miss} pileup	$+0.0$ -0.0	$+0.0$ -0.1	$+0.1$ -0.0	$+0.1$ -0.0
e trigger	± 0.1	± 0.0	± 0.3	± 0.3
e smearing	± 0.0	± 0.0	± 0.0	± 0.0
e recID	± 0.1	± 0.1	± 0.5	± 0.5
MC e -energy scale	$+0.0$ -0.0	$+0.0$ -0.0	$+0.2$ -0.2	$+0.2$ -0.2
μ trigger	$+0.0$ -0.0	$+0.0$ -0.0	$+0.0$ -0.0	$+0.0$ -0.0
μ smearing	$+0.1$ -0.1	$+0.0$ -0.1	$+0.6$ -0.7	$+0.7$ -0.6
μ recID	± 0.1	± 0.0	± 0.3	± 0.2
MC μ energy scale	± 0.0	± 0.0	± 0.0	± 0.0
Luminosity	± 0.3	± 0.4	± 5.0	± 5.2
Statistical	± 0.5	± 0.4	± 0.6	± 0.6
Total Systematic	$+12.2$ -12.2	$+10.9$ -10.9	$+14.7$ -14.2	$+16.4$ -15.5
Total	$+12.2$ -12.2	$+10.9$ -10.9	$+14.7$ -14.2	$+16.4$ -15.5

Table 7.1: Table of relative uncertainties in % for the simultaneous measurement of R and $\sigma_{t\bar{t}}$

been reapplied to the $t\bar{t}$ Monte Carlo simulation parameters, R and $\sigma_{t\bar{t}}$. The results of this rescaling are shown in Fig. 7.9 though 7.13.

From inspection of Fig. 7.9 though 7.13, the ee decay channel shows the poorest level of data/MC agreement. It is possible that there is an overestimate of the

	R MV1 60%	R MV1 70%	$\sigma_{t\bar{t}}$ MV1 60%	$\sigma_{t\bar{t}}$ MV1 70%
ISR/FSR	± 8.0	± 6.4	± 9.4	± 8.8
Generator	± 1.4	± 1.0	± 1.3	± 1.4
Fragmentation	± 1.6	± 0.6	± 1.5	± 1.4
Diboson	± 0.0	± 0.0	± 0.5	± 0.5
single top	$+0.1$ -0.0	$+0.0$ -0.0	$+0.0$ -1.3	$+0.0$ -1.2
Z + jets	± 0.4	± 0.5	± 0.9	± 1.0
W + jets	± 0.1	± 0.1	± 0.8	± 1.1
Multijets	± 0.0	± 0.3	± 1.9	± 2.0
$\sigma_{t\bar{t}}$	$+7.7$ -0.0	$+2.9$ -4.0	-	-
JES	$+3.2$ -4.1	$+1.6$ -2.4	$+9.8$ -10.3	$+11.0$ -11.1
JER	± 0.2	± 0.4	± 0.3	± 0.7
JRE	± 0.0	± 0.0	± 0.6	± 0.6
JVF	± 0.7	± 0.4	± 1.6	± 1.6
W+HF SF	$+0.1$ -0.1	$+0.0$ -0.0	$+0.0$ -1.7	$+0.0$ -1.6
ε_b	± 9.4	± 8.5	± 5.8	± 4.9
ε_c	± 1.3	± 1.0	± 1.4	± 1.4
ε_{light}	± 0.1	± 0.5	± 0.6	± 0.5
E_T^{miss} cellout	$+0.1$ -0.0	$+0.0$ -0.0	$+0.0$ -0.7	$+0.0$ -0.7
E_T^{miss} pileup	$+0.0$ -0.0	$+0.0$ -0.0	$+0.0$ -0.6	$+0.0$ -0.6
e trigger	± 0.1	± 0.0	± 0.5	± 0.5
e smearing	± 0.0	± 0.0	± 0.5	± 0.5
e recID	± 0.2	± 0.1	± 0.5	± 0.5
MC e -energy scale	$+0.1$ -0.1	$+0.0$ -0.0	$+0.0$ -0.7	$+0.0$ -0.7
μ trigger	$+0.0$ -0.0	$+0.0$ -0.0	$+0.0$ -0.0	$+0.0$ -0.0
μ smearing	$+0.2$ -0.2	$+0.2$ -0.2	$+0.1$ -1.3	$+0.2$ -1.3
μ recID	± 0.0	± 0.0	± 0.4	± 0.4
MC μ energy scale	± 0.0	± 0.0	± 0.5	± 0.5
Luminosity	± 2.0	± 1.3	± 4.9	± 5.0
Statistical	± 0.5	± 0.4	± 0.5	± 0.5
Total Systematic	$+15.2$ -13.4	$+11.3$ -11.8	$+16.0$ -16.5	$+16.3$ -16.6
Total	$+15.2$ -13.4	$+11.3$ -11.8	$+16.0$ -16.6	$+16.3$ -16.6

Table 7.2: Table of relative uncertainties in % for the measurements of R and $\sigma_{t\bar{t}}$, with $\sigma_{t\bar{t}}$ being fixed at 166.8 pb in the fit for the measurement of R and R fixed at 0.999 for the measurement of $\sigma_{t\bar{t}}$.

QCD multijet electron fake rate. This hypothesis is further supported by the e +jets channel, which shows a small excess of predicted events in low E_T^{miss} regions and low $M_T(W)$ regions illustrated in Fig. D.1 and D.2. Additionally, the results of the

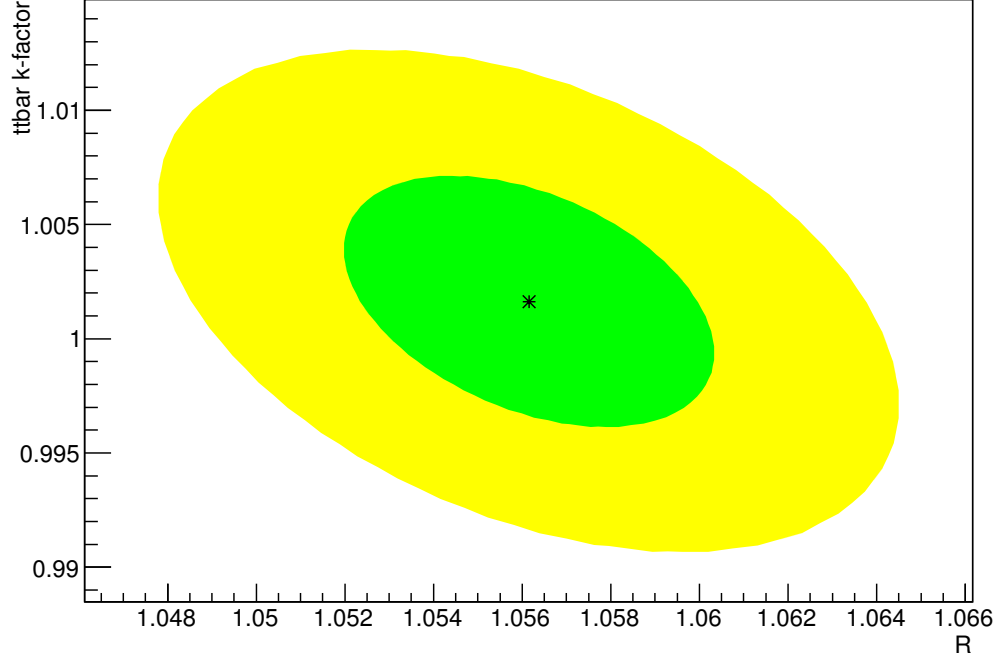


Figure 7.8: Contour from the likelihood fit. The $1\text{-}\sigma$ (green) and $2\text{-}\sigma$ (yellow) bands corresponding to the statistical error of the fit are shown.

individual channel fits for the e +jets and ee channels fit a lower $t\bar{t}$ cross section than the other channels which might be due to a over-estimation of the QCD multijet background. In the ee channel, the fake rate is effectively squared so any mis-estimation will be more dramatic than the e +jets channel. The effects on the final result are quite small since the ee channel has relatively low statistics so it has a small influence on the combined fit as shown in Fig. E.1.

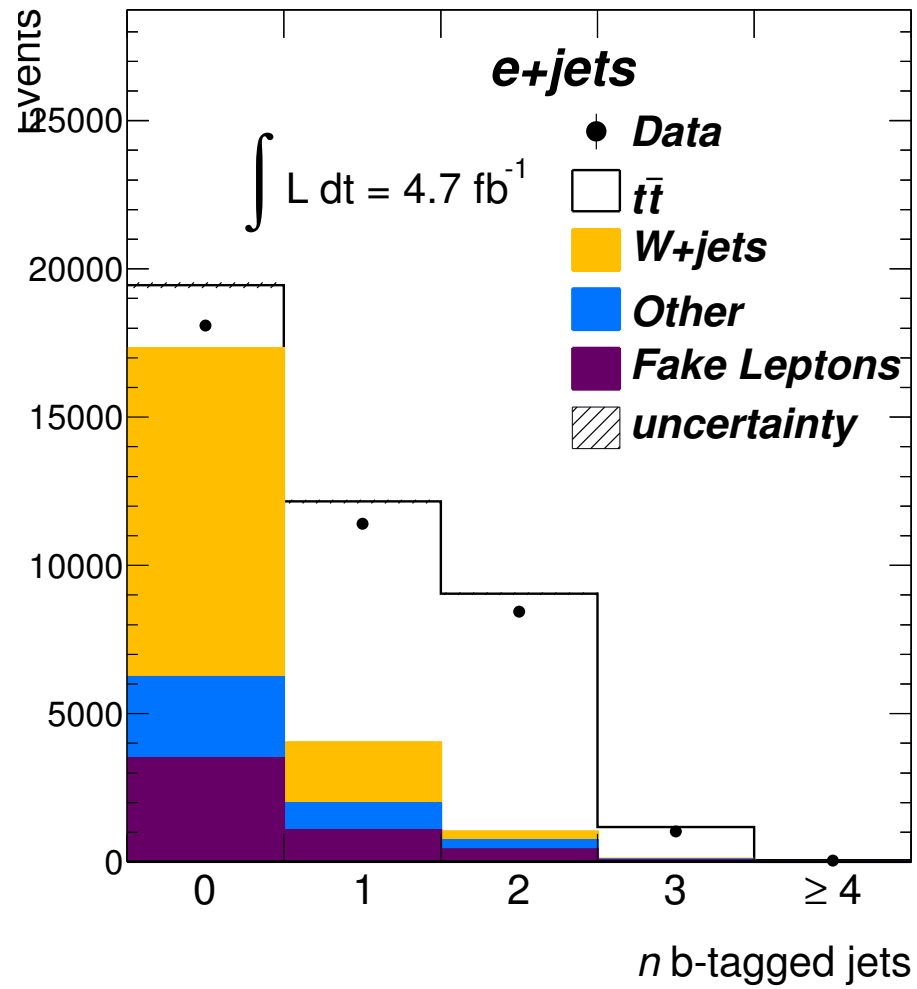


Figure 7.9: The n -tag distribution for the electron + jets channel after fitting showing the statistical uncertainty. The 0-tag bin is shown for illustrative purposes only.

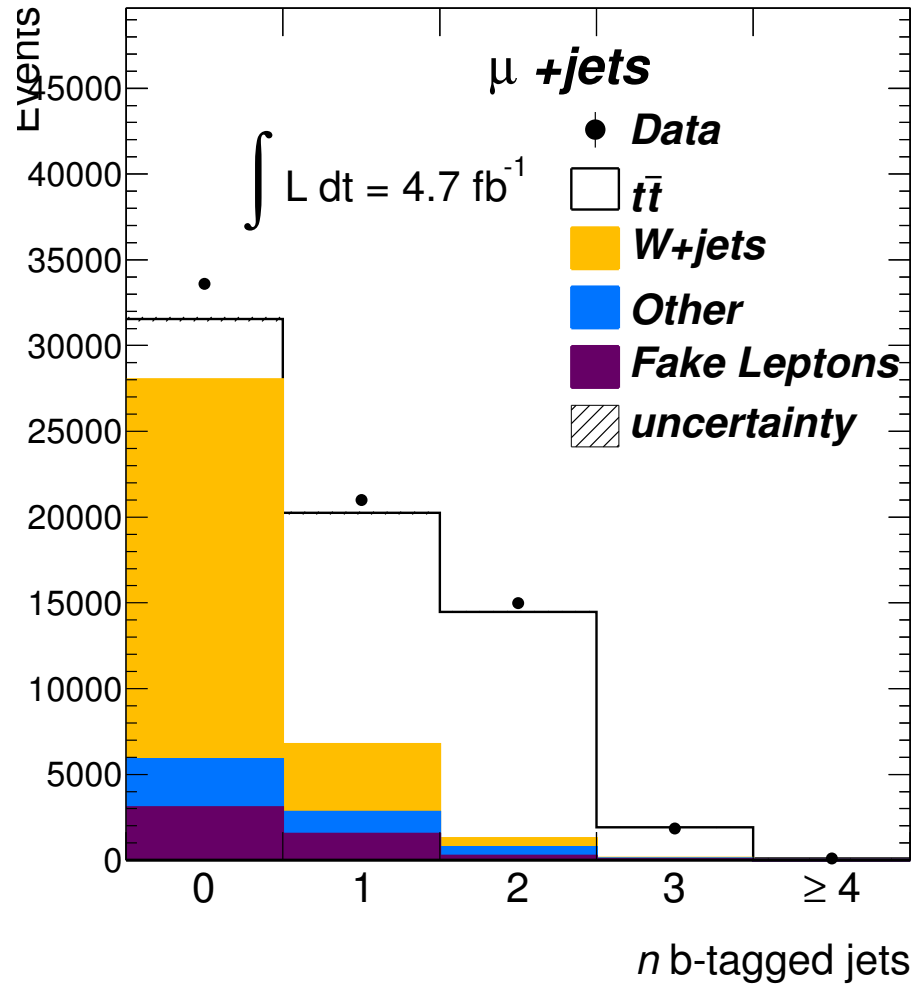


Figure 7.10: The n -tag distribution for the muon + jets channel after fitting showing the statistical uncertainty. The 0-tag bin is shown for illustrative purposes only.

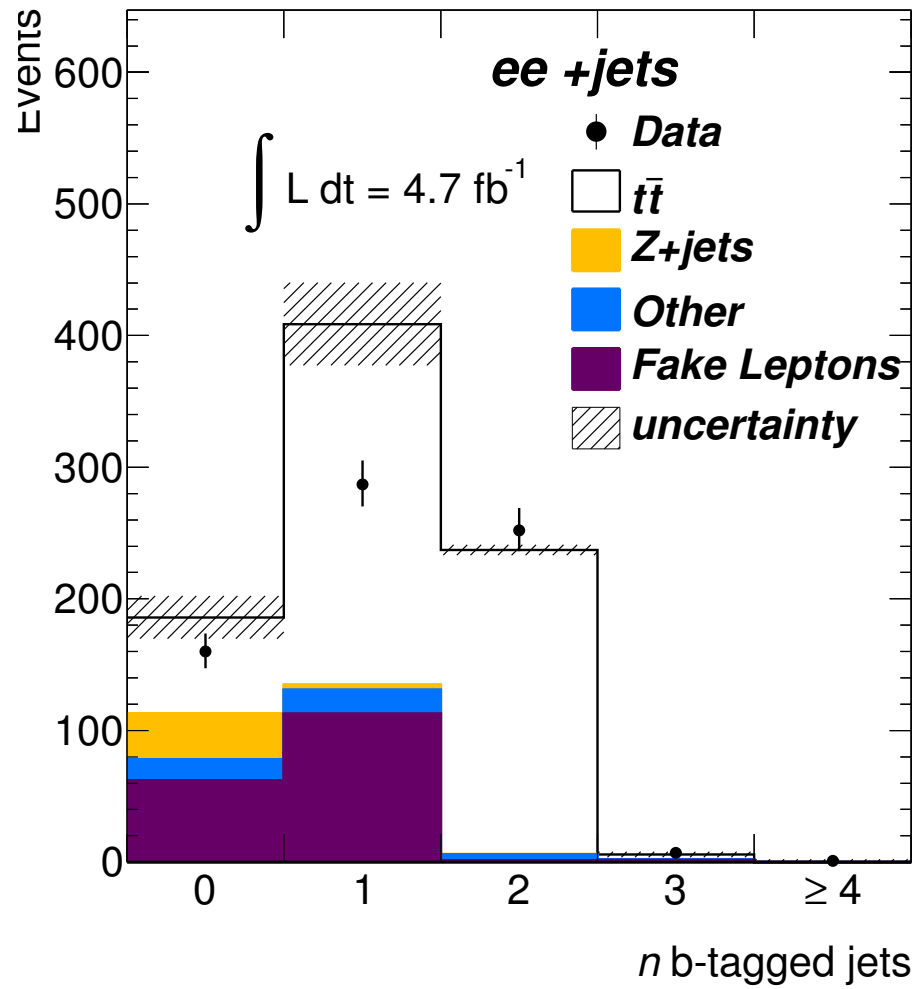


Figure 7.11: The n -tag distribution for the electron-electron channel after fitting showing the statistical uncertainty.

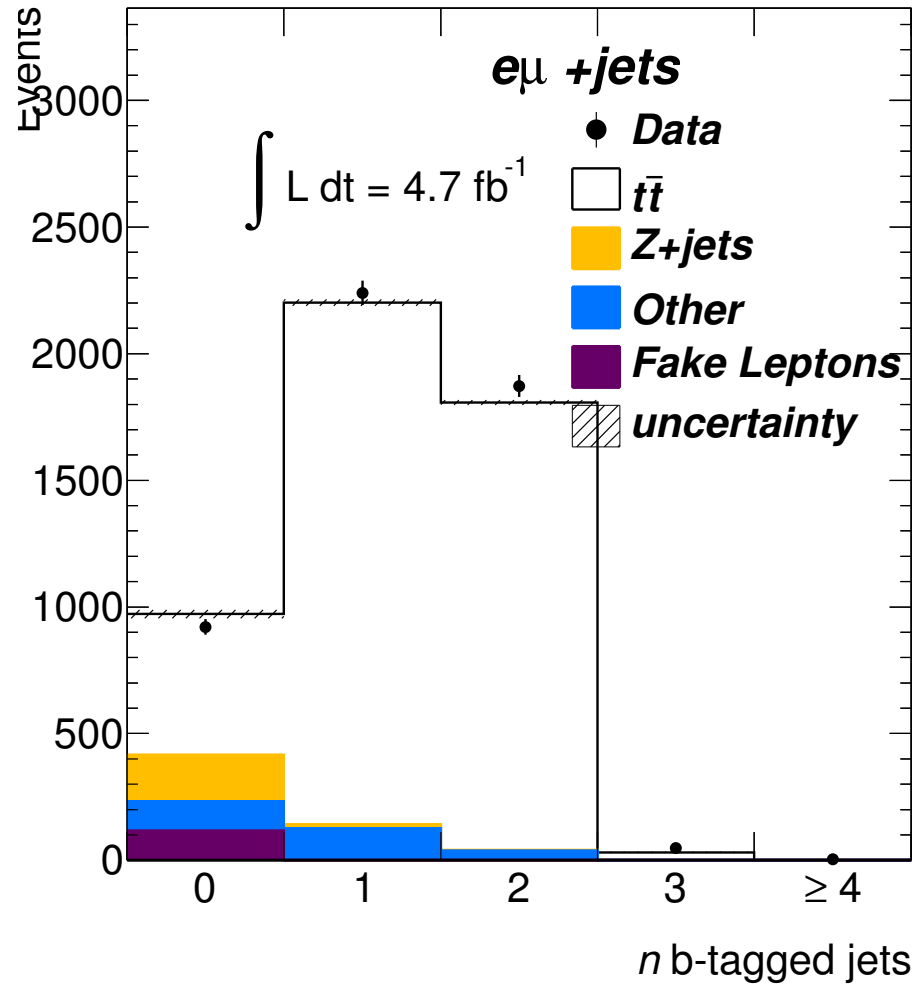


Figure 7.12: The n -tag distribution for the electron-muon channel after fitting showing the statistical uncertainty.

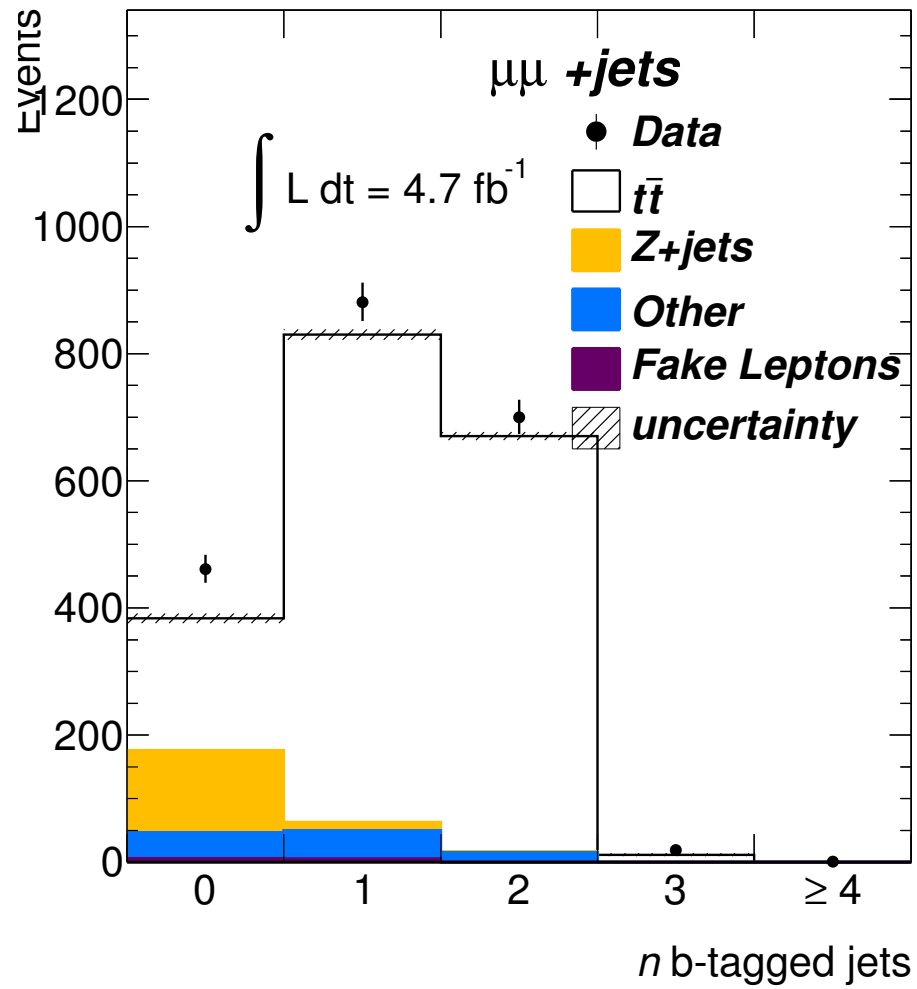


Figure 7.13: The n -tag distribution for the muon-muon channel after fitting showing the statistical uncertainty.

CHAPTER 8

CONCLUSIONS

In this thesis, we have performed a calibration of various b -tagging algorithms, which are a key component of many physics analyses, as well as using b -tagging information to extract the $t\bar{t}$ cross section and the $t \rightarrow Wb$ branching ratio. We used proton-proton collision data at $\sqrt{s} = 7$ TeV collected by the ATLAS detector during 2011 corresponding to an integrated luminosity of 4.7 fb^{-1} after data quality cuts were applied. Both the lepton+jets and dilepton channels were utilized.

The b -tagging calibration has been performed using a tag counting method that exploits our knowledge of the $t\bar{t}$ flavor content. By isolating and treating each p_T bin separately, we were able to perform calibrations as a function of jet p_T . The results are consistent across all channels and are competitive with other $t\bar{t}$ based calibration methods used at ATLAS [4]. Ultimately the majority of the data/MC scale factors are found to be compatible with one and are also consistent with the p_T^{rel} and *System8* calibrations within uncertainties.

The tag counting method assumed that the branching ratio of top quarks to Wb is 100%. This assumption has been verified by measuring the branching ratio, R , through fitting the n -tag distributions to templates produced with varying branching ratios. The result of the simultaneous measurement of R and $\sigma_{t\bar{t}}$ yields $R = 1.06 \pm 0.11$ and $\sigma_{t\bar{t}} = 167^{+27}_{-26} \text{ pb}$. Both values are consistent with the Standard Model expectations. The value of R was allowed to float above one to allow for averaging with other measurements and to avoid biasing the result by introducing an edge in the parameter space. The above result is indeed above one but this should

pose no problem in the global context of previous measurements shown in Fig. 8.1.

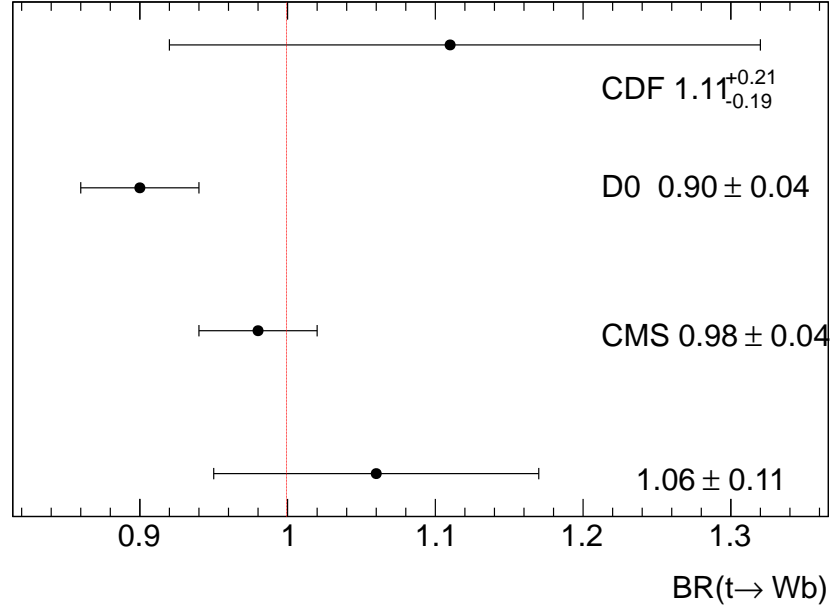


Figure 8.1: The result of the measurement of R presented in this thesis is shown along with the latest results from CDF [16], D0 [17] and CMS [18].

The CMS collaboration's measurement of R has a higher precision than this method because it takes a different approach [18]. Rather than doing a simple likelihood fit, the CMS collaboration uses a profile likelihood fit where each systematic uncertainty is constrained by the data using a Gaussian function. The b -tagging efficiency is also profiled and they report an uncertainty of $\approx 3\%$, which is much less than the 8.5% b -tagging uncertainty in this thesis. The CMS analysis also claims that the effects due to ISR/FSR are small enough to be neglected but we found that the ISR/FSR uncertainties were actually the second largest systematic uncertainty.

8.1 Remarks for the future

The results presented in this thesis are for a 7 TeV center of mass energy. As of this writing, the LHC has delivered three times as much data at 8 TeV center of mass energy. The $t\bar{t}$ cross section grows substantially as the center of mass energy increases, yielding a large sample of $t\bar{t}$ events at 8 TeV in the LHC dataset. With more statistics, one might consider applying tighter event and object selection criteria to select a purer $t\bar{t}$ sample. As the tag counting analysis is already systematically limited, this is probably a worthwhile endeavor. The high-pileup 8 TeV LHC environment is a new regime for both physics and detector performance. The tag counting method presented in this thesis can be applied to calibrate b -tagging algorithms in this new region. With the higher center of mass energy, it should be possible to extend the calibrated b -tagging range beyond 300 GeV in jet p_T .

The measurement of R would benefit from a reduction of b -tagging calibration uncertainties since this is the dominant uncertainty. Since the $t\bar{t}$ based methods usually assume $R=1$, which will bias the result, any improvements will have to come through the muon based calibration methods that are used in the analysis. Using a muon-based tagger may reduce the uncertainty since these typically have lower calibration uncertainties than lifetime taggers but they have poor light and charm jet rejection. The poorer light/charm rejection performance would increase the non- $t\bar{t}$ backgrounds in the lepton+jets channel. This would increase the systematic uncertainties due to W +jet and QCD multijet normalization uncertainties so it is not obvious that this approach will yield a lower overall uncertainty and further study is needed.

The $t\bar{t}$ cross section should be measured at the new center of mass energy. Deviations from the Standard Model values can be indicative of new physics such as new heavy particles. More sophisticated techniques to extract the $t\bar{t}$ signal from the data can be applied. The additional constraints on the $t\bar{t}$ production rate can be used to measure R with greater precision. A simple 2-D likelihood measurement at 7 TeV has been explored but yielded no significant improvements with respect to the simple 1-D analysis. The description of this method can be found in Appendix C.

REFERENCES

- [1] D. Fournier, *Performance of the LHC, ATLAS and CMS in 2011*, *EPJ Web Conf.* **28** (2012) 01003 [1201.4681].
- [2] The **ATLAS** Collaboration, “Trigger operation public results.”
<https://twiki.cern.ch/twiki/bin/view/AtlasPublic/TriggerOperationPublicResults>. Accessed October 2012.
- [3] The **ATLAS** Collaboration, *Alignment of the ATLAS inner detector tracking system with 2010 LHC proton-proton collisions at $\sqrt{s} = 7$ TeV*, ATLAS-CONF-2011-012, Mar, 2011.
- [4] The **ATLAS** Collaboration, *Measuring the b-tag efficiency in a top-pair sample with 4.7/fb of data from the ATLAS detector*, ATLAS-CONF-2012-097, Jul, 2012.
- [5] M. Baak, M. Goebel, J. Haller, A. Hoecker, D. Kennedy *et. al.*, *The Electroweak Fit of the Standard Model after the Discovery of a New Boson at the LHC*, *The Electroweak Fit of the Standard Model after the Discovery of a New Boson at the LHC*, [hep-ph/1209.2716].
- [6] The **D0** Collaboration, “A search for charged higgs boson in tt events.”
<http://www-d0.fnal.gov/Run2Physics/WWW/results/prelim/TOP/T70/>, July, 2008.
- [7] C. Lefvre, “The CERN accelerator complex. complexe des accélérateurs du CERN.” <http://cdsweb.cern.ch/record/1260465>, Dec, 2008.

- [8] The **ATLAS** Collaboration, G. Aad *et. al.*, *The ATLAS Experiment at the CERN Large Hadron Collider*, *JINST* **3** (2008) S08003.
- [9] The **ATLAS** Collaboration, *Performance of the ATLAS inner detector track and vertex reconstruction in the high pile-up LHC environment*, ATLAS-CONF-2012-042, Mar, 2012.
- [10] The **ATLAS** Collaboration, G. Aad *et. al.*, *Performance of the ATLAS Detector using First Collision Data*, *JHEP* **1009** (2010) [[hep-ex/1005.5254](#)].
- [11] A. Salvucci, *Measurement of muon momentum resolution of the ATLAS detector*, *European Physical Journal Web of Conferences* **28** (June, 2012) 12039 [[physics.ins-det/1201.4704](#)].
- [12] O. Kortner and E. Moyse, *Pile-up dependence of the ATLAS muon performance*, ATL-COM-PHYS-2011-1640, Dec, 2011.
- [13] The **ATLAS** Collaboration, *Reconstructed jet multiplicities from the top-quark pair decays and associated jets in pp collisions at $\sqrt{s} = 7$ TeV measured with the ATLAS detector at the LHC*, ATLAS-CONF-2011-142, Sep, 2011.
- [14] The **ATLAS** Collaboration, G. Aad *et. al.*, *Study of jets produced in association with a W boson in pp collisions at $\sqrt{s} = 7$ TeV with the ATLAS detector*, *Phys.Rev.* **D85** (2012) 092002 [[hep-ex/1201.1276](#)].
- [15] The **ATLAS** Collaboration, *Top quark pair production cross-section measurements in ATLAS in the single lepton+jets channel without b-tagging*, ATLAS-CONF-2011-023, Mar, 2011.

- [16] The **CDF** Collaboration, *Measurement of $B(t \rightarrow Wb)/B(t \rightarrow Wq)$* , cdf note 7172, August, 2004.
- [17] The **D0** Collaboration, V. M. *et. al.*. Abazov, *Precision measurement of the ratio $B(t \rightarrow Wb)/B(t \rightarrow Wq)$ and extraction of V_{tb}* , *Phys. Rev. Lett.* **107** (Sep, 2011) 121802.
- [18] The **CMS** Collaboration, *First measurement of $B(t \rightarrow Wb)/B(t \rightarrow Wq)$ in the dilepton channel in pp collisions at $\sqrt{s}=7$ TeV*, CMS-PAS-TOP-11-029, 2012.
- [19] The **ATLAS** Collaboration, *Performance of the ATLAS secondary vertex b -tagging algorithm in 7 TeV collision data*, ATLAS-CONF-2010-042, Jul, 2010.
- [20] The **ATLAS** Collaboration, *Measurement of the b -tag efficiency in a sample of jets containing muons with 5 fb^{-1} of data from the ATLAS detector*, ATLAS-CONF-2012-043, Mar, 2012.
- [21] S. Weinberg, *A model of leptons*, *Phys. Rev. Lett.* **19** (Nov, 1967) 1264–1266.
- [22] G. 't Hooft, *Renormalization of Massless Yang-Mills Fields*, *Nucl. Phys.* **B33** (1971) 173–199.
- [23] G. 't Hooft, *Renormalizable Lagrangians for Massive Yang-Mills Fields*, *Nucl. Phys.* **B35** (1971) 167–188.
- [24] G. Lepage, *Lattice QCD for novices*, *Proceedings of HUGS 98* (1998) [[hep-lat/0506036](#)].
- [25] M. Kobayashi and T. Maskawa, *cp -violation in the renormalizable theory of weak interaction*, *Progress of Theoretical Physics* **49** (1973), no. 2 652–657.

- [26] The **D0** Collaboration, V. M. Abazov *et. al.*, *Simultaneous measurement of the ratio $B(t \rightarrow Wb)/B(t \rightarrow Wq)$ and the top quark pair production cross section with the D0 detector at $\sqrt{s} = 1.96$ TeV*, *Phys. Rev. Lett.* **100** (2008) [[hep-ex/0801.1326](#)].
- [27] The **CDF and D0, The Tevatron Electroweak Working Group** Collaboration, *Combination of CDF and D0 Measurements of the Single Top Production Cross Section*, [[hep-ex/0908.2171](#)].
- [28] D. Griffiths, *Introduction to Elementary Particles*. Wiley-vch, 2004.
- [29] The **CDF** Collaboration, T. Affolder *et. al.*, *Measurement of the strong coupling constant from inclusive jet production at the Tevatron $\bar{p}p$ collider*, *Phys.Rev.Lett.* **88** (2002) [[hep-ex/0108034](#)].
- [30] C. Itzykson and J. Zuber, *Quantum field theory*. Dover books on physics. Dover Publications, 2006.
- [31] C. N. Yang and R. L. Mills, *Conservation of isotopic spin and isotopic gauge invariance*, *Phys. Rev.* **96** (Oct, 1954) 191–195.
- [32] M. E. Peskin and D. V. Schroeder, *An Introduction To Quantum Field Theory (Frontiers in Physics)*. Westview Press, 1995.
- [33] S. Dawson, *Introduction to electroweak symmetry breaking, Proceedings of ICTP Summer School in High-Energy Physics and Cosmology* (1998) [[hep-ph/9901280](#)].
- [34] D. J. Gross and F. Wilczek, *Ultraviolet behavior of non-abelian gauge theories*, *Phys. Rev. Lett.* **30** (Jun, 1973) 1343–1346.

- [35] G. C. Blazey, J. R. Dittmann, S. D. Ellis, V. Elvira, K. Frame *et. al.*, *Run II jet physics*, [[hep-ex/0005012](#)].
- [36] S. Catani, Y. Dokshitzer and B. Webber, *The k-clustering algorithm for jets in deep inelastic scattering and hadron collisions*, *Physics Letters B* **285** (1992), no. 3 291 – 299.
- [37] Y. Dokshitzer, G. Leder, S. Moretti and B. Webber, *Better jet clustering algorithms*, *Journal of High Energy Physics* **1997** (1997), no. 08 001.
- [38] M. Cacciari, G. P. Salam and G. Soyez, *The anti- k_t jet clustering algorithm*, *JHEP* **04** (2008) [[hep-ph/0802.1189](#)].
- [39] The **Particle Data Group** Collaboration, J. Beringer *et. al.*, *Review of Particle Physics (RPP)*, *Phys.Rev.* **D86** (2012) 010001.
- [40] The **CDF** Collaboration, F. Abe *et. al.*, *Observation of top quark production in anti- p p collisions*, *Phys. Rev. Lett.* **74** (1995) 2626–2631 [[hep-ex/9503002](#)].
- [41] The **D0** Collaboration, S. Abachi *et. al.*, *Observation of the top quark*, *Phys. Rev. Lett.* **74** (1995) 2632–2637 [[hep-ex/9503003](#)].
- [42] The **ATLAS** Collaboration, G. Aad *et. al.*, *Measurement of the top quark-pair production cross section with ATLAS in pp collisions at $\sqrt{s} = 7$ TeV*, *Eur.Phys.J.* **C71** (2011) [[hep-ex/1012.1792](#)].
- [43] The **CMS** Collaboration, V. Khachatryan *et. al.*, *First Measurement of the Cross Section for Top-Quark Pair Production in Proton-Proton Collisions at $\sqrt{s}=7$ TeV*, *Phys.Lett.* **B695** (2011) [[hep-ex/1010.5994](#)].

- [44] K. N. *et al.* (Particle Data Group), *The review of particle physics*, *J. Phys. G* **37** (2010) 075021.
- [45] S. Moch and P. Uwer, *Theoretical status and prospects for top-quark pair production at hadron colliders*, *Phys. Rev. D* **78** (Aug, 2008) 034003.
- [46] Calculation at approximate NNLO in QCD using Hathor 1.2 (M. Aliev et al. Comput.Phys.Commun.182:1034-1046,2011) using the MSTW2008 90% NNLO PDF sets (A.D. Martin et al. Eur.Phys.J.C63:189-285,2009) incorporating PDF+ α_S uncertainties according to the MSTW prescription (Eur.Phys.J.C64:653-680,2009). Cross checked with the NLO+NNLL calculation of Cacciari et al. (M. Cacciari et al., <http://arxiv.org/abs/1111.5869>) as implemented in Top++ 1.0 (M. Czakon and A. Mitov, <http://arxiv.org/abs/1112.5675>).
- [47] The **D0** Collaboration, V. M. Abazov *et. al.*, *Forward-backward asymmetry in top quark-antiquark production*, *Phys.Rev.* **D84** (2011) 112005 [1107.4995].
- [48] The **CDF** Collaboration, T. Aaltonen *et. al.*, *Evidence for a Mass Dependent Forward-Backward Asymmetry in Top Quark Pair Production*, *Phys.Rev.* **D83** (2011) [hep-ex/1101.0034].
- [49] The **ATLAS** Collaboration, *Measurement of the charge asymmetry in top quark pair production in pp collisions at $\sqrt{s}=7$ TeV using the ATLAS detector*, ATLAS-CONF-2011-106, Aug, 2011.
- [50] The **CMS** Collaboration, *Measurement of the charge asymmetry in top quark pair production*, CMS-PAS-TOP-11-014, 2011.

- [51] The **CDF** Collaboration, *Observation of single top quark production and measurement of $|V_{tb}|$ with CDF*, *Phys. Rev. D* **82** (Dec, 2010) 112005.
- [52] The **DØ** Collaboration, *Evidence for production of single top quarks and first direct measurement of $|V_{tb}|$* , *Phys. Rev. Lett.* **98** (May, 2007) 181802.
- [53] The **D0** Collaboration, V. M. Abazov *et. al.*, *Evidence for production of single top quarks*, *Phys. Rev.* **D78** (2008) [[hep-ex/0803.0739](#)].
- [54] The **CDF** Collaboration, T. Aaltonen *et. al.*, *Measurement of the Single Top Quark Production Cross Section at CDF*, *Phys.Rev.Lett.* **101** (2008) [[hep-ex/0809.2581](#)].
- [55] The **CDF, D0** Collaboration, Z. Wu, *Single Top Production at the Tevatron, Single Top Production at the Tevatron*, [[hep-ex/1205.3824](#)].
- [56] The **ATLAS** Collaboration, *Observation of t channel single top-quark production in pp collisions at $\sqrt{s} = 7$ TeV with the ATLAS detector*, ATLAS-CONF-2011-088, Jun, 2011.
- [57] The **CMS** Collaboration, *Measurement of the single-top t -channel cross section in pp collisions at $\sqrt{s}=7$ TeV*, CMS-PAS-TOP-10-008, 2011.
- [58] The **ATLAS** Collaboration, *A combined measurement of the top quark pair production cross-section using dilepton and single-lepton final states*, ATLAS-CONF-2011-040, Mar, 2011.
- [59] http://www-cdf.fnal.gov/physics/new/top/public_searches.html.
- [60] The **D0** Collaboration, V. Abazov *et. al.*, *Search for $t\bar{t}$ resonances in the lepton plus jets final state in $p\bar{p}$ collisions at $\sqrt{s} = 1.96$ TeV*, *Phys.Lett.* **B668** (2008) [[hep-ex/0804.3664](#)].

- [61] The **ATLAS** Collaboration, *A search for $t\bar{t}$ resonances in the dilepton channel in 1.04/fb of pp collisions at $\sqrt{s} = 7$ TeV*, ATLAS-CONF-2011-123, Aug, 2011.
- [62] The **CMS** Collaboration, *Search for resonances in semi-leptonic top-pair decays close to production threshold*, CMS-PAS-TOP-10-007, 2011.
- [63] S. P. Martin, *A Supersymmetry primer*, [[hep-ph/9709356](#)].
- [64] The **LEP Higgs Working Group for Higgs boson searches**, **ALEPH Collaboration**, **DELPHI Collaboration**, **L3 Collaboration**, **OPAL Collaboration** Collaboration, *Search for charged Higgs bosons: Preliminary combined results using LEP data collected at energies up to 209 GeV*, *Search for charged Higgs bosons: Preliminary combined results using LEP data collected at energies up to 209 GeV*, [[hep-ex/0107031](#)].
- [65] The **ATLAS** Collaboration, *Search for a charged higgs boson decaying via $h \rightarrow \tau(\text{lep}) + \nu$ in $t\bar{t}$ events with one or two light leptons in the final state using 1.03/fb of pp collision data recorded at $\sqrt{s} = 7$ TeV with the ATLAS detector*, ATLAS-CONF-2011-151, Nov, 2011.
- [66] The **CMS** Collaboration, *$H^\pm \rightarrow \tau$ in top quark decays*, CMS-PAS-HIG-11-008, 2011.
- [67] The **CDF** Collaboration, *Search for light higgs boson from top quark decays*, cdf note 10104, July, 2010.
- [68] The **D0** Collaboration, V. Abazov *et. al.*, *Search for charged Higgs bosons in top quark decays*, *Phys.Lett.* **B682** (2009) [[hep-ex/0908.1811](#)].

- [69] The **ATLAS** Collaboration, *A search for a light charged higgs boson decaying to cs in pp collisions at $\sqrt{s} = 7$ TeV with the ATLAS detector*, ATLAS-CONF-2011-094, Jul, 2011.
- [70] The **CDF** Collaboration, T. Aaltonen *et. al.*, *Search for charged Higgs bosons in decays of top quarks in p anti- p collisions at $\sqrt{s} = 1.96$ TeV*, *Phys.Rev.Lett.* **103** (2009) [[hep-ex/0907.1269](#)].
- [71] The **CMS** Collaboration, R. Adolphi *et. al.*, *The CMS experiment at the CERN LHC*, *JINST* **3** (2008) S08004.
- [72] The **ALICE** Collaboration, K. Aamodt *et. al.*, *The ALICE experiment at the CERN LHC*, *JINST* **3** (2008) S08002.
- [73] The **LHCb** Collaboration, A. Alves *et. al.*, *The LHCb Detector at the LHC*, *JINST* **3** (2008) S08005.
- [74] L. Evans and P. Bryant, *LHC machine*, *Journal of Instrumentation* **3** (2008), no. 08 S08001.
- [75] G. Aad *et. al.*, *The ATLAS inner detector commissioning and calibration*. [oai:cds.cern.ch:1262789](#), *Eur. Phys. J. C* **70** (Jun, 2010) 787–821. 34 p.
Comments: 34 pages, 25 figures.
- [76] The **ATLAS** Collaboration, G. Aad *et. al.*, *ATLAS pixel detector electronics and sensors*, *Journal of Instrumentation* **3** (2008), no. 07 P07007.
- [77] The **ATLAS TRT** Collaboration, *The ATLAS transition radiation tracker (TRT) proportional drift tube: design and performance*, *Journal of Instrumentation* **3** (2008), no. 02 P02013.

- [78] J. Wotschack, *ATLAS muon chamber construction parameters for CSC, MDT, and RPC chambers*, ATL-MUON-PUB-2008-006.
ATL-COM-MUON-2008-008, Apr, 2008. Back-up document for the ATLAS Detector Paper.
- [79] G. A. *et al.*, *Readiness of the ATLAS liquid argon calorimeter for LHC collisions*. *oai:cds.cern.ch:1228823*, *Eur. Phys. J. C* **70** (May, 2010) 723–753. 31 p. Comments: 31 pages, 34 figures, accepted in EPJC.
- [80] G. A. *et al.*, *Readiness of the ATLAS tile calorimeter for LHC collisions*. *oai:cds.cern.ch:1282535*, *Eur. Phys. J. C* **70** (Jul, 2010) 1193–1236. 64 p. Comments: Submitted for publication in EPJC.
- [81] The **ATLAS** Collaboration, G. Aad *et. al.*, *Expected Performance of the ATLAS Experiment - Detector, Trigger and Physics*, [[hep-ex/0901.0512](#)].
- [82] R. Blair, J. Dawson, G. Drake, W. Haberichter, J. Schlereth, J. Zhang, M. Abolins, Y. Ermoline and B. Pope, *The ATLAS high level trigger region of interest builder*, *Journal of Instrumentation* **3** (2008), no. 04 P04001.
- [83] V. Cindro, D. Dobos, I. Dolenc, H. Fraiss-Kolbl, H. Fraiss-Koelbl *et. al.*, *The ATLAS beam conditions monitor*, *JINST* **3** (2008) P02004.
- [84] P. Jenni and M. Nessi, *ATLAS forward detectors for luminosity measurement and monitoring*, CERN-LHCC-2004-010. LHCC-I-014, Mar, 2004.
- [85] P. Jenni, M. Nordberg, M. Nessi and K. Jon-And, *ATLAS Forward Detectors for Measurement of Elastic Scattering and Luminosity*. Technical Design Report. CERN, Geneva, 2008.

- [86] The **ATLAS** Collaboration, G. Aad *et. al.*, *Luminosity Determination in pp Collisions at $\sqrt{s}=7$ TeV Using the ATLAS Detector at the LHC*, *Eur.Phys.J. C* **71** (2011) [[hep-ex/1101.2185](#)].
- [87] S. van der Meer, *Calibration of the effective beam height in the isr.* [oai:cds.cern.ch:296752](#), CERN-ISR-PO-68-31. ISR-PO-68-31, 1968.
- [88] The **ATLAS** Collaboration, *Luminosity determination in pp collisions at $\sqrt{s} = 7$ TeV using the ATLAS detector in 2011*, ATLAS-CONF-2011-116, Aug, 2011.
- [89] The **ATLAS** Collaboration, *Improved electron reconstruction in ATLAS using the Gaussian sum filter-based model for bremsstrahlung*, ATLAS-CONF-2012-047, May, 2012.
- [90] The **ATLAS** Collaboration, “Topcommonobjects.” <https://twiki.cern.ch/twiki/bin/viewauth/ATLASProtected/TopCommon0bjects>. ATLAS Internal; Accessed Mar 2012.
- [91] The **ATLAS** Collaboration, *Muon reconstruction efficiency in reprocessed 2010 LHC proton-proton collision data recorded with the ATLAS detector*, ATLAS-CONF-2011-063, Apr, 2011.
- [92] The **ATLAS** Collaboration, *Reconstruction of jets from tracks in proton-proton collisions at centre-of-mass energy $\sqrt{s} = 900$ GeV with the ATLAS detector*, ATLAS-CONF-2010-002, Jun, 2010.
- [93] M. Cacciari and G. P. Salam, *Dispelling the N^3 myth for the k_t jet-finder*, *Phys. Lett. B* **641** (2006) 57–61 [[hep-ph/0512210](#)].

- [94] The **ATLAS** Collaboration, *Jet energy measurement with the ATLAS detector in proton-proton collisions at $\sqrt{s} = 7$ TeV*, [[hep-ex/1112.6426](#)].
- [95] The **ATLAS** Collaboration, *ATLAS calorimeter response to single isolated hadrons and estimation of the calorimeter jet scale uncertainty*, ATLAS-CONF-2011-028, Mar, 2011.
- [96] The **ATLAS** Collaboration, *Reconstruction and calibration of missing transverse energy and performance in Z and W events in ATLAS proton-proton collisions at 7 TeV*, ATLAS-CONF-2011-080, Jun, 2011.
- [97] The **ATLAS** Collaboration, G. Aad *et. al.*, *Performance of Missing Transverse Momentum Reconstruction in Proton-Proton Collisions at 7 TeV with ATLAS*, *Eur.Phys.J.* **C72** (2012) [[hep-ex/1108.5602](#)].
- [98] F. Caravaglios and M. Moretti, *An algorithm to compute Born scattering amplitudes without Feynman graphs*, *Phys.Lett.* **B358** (1995) [[hep-ph/9507237](#)].
- [99] J. Alwall, M. Herquet, F. Maltoni, O. Mattelaer and T. Stelzer, *MadGraph 5 : Going Beyond*, *JHEP* **1106** (2011) [[hep-ph/1106.0522](#)].
- [100] C. Berger, Z. Bern, L. Dixon, F. Febres Cordero, D. Forde *et. al.*, *An Automated Implementation of On-Shell Methods for One-Loop Amplitudes*, *Phys.Rev.* **D78** (2008) [[hep-ph/0803.4180](#)].
- [101] T. Sjostrand, S. Mrenna and P. Z. Skands, *PYTHIA 6.4 Physics and Manual*, *JHEP* **0605** (2006) 026 [[hep-ph/0603175](#)].
- [102] G. Altarelli and G. Parisi, *Asymptotic Freedom in Parton Language*, *Nucl. Phys.* **B126** (1977) 298.

- [103] Y. L. Dokshitzer, *Calculation of the Structure Functions for Deep Inelastic Scattering and $e^+ e^-$ Annihilation by Perturbation Theory in Quantum Chromodynamics*, *Sov. Phys. JETP* **46** (1977) 641–653.
- [104] V. N. Gribov and L. N. Lipatov, *Deep inelastic $e p$ scattering in perturbation theory*, *Sov. J. Nucl. Phys.* **15** (1972) 438–450.
- [105] G. Corcella, I. Knowles, G. Marchesini, S. Moretti, K. Odagiri *et. al.*, *HERWIG 6: An Event generator for hadron emission reactions with interfering gluons (including supersymmetric processes)*, *JHEP* **0101** (2001) [[hep-ph/0011363](#)].
- [106] G. Corcella *et. al.*, *HERWIG 6.5 release note*, *HERWIG 6.5 release note*, [[hep-ph/0210213](#)].
- [107] P. Nason, *A New method for combining NLO QCD with shower Monte Carlo algorithms*, *JHEP* **0411** (2004) [[hep-ph/0409146](#)].
- [108] S. Frixione, P. Nason and C. Oleari, *Matching NLO QCD computations with Parton Shower simulations: the POWHEG method*, *JHEP* **0711** (2007) [[hep-ph/0709.2092](#)]. * Temporary entry *.
- [109] J. M. Butterworth, J. R. Forshaw and M. H. Seymour, *Multiparton interactions in photoproduction at HERA*, *Z. Phys.* **C72** (1996) 637–646 [[hep-ph/9601371](#)].
- [110] “JIMMY Generator, Multiparton Interactions in HERWIG.”
<http://projects.hepforge.org/jimmy/>. Accessed Jan 2012.
- [111] S. Frixione, E. Laenen, P. Motylinski and B. R. Webber, *Single-top production in MC@NLO*, *JHEP* **03** (2006) 092 [[hep-ph/0512250](#)].

- [112] A. G. Buckley and H. Schulz, *First tuning of HERWIG/JIMMY to ATLAS data*, ATL-COM-PHYS-2010-620, Aug, 2010.
- [113] *New ATLAS event generator tunes to 2010 data*, ATL-PHYS-PUB-2011-008, Apr, 2011.
- [114] S. Frixione and B. R. Webber, *Matching NLO QCD computations and parton shower simulations*, *JHEP* **06** (2002) 029 [[hep-ph/0204244](#)].
- [115] S. Frixione, P. Nason and B. R. Webber, *Matching NLO QCD and parton showers in heavy flavour production*, *JHEP* **08** (2003) 007 [[hep-ph/0305252](#)].
- [116] The **ATLAS** Collaboration, “The common parameters used for ATLAS mc production 2010.” <https://twiki.cern.ch/twiki/bin/view/ATLASProtected/McProductionCommonParameters10>. ATLAS Internal; Accessed Jan 2012.
- [117] M. Aliev, H. Lacker, U. Langenfeld, S. Moch, P. Uwer *et. al.*, **HATHOR: HAdronic Top and Heavy quarks crOss section calculatoR**, *Comput.Phys.Commun.* **182** (2011) [[hep-ph/1007.1327](#)].
- [118] The **ATLAS** Collaboration, “The common parameters used for ATLAS mc production 2011.” <https://twiki.cern.ch/twiki/bin/view/ATLASProtected/McProductionCommonParameters>. ATLAS Internal; Accessed Jan 2012.
- [119] B. P. Kersevan and E. Richter-Was, *The Monte Carlo event generator AcerMC version 2.0 with interfaces to PYTHIA 6.2 and HERWIG 6.5*, [[hep-ph/0405247](#)].

- [120] M. L. Mangano, M. Moretti, F. Piccinini, R. Pittau and A. D. Polosa,
ALPGEN, a generator for hard multiparton processes in hadronic collisions,
JHEP **0307** (2003) [[hep-ph/0206293](#)].
- [121] T. Gleisberg *et. al.*, *Event generation with SHERPA 1.1*, *JHEP* **02** (2009) [[hep-ph/0811.4622](#)].
- [122] J. Pumplin *et. al.*, *New generation of parton distributions with uncertainties from global QCD analysis*, *JHEP* **07** (2002) 012 [[hep-ph/0201195](#)].
- [123] B. Acharya, J.-F. Arguin, M. Barisonzi, I. Besana, M. Bosman, I. Brock, R. Calkins, D. Charkaborty, M. Cobal, M. Cristinziani, J. Ferrando, L. Fiorini, A. Henrichs, B. Heinemann, C. Helsens, G. Khorauli, T. Kuhl, A. Juste, T. Lari, F. Meloni, L. Mir, J. Nadal, E. Nuncio-Quiroz, M. Pinamonti, B. Radics, U. de Sanctis, E. Shabalina, L.-Y. Shan, K. Suruliz, D. Ta, C. Troncon and V. Vorwerk, *Estimation of the W +jets background for top quark re-discovery in the single lepton+jets channel*, ATL-PHYS-INT-2010-136, Dec, 2010.
- [124] M. Cacciari, G. P. Salam, G. Soyez, <http://fastjet.fr/>.
- [125] B. Cooper, J. Katzy, M. Mangano, A. Messina, L. Mijovic *et. al.*, *Importance of a consistent choice of α_s in the matching of AlpGen and Pythia*, *Eur.Phys.J.* **C72** (2012) 2078 [[1109.5295](#)].
- [126] P. Z. Skands, *The Perugia Tunes*, [[hep-ph/0905.3418](#)].
- [127] The **ATLAS** Collaboration, G. Aad *et. al.*, *Measurement of the top quark pair production cross-section with ATLAS in the single lepton channel*, [[hep-ex/1201.1889](#)].

- [128] The **ATLAS** Collaboration, “Heavy flavor overlap removal tool.” <https://twiki.cern.ch/twiki/bin/viewauth/ATLASProtected/HforTool>.
ATLAS Internal; Accessed Mar 2012.
- [129] The **GEANT4** Collaboration, S. Agostinelli *et. al.*, *GEANT4: A simulation toolkit*, *Nucl. Instrum. Meth.* **A506** (2003) 250–303.
- [130] The **ATLAS** Collaboration, G. Aad *et. al.*, *The ATLAS Simulation Infrastructure*, *Eur. Phys. J.* **C70** (2010) [[physics.ins-det/1005.4568](https://arxiv.org/abs/physics.ins-det/1005.4568)].
- [131] The **GEANT4** Collaboration, “Reference physics lists.”
- [132] The **GEANT4** Collaboration, “Summary of hadronic processes, models and cross sections for physics list QGSP_BERT.”
- [133] The **D0** Collaboration, V. M. Abazov *et. al.*, *An Improved determination of the width of the top quark*, *Phys.Rev.* **D85** (2012) 091104 [[1201.4156](https://arxiv.org/abs/1201.4156)].
- [134] The **CDF** Collaboration, *Measurement of single top quark production in 7.5 fb⁻¹ of CDF data using neural networks*,
- [135] The **ATLAS** Collaboration, G. Aad *et. al.*, *Measurement of the t-channel single top-quark production cross section in pp collisions at $\sqrt{s} = 7$ TeV with the ATLAS detector*, *Measurement of the t-channel single top-quark production cross section in pp collisions at $\sqrt{s} = 7$ TeV with the ATLAS detector*, [[hep-ex/1205.3130](https://arxiv.org/abs/hep-ex/1205.3130)].
- [136] The **CMS** Collaboration, S. Chatrchyan *et. al.*, *Measurement of the single-top-quark t-channel cross section in pp collisions at $\sqrt{s} = 7$ TeV*, *Measurement of the single-top-quark t-channel cross section in pp collisions at $\sqrt{s} = 7$ TeV*, [[1209.4533](https://arxiv.org/abs/1209.4533)].

- [137] The **ATLAS** Collaboration, *Measurement of t -channel single top-quark production in pp collisions at $\sqrt{s} = 8$ TeV with the ATLAS detector*, ATLAS-CONF-2012-132, Sep, 2012.
- [138] The **CMS** Collaboration, *Measurement of the single-top t -channel cross section in pp collisions at centre-of-mass energy of 8 TeV*, CMS-PAS-TOP-12-011.
- [139] The **ATLAS** Collaboration, *Calibrating the b -Tag Efficiency and Mistag Rate in 35 pb^{-1} of Data with the ATLAS Detector*, ATLAS-CONF-2011-089, Jun, 2011.
- [140] The **ATLAS** Collaboration, *Commissioning of the ATLAS high-performance b -tagging algorithms in the 7 TeV collision data*, ATLAS-CONF-2011-102, Jul, 2011.
- [141] G. Piacquadio and C. Weiser, *A new inclusive secondary vertex algorithm for b -jet tagging in atlas*, *Journal of Physics: Conference Series* **119** (2008), no. 3 032032.
- [142] F. James, *Minuit - function minimization and error analysis*, D506, August, 1998.
- [143] “Root — a data analysis framework.” <http://root.cern.ch>.
- [144] The **ATLAS** Collaboration, *Statistical combination of top quark pair production cross-section measurements using dilepton, single-lepton, and all-hadronic final states at $\sqrt{s} = 7$ TeV with the ATLAS detector*, ATLAS-CONF-2012-024, Mar, 2012.

- [145] The **ATLAS** Collaboration, *b-jet tagging efficiency calibration using the System8 method*, ATLAS-CONF-2011-143, Oct, 2011.

APPENDIX A
B-TAGGING CALIBRATION

Since top quarks decay into a W -boson and a b -quark nearly 100% of the time, identifying the flavor of jets can provide discrimination between $t\bar{t}$ signal and background events. b -jets are an important signature in many physics processes besides top, such as $H \rightarrow b\bar{b}$. The b -quark has a mass around 5 GeV, which means bound states containing b -quarks are quite massive relative to the particles it can decay into. Hadrons containing b -quarks tend to be long-lived with lifetimes on the order of picoseconds. Because of this, b -hadrons can travel a measurable distance before decaying, sometimes causing a displaced vertex to be resolved as shown in Fig. A.1. This causes jets originating from b -quarks to typically have more tracks with large impact parameters, than light jets. In $t\bar{t}$ events, the typical displacement distances are around the 1 mm scale [81]. They are also massive enough to have decay chains containing muons. Algorithms have been developed to exploit these properties of b -jets to “tag” them as to distinguish them from light or charm jets. The output of these algorithms is seldom a binary decision. It is usually a weight that is indicative of the probability that a jet originated from a b -quark. By varying the cut point at which a jet is labeled as a b -jet, the efficiency and background rejection can be tuned. Before these algorithms can be used in a physics analysis, they must be calibrated by data.

Accurate b -tagging performance is crucial to the measurement of R and is the dominant systematic uncertainty so it must be understood very precisely. This appendix begins by introducing the b -tagging algorithms that are employed at ATLAS and attempts to illustrate how they work. One calibration technique that utilizes $t\bar{t}$ events, tag counting, is shown in detail. This method relies on the assumption that $R = 1$ which is later confirmed to be valid in Chapter 7. Other methods to calibrate b -tagging algorithms based on soft muons and $t\bar{t}$ events are presented. The appendix concludes with a comparison of the results from all of the methods.

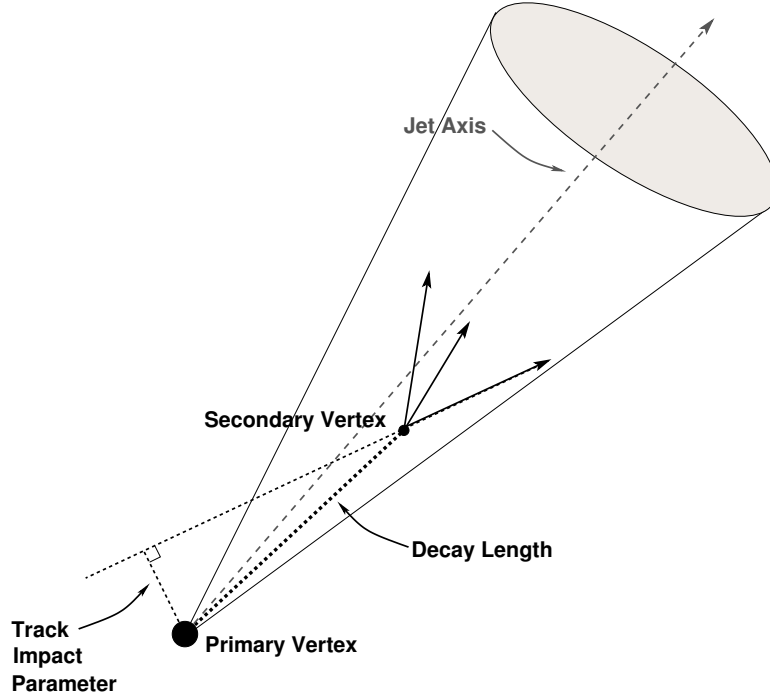


Figure A.1: Figure illustrating key parameters in b -tagging algorithms [19]. Since b -hadrons travel some distances before decaying, there is often a secondary vertex in the event. Tracks coming from such a vertex will have large impact parameters with respect to the primary vertex.

A.1 B-tagging Algorithms

Flavor tagging of jets relies on differences in kinematic distributions but algorithms can generally be separated into several categories. One of the simplest is soft muon tagging, which simply looks for a muon within the cone of a jet. Other tagging algorithms rely on reconstructing a secondary vertex from tracks associated with the jet. The displacement of these vertices are measured with respect to a primary “collision” vertex, which must contain at least five tracks. The displacement along the z -axis, referred to as the longitudinal impact parameter, and in the transverse plane, which is the transverse impact parameter, are used as inputs to the various b -tagging algorithms.

The SV0 tagger relies on reconstructing a displaced secondary vertex with respect to a primary vertex in the event [19,139]. Tracks are assigned to a jet through a ΔR cut of 0.4 and are assigned to the closest jet to avoid being associated with multiple jets. A track must have $p_T > 0.5$ GeV and pass additional quality criteria to be used in the SV0 algorithm. From the track collection, vertices are built out of pairs of tracks based on the impact parameter of the track in 3-dimensions. The impact parameter significance of a 2-track vertex must be greater than 6.6. Cuts are made to remove vertices most likely corresponding to decays from mesons not originating from a b -quark or photon conversions. The surviving 2-track vertices are fit into a single secondary vertex by iteratively removing tracks most likely to originate from the primary vertex and refitting. The output of the algorithm is the signed decay length significance, $\frac{L}{\sigma(L)}$, where L is the decay length and $\sigma(L)$ is the uncertainty.

A more advanced version of the SV0 algorithm exists as the SV1 tagging algorithm [140]. The track selection differs with a slightly lower p_T selection cut (0.4 GeV), tracks cannot have more than one shared hit with another track and an additional cut on the transverse impact parameter, $|d_0| < 3.5$ mm. Properties of the vertex, such as the invariant mass of the tracks and the number of 2-track vertices, are used in a likelihood ratio to boost discrimination power. Similarly, the IP3D tagger utilizes the longitudinal and transverse impact parameters of tracks in a likelihood ratio to discriminate between b and light flavor jets. These two algorithms are used in combination as the IP3D+SV1 tagger.

A b -hadron will decay through a c -hadron, which can sometimes decay displaced with respect to the b -hadron flight path. The JetFitter algorithm exploits the differences in topologies to discriminate between jet flavors [141]. In addition to many of the variables used in the IP3D+SV1 tagger, the number of single-track vertices

along the b -hadron flight axis is utilized along with the significance of flight lengths of the b and c hadrons.

The variety of taggers available tends to utilize different discriminating aspects of b decays. Even more discrimination power can be achieved through the combination of several of these. One example of this is the JetFitterCombNN tagger, which combines the JetFitter tagger with the IP3D tagger using a neural network. Combining the output of several different taggers is the basis for the MV1 algorithm [20]. The input of the MV1 algorithm is the tagging weights from the IP3D, SV1 and JetFitterCombNN algorithms. These are fed through a neural network (NN) to generate a b -tagging weight. Compared to the individual taggers that are inputs to MV1, the light jet rejection power of MV1 is superior for the same b -tagging efficiency as illustrated by Fig. A.2. The actual b -tagging efficiency can be tuned by varying the cut on the b -tagging weight. Typical values for b -tagging efficiency range from 50% to 90% depending on the analysis. Most $t\bar{t}$ analyses use working points in the 60-70% b -tagging efficiency range. Many b -tagging algorithms have a strong dependence on the p_T of the jet so the term working point applies to the average expected b -tagging efficiency over the entire jet p_T range.

A.2 Tag Counting Method

The tag counting method is a data-based method for calibrating b -tagging algorithms that utilizes knowledge of the flavor content of the event sample and the distribution of number of tagged jets (N-tag) per event. The large number of $t\bar{t}$ candidate events collected by ATLAS provide an excellent sample to calibrate the various b -tagging algorithms since in a perfect world, we expect two b -jets in the

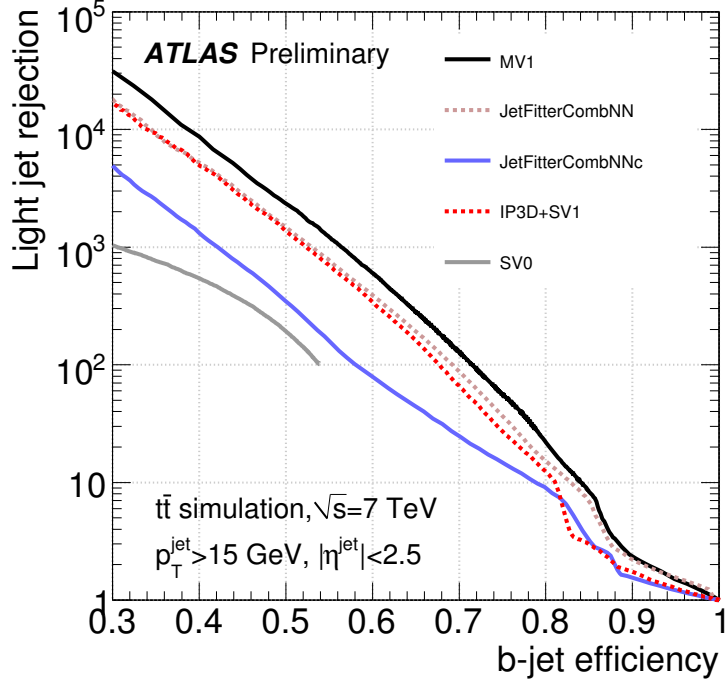


Figure A.2: B-jet efficiency and light jet rejection curves for a variety of ATLAS b -tagging algorithms based on simulated $t\bar{t}$ events. The MV1 tagging algorithm performs well across the entire range of efficiency working points [20].

final state. In addition to real¹ b -jets, jets originating from charmed hadrons and light quarks or gluons can be mis-tagged as b -jets. The actual number of final state b -jets in $t\bar{t}$ events can differ from two since one or both b -jets may fall outside of the acceptance or gluon splitting may contribute additional b -jets to the final state.

To use what we know about $t\bar{t}$ decays to calibration b -tagging, we need to derive an equation to predict the events with n -tagged jets. Since we are relying on $t\bar{t}$ events to provide us with real b -jets, we need to estimate the number of $t\bar{t}$ events in our dataset passing the selection criteria and accounting for the branching ratios and detector acceptance. It is also important to describe the fractions of events with various jet flavor configurations. In addition to $t\bar{t}$, there will also be contributions

¹Real is defined as having a B -hadron within $\Delta R(B - \text{hadron}, \text{jet}) < 0.2$

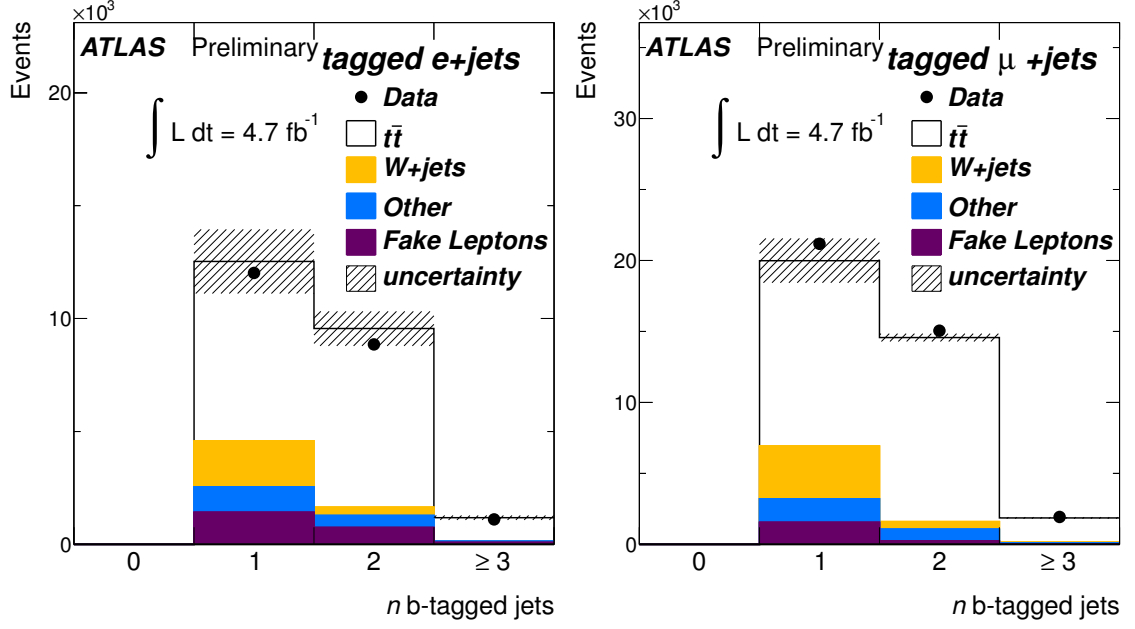


Figure A.3: The n -tag distributions for the electron (left) and muon (right) channels for data and Monte Carlo [4]. The MV1 tagger at a 70% efficiency working point was used in these particular figures. The uncertainty band shows the normalization uncertainties for the QCD fake lepton background.

from background processes that need to be accounted for. In addition to tagging b -jets, light and charm jets will contribute to the n -tag distribution. The actual number of expected events (N) with n b -tagged jets is given by :

$$\begin{aligned}
 \langle N_n \rangle = & \sum_{i,j,k} \left\{ (\sigma_{t\bar{t}} \cdot BR \cdot A_{t\bar{t}} \cdot F_{ijk}^{t\bar{t}} \cdot \mathcal{L} + N_{\text{bkg}} \cdot F_{ijk}^{\text{bkg}}) \times \right. \\
 & \sum_{i'+j'+k'=n} \binom{i}{i'} \cdot \varepsilon_b^{i'} \cdot (1 - \varepsilon_b)^{i-i'} \cdot \binom{j}{j'} \cdot \varepsilon_c^{j'} \cdot (1 - \varepsilon_c)^{j-j'} \times \\
 & \left. \binom{k}{k'} \cdot \varepsilon_l^{k'} \cdot (1 - \varepsilon_l)^{k-k'} \right\} \quad (\text{A.1})
 \end{aligned}$$

. The first term in the summation in Eq. A.1 accounts for the total number of $t\bar{t}$ events, taking the $t\bar{t}$ cross section ($\sigma_{t\bar{t}}$), branching ratio (BR) for that particular channel, acceptance (A) and integrated luminosity (\mathcal{L}) into account. This is

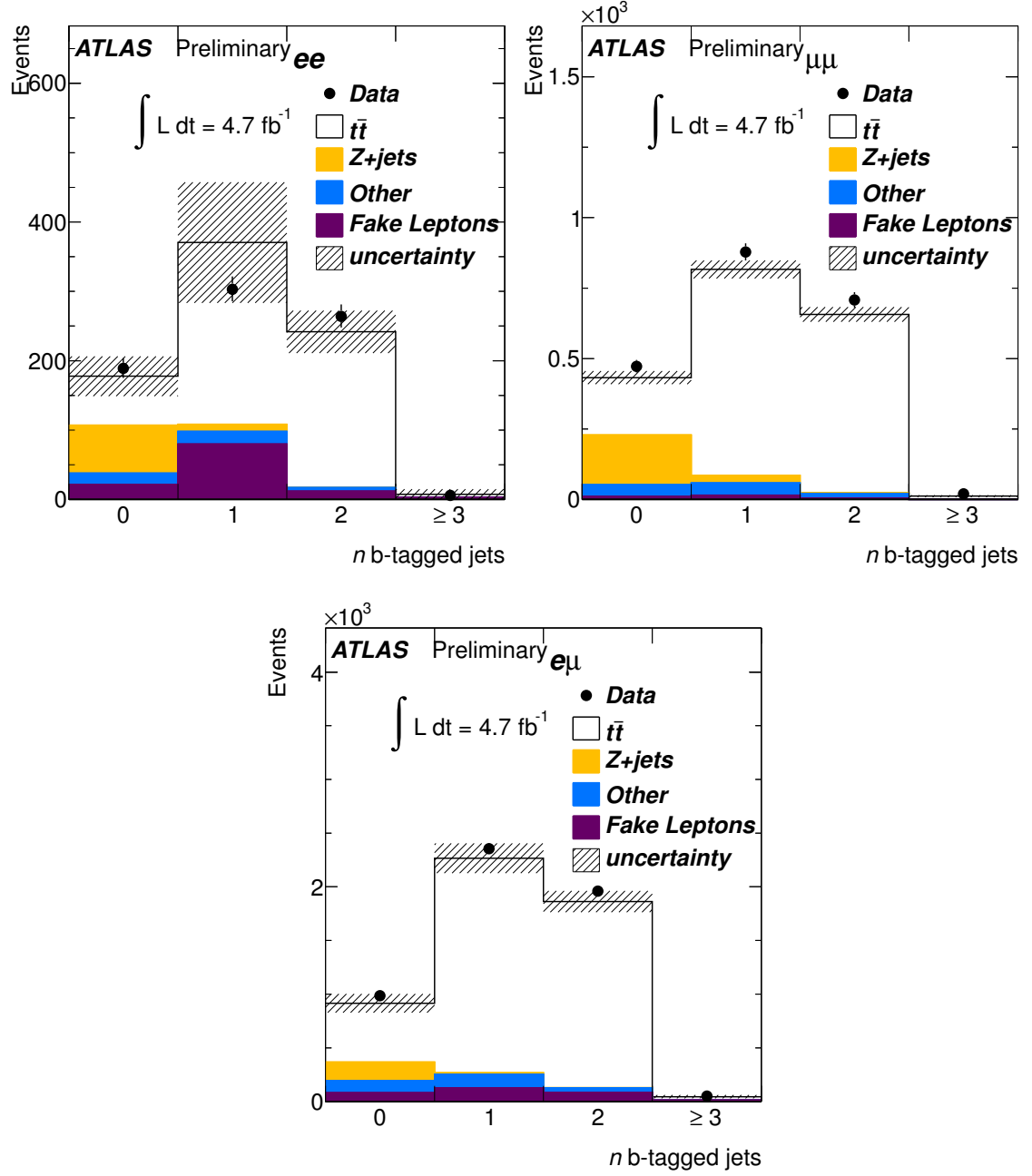


Figure A.4: The n -tag distributions for the electron-electron, muon-muon and electron-muon channels for data and Monte Carlo [4]. The statistical uncertainty is shown on the data points while the QCD multijet normalization uncertainty is the uncertainty band attached to the Monte Carlo distribution.

multiplied by $F_{ijk}^{t\bar{t}}$, which is the fraction of $t\bar{t}$ events with i b -jets, j c -jets and k l -light reconstructed detector-level jets. For an example, an ideal semi-leptonic $t\bar{t}$ event with two b -jets and two light jets would contribute to the F_{202} term, which constitutes about 30% of lepton+jets $t\bar{t}$ events. Labeling of jet flavor in Monte Carlo simulation is done using a ΔR cut between truth particles and reconstructed jets. Hadronically decaying τ 's are treated as light jets. The dominant F_{ijk} terms are shown in table A.1 for jets with $p_T > 25$ GeV and Tab. A.2 for jets with p_T between 30 and 40 GeV. There is a similar term, $N_{\text{bkg}} \cdot F_{ijk}^{\text{bkg}}$, for the contributions from background. The second summation accounts for the various combinations and probabilities to tag each jet flavor. This summation is over the number of i' b -jets, j' c -jets and k' l -light tagged jets and is constrained that the total number of tagged jets is n . The ε terms correspond to the tagging efficiency for that particular jet flavor. Combinations of how the n -tags can be distributed among the jets are accounted for by the binomial coefficient terms.

F_{ijk}	$t\bar{t}$ e channel	F_{ijk}	e channel backgrounds
F_{202}	0.291 ± 0.001	F_{004}	0.510 ± 0.005
F_{211}	0.148 ± 0.001	F_{013}	0.136 ± 0.002
F_{203}	0.129 ± 0.001	F_{005}	0.120 ± 0.002
F_{103}	0.09 ± 0.01	F_{103}	0.04 ± 0.01
F_{212}	0.08 ± 0.01	F_{014}	0.03 ± 0.01

F_{ijk}	$t\bar{t}$ μ channel	F_{ijk}	μ channel backgrounds
F_{202}	0.289 ± 0.001	F_{004}	0.530 ± 0.004
F_{211}	0.151 ± 0.001	F_{013}	0.138 ± 0.001
F_{203}	0.129 ± 0.001	F_{005}	0.108 ± 0.002
F_{103}	0.09 ± 0.01	F_{103}	0.04 ± 0.01
F_{212}	0.08 ± 0.01	F_{022}	0.03 ± 0.01

Table A.1: The five largest F_{ijk} terms for jets with p_T above 25 GeV for the e channel (top) and μ channel (bottom) [4]. The largest $t\bar{t}$ term is F_{202} , which are events with two b -jets and two light jets. The background is dominated by the F_{004} term, which are events with four light jets. Uncertainties are statistical only.

F_{ijk}	$t\bar{t}$ e channel	F_{ijk}	e channel backgrounds
F_{000}	0.410 ± 0.001	F_{001}	0.376 ± 1.005
F_{001}	0.251 ± 0.001	F_{000}	0.374 ± 0.008
F_{100}	0.116 ± 0.001	F_{002}	0.138 ± 0.005
F_{101}	0.07 ± 0.01	F_{003}	0.03 ± 0.03
F_{010}	0.05 ± 0.01	F_{100}	0.02 ± 0.01

F_{ijk}	$t\bar{t}$ μ channel	F_{ijk}	μ channel backgrounds
F_{000}	0.407 ± 0.001	F_{001}	0.374 ± 0.005
F_{001}	0.253 ± 0.001	F_{000}	0.364 ± 0.003
F_{100}	0.114 ± 0.001	F_{002}	0.144 ± 0.002
F_{101}	0.07 ± 0.01	F_{003}	0.03 ± 0.01
F_{002}	0.05 ± 0.01	F_{010}	0.03 ± 0.01

Table A.2: The five largest F_{ijk} contributions for the 30-40 GeV p_T bin. Most $t\bar{t}$ events don't have any jets with p_T in the 30-40 GeV range and about 25% have one light jet that falls within the p_T acceptance. The background event terms are dominated by the case where no jets are contributed and the case where just one light jet falls within the p_T bin acceptance.

To extract the parameters of equation A.1 from the data, a maximum likelihood fit is performed over the n -tag distributions (Fig. A.3 and A.4) using the MINUIT program within the ROOT framework [142,143]. The likelihood function is given by :

$$L = \text{Gaus}(\sigma_{t\bar{t}}|\sigma_{t\bar{t},MC}, \delta_{\sigma_{t\bar{t},MC}}) \text{Gaus}(N_{\text{bkg}}|N_{\text{bkg},MC}, \delta_{N_{\text{bkg}}}) \prod_{n\text{-tags}} \text{Pois}(N_n| \langle N_n \rangle) \quad (\text{A.2})$$

. In Eq. A.2, L is the likelihood being maximized. The $t\bar{t}$ cross section ($\sigma_{t\bar{t}}$) is allowed to float as a nuisance parameter but is constrained by a Gaussian function centered around the predicted cross section value ($\sigma_{t\bar{t},MC}$) 166.8 pb with a 10% relative uncertainty for the width ($\delta_{\sigma_{t\bar{t},MC}}$), which corresponds to the estimated theory uncertainty [46]. The background normalization (N_{bkg}), which is dominated by W +jets events, is also constrained in similar fashion but the uncertainty ($\delta_{N_{\text{bkg}}}$) is 10% for the number of background events in the electron channel and 8% for number of background events in the muon channel, which are the estimated W +jets normalization uncertainties based on data-driven methods [4]. Letting the normalization float reduces the overall uncertainties as shown in Fig. A.5. The number of events in each n -tag bin is expected to follow Poisson statistics so the probability to measure N_n events when $\langle N_n \rangle$ events are expected is described by the Poisson probability function.

For the fit in the lepton+jets channel, the 0-tag bin is omitted from the fit since it mostly contains W +jet events and QCD multijet backgrounds. The dilepton channels have a much higher purity of $t\bar{t}$ events but smaller statistics so the 0-tag bin is included in the analysis. The n -tag distributions for each channel for all jets with $p_T > 25$ GeV are shown in Figures A.3 and A.4 for data and Monte Carlo simulation. The fit response is evaluated using the average result from ensemble

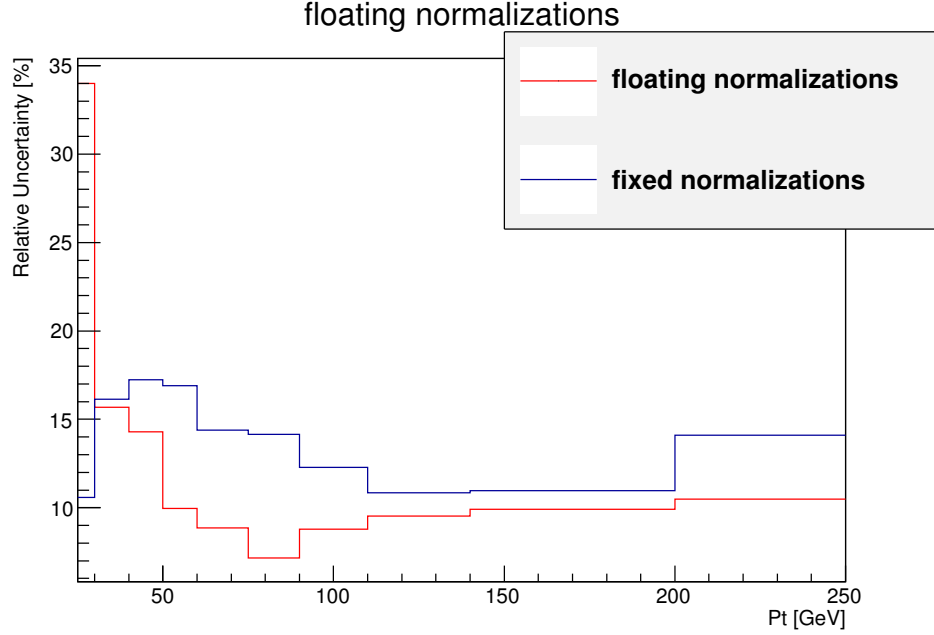


Figure A.5: Comparison of the overall uncertainties for the analysis when fixing the normalization as opposed to letting them float. For the majority of the p_T bins, the uncertainty is lower when allowing both the $t\bar{t}$ normalization and the backgrounds float.

tests of 1000 pseudo-experiments. The response is very linear with respect to input b -tagging efficiency as shown in Fig. A.6.

A.2.1 p_T binning

The efficiency of a b -tagging algorithm is sensitive to the p_T of the jet. For high p_T jets, the tracks tend to be collimated and vertex resolution in the transverse plane will be degraded. For lower p_T jets, the long lived particles may not be boosted enough to travel significant distances before decaying. The sensitivity to these effects depends on the algorithm and the cut point which defines whether or not a jet is classified as "tagged" or not.

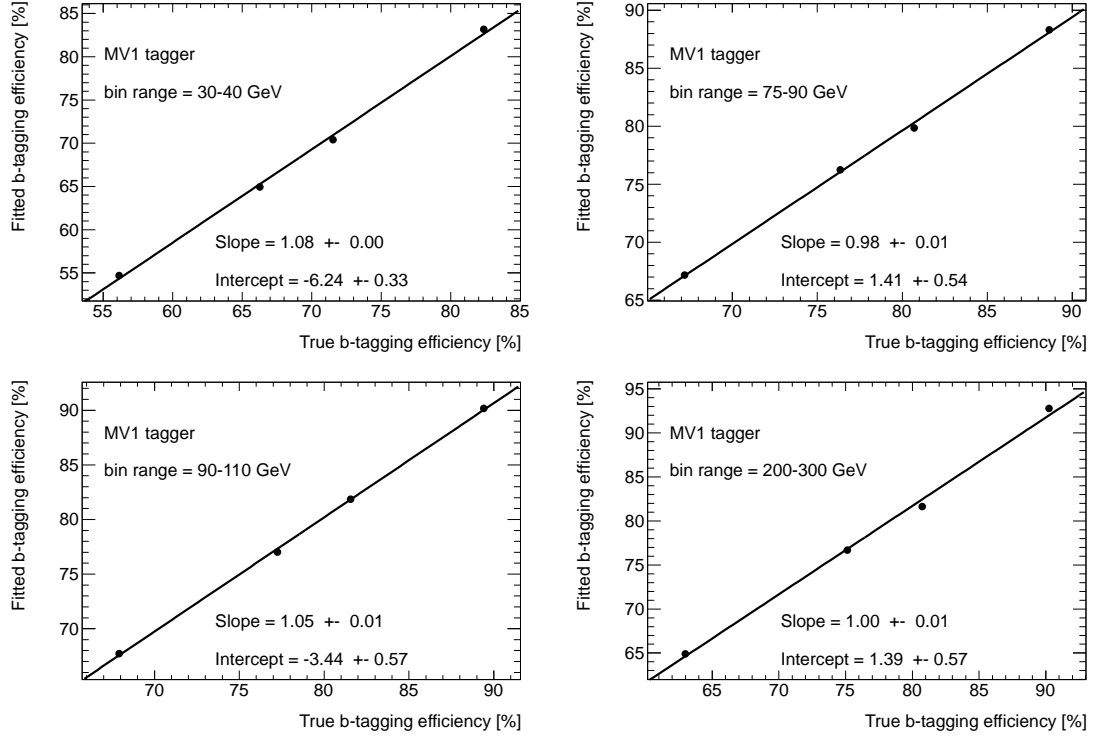


Figure A.6: The linearity of the fit is shown for the MV1 tagger for several p_T bins. The top left plots shows the linearity for the 30-40 GeV bin, followed by the 75-90 GeV bin on the top right. The bottom row shows the linearity plot for the 90-110 GeV p_T bin on the left and the 200-300 GeV p_T bin on the right. The deviations from linearity are typically small.

To apply the tag counting method as a function of p_T , it is necessary to examine each p_T bin separately. This is accomplished by taking Eq. A.1 and adding p_T dependence to the F_{ijk} terms and the tagging efficiency. The p_T dependent efficiencies are calculated by considering only jets that fall within the p_T bin's range. Similarly, the F_{ijk} tables are calculated using just jets within each p_T bin and ignoring all other jets in the event. The largest contribution for $t\bar{t}$ is F_{000} which are events with no jets falling within that p_T bin's range. This approach makes the most of the available statistics in the $t\bar{t}$ sample since each event can contribute jets to several p_T bins. The $t\bar{t}$ cross section is a parameter of the fit and can be extracted but because

there are events shared between p_T bins, there are significant statistical correlations between the various results. The linearity for each p_T bin is generally very good as show in Fig. A.6 and any remaining biases are taken as corrections on a bin by bin basis.

A.2.2 Systematic uncertainties

This analysis technique is sensitive to all of the systematic uncertainties associated with a full “cut and count” $t\bar{t}$ analysis since it relies on knowledge of the $t\bar{t}$ selection efficiency and background normalization. In order to assess the overall effect of each source of systematic uncertainty, ensembles of n -tag templates were produced using pseudo-experiments with each systematic uncertainty varied within uncertainties and fits performed using the nominal parameters and expected number of events. Figure A.7 shows an example of the n -tag distribution for the nominal parameters and for the jet energy scale systematic uncertainty varied up and down by 1σ . To evaluate the JES systematic, the fit is performed to the two JES distributions assuming the nominal JES value.

The systematic uncertainty is taken as the difference between the average fitted ε_b from the ensemble of pseudo-experiments and the truth value as determined for that particular sample. The tables of systematic uncertainties for all taggers and working points can be found in Appendix B. The uncertainties vary depending on the p_T bin and working point but they are typically dominated by ISR/FSR, MC generator, jet energy scale (JES) and jet energy resolution (JER), which affects both the signal acceptance as well as jet bin to bin migration.

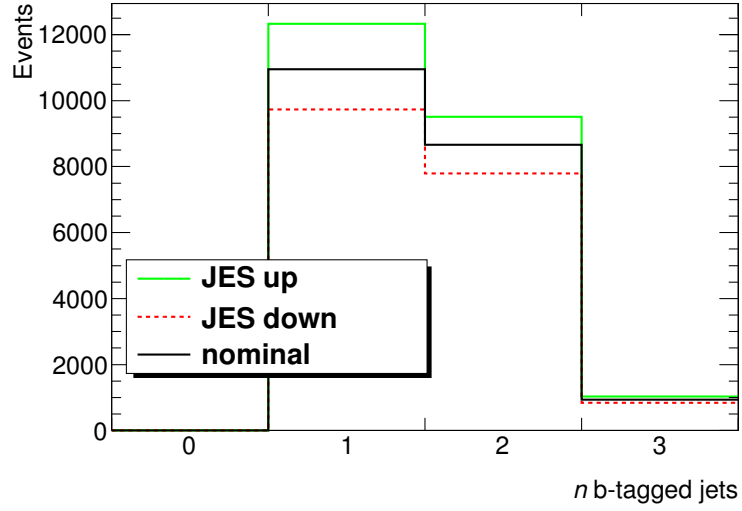


Figure A.7: This figure shows the n -tag distribution for the electron channel for the nominal MC sample and the JES systematic varied up and down by 1σ .

A.2.3 Results

The analysis was run over the full 2011 ATLAS dataset after removing data rendered unusable by detector conditions. The total amount of data after detector condition selection criteria is applied corresponds to 4.7^{-1} fb. The overall uncertainties are dominated by systematic uncertainties which are given in Appendix B and vary depending on the p_T bin, tagger and working point.

The $t\bar{t}$ cross section is a floating parameter of the fit and can be extracted from each p_T bin and working point. The main purpose of the tag counting method is the calibration of the various b -tagging algorithms so the result of the fit for the $t\bar{t}$ cross section serves primarily as a cross check that the analysis is fitting a reasonable value for $\sigma_{t\bar{t}}$. The values for each cross section measurement are plotted in Fig. A.8, which are consistent with the ATLAS $t\bar{t}$ cross section measurement of 177

$\pm 3(\text{stat.})_{-7}^{+8}(\text{syst.}) \pm 7(\text{lumi.})$ pb [144]. Each point utilizes the same dataset, which makes a statistical combination extremely difficult.

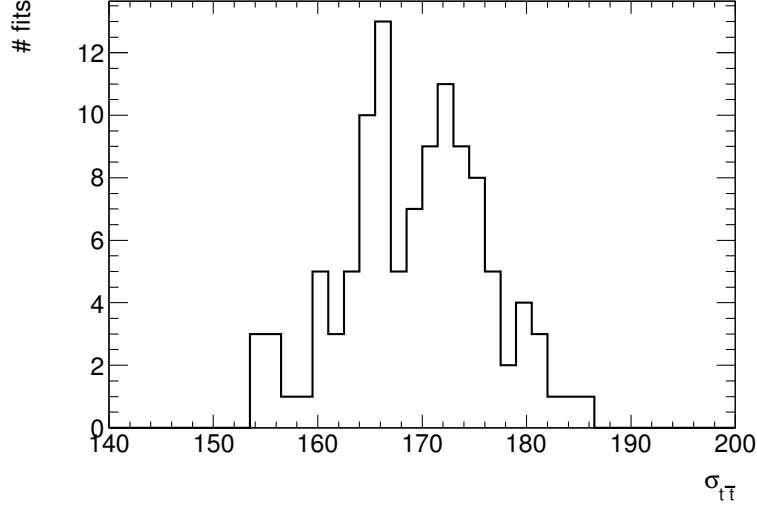


Figure A.8: The $t\bar{t}$ cross section results as extracted from the numerous fits to data. Each entry corresponds to an individual p_T bin, tagger and working point. The peak around 165pb is due to the Gaussian constraint on the $t\bar{t}$ cross section fit, which makes this a preferred value.

The results of the b -tagging calibration for the tag counting method using the lepton+jets channel for all taggers and working points are shown in Fig. A.9 though A.12. The results for most of the p_T bins and taggers are consistent with one within the uncertainties, showing that the Monte Carlo simulations do correctly predict the b -tagging efficiency.

A.3 Other Calibration Methods

In addition to the tag counting method, there are several other methods used to calibrate b -tagging algorithms. They can be separated into two broad categories, $t\bar{t}$ -based and muon-based. The $t\bar{t}$ -based methods exploit the heavy flavor rich events

produced in $t\bar{t}$ decays to measure b -tagging efficiencies, while the muon-based methods exploit the fact that heavy flavor decays often have soft muons within the jet that can be used as an identifying characteristic independent of the reconstruction of a secondary vertex.

A.3.1 other $t\bar{t}$ -based methods

The tag counting method relies on b -tagged jet multiplicity but there are more aspects of $t\bar{t}$ events that can be exploited to extract the b -tagging efficiency from the data.

The kinematic selection method. The kinematic selection method uses the expected fractions of b , c and light jets to derive an equation (Eq. A.3) relating the fraction of tagged jets to the b -tagging efficiency:

$$\varepsilon_b = \frac{1}{f_{b\text{-jets}}} (f_{b\text{-tagged}} - \varepsilon_c f_{c\text{-jets}} - \varepsilon_l f_{l\text{-jets}} - \varepsilon_{\text{fake}} f_{\text{fake}}) \quad (\text{A.3})$$

relying on the fact that the total fraction of tagged jets is the sum of the contributions from the individual flavor components :

$$\varepsilon_b f_{b\text{-jets}} + \varepsilon_c f_{c\text{-jets}} + \varepsilon_l f_{l\text{-jets}} + \varepsilon_{\text{fake}} f_{\text{fake}} = f_{b\text{-tagged}} \quad (\text{A.4})$$

[4]. The $f_{b\text{-tagged}}$ term is measured in the $t\bar{t}$ signal region from the data while the $\varepsilon_{\text{fake}} f_{\text{fake}}$ quantity, which is the fraction of b -tagged jets coming from QCD multijet background events, is measured in a QCD multijet control region with low E_T^{miss} . The other terms on the right hand side, light and charm fractions (f) and tagging

efficiencies (ε), are estimated from Monte Carlo simulations. This method can be applied to lepton+jets or dilepton events.

The kinematic fit method. The kinematic fit method relies on reconstructing the individual top quarks in the semi-leptonic decay channel and identifying the jets originating from the parton level b -quarks [4]. The reconstruction and assignment of jets to quarks is done by minimizing a χ^2 function that uses the reconstructed W -boson and top quark masses as constraints. Only the jet assigned to the leptonic top decay is used to extract the b -tagging efficiency since the b -jet on the hadronic side of the event is used to estimate the combinatoric backgrounds by measuring the rate a b -tagged jet is assigned to the W -boson. The backgrounds are normalized in the large χ^2 region and the b -tagging efficiency is extracted from the tagger weight distribution after background subtraction has been applied.

A.3.2 p_T^{rel} method

Kinematic information derived from muons within jets can be used to calibrate vertex based b -tagging algorithms. One such method utilizes the p_T^{rel} variable which is defined as the p_T of the muon with respect to the axis of the jet-muon system [139,145]. This particular variable has different distribution depending on the flavor of the original jet as shown in Fig. A.13. Templates are fitted to the p_T^{rel} distributions before and after applying b -tagging criteria to extract the fraction of tagged and untagged b , c and light jets in the sample. This method breaks down at high p_T since the jet and muon axes become co-linear.

p_T^{rel} Systematic uncertainties. Since the p_T^{rel} method relies on templates produced from Monte Carlo samples with finite statistics, it is possible that statistical fluctuations in the template shapes can affect the results. To assess the systematic associated with Monte Carlo statistics, ensemble tests of pseudo-experiments are performed while smearing the templates by a Gaussian function. The templates rely on correct modeling of the b -hadron directions which is checked in data by examining the ΔR distribution between the calorimeter jet and a jet built out of charged tracks. The distribution from Monte Carlo simulation is smeared to match the distribution observed in the data and a systematic uncertainty is assigned based on the difference between the smeared and un-smeared templates. Effects from b -jet contamination in the light jet templates are estimated from Monte Carlo and fluctuated by 25% [20].

Pairs of heavy flavor partons can originate from gluon splitting which tend to have small angular separation. In many of these cases, both partons are reconstructed in the same jet. Systematic effects from jets containing two heavy flavor partons are estimated by removing or doubling this contribution from the templates and comparing the effects. The p_T spectrum of the muon also depends on whether it originates from a direct decay ($b \rightarrow lX$) or through a cascade ($b \rightarrow c \rightarrow lX$). The relative fractions of these contributions are varied and the effects taken as a systematic uncertainty. Effects from fragmentation modeling are assessed by varying the fraction of energy carried by the B -hadron by 5%. The muon p_T spectrum in Monte Carlo was reweighted to reproduce the spectrum measured in data and the difference between the two is taken as a source of systematic uncertainty. Monte Carlo simulations typically do a poor job at estimating fake rates for leptons, so the fake muon rate is increased by a factor of three to compensate for the lower fake muon efficiency in Monte Carlo simulations. Differences between semi-leptonic

and inclusive b -jet tagging efficiencies are accounted for by comparing the number of tagged semi-leptonic and inclusive b -jets in data and Monte Carlo simulation as a function of number of displaced tracks in a jet. The difference between Monte Carlo simulation and data is taken as a systematic uncertainty.

A.3.3 System8 method

The *System8* method extracts the b -tagging efficiency by solving a set of simultaneous equations that describe event counts in various subsets of the data sample [20, 145]. Three selection criteria -

1. whether or not the jet was tagged by the algorithm being calibrated
2. if there is a muon in the jet with p_T^{rel} above 700 MeV or not
3. if there is an b -tagged jet on the opposite side of the detector or not

- are expected to be orthogonal and are used to classify events. These can be further separated into muon-based b -tagging and lifetime-based b -tagging plus samples with and without a back-to-back jet topology. By counting the number of jets with/without an opposite b -tagged jet, tagged/untagged by a muon based-tagger, tagged/untagged by a lifetime-based tagger, and tagged/untagged by both a lifetime and a muon-based tagger, a system of eight equations with eight unknowns (including the b -tagging efficiencies for the lifetime-based and muon-based tagger) can be written down (see Ref. [20]). The solution is extracted using a χ^2 method with MINUIT while constraining the b -tagging efficiency to be higher than the c and light jet tagging efficiencies.

System8 Systematic uncertainties. The *System8* method shares many of the same systematic effects as the p_T^{rel} analysis, in addition to some that are unique to the method. The *System8* method relies on correctly measuring the correlations between the eight regions, which are derived from Monte Carlo simulations. To account for limited statistics, the correlation factors are allowed to float in the fit but are constrained by a Gaussian and are incorporated as an extra term in the χ^2 : $\chi^2 \rightarrow \chi^2 + (\vec{\alpha} - \vec{\alpha}_0)^T V^{-1} (\vec{\alpha} - \vec{\alpha}_0)$, where $\vec{\alpha}_0$ are the nominal values and V is the correlation factor covariance matrix [145]. One of the *System8* selection regions is determined by a cut on the p_T^{rel} variable. This is varied up and down by 100 MeV and the largest difference between the results is taken as a systematic uncertainty. In addition to varying the fragmentation modeling, the relative fractions of ground state b hadrons were also varied within uncertainties quoted by LEP and Tevatron experiments since the lifetime and muon p_T are dependent on the parent hadron. The fraction of charm jets in the sample affects the p_T^{rel} templates and the correlation factors between various regions. This has been varied by a factor of two to assess the sensitivity to this uncertainty.

A.4 Results

The ultimate goal of these various calibration methods is to provide scale factors to correct the b -tagging efficiencies in Monte Carlo simulation to match those measured in data. Since b -tagging performance strongly depends on the p_T of the jet, all calibration methods provide scale factors as a function of p_T bin, which have consistent ranges with the exception of the lowest and highest p_T bins. The dependence on η is small enough to be neglected. The lowest p_T bin for the *System8*

and p_T^{rel} methods starts at 20 GeV but the $t\bar{t}$ based calibrations start at 25 GeV since this is the lowest jet p_T cut supported by the ATLAS top group. At high jet p_T , muons within jets become colinear with the jet axis and resolution of p_T^{rel} is degraded. Consequently, the p_T^{rel} and *System8* methods loose effectiveness since they both depend on the p_T^{rel} variable.

The muon based calibrations, p_T^{rel} and *System8*, are combined using a maximum likelihood technique [20]. Systematic uncertainties are treated as nuisance parameters that are correlated across p_T bins. Since there are some shared events between the p_T^{rel} and *System8* methods, correlation coefficients are calculated from pseudo-experiments. The $t\bar{t}$ dilepton and lepton+jets channels are orthogonal to each other by selection, but the results between methods for each channel are fully correlated so a combination between the same channel $t\bar{t}$ based calibration results is not performed. Work is on going to combine the results from one of the $t\bar{t}$ based methods with the p_T^{rel} and *System8* results.

The total uncertainties for the combined p_T^{rel} and *System8* calibrations range from 5% to 19% [20] while the $t\bar{t}$ -based methods range from 5% to about 30% relative uncertainty [4]. The scale factor results for all methods are shown in Fig. A.14. It is important that b -tagging be well understood for the result of this thesis as it is the dominant systematic. These results confirm that the Monte Carlo simulations are roughly correct in the prediction of the b -tagging efficiency. This is further strengthened by the agreement between the muon based and $t\bar{t}$ based calibrations, which take very different approaches to calibrating the b -tagging efficiency.

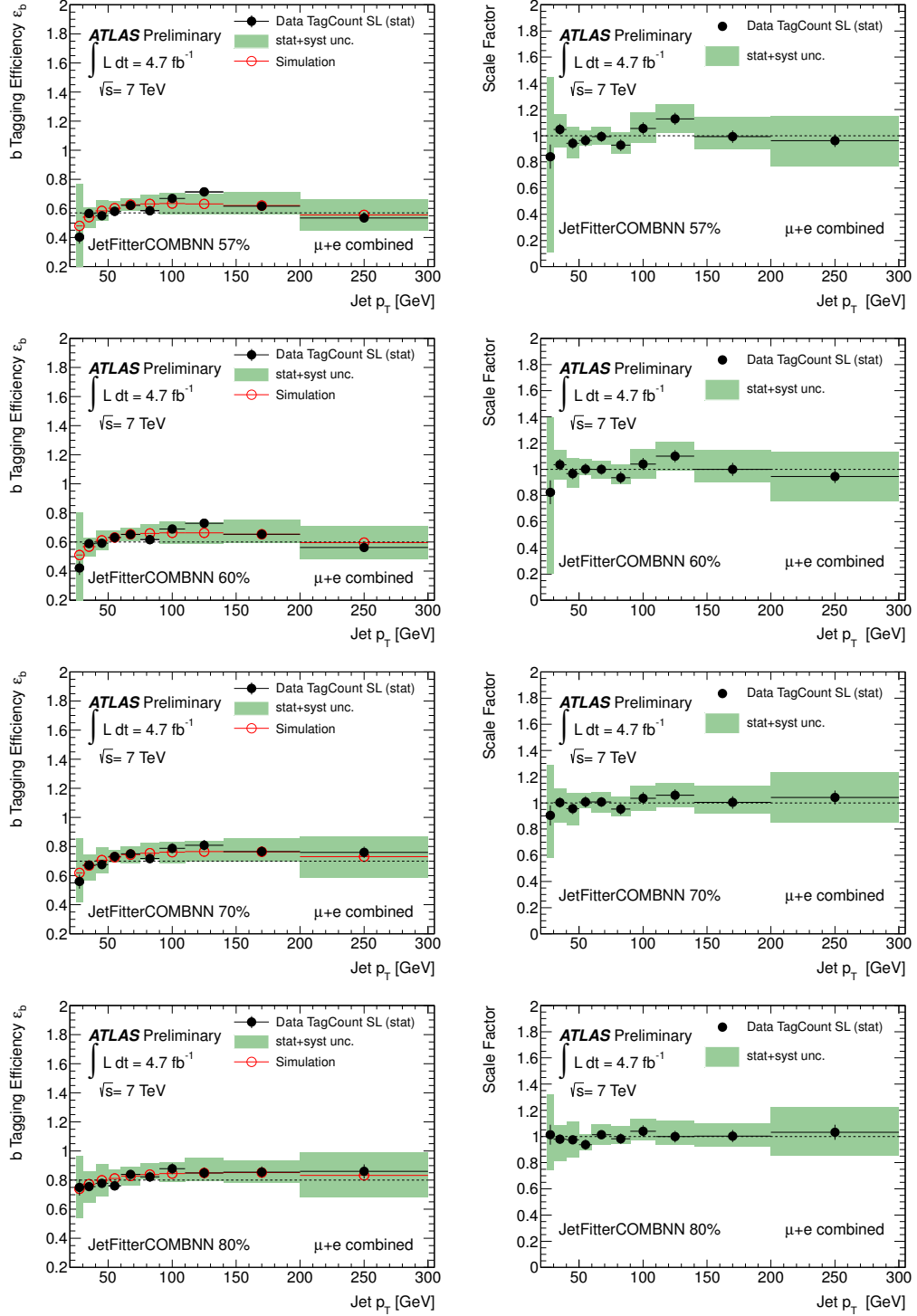


Figure A.9: The b -tagging efficiency in MC and as measured in data for the JetFitterCombNN tagger at the 57% ,60%, 70% and 80% average efficiency working points(left) for the lepton+jets channel. The plots on the right show the scale factor (data/MC) needed to scale the MC b -tagging efficiency to the data [4].

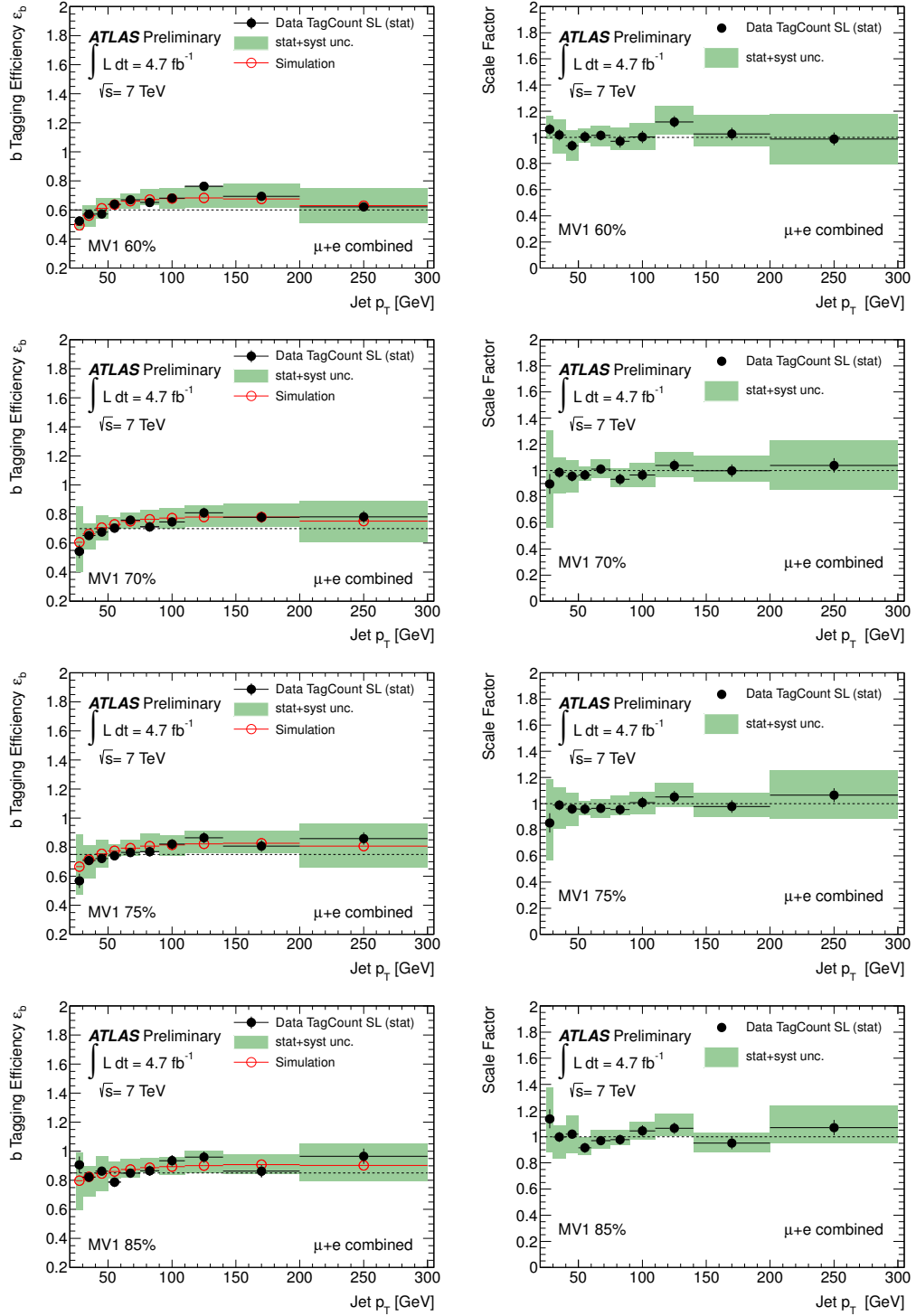


Figure A.10: The b -tagging efficiency in MC and as measured in data for the MV1 tagger at the 60%, 70%, 75% and 85% average efficiency working points (left) for the lepton+jets channel. The plots on the right show the scale factor (data/MC) needed to scale the MC b -tagging efficiency to the data [4].

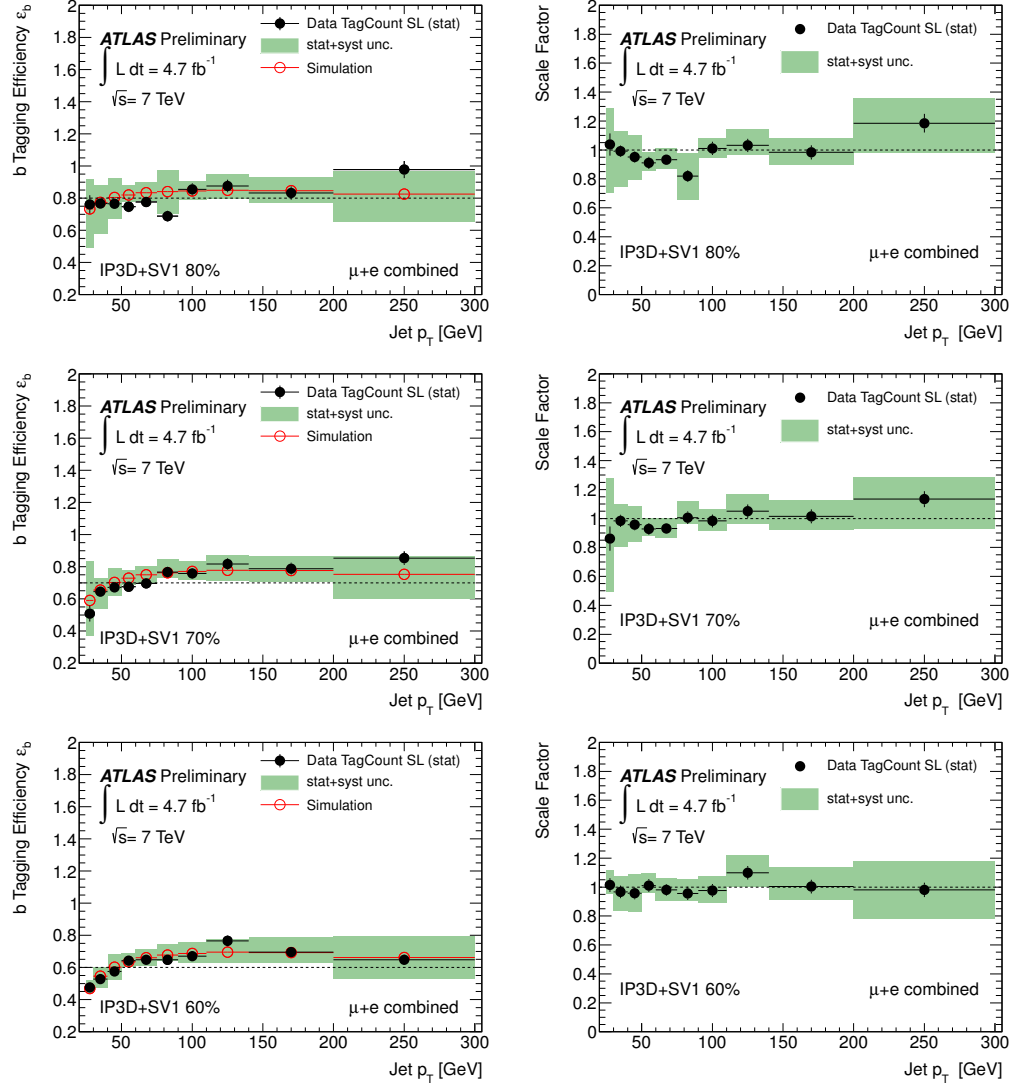


Figure A.11: The b-tagging efficiency in MC and as measured in data for the IP3D+SV1 tagger at the 60%, 70% and 80% average efficiency working points (left) for the lepton+jets channel. The plots on the right show the scale factor (data/MC) needed to scale the MC b -tagging efficiency to the data [4].

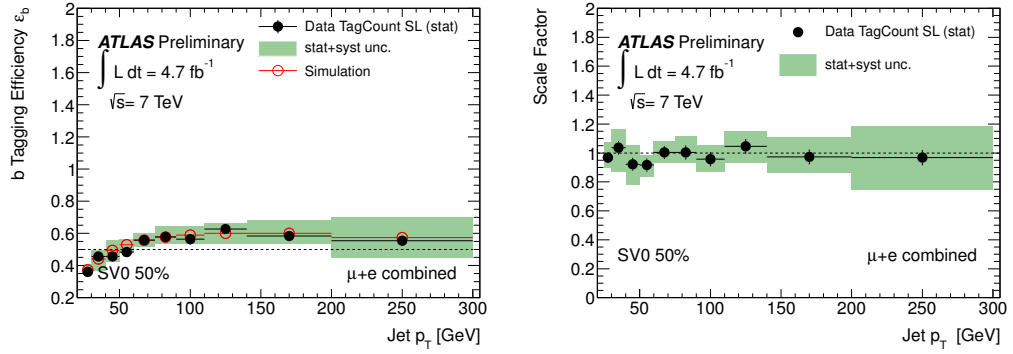


Figure A.12: The b -tagging efficiency in MC and as measured in data for the SV0 tagger at a 50% average efficiency working point (left) for the lepton+jets channel. The plot on the right shows the scale factor (data/MC) needed to scale the MC b -tagging efficiency to the data [4].

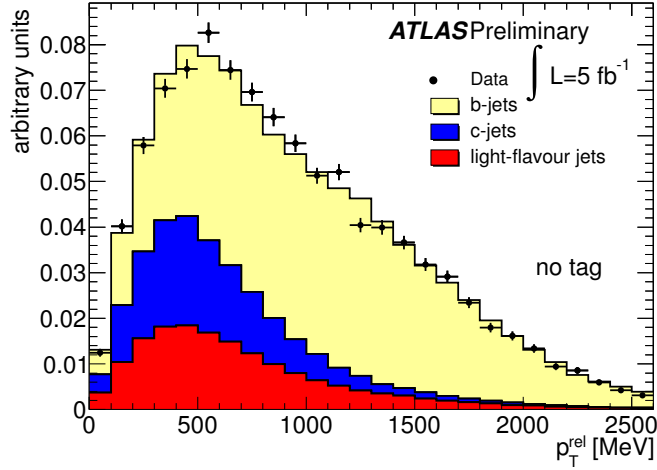


Figure A.13: Distribution of the p_T^{rel} variable for b , c and light jets with p_T between 40 and 50 GeV before any b -tagging selection has been applied for data and Monte Carlo simulation [20].

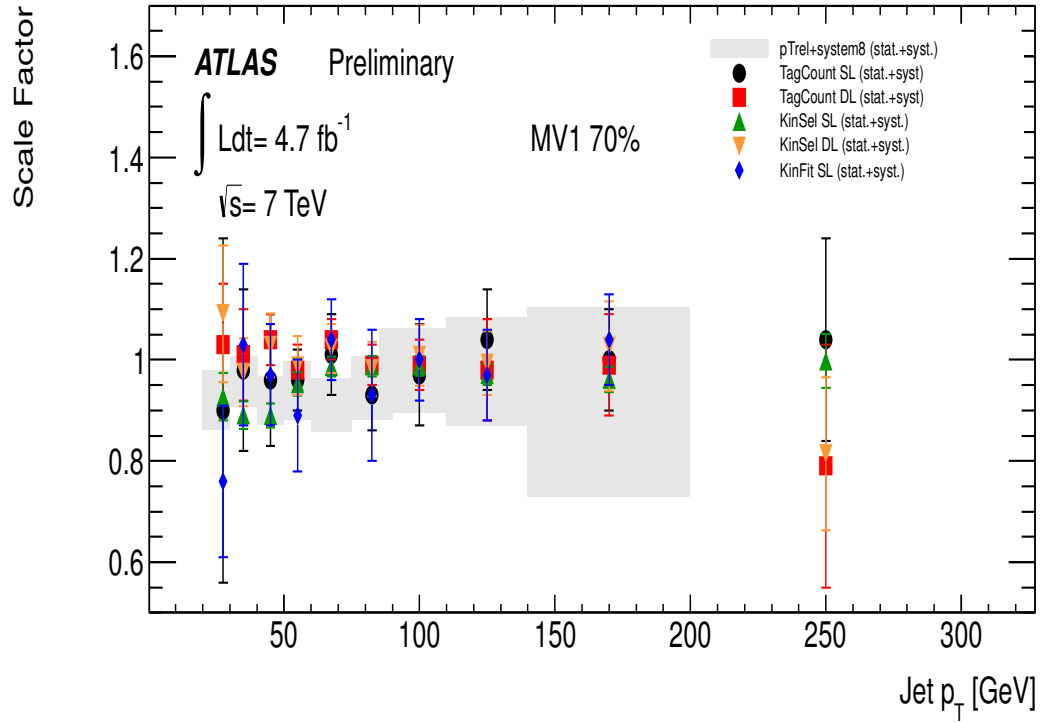


Figure A.14: Scale factors for the muon and $t\bar{t}$ based calibrations as a function of jet p_T [4]. For all methods, the results are consistent with unity and all methods agree within the uncertainties. The muon based calibrations are only valid up to 200 GeV whereas the $t\bar{t}$ based calibrations extend up to 300 GeV.

APPENDIX B

TABLES OF SYSTEMATIC UNCERTAINTIES FOR THE TAG COUNTING METHOD

Complete tables of systematic uncertainties for the e , μ and combined fits for all taggers and working points. Uncertainties have been symmeterized and are relative.

$p_T[GeV]$	25-30	30-40	40-50	50-60	60-75	75-90	90-110	110-140	140-200	200-300
ISR/FSR	± 3.9	± 2.7	± 2.7	± 3.6	± 3.2	± 1.4	± 3.2	± 2.5	± 4.4	± 6.3
Generator	± 0.7	± 5.5	± 0.4	± 0.4	± 5.3	± 1.4	± 4.0	± 0.5	± 0.6	± 2.3
Fragmentation	± 6.4	± 8.1	± 5.4	± 4.9	± 4.4	± 0.5	± 1.0	± 6.9	± 4.8	± 4.5
Diboson	± 2.3	± 2.0	± 0.4	± 0.3	± 0.1	± 0.5	± 0.3	± 0.8	± 0.2	± 0.2
single top	± 3.2	± 2.2	± 0.5	± 0.4	± 0.2	± 0.7	± 0.6	± 1.1	± 0.3	± 0.4
Z + jets	± 2.7	± 1.8	± 0.9	± 0.7	± 1.1	± 0.6	± 0.8	± 0.8	± 0.4	± 1.3
W + jets	± 2.2	± 1.8	± 1.0	± 0.8	± 1.0	± 0.5	± 0.6	± 0.7	± 0.7	± 1.6
Multijets	± 4.2	± 1.3	± 4.8	± 8.8	± 6.6	± 17.9	± 1.3	± 3.3	± 1.5	± 19.1
JES	± 10.7	± 6.6	± 4.9	± 2.5	± 0.9	± 1.2	± 3.4	± 4.7	± 6.0	± 15.7
JER	± 11.2	± 12.2	± 13.5	± 3.2	± 0.5	± 2.6	± 2.4	± 3.2	± 5.3	± 7.2
JRE	± 2.5	± 1.9	± 0.4	± 0.0	± 0.2	± 0.2	± 0.3	± 0.9	± 0.1	± 0.4
JVF	± 10.0	± 1.8	± 0.4	± 0.3	± 0.3	± 8.9	± 0.2	± 0.9	± 0.1	± 1.7
W+HF SF	± 4.0	± 2.9	± 0.6	± 0.6	± 0.3	± 0.9	± 0.5	± 1.4	± 0.5	± 0.5
ε_c	± 4.2	± 2.6	± 2.5	± 2.0	± 2.1	± 1.4	± 2.3	± 2.0	± 2.2	± 2.7
ε_{light}	± 13.6	± 3.5	± 2.2	± 1.8	± 1.4	± 5.5	± 0.8	± 0.9	± 1.1	± 3.2
E_T^{miss} cellout	± 2.6	± 1.8	± 0.6	± 0.3	± 0.2	± 0.8	± 0.1	± 0.8	± 0.2	± 0.8
E_T^{miss} pileup	± 2.9	± 2.0	± 0.7	± 0.3	± 0.1	± 0.6	± 0.4	± 0.9	± 0.1	± 0.5
e trigger	± 2.5	± 2.0	± 0.4	± 0.2	± 0.2	± 0.6	± 0.3	± 1.0	± 0.2	± 0.3
e smearing	± 2.9	± 2.1	± 0.5	± 0.3	± 0.1	± 0.6	± 0.3	± 0.9	± 0.1	± 0.2
e recID	± 2.6	± 1.9	± 0.5	± 0.5	± 0.1	± 0.5	± 0.5	± 0.8	± 0.4	± 0.9
MC e -energy scale	± 2.5	± 1.9	± 0.3	± 0.3	± 0.0	± 0.6	± 0.3	± 0.9	± 0.2	± 0.2
μ trigger	± 2.2	± 1.9	± 0.4	± 0.2	± 0.2	± 0.4	± 0.4	± 0.9	± 0.0	± 0.7
μ smearing	± 0.8	± 0.7	± 0.4	± 0.3	± 0.3	± 0.4	± 0.4	± 0.5	± 0.2	± 0.4
μ recID	± 2.6	± 2.0	± 0.3	± 0.3	± 0.0	± 0.6	± 0.3	± 0.9	± 0.0	± 0.3
MC μ -en. sc.	± 2.2	± 1.7	± 0.5	± 0.3	± 0.1	± 0.5	± 0.0	± 1.0	± 0.3	± 0.2
Lumi	± 2.4	± 1.9	± 0.4	± 0.3	± 0.2	± 0.6	± 0.5	± 0.8	± 1.1	± 3.7
Stat.	± 6.7	± 4.0	± 4.0	± 4.2	± 3.4	± 3.5	± 4.5	± 4.7	± 4.9	± 6.5
Total Syst.	± 27.1	± 19.6	± 16.8	± 11.9	± 10.5	± 21.2	± 7.4	± 10.8	± 10.9	± 26.8
Total	± 27.9	± 20.0	± 17.2	± 12.6	± 11.1	± 21.5	± 8.7	± 11.8	± 12.0	± 27.5

Table B.1: ($\mu+e$ combined). Systematic and statistical uncertainties for the IP3D+SV1 tagger at a working point corresponding to a 80% b -tagging efficiency.

$p_T[GeV]$	25-30	30-40	40-50	50-60	60-75	75-90	90-110	110-140	140-200	200-300
ISR/FSR	± 3.6	± 2.4	± 3.3	± 3.4	± 3.0	± 2.1	± 3.4	± 1.9	± 4.4	± 7.5
Generator	± 3.4	± 2.4	± 0.3	± 0.2	± 5.3	± 0.3	± 4.4	± 2.1	± 0.4	± 2.3
Fragmentation	± 0.2	± 8.6	± 4.5	± 3.7	± 2.7	± 3.4	± 0.7	± 6.2	± 4.1	± 5.0
Diboson	± 0.4	± 0.9	± 0.0	± 0.1	± 0.1	± 0.9	± 0.4	± 0.7	± 0.5	± 0.2
single top	± 0.3	± 1.0	± 0.2	± 0.3	± 0.2	± 1.2	± 0.4	± 1.1	± 0.6	± 0.4
Z + jets	± 1.0	± 0.7	± 0.3	± 0.1	± 0.5	± 1.0	± 0.4	± 0.9	± 0.3	± 0.7
W + jets	± 2.6	± 0.7	± 0.3	± 0.6	± 0.3	± 1.0	± 0.2	± 1.0	± 0.5	± 1.2
Multijets	± 13.4	± 1.7	± 4.0	± 4.7	± 6.8	± 0.6	± 1.5	± 5.3	± 1.7	± 14.0
JES	± 21.6	± 6.6	± 2.7	± 1.2	± 2.7	± 5.4	± 4.2	± 6.3	± 7.6	± 14.9
JER	± 16.4	± 10.3	± 11.1	± 4.7	± 0.3	± 1.1	± 3.1	± 3.9	± 5.3	± 5.9
JRE	± 0.0	± 1.0	± 0.0	± 0.0	± 0.1	± 1.0	± 0.3	± 0.7	± 0.4	± 0.5
JVF	± 17.4	± 0.8	± 0.2	± 0.4	± 0.2	± 1.1	± 0.4	± 0.9	± 0.5	± 2.4
W+HF SF	± 0.7	± 1.3	± 0.3	± 0.3	± 0.2	± 1.7	± 0.6	± 1.4	± 0.7	± 0.5
ε_c	± 3.5	± 2.1	± 1.9	± 1.8	± 2.0	± 1.8	± 1.9	± 1.5	± 1.5	± 2.5
ε_{light}	± 15.2	± 1.6	± 1.6	± 0.8	± 0.6	± 1.0	± 0.6	± 1.0	± 0.6	± 1.9
E_T^{miss} cellout	± 0.3	± 0.8	± 0.2	± 0.2	± 0.1	± 1.2	± 0.2	± 0.9	± 0.4	± 0.3
E_T^{miss} pileup	± 0.4	± 0.9	± 0.1	± 0.3	± 0.1	± 1.0	± 0.3	± 0.8	± 0.6	± 0.3
e trigger	± 0.4	± 1.0	± 0.1	± 0.1	± 0.0	± 1.0	± 0.3	± 0.9	± 0.5	± 0.3
e smearing	± 0.2	± 0.8	± 0.1	± 0.2	± 0.1	± 0.9	± 0.4	± 0.8	± 0.5	± 0.5
e recID	± 1.4	± 1.0	± 0.3	± 0.2	± 0.0	± 0.9	± 0.3	± 0.6	± 0.5	± 0.9
MC e -energy scale	± 0.1	± 0.9	± 0.1	± 0.2	± 0.2	± 1.0	± 0.1	± 0.7	± 0.4	± 0.1
μ trigger	± 0.3	± 0.8	± 0.1	± 0.2	± 0.1	± 1.0	± 0.5	± 0.7	± 0.6	± 0.6
μ smearing	± 0.4	± 0.5	± 0.4	± 0.2	± 0.3	± 0.6	± 0.4	± 0.5	± 0.4	± 0.3
μ recID	± 0.5	± 0.8	± 0.1	± 0.2	± 0.1	± 1.0	± 0.4	± 0.9	± 0.5	± 0.2
MC μ -en. sc.	± 0.9	± 0.8	± 0.1	± 0.1	± 0.1	± 0.8	± 0.3	± 1.0	± 0.8	± 0.3
Lumi	± 3.1	± 1.0	± 0.5	± 0.8	± 0.4	± 0.9	± 0.9	± 1.0	± 1.2	± 3.8
Stat.	± 6.9	± 4.2	± 3.9	± 4.1	± 3.7	± 4.4	± 4.4	± 4.7	± 4.9	± 5.5
Total Syst.	± 38.8	± 16.1	± 13.6	± 8.7	± 10.2	± 8.4	± 8.2	± 12.1	± 11.6	± 23.2
Total	± 39.4	± 16.7	± 14.2	± 9.6	± 10.8	± 9.5	± 9.3	± 13.0	± 12.5	± 23.9

Table B.2: ($\mu+e$ combined). Systematic and statistical uncertainties for the IP3D+SV1 tagger at a working point corresponding to a 70% b -tagging efficiency.

$p_T[GeV]$	25-30	30-40	40-50	50-60	60-75	75-90	90-110	110-140	140-200	200-300
ISR/FSR	± 2.3	± 2.0	± 3.2	± 3.3	± 2.5	± 2.5	± 3.3	± 1.9	± 2.9	± 7.5
Generator	± 3.9	± 1.4	± 0.3	± 1.8	± 5.7	± 0.6	± 5.7	± 2.0	± 2.7	± 1.2
Fragmentation	± 2.3	± 5.3	± 5.0	± 4.8	± 3.9	± 1.6	± 1.2	± 6.4	± 4.2	± 5.4
Diboson	± 0.5	± 0.5	± 0.1	± 0.1	± 0.1	± 0.6	± 0.5	± 0.9	± 0.9	± 0.1
single top	± 0.5	± 0.4	± 0.4	± 0.2	± 0.3	± 0.6	± 0.7	± 1.1	± 1.1	± 0.3
Z + jets	± 1.0	± 0.3	± 0.3	± 0.2	± 0.3	± 0.5	± 0.6	± 1.0	± 0.7	± 0.9
W + jets	± 1.1	± 0.3	± 0.3	± 0.3	± 0.2	± 0.6	± 0.5	± 0.8	± 0.9	± 1.2
Multijets	± 1.7	± 3.2	± 4.0	± 1.1	± 1.8	± 4.1	± 2.3	± 10.2	± 0.6	± 2.3
JES	± 2.6	± 4.9	± 1.9	± 2.0	± 3.2	± 6.6	± 5.2	± 7.2	± 8.5	± 18.1
JER	± 2.0	± 9.4	± 11.9	± 4.5	± 1.0	± 1.6	± 3.7	± 3.8	± 4.2	± 4.3
JRE	± 0.9	± 0.5	± 0.2	± 0.1	± 0.2	± 0.6	± 0.8	± 0.7	± 0.7	± 0.4
JVF	± 1.9	± 0.3	± 0.3	± 0.2	± 0.1	± 0.6	± 0.8	± 1.0	± 1.0	± 2.6
W+HF SF	± 0.9	± 0.7	± 0.4	± 0.2	± 0.4	± 0.8	± 0.9	± 1.4	± 1.3	± 0.6
ε_c	± 2.9	± 1.8	± 2.0	± 1.5	± 2.3	± 1.5	± 1.7	± 1.4	± 1.3	± 2.1
ε_{light}	± 1.3	± 0.9	± 0.6	± 0.2	± 0.4	± 0.5	± 0.8	± 0.9	± 0.9	± 1.4
E_T^{miss} cellout	± 0.4	± 0.4	± 0.5	± 0.3	± 0.1	± 0.6	± 0.6	± 0.7	± 0.9	± 0.2
E_T^{miss} pileup	± 0.5	± 0.4	± 0.3	± 0.1	± 0.3	± 0.5	± 0.4	± 0.7	± 0.9	± 0.3
e trigger	± 0.5	± 0.7	± 0.3	± 0.0	± 0.2	± 0.5	± 0.5	± 1.0	± 1.0	± 0.2
e smearing	± 0.5	± 0.5	± 0.3	± 0.1	± 0.1	± 0.7	± 0.5	± 1.1	± 0.7	± 0.5
e recID	± 1.1	± 0.4	± 0.4	± 0.3	± 0.2	± 0.5	± 0.6	± 0.8	± 0.8	± 1.0
MC e -energy scale	± 0.5	± 0.4	± 0.2	± 0.1	± 0.1	± 0.4	± 0.7	± 0.8	± 0.7	± 0.1
μ trigger	± 0.8	± 0.4	± 0.2	± 0.2	± 0.3	± 0.5	± 0.5	± 0.9	± 1.0	± 0.5
μ smearing	± 0.4	± 0.4	± 0.3	± 0.3	± 0.3	± 0.4	± 0.5	± 0.5	± 0.5	± 0.2
μ recID	± 0.5	± 0.5	± 0.3	± 0.1	± 0.2	± 0.5	± 0.5	± 0.8	± 0.8	± 0.2
MC μ -en. sc.	± 0.6	± 0.4	± 0.6	± 0.1	± 0.2	± 0.3	± 0.5	± 0.9	± 1.1	± 0.1
Lumi	± 3.5	± 1.2	± 0.8	± 1.0	± 0.5	± 1.0	± 1.4	± 1.3	± 1.9	± 3.6
Stat.	± 4.7	± 4.4	± 4.2	± 4.4	± 4.0	± 4.6	± 4.5	± 4.7	± 4.7	± 4.9
Total Syst.	± 8.5	± 12.9	± 14.3	± 8.1	± 8.6	± 9.0	± 10.1	± 15.4	± 11.9	± 21.3
Total	± 9.7	± 13.6	± 14.9	± 9.3	± 9.5	± 10.1	± 11.1	± 16.1	± 12.8	± 21.8

Table B.3: ($\mu+e$ combined). Systematic and statistical uncertainties for the IP3D+SV1 tagger at a working point corresponding to a 60% b -tagging efficiency.

$p_T [GeV]$	25-30	30-40	40-50	50-60	60-75	75-90	90-110	110-140	140-200	200-300
ISR/FSR	± 3.6	± 2.1	± 3.1	± 3.7	± 3.5	± 2.8	± 3.8	± 1.9	± 4.4	± 7.4
Generator	± 3.2	± 2.5	± 0.2	± 1.2	± 6.5	± 0.6	± 7.1	± 0.2	± 0.8	± 0.7
Fragmentation	± 4.3	± 6.8	± 3.5	± 4.0	± 2.4	± 5.3	± 2.2	± 3.3	± 3.2	± 4.0
Diboson	± 0.8	± 0.4	± 0.0	± 0.3	± 0.3	± 0.2	± 0.4	± 0.4	± 0.8	± 0.1
single top	± 1.1	± 0.4	± 0.2	± 0.3	± 0.3	± 0.5	± 0.3	± 0.6	± 1.0	± 0.3
Z + jets	± 1.0	± 0.3	± 0.3	± 0.2	± 0.5	± 0.5	± 0.3	± 0.4	± 0.9	± 0.6
W + jets	± 2.7	± 0.3	± 0.4	± 0.3	± 0.4	± 0.5	± 0.1	± 0.4	± 1.0	± 0.9
Multijets	± 9.2	± 2.0	± 4.2	± 3.4	± 1.0	± 4.6	± 3.7	± 6.0	± 0.7	± 4.4
JES	± 20.2	± 5.3	± 2.7	± 1.1	± 2.7	± 6.0	± 4.4	± 7.2	± 7.9	± 17.7
JER	± 7.4	± 10.2	± 11.4	± 4.0	± 1.8	± 1.9	± 3.2	± 4.2	± 4.4	± 4.2
JRE	± 1.5	± 0.5	± 0.0	± 0.2	± 0.3	± 0.0	± 0.2	± 0.2	± 0.7	± 0.1
JVF	± 16.0	± 0.3	± 0.1	± 0.1	± 0.2	± 0.4	± 0.3	± 0.5	± 0.8	± 2.4
W+HF SF	± 1.3	± 0.5	± 0.3	± 0.4	± 0.5	± 0.5	± 0.4	± 0.7	± 1.5	± 0.6
ε_c	± 3.0	± 1.8	± 2.0	± 1.6	± 1.8	± 1.5	± 2.1	± 1.2	± 1.4	± 2.1
ε_{light}	± 16.6	± 0.6	± 0.3	± 0.5	± 0.5	± 0.7	± 0.2	± 0.4	± 0.7	± 1.2
E_T^{miss} cellout	± 0.6	± 0.2	± 0.4	± 0.4	± 0.3	± 0.3	± 0.1	± 0.5	± 0.9	± 0.2
E_T^{miss} pileup	± 0.9	± 0.4	± 0.2	± 0.1	± 0.4	± 0.3	± 0.5	± 0.4	± 0.7	± 0.2
e trigger	± 1.0	± 0.3	± 0.2	± 0.4	± 0.3	± 0.4	± 0.2	± 0.5	± 0.9	± 0.2
e smearing	± 0.4	± 0.1	± 0.2	± 0.3	± 0.3	± 0.3	± 0.1	± 0.5	± 0.8	± 0.3
e recID	± 1.3	± 0.2	± 0.3	± 0.3	± 0.3	± 0.3	± 0.4	± 0.5	± 0.9	± 0.9
MC e -energy scale	± 0.5	± 0.3	± 0.1	± 0.3	± 0.2	± 0.2	± 0.1	± 0.6	± 1.0	± 0.2
μ trigger	± 0.8	± 0.4	± 0.1	± 0.2	± 0.3	± 0.3	± 0.3	± 0.7	± 1.0	± 0.7
μ smearing	± 0.6	± 0.3	± 0.3	± 0.2	± 0.2	± 0.3	± 0.3	± 0.4	± 0.5	± 0.4
μ recID	± 0.8	± 0.3	± 0.0	± 0.2	± 0.2	± 0.3	± 0.2	± 0.6	± 0.9	± 0.3
MC μ -en. sc.	± 1.0	± 0.2	± 0.0	± 0.2	± 0.3	± 0.2	± 0.3	± 0.4	± 0.9	± 0.1
Lumi	± 2.7	± 0.7	± 0.5	± 0.8	± 0.4	± 0.7	± 0.8	± 1.4	± 1.4	± 3.5
Stat.	± 6.5	± 4.1	± 4.2	± 4.3	± 3.7	± 4.4	± 4.6	± 4.7	± 4.8	± 5.2
Total Syst.	± 34.0	± 14.1	± 13.5	± 8.0	± 8.8	± 10.1	± 10.9	± 11.3	± 11.4	± 20.8
Total	± 34.6	± 14.7	± 14.1	± 9.1	± 9.5	± 11.0	± 11.9	± 12.2	± 12.4	± 21.4

Table B.4: ($\mu+e$ combined). Systematic and statistical uncertainties for the JetFitterCOMBNN tagger at a working point corresponding to a 70% b -tagging efficiency.

$p_T[GeV]$	25-30	30-40	40-50	50-60	60-75	75-90	90-110	110-140	140-200	200-300
ISR/FSR	± 3.9	± 2.9	± 3.2	± 3.5	± 3.1	± 1.7	± 3.0	± 1.9	± 4.5	± 6.0
Generator	± 5.2	± 3.5	± 0.1	± 0.1	± 6.7	± 0.3	± 5.6	± 1.3	± 0.3	± 1.2
Fragmentation	± 4.0	± 7.4	± 4.5	± 4.6	± 2.1	± 3.3	± 1.5	± 7.4	± 3.7	± 2.3
Diboson	± 0.1	± 0.3	± 0.1	± 0.2	± 0.0	± 0.9	± 0.4	± 0.9	± 0.0	± 0.1
single top	± 0.5	± 0.5	± 0.2	± 0.4	± 0.3	± 1.1	± 0.5	± 1.3	± 0.2	± 0.4
Z + jets	± 0.5	± 0.6	± 0.6	± 0.5	± 0.6	± 0.8	± 0.3	± 0.9	± 0.3	± 0.9
W + jets	± 1.6	± 1.1	± 0.7	± 0.6	± 0.7	± 1.1	± 0.5	± 0.9	± 0.3	± 1.4
Multijets	± 1.5	± 2.0	± 2.4	± 4.0	± 1.6	± 1.6	± 4.2	± 0.1	± 0.5	± 3.5
JES	± 13.4	± 4.5	± 4.2	± 1.3	± 2.4	± 4.4	± 4.2	± 5.2	± 6.5	± 16.6
JER	± 9.3	± 10.0	± 12.1	± 3.9	± 0.3	± 0.0	± 1.6	± 3.3	± 4.5	± 5.1
JRE	± 0.2	± 0.5	± 0.0	± 0.2	± 0.0	± 0.6	± 0.4	± 0.6	± 0.2	± 0.3
JVF	± 10.2	± 0.3	± 0.2	± 0.4	± 0.2	± 1.0	± 0.4	± 0.8	± 0.2	± 2.1
W+HF SF	± 0.6	± 0.7	± 0.3	± 0.6	± 0.2	± 1.5	± 0.7	± 1.3	± 0.3	± 0.3
ε_c	± 3.4	± 2.9	± 2.6	± 2.1	± 1.8	± 1.6	± 2.3	± 1.5	± 2.0	± 2.0
ε_{light}	± 11.7	± 2.3	± 1.7	± 1.1	± 0.7	± 1.0	± 0.6	± 1.0	± 0.4	± 2.7
E_T^{miss} cellout	± 0.2	± 0.3	± 0.2	± 0.4	± 0.1	± 0.9	± 0.4	± 1.0	± 0.3	± 0.2
E_T^{miss} pileup	± 0.2	± 0.5	± 0.1	± 0.3	± 0.1	± 0.9	± 0.4	± 0.9	± 0.1	± 0.3
e trigger	± 0.4	± 0.4	± 0.1	± 0.2	± 0.1	± 0.9	± 0.3	± 1.0	± 0.1	± 0.2
e smearing	± 0.4	± 0.3	± 0.1	± 0.3	± 0.1	± 1.0	± 0.6	± 0.9	± 0.2	± 0.5
e recID	± 0.8	± 0.5	± 0.2	± 0.3	± 0.0	± 1.0	± 0.4	± 1.0	± 0.3	± 0.9
MC e -energy scale	± 0.2	± 0.6	± 0.1	± 0.4	± 0.1	± 1.0	± 0.3	± 0.8	± 0.1	± 0.4
μ trigger	± 0.2	± 0.3	± 0.1	± 0.2	± 0.1	± 0.8	± 0.5	± 0.7	± 0.4	± 0.5
μ smearing	± 0.5	± 0.4	± 0.3	± 0.3	± 0.2	± 0.5	± 0.4	± 0.5	± 0.3	± 0.4
μ recID	± 0.2	± 0.6	± 0.2	± 0.3	± 0.1	± 0.7	± 0.5	± 0.8	± 0.1	± 0.2
MC μ -en. sc.	± 0.2	± 0.3	± 0.0	± 0.1	± 0.2	± 1.1	± 0.4	± 0.9	± 0.3	± 0.2
Lumi	± 2.1	± 0.4	± 0.4	± 0.4	± 0.1	± 0.8	± 0.5	± 0.9	± 1.1	± 3.1
Stat.	± 6.3	± 3.8	± 3.6	± 4.0	± 3.4	± 4.1	± 4.4	± 4.5	± 4.7	± 5.7
Total Syst.	± 24.2	± 14.7	± 14.5	± 8.7	± 8.5	± 7.4	± 9.5	± 10.8	± 10.2	± 19.0
Total	± 25.1	± 15.2	± 15.0	± 9.6	± 9.1	± 8.5	± 10.4	± 11.7	± 11.2	± 19.9

Table B.5: ($\mu+e$ combined). Systematic and statistical uncertainties for the JetFitterCOMBNN tagger at a working point corresponding to a 80% b -tagging efficiency.

$p_T[GeV]$	25-30	30-40	40-50	50-60	60-75	75-90	90-110	110-140	140-200	200-300
ISR/FSR	± 2.8	± 1.7	± 3.7	± 3.7	± 3.8	± 2.7	± 3.5	± 1.9	± 3.5	± 7.5
Generator	± 5.2	± 2.0	± 0.5	± 1.3	± 5.1	± 0.8	± 7.7	± 0.3	± 2.2	± 0.8
Fragmentation	± 1.9	± 3.8	± 4.3	± 5.0	± 1.9	± 2.9	± 3.5	± 4.3	± 3.4	± 3.2
Diboson	± 1.4	± 0.2	± 0.0	± 0.3	± 0.4	± 0.4	± 0.1	± 0.6	± 0.9	± 0.1
single top	± 1.7	± 0.2	± 0.2	± 0.5	± 0.4	± 0.5	± 0.4	± 0.9	± 1.2	± 0.4
Z + jets	± 1.6	± 0.1	± 0.0	± 0.3	± 0.4	± 0.7	± 0.2	± 0.5	± 1.0	± 0.8
W + jets	± 3.5	± 0.1	± 0.2	± 0.4	± 0.4	± 0.3	± 0.5	± 0.9	± 0.7	± 1.0
Multijets	± 17.3	± 1.9	± 3.1	± 0.1	± 0.9	± 6.2	± 4.1	± 10.3	± 0.2	± 5.4
JES	± 27.9	± 4.3	± 1.6	± 1.7	± 3.0	± 6.3	± 6.0	± 8.2	± 9.8	± 17.3
JER	± 22.8	± 9.3	± 10.2	± 3.5	± 1.1	± 2.1	± 4.0	± 4.8	± 4.0	± 3.3
JRE	± 1.7	± 0.2	± 0.2	± 0.5	± 0.2	± 0.4	± 0.3	± 0.4	± 1.0	± 0.2
JVF	± 22.2	± 0.5	± 0.1	± 0.3	± 0.3	± 0.6	± 0.4	± 0.8	± 0.9	± 3.1
W+HF SF	± 2.3	± 0.3	± 0.3	± 0.7	± 0.7	± 0.8	± 0.6	± 1.1	± 1.6	± 0.5
ε_c	± 2.6	± 1.5	± 1.8	± 1.4	± 1.9	± 1.4	± 2.0	± 1.3	± 1.5	± 2.4
ε_{light}	± 34.4	± 0.4	± 0.3	± 0.3	± 0.4	± 0.6	± 0.4	± 0.7	± 0.9	± 1.0
E_T^{miss} cellout	± 1.4	± 0.1	± 0.3	± 0.2	± 0.4	± 0.5	± 0.2	± 0.6	± 0.9	± 0.3
E_T^{miss} pileup	± 1.3	± 0.2	± 0.1	± 0.3	± 0.2	± 0.5	± 0.3	± 0.8	± 0.9	± 0.4
e trigger	± 1.5	± 0.1	± 0.0	± 0.5	± 0.4	± 0.4	± 0.3	± 0.5	± 0.8	± 0.3
e smearing	± 1.0	± 0.2	± 0.1	± 0.4	± 0.3	± 0.4	± 0.4	± 0.7	± 1.1	± 0.3
e recID	± 2.1	± 0.5	± 0.2	± 0.2	± 0.3	± 0.6	± 0.4	± 0.6	± 0.8	± 1.3
MC e -energy scale	± 1.2	± 0.1	± 0.1	± 0.4	± 0.5	± 0.3	± 0.3	± 0.6	± 0.9	± 0.1
μ trigger	± 1.6	± 0.4	± 0.2	± 0.3	± 0.5	± 0.4	± 0.3	± 0.5	± 0.9	± 0.6
μ smearing	± 0.6	± 0.4	± 0.2	± 0.4	± 0.3	± 0.4	± 0.4	± 0.4	± 0.5	± 0.3
μ recID	± 1.3	± 0.2	± 0.1	± 0.4	± 0.5	± 0.5	± 0.5	± 0.5	± 1.0	± 0.4
MC μ -en. sc.	± 1.3	± 0.1	± 0.0	± 0.5	± 0.3	± 0.5	± 0.2	± 0.8	± 1.0	± 0.1
Lumi	± 3.5	± 1.1	± 0.8	± 1.0	± 0.6	± 1.3	± 1.3	± 1.4	± 2.0	± 3.8
Stat.	± 7.3	± 4.4	± 4.3	± 4.4	± 4.0	± 4.5	± 4.6	± 4.7	± 5.0	± 4.8
Total Syst.	± 58.1	± 11.7	± 12.4	± 7.8	± 7.9	± 10.4	± 12.7	± 15.1	± 12.8	± 20.7
Total	± 58.6	± 12.4	± 13.1	± 9.0	± 8.9	± 11.3	± 13.5	± 15.8	± 13.8	± 21.3

Table B.6: ($\mu+e$ combined). Systematic and statistical uncertainties for the JetFitterCOMBNN tagger at a working point corresponding to a 60% b -tagging efficiency.

$p_T[GeV]$	25-30	30-40	40-50	50-60	60-75	75-90	90-110	110-140	140-200	200-300
ISR/FSR	± 2.7	± 2.3	± 4.0	± 3.6	± 3.6	± 2.6	± 3.8	± 2.0	± 3.5	± 7.2
Generator	± 5.7	± 3.0	± 1.3	± 1.3	± 4.7	± 0.8	± 7.8	± 0.2	± 1.8	± 0.5
Fragmentation	± 2.6	± 5.1	± 5.6	± 4.5	± 2.8	± 3.0	± 2.8	± 4.7	± 4.0	± 3.5
Diboson	± 1.6	± 0.5	± 0.1	± 0.3	± 0.1	± 0.3	± 0.5	± 0.5	± 0.9	± 0.1
single top	± 1.7	± 0.5	± 0.1	± 0.2	± 0.2	± 0.3	± 0.5	± 0.5	± 1.2	± 0.4
Z + jets	± 1.6	± 0.4	± 0.1	± 0.2	± 0.2	± 0.1	± 0.4	± 0.6	± 0.9	± 0.8
W + jets	± 3.7	± 0.3	± 0.2	± 0.4	± 0.2	± 0.1	± 0.3	± 0.2	± 1.1	± 0.9
Multijets	± 15.7	± 5.0	± 5.7	± 3.4	± 1.8	± 7.1	± 5.7	± 13.2	± 0.7	± 3.6
JES	± 29.0	± 4.2	± 1.4	± 2.0	± 3.6	± 6.8	± 6.6	± 8.4	± 10.0	± 17.5
JER	± 24.5	± 10.4	± 10.7	± 3.5	± 1.0	± 3.1	± 3.9	± 4.7	± 3.9	± 2.9
JRE	± 1.5	± 0.3	± 0.3	± 0.2	± 0.1	± 0.1	± 0.6	± 0.0	± 1.0	± 0.2
JVF	± 23.5	± 0.4	± 0.1	± 0.3	± 0.2	± 0.3	± 0.4	± 0.7	± 0.8	± 3.4
W+HF SF	± 2.5	± 0.5	± 0.3	± 0.5	± 0.3	± 0.4	± 0.7	± 0.7	± 1.6	± 0.4
ε_c	± 2.3	± 1.7	± 1.8	± 1.4	± 2.0	± 1.5	± 2.2	± 1.5	± 1.6	± 2.3
ε_{light}	± 41.6	± 0.3	± 0.1	± 0.2	± 0.2	± 0.1	± 0.1	± 0.4	± 0.8	± 1.5
E_T^{miss} cellout	± 1.6	± 0.3	± 0.2	± 0.2	± 0.2	± 0.2	± 0.3	± 0.5	± 1.0	± 0.3
E_T^{miss} pileup	± 1.3	± 0.3	± 0.1	± 0.3	± 0.1	± 0.3	± 0.3	± 0.6	± 0.9	± 0.3
e trigger	± 1.4	± 0.3	± 0.2	± 0.2	± 0.2	± 0.2	± 0.5	± 0.4	± 1.1	± 0.3
e smearing	± 1.7	± 0.3	± 0.2	± 0.5	± 0.2	± 0.1	± 0.5	± 0.3	± 1.1	± 0.6
e recID	± 1.6	± 0.5	± 0.3	± 0.3	± 0.1	± 0.3	± 0.5	± 0.7	± 1.0	± 1.2
MC e -energy scale	± 1.7	± 0.5	± 0.1	± 0.3	± 0.1	± 0.2	± 0.3	± 0.5	± 1.0	± 0.3
μ trigger	± 1.3	± 0.3	± 0.1	± 0.2	± 0.3	± 0.1	± 0.3	± 0.5	± 1.0	± 0.9
μ smearing	± 0.6	± 0.4	± 0.4	± 0.3	± 0.2	± 0.2	± 0.3	± 0.3	± 0.5	± 0.3
μ recID	± 1.5	± 0.5	± 0.3	± 0.0	± 0.2	± 0.2	± 0.4	± 0.4	± 1.0	± 0.3
MC μ -en. sc.	± 1.6	± 0.4	± 0.0	± 0.2	± 0.1	± 0.2	± 0.3	± 0.3	± 0.9	± 0.2
Lumi	± 3.6	± 1.1	± 0.8	± 1.1	± 0.7	± 1.3	± 1.5	± 1.7	± 2.0	± 3.8
Stat.	± 7.3	± 4.4	± 4.2	± 4.5	± 4.0	± 4.5	± 4.7	± 4.6	± 4.8	± 4.7
Total Syst.	± 63.9	± 14.1	± 14.2	± 8.2	± 8.1	± 11.3	± 13.6	± 17.4	± 13.1	± 20.6
Total	± 64.3	± 14.7	± 14.8	± 9.4	± 9.0	± 12.2	± 14.4	± 18.0	± 13.9	± 21.1

Table B.7: ($\mu+e$ combined). Systematic and statistical uncertainties for the JetFitterCOMBNN tagger at a working point corresponding to a 57% b -tagging efficiency.

$p_T[GeV]$	25-30	30-40	40-50	50-60	60-75	75-90	90-110	110-140	140-200	200-300
ISR/FSR	± 4.4	± 3.3	± 2.5	± 3.4	± 2.3	± 1.8	± 2.5	± 1.5	± 3.4	± 3.5
Generator	± 0.9	± 4.6	± 0.1	± 0.3	± 6.1	± 0.4	± 4.8	± 0.6	± 0.8	± 0.1
Fragmentation	± 6.4	± 7.3	± 3.2	± 5.6	± 1.4	± 4.3	± 1.3	± 5.5	± 2.8	± 2.6
Diboson	± 1.2	± 0.7	± 0.2	± 0.2	± 0.3	± 0.4	± 0.4	± 1.0	± 0.3	± 0.1
single top	± 1.6	± 0.9	± 0.3	± 0.2	± 0.5	± 0.4	± 0.4	± 1.3	± 0.4	± 0.6
Z + jets	± 1.1	± 1.2	± 1.0	± 0.8	± 1.0	± 0.3	± 0.7	± 1.0	± 0.3	± 1.1
W + jets	± 1.4	± 1.1	± 1.4	± 0.9	± 1.1	± 0.8	± 0.9	± 1.1	± 0.8	± 1.2
Multijets	± 13.7	± 1.5	± 2.0	± 8.4	± 2.8	± 2.1	± 4.7	± 6.7	± 4.8	± 7.4
JES	± 8.7	± 4.3	± 5.5	± 1.9	± 1.4	± 3.9	± 3.0	± 4.5	± 5.0	± 11.2
JER	± 13.6	± 6.3	± 12.2	± 4.6	± 0.6	± 0.9	± 1.3	± 2.7	± 3.8	± 5.3
JRE	± 0.4	± 0.4	± 0.3	± 0.1	± 0.3	± 0.1	± 0.2	± 0.9	± 0.1	± 0.1
JVF	± 7.1	± 1.8	± 0.7	± 0.2	± 0.3	± 0.6	± 0.3	± 1.0	± 0.2	± 1.2
W+HF SF	± 1.9	± 1.3	± 0.5	± 0.3	± 0.6	± 0.5	± 0.6	± 1.7	± 0.6	± 0.3
ε_c	± 3.1	± 2.6	± 2.4	± 1.8	± 2.2	± 2.0	± 2.0	± 1.9	± 2.3	± 2.9
ε_{light}	± 10.7	± 4.4	± 1.5	± 1.4	± 1.0	± 1.1	± 0.8	± 1.0	± 0.9	± 3.7
E_T^{miss} cellout	± 1.2	± 0.7	± 0.3	± 0.2	± 0.2	± 0.2	± 0.4	± 1.0	± 0.2	± 0.2
E_T^{miss} pileup	± 1.1	± 0.8	± 0.3	± 0.2	± 0.2	± 0.2	± 0.4	± 0.9	± 0.1	± 0.3
e trigger	± 1.2	± 0.8	± 0.2	± 0.1	± 0.5	± 0.1	± 0.3	± 0.9	± 0.2	± 0.4
e smearing	± 1.5	± 0.7	± 0.3	± 0.1	± 0.3	± 0.2	± 0.3	± 0.9	± 0.2	± 0.2
e recID	± 1.2	± 0.7	± 0.1	± 0.1	± 0.4	± 0.2	± 0.2	± 1.0	± 0.2	± 0.5
MC e -energy scale	± 1.3	± 0.7	± 0.3	± 0.0	± 0.4	± 0.3	± 0.4	± 1.0	± 0.2	± 0.2
μ trigger	± 1.1	± 0.9	± 0.3	± 0.1	± 0.4	± 0.1	± 0.4	± 0.8	± 0.3	± 0.4
μ smearing	± 0.6	± 0.5	± 0.3	± 0.4	± 0.4	± 0.3	± 0.3	± 0.5	± 0.3	± 0.4
μ recID	± 1.2	± 0.7	± 0.1	± 0.1	± 0.4	± 0.2	± 0.3	± 0.9	± 0.3	± 0.1
MC μ -en. sc.	± 0.9	± 0.6	± 0.2	± 0.0	± 0.2	± 0.1	± 0.4	± 1.0	± 0.1	± 0.3
Lumi	± 1.9	± 0.9	± 0.2	± 0.1	± 0.3	± 0.3	± 0.2	± 1.2	± 0.7	± 2.9
Stat.	± 6.5	± 3.7	± 3.6	± 3.9	± 3.3	± 4.0	± 4.3	± 4.4	± 4.6	± 5.7
Total Syst.	± 26.7	± 13.7	± 14.6	± 12.0	± 8.1	± 7.1	± 8.4	± 11.3	± 9.5	± 15.3
Total	± 27.4	± 14.2	± 15.0	± 12.6	± 8.7	± 8.1	± 9.5	± 12.2	± 10.6	± 16.3

Table B.8: ($\mu+e$ combined). Systematic and statistical uncertainties for the MV1 tagger at a working point corresponding to a 85% b -tagging efficiency.

$p_T [GeV]$	25-30	30-40	40-50	50-60	60-75	75-90	90-110	110-140	140-200	200-300
ISR/FSR	± 3.6	± 2.8	± 2.8	± 3.3	± 2.9	± 2.2	± 3.6	± 1.7	± 4.4	± 6.9
Generator	± 3.5	± 2.8	± 0.8	± 0.9	± 6.1	± 0.2	± 6.2	± 1.3	± 0.4	± 1.2
Fragmentation	± 3.6	± 9.0	± 3.1	± 3.3	± 2.0	± 3.0	± 3.1	± 5.0	± 4.2	± 4.4
Diboson	± 0.2	± 0.4	± 0.4	± 0.1	± 0.2	± 0.9	± 0.1	± 0.6	± 0.7	± 0.2
single top	± 0.5	± 0.5	± 0.5	± 0.1	± 0.2	± 0.9	± 0.2	± 0.8	± 0.8	± 0.4
Z + jets	± 0.5	± 0.5	± 0.4	± 0.3	± 0.5	± 1.0	± 0.2	± 0.7	± 0.6	± 0.7
W + jets	± 2.2	± 0.5	± 0.4	± 0.3	± 0.5	± 0.9	± 0.2	± 0.7	± 0.3	± 0.8
Multijets	± 14.5	± 2.1	± 3.9	± 3.5	± 3.5	± 4.4	± 0.8	± 5.3	± 2.1	± 6.9
JES	± 17.8	± 5.8	± 3.5	± 0.6	± 2.3	± 5.9	± 4.0	± 6.2	± 6.8	± 16.9
JER	± 9.0	± 12.3	± 11.2	± 4.0	± 0.7	± 0.0	± 3.1	± 4.0	± 4.2	± 4.6
JRE	± 0.4	± 0.5	± 0.5	± 0.1	± 0.3	± 0.7	± 0.3	± 0.4	± 0.3	± 0.2
JVF	± 14.2	± 0.4	± 0.3	± 0.1	± 0.2	± 0.7	± 0.2	± 0.7	± 0.6	± 2.0
W+HF SF	± 0.8	± 0.7	± 0.6	± 0.3	± 0.3	± 1.4	± 0.3	± 1.0	± 0.9	± 0.4
ε_c	± 3.4	± 2.3	± 1.9	± 1.7	± 1.8	± 1.5	± 1.9	± 1.4	± 1.5	± 2.4
ε_{light}	± 12.2	± 1.5	± 0.8	± 0.7	± 0.7	± 0.8	± 0.5	± 0.7	± 0.7	± 1.3
E_T^{miss} cellout	± 0.3	± 0.4	± 0.4	± 0.1	± 0.1	± 0.7	± 0.1	± 0.4	± 0.4	± 0.2
E_T^{miss} pileup	± 0.7	± 0.5	± 0.2	± 0.0	± 0.2	± 0.8	± 0.2	± 0.8	± 0.5	± 0.4
e trigger	± 0.3	± 0.4	± 0.3	± 0.2	± 0.2	± 0.7	± 0.2	± 0.8	± 0.5	± 0.1
e smearing	± 0.6	± 0.3	± 0.2	± 0.2	± 0.1	± 0.8	± 0.1	± 0.9	± 0.5	± 0.2
e recID	± 1.1	± 0.4	± 0.3	± 0.1	± 0.2	± 0.7	± 0.2	± 0.7	± 0.6	± 1.1
MC e -energy scale	± 0.4	± 0.4	± 0.3	± 0.2	± 0.1	± 0.7	± 0.1	± 0.6	± 0.5	± 0.2
μ trigger	± 0.3	± 0.5	± 0.4	± 0.2	± 0.1	± 0.5	± 0.2	± 0.8	± 0.4	± 0.6
μ smearing	± 0.8	± 0.4	± 0.3	± 0.3	± 0.3	± 0.5	± 0.4	± 0.5	± 0.5	± 0.3
μ recID	± 0.2	± 0.5	± 0.3	± 0.1	± 0.0	± 0.9	± 0.3	± 0.7	± 0.6	± 0.1
MC μ -en. sc.	± 0.1	± 0.7	± 0.2	± 0.0	± 0.0	± 0.7	± 0.0	± 0.6	± 0.6	± 0.3
Lumi	± 2.4	± 0.6	± 0.4	± 0.4	± 0.3	± 0.7	± 0.8	± 1.0	± 1.2	± 3.4
Stat.	± 6.3	± 4.0	± 3.8	± 4.0	± 3.5	± 4.1	± 4.4	± 4.6	± 4.9	± 5.2
Total Syst.	± 31.9	± 17.3	± 13.3	± 7.4	± 8.5	± 9.1	± 9.6	± 11.2	± 10.7	± 20.8
Total	± 32.6	± 17.7	± 13.9	± 8.4	± 9.2	± 10.0	± 10.5	± 12.1	± 11.8	± 21.4

Table B.9: ($\mu+e$ combined). Systematic and statistical uncertainties for the MV1 tagger at a working point corresponding to a 75% b -tagging efficiency.

$p_T[GeV]$	25-30	30-40	40-50	50-60	60-75	75-90	90-110	110-140	140-200	200-300
ISR/FSR	± 4.0	± 2.5	± 2.8	± 3.1	± 2.9	± 2.1	± 3.5	± 2.1	± 4.2	± 7.9
Generator	± 3.7	± 2.7	± 0.1	± 0.6	± 5.9	± 0.6	± 6.4	± 1.6	± 0.6	± 1.0
Fragmentation	± 2.3	± 8.0	± 2.9	± 3.7	± 2.9	± 3.4	± 2.4	± 4.1	± 3.5	± 4.4
Diboson	± 0.7	± 0.4	± 0.0	± 0.1	± 0.2	± 0.3	± 0.3	± 0.7	± 0.7	± 0.1
single top	± 0.7	± 0.5	± 0.1	± 0.3	± 0.1	± 0.2	± 0.3	± 0.8	± 0.9	± 0.4
Z + jets	± 1.3	± 0.3	± 0.3	± 0.2	± 0.3	± 0.2	± 0.2	± 0.6	± 0.6	± 0.6
W + jets	± 2.5	± 0.4	± 0.3	± 0.3	± 0.2	± 0.5	± 0.3	± 0.7	± 0.5	± 1.1
Multijets	± 9.9	± 1.4	± 4.3	± 2.9	± 1.2	± 6.7	± 3.3	± 4.0	± 1.3	± 4.1
JES	± 21.0	± 6.2	± 3.3	± 1.0	± 2.3	± 6.3	± 4.8	± 7.0	± 7.4	± 17.3
JER	± 14.1	± 9.8	± 11.1	± 3.8	± 0.8	± 1.4	± 3.2	± 4.0	± 4.8	± 4.2
JRE	± 0.8	± 0.5	± 0.1	± 0.2	± 0.2	± 0.0	± 0.2	± 0.3	± 0.2	± 0.1
JVF	± 16.6	± 0.4	± 0.2	± 0.1	± 0.3	± 0.3	± 0.3	± 0.8	± 0.7	± 2.2
W+HF SF	± 0.9	± 0.7	± 0.2	± 0.4	± 0.3	± 0.5	± 0.4	± 1.1	± 1.0	± 0.4
ε_c	± 3.5	± 1.8	± 1.9	± 1.7	± 1.6	± 1.4	± 2.0	± 1.2	± 1.3	± 2.1
ε_{light}	± 14.4	± 1.1	± 0.6	± 0.5	± 0.8	± 0.6	± 0.3	± 0.8	± 0.6	± 1.1
E_T^{miss} cellout	± 0.6	± 0.3	± 0.1	± 0.3	± 0.2	± 0.4	± 0.2	± 0.7	± 0.6	± 0.0
E_T^{miss} pileup	± 0.6	± 0.5	± 0.2	± 0.2	± 0.2	± 0.2	± 0.1	± 0.7	± 0.6	± 0.1
e trigger	± 0.6	± 0.5	± 0.1	± 0.2	± 0.1	± 0.2	± 0.1	± 0.7	± 0.6	± 0.3
e smearing	± 0.4	± 0.3	± 0.2	± 0.2	± 0.0	± 0.2	± 0.3	± 0.7	± 0.9	± 0.3
e recID	± 1.3	± 0.2	± 0.2	± 0.4	± 0.3	± 0.3	± 0.3	± 0.7	± 0.7	± 1.0
MC e -energy scale	± 0.6	± 0.4	± 0.1	± 0.1	± 0.1	± 0.2	± 0.3	± 0.6	± 0.6	± 0.2
μ trigger	± 0.8	± 0.7	± 0.2	± 0.3	± 0.1	± 0.2	± 0.1	± 0.6	± 0.8	± 0.6
μ smearing	± 0.5	± 0.4	± 0.2	± 0.4	± 0.3	± 0.3	± 0.3	± 0.5	± 0.5	± 0.4
μ recID	± 1.0	± 0.2	± 0.1	± 0.2	± 0.1	± 0.2	± 0.2	± 0.8	± 0.8	± 0.1
MC μ -en. sc.	± 0.8	± 0.4	± 0.1	± 0.2	± 0.2	± 0.6	± 0.0	± 0.7	± 0.8	± 0.1
Lumi	± 2.9	± 0.8	± 0.7	± 0.6	± 0.4	± 0.7	± 0.9	± 1.0	± 1.4	± 3.4
Stat.	± 6.4	± 4.0	± 4.0	± 4.0	± 3.7	± 4.4	± 4.3	± 4.6	± 4.9	± 5.4
Total Syst.	± 35.9	± 15.0	± 13.2	± 7.2	± 8.0	± 10.3	± 10.4	± 10.8	± 11.1	± 20.6
Total	± 36.5	± 15.5	± 13.8	± 8.2	± 8.8	± 11.2	± 11.3	± 11.7	± 12.1	± 21.3

Table B.10: ($\mu+e$ combined). Systematic and statistical uncertainties for the MV1 tagger at a working point corresponding to a 70% b -tagging efficiency.

$p_T[GeV]$	25-30	30-40	40-50	50-60	60-75	75-90	90-110	110-140	140-200	200-300
ISR/FSR	± 2.3	± 1.9	± 3.5	± 3.3	± 2.9	± 2.5	± 3.7	± 1.7	± 3.6	± 7.4
Generator	± 4.3	± 2.8	± 0.8	± 1.0	± 6.0	± 0.2	± 6.9	± 1.1	± 2.8	± 1.4
Fragmentation	± 2.5	± 5.0	± 3.8	± 4.0	± 2.6	± 2.3	± 1.0	± 5.0	± 3.7	± 3.9
Diboson	± 0.5	± 0.3	± 0.1	± 0.2	± 0.5	± 0.5	± 0.4	± 1.0	± 1.1	± 0.1
single top	± 0.7	± 0.5	± 0.2	± 0.1	± 0.6	± 0.6	± 0.5	± 1.0	± 1.4	± 0.5
Z + jets	± 0.9	± 0.3	± 0.1	± 0.1	± 0.5	± 0.5	± 0.4	± 0.9	± 1.2	± 0.5
W + jets	± 0.9	± 0.5	± 0.4	± 0.2	± 0.3	± 0.5	± 0.4	± 0.8	± 1.0	± 1.0
Multijets	± 6.3	± 2.0	± 6.2	± 0.4	± 1.6	± 2.9	± 0.8	± 12.1	± 2.9	± 2.9
JES	± 2.2	± 5.2	± 1.9	± 1.8	± 3.2	± 7.4	± 5.7	± 8.1	± 9.1	± 17.5
JER	± 4.1	± 10.4	± 10.9	± 3.7	± 1.5	± 1.9	± 4.1	± 4.1	± 3.7	± 3.2
JRE	± 1.0	± 0.2	± 0.0	± 0.2	± 0.5	± 0.3	± 0.5	± 0.5	± 1.0	± 0.1
JVF	± 1.8	± 0.3	± 0.1	± 0.0	± 0.3	± 0.8	± 0.6	± 0.9	± 1.2	± 2.9
W+HF SF	± 0.9	± 0.6	± 0.2	± 0.4	± 0.6	± 0.8	± 0.6	± 1.3	± 1.8	± 0.4
ε_c	± 2.7	± 1.6	± 1.6	± 1.4	± 1.9	± 1.4	± 1.6	± 1.0	± 1.2	± 1.9
ε_{light}	± 0.5	± 0.7	± 0.3	± 0.1	± 0.4	± 0.6	± 0.2	± 0.8	± 1.3	± 1.1
E_T^{miss} cellout	± 0.7	± 0.5	± 0.2	± 0.4	± 0.2	± 0.5	± 0.3	± 0.9	± 1.1	± 0.2
E_T^{miss} pileup	± 0.6	± 0.3	± 0.0	± 0.2	± 0.6	± 0.5	± 0.4	± 0.9	± 1.0	± 0.2
e trigger	± 0.5	± 0.4	± 0.1	± 0.2	± 0.3	± 0.4	± 0.4	± 0.8	± 1.2	± 0.1
e smearing	± 0.4	± 0.6	± 0.2	± 0.2	± 0.3	± 0.4	± 0.5	± 0.8	± 1.2	± 0.0
e recID	± 0.8	± 0.5	± 0.3	± 0.2	± 0.6	± 0.5	± 0.3	± 0.6	± 1.2	± 1.2
MC e -energy scale	± 0.5	± 0.4	± 0.1	± 0.1	± 0.4	± 0.3	± 0.2	± 0.8	± 1.3	± 0.1
μ trigger	± 0.6	± 0.4	± 0.3	± 0.3	± 0.4	± 0.4	± 0.4	± 0.9	± 1.0	± 0.5
μ smearing	± 0.4	± 0.4	± 0.3	± 0.4	± 0.4	± 0.3	± 0.4	± 0.5	± 0.6	± 0.1
μ recID	± 0.5	± 0.5	± 0.2	± 0.1	± 0.5	± 0.4	± 0.4	± 0.7	± 1.1	± 0.1
MC μ -en. sc.	± 0.5	± 0.3	± 0.1	± 0.0	± 0.6	± 0.3	± 0.4	± 0.9	± 1.2	± 0.1
Lumi	± 3.1	± 1.3	± 1.0	± 1.0	± 0.5	± 1.0	± 1.3	± 1.3	± 1.7	± 3.6
Stat.	± 4.5	± 4.3	± 4.0	± 4.3	± 3.8	± 4.7	± 4.7	± 4.5	± 4.9	± 4.8
Total Syst.	± 10.9	± 13.5	± 13.9	± 7.0	± 8.6	± 9.3	± 11.0	± 16.5	± 13.0	± 20.4
Total	± 11.8	± 14.2	± 14.4	± 8.2	± 9.4	± 10.4	± 11.9	± 17.1	± 13.9	± 21.0

Table B.11: ($\mu+e$ combined). Systematic and statistical uncertainties for the MV1 tagger at a working point corresponding to a 60% b -tagging efficiency.

$p_T[GeV]$	25-30	30-40	40-50	50-60	60-75	75-90	90-110	110-140	140-200	200-300
ISR/FSR	± 2.6	± 1.6	± 3.1	± 2.5	± 2.7	± 3.0	± 3.4	± 2.2	± 3.3	± 8.4
Generator	± 4.0	± 1.9	± 0.9	± 1.5	± 5.3	± 0.6	± 5.4	± 1.8	± 2.9	± 2.0
Fragmentation	± 1.8	± 3.7	± 3.3	± 1.4	± 1.8	± 1.0	± 0.6	± 5.1	± 3.2	± 7.9
Diboson	± 0.3	± 0.9	± 0.5	± 0.8	± 0.1	± 0.5	± 0.1	± 0.2	± 0.3	± 0.3
single top	± 0.6	± 0.9	± 0.9	± 0.8	± 0.3	± 0.6	± 0.5	± 0.3	± 0.9	± 0.5
Z + jets	± 1.0	± 0.7	± 0.6	± 0.7	± 0.1	± 0.4	± 0.2	± 0.4	± 0.7	± 1.0
W + jets	± 1.2	± 0.8	± 0.7	± 0.8	± 0.2	± 0.6	± 0.4	± 0.5	± 0.8	± 1.3
Multijets	± 3.1	± 3.9	± 7.6	± 8.2	± 0.9	± 0.3	± 4.1	± 4.8	± 2.5	± 3.0
JES	± 3.0	± 4.3	± 1.0	± 2.4	± 4.2	± 8.3	± 5.6	± 7.9	± 9.5	± 19.3
JER	± 3.8	± 12.0	± 12.6	± 5.2	± 1.9	± 2.7	± 4.1	± 4.9	± 5.2	± 4.3
JRE	± 0.9	± 0.8	± 0.5	± 0.9	± 0.1	± 0.3	± 0.6	± 0.2	± 0.7	± 0.7
JVF	± 2.5	± 0.7	± 0.8	± 0.5	± 0.2	± 0.5	± 0.6	± 0.8	± 0.9	± 3.3
W+HF SF	± 0.8	± 1.2	± 1.0	± 1.2	± 0.3	± 1.0	± 0.6	± 0.6	± 1.0	± 0.4
ε_c	± 2.4	± 2.1	± 1.9	± 1.9	± 1.9	± 1.6	± 1.6	± 1.4	± 1.6	± 2.9
ε_{light}	± 1.8	± 0.7	± 0.7	± 0.7	± 0.3	± 0.4	± 0.4	± 0.7	± 0.5	± 1.6
E_T^{miss} cellout	± 0.4	± 0.6	± 0.8	± 0.9	± 0.3	± 0.6	± 0.1	± 0.4	± 0.9	± 0.3
E_T^{miss} pileup	± 0.7	± 0.8	± 0.6	± 0.7	± 0.1	± 0.4	± 0.2	± 0.3	± 0.6	± 0.4
e trigger	± 0.2	± 0.8	± 0.6	± 0.8	± 0.0	± 0.5	± 0.2	± 0.4	± 0.7	± 0.2
e smearing	± 0.4	± 0.8	± 0.7	± 0.6	± 0.1	± 0.5	± 0.4	± 0.3	± 0.4	± 0.7
e recID	± 1.1	± 0.7	± 0.6	± 0.5	± 0.1	± 0.6	± 0.5	± 0.6	± 0.7	± 1.4
MC e -energy scale	± 0.4	± 0.8	± 0.7	± 0.6	± 0.3	± 0.6	± 0.3	± 0.3	± 0.6	± 0.2
μ trigger	± 0.6	± 0.7	± 0.6	± 0.8	± 0.2	± 0.5	± 0.3	± 0.4	± 0.3	± 0.9
μ smearing	± 0.4	± 0.5	± 0.5	± 0.5	± 0.3	± 0.4	± 0.4	± 0.4	± 0.5	± 0.3
μ recID	± 0.3	± 0.6	± 0.6	± 0.7	± 0.2	± 0.5	± 0.5	± 0.3	± 0.7	± 0.4
MC μ -en. sc.	± 0.5	± 0.5	± 0.5	± 1.0	± 0.1	± 0.3	± 0.3	± 0.3	± 0.6	± 0.2
Lumi	± 3.6	± 1.8	± 1.6	± 1.2	± 0.9	± 1.3	± 1.5	± 1.6	± 2.3	± 3.9
Stat.	± 4.0	± 4.9	± 4.5	± 4.7	± 4.4	± 4.9	± 5.0	± 5.2	± 5.2	± 5.2
Total Syst.	± 9.7	± 14.7	± 15.9	± 11.2	± 8.1	± 9.8	± 10.7	± 12.3	± 13.0	± 23.8
Total	± 10.5	± 15.5	± 16.5	± 12.2	± 9.2	± 10.9	± 11.8	± 13.4	± 14.0	± 24.3

Table B.12: ($\mu+e$ combined). Systematic and statistical uncertainties for the SV0 tagger at a working point corresponding to a 50% b -tagging efficiency.

$p_T[GeV]$	25-30	30-40	40-50	50-60	60-75	75-90	90-110	110-140	140-200	200-300
ISR/FSR	± 3.9	± 2.7	± 2.7	± 3.6	± 3.2	± 1.4	± 3.2	± 2.5	± 4.4	± 6.3
Generator	± 0.7	± 5.5	± 0.4	± 0.4	± 5.3	± 1.4	± 4.0	± 0.5	± 0.6	± 2.3
Fragmentation	± 6.4	± 8.1	± 5.4	± 4.9	± 4.4	± 0.5	± 1.0	± 6.9	± 4.8	± 4.5
Diboson	± 2.3	± 2.0	± 0.4	± 0.3	± 0.1	± 0.5	± 0.3	± 0.8	± 0.2	± 0.2
single top	± 3.2	± 2.2	± 0.5	± 0.4	± 0.2	± 0.7	± 0.6	± 1.1	± 0.3	± 0.4
Z + jets	± 2.7	± 1.8	± 0.9	± 0.7	± 1.1	± 0.6	± 0.8	± 0.8	± 0.4	± 1.3
W + jets	± 2.2	± 1.8	± 1.0	± 0.8	± 1.0	± 0.5	± 0.6	± 0.7	± 0.7	± 1.6
Multijets	± 4.2	± 1.3	± 4.8	± 8.8	± 6.6	± 17.9	± 1.3	± 3.3	± 1.5	± 19.1
JES	± 10.7	± 6.6	± 4.9	± 2.5	± 0.9	± 1.2	± 3.4	± 4.7	± 6.0	± 15.7
JER	± 11.2	± 12.2	± 13.5	± 3.2	± 0.5	± 2.6	± 2.4	± 3.2	± 5.3	± 7.2
JRE	± 2.5	± 1.9	± 0.4	± 0.0	± 0.2	± 0.2	± 0.3	± 0.9	± 0.1	± 0.4
JVF	± 10.0	± 1.8	± 0.4	± 0.3	± 0.3	± 8.9	± 0.2	± 0.9	± 0.1	± 1.7
W+HF SF	± 4.0	± 2.9	± 0.6	± 0.6	± 0.3	± 0.9	± 0.5	± 1.4	± 0.5	± 0.5
ε_c	± 4.2	± 2.6	± 2.5	± 2.0	± 2.1	± 1.4	± 2.3	± 2.0	± 2.2	± 2.7
ε_{light}	± 13.6	± 3.5	± 2.2	± 1.8	± 1.4	± 5.5	± 0.8	± 0.9	± 1.1	± 3.2
E_T^{miss} cellout	± 2.6	± 1.8	± 0.6	± 0.3	± 0.2	± 0.8	± 0.1	± 0.8	± 0.2	± 0.8
E_T^{miss} pileup	± 2.9	± 2.0	± 0.7	± 0.3	± 0.1	± 0.6	± 0.4	± 0.9	± 0.1	± 0.5
e trigger	± 2.5	± 2.0	± 0.4	± 0.2	± 0.2	± 0.6	± 0.3	± 1.0	± 0.2	± 0.3
e smearing	± 2.9	± 2.1	± 0.5	± 0.3	± 0.1	± 0.6	± 0.3	± 0.9	± 0.1	± 0.2
e recID	± 2.6	± 1.9	± 0.5	± 0.5	± 0.1	± 0.5	± 0.5	± 0.8	± 0.4	± 0.9
MC e -energy scale	± 2.5	± 1.9	± 0.3	± 0.3	± 0.0	± 0.6	± 0.3	± 0.9	± 0.2	± 0.2
μ trigger	± 2.2	± 1.9	± 0.4	± 0.2	± 0.2	± 0.4	± 0.4	± 0.9	± 0.0	± 0.7
μ smearing	± 0.8	± 0.7	± 0.4	± 0.3	± 0.3	± 0.4	± 0.4	± 0.5	± 0.2	± 0.4
μ recID	± 2.6	± 2.0	± 0.3	± 0.3	± 0.0	± 0.6	± 0.3	± 0.9	± 0.0	± 0.3
MC μ -en. sc.	± 2.2	± 1.7	± 0.5	± 0.3	± 0.1	± 0.5	± 0.0	± 1.0	± 0.3	± 0.2
Lumi	± 2.4	± 1.9	± 0.4	± 0.3	± 0.2	± 0.6	± 0.5	± 0.8	± 1.1	± 3.7
Stat.	± 6.7	± 4.0	± 4.0	± 4.2	± 3.4	± 3.5	± 4.5	± 4.7	± 4.9	± 6.5
Total Syst.	± 27.1	± 19.6	± 16.8	± 11.9	± 10.5	± 21.2	± 7.4	± 10.8	± 10.9	± 26.8
Total	± 27.9	± 20.0	± 17.2	± 12.6	± 11.1	± 21.5	± 8.7	± 11.8	± 12.0	± 27.5

Table B.13: (e +jets). Systematic and statistical uncertainties for the IP3D+SV1 tagger at a working point corresponding to a 80% b -tagging efficiency.

$p_T[GeV]$	25-30	30-40	40-50	50-60	60-75	75-90	90-110	110-140	140-200	200-300
ISR/FSR	± 3.6	± 2.4	± 3.3	± 3.4	± 3.0	± 2.1	± 3.4	± 1.9	± 4.4	± 7.5
Generator	± 3.4	± 2.4	± 0.3	± 0.2	± 5.3	± 0.3	± 4.4	± 2.1	± 0.4	± 2.3
Fragmentation	± 0.2	± 8.6	± 4.5	± 3.7	± 2.7	± 3.4	± 0.7	± 6.2	± 4.1	± 5.0
Diboson	± 0.4	± 0.9	± 0.0	± 0.1	± 0.1	± 0.9	± 0.4	± 0.7	± 0.5	± 0.2
single top	± 0.3	± 1.0	± 0.2	± 0.3	± 0.2	± 1.2	± 0.4	± 1.1	± 0.6	± 0.4
Z + jets	± 1.0	± 0.7	± 0.3	± 0.1	± 0.5	± 1.0	± 0.4	± 0.9	± 0.3	± 0.7
W + jets	± 2.6	± 0.7	± 0.3	± 0.6	± 0.3	± 1.0	± 0.2	± 1.0	± 0.5	± 1.2
Multijets	± 13.4	± 1.7	± 4.0	± 4.7	± 6.8	± 0.6	± 1.5	± 5.3	± 1.7	± 14.0
JES	± 21.6	± 6.6	± 2.7	± 1.2	± 2.7	± 5.4	± 4.2	± 6.3	± 7.6	± 14.9
JER	± 16.4	± 10.3	± 11.1	± 4.7	± 0.3	± 1.1	± 3.1	± 3.9	± 5.3	± 5.9
JRE	± 0.0	± 1.0	± 0.0	± 0.0	± 0.1	± 1.0	± 0.3	± 0.7	± 0.4	± 0.5
JVF	± 17.4	± 0.8	± 0.2	± 0.4	± 0.2	± 1.1	± 0.4	± 0.9	± 0.5	± 2.4
W+HF SF	± 0.7	± 1.3	± 0.3	± 0.3	± 0.2	± 1.7	± 0.6	± 1.4	± 0.7	± 0.5
ε_c	± 3.5	± 2.1	± 1.9	± 1.8	± 2.0	± 1.8	± 1.9	± 1.5	± 1.5	± 2.5
ε_{light}	± 15.2	± 1.6	± 1.6	± 0.8	± 0.6	± 1.0	± 0.6	± 1.0	± 0.6	± 1.9
E_T^{miss} cellout	± 0.3	± 0.8	± 0.2	± 0.2	± 0.1	± 1.2	± 0.2	± 0.9	± 0.4	± 0.3
E_T^{miss} pileup	± 0.4	± 0.9	± 0.1	± 0.3	± 0.1	± 1.0	± 0.3	± 0.8	± 0.6	± 0.3
e trigger	± 0.4	± 1.0	± 0.1	± 0.1	± 0.0	± 1.0	± 0.3	± 0.9	± 0.5	± 0.3
e smearing	± 0.2	± 0.8	± 0.1	± 0.2	± 0.1	± 0.9	± 0.4	± 0.8	± 0.5	± 0.5
e recID	± 1.4	± 1.0	± 0.3	± 0.2	± 0.0	± 0.9	± 0.3	± 0.6	± 0.5	± 0.9
MC e -energy scale	± 0.1	± 0.9	± 0.1	± 0.2	± 0.2	± 1.0	± 0.1	± 0.7	± 0.4	± 0.1
μ trigger	± 0.3	± 0.8	± 0.1	± 0.2	± 0.1	± 1.0	± 0.5	± 0.7	± 0.6	± 0.6
μ smearing	± 0.4	± 0.5	± 0.4	± 0.2	± 0.3	± 0.6	± 0.4	± 0.5	± 0.4	± 0.3
μ recID	± 0.5	± 0.8	± 0.1	± 0.2	± 0.1	± 1.0	± 0.4	± 0.9	± 0.5	± 0.2
MC μ -en. sc.	± 0.9	± 0.8	± 0.1	± 0.1	± 0.1	± 0.8	± 0.3	± 1.0	± 0.8	± 0.3
Lumi	± 3.1	± 1.0	± 0.5	± 0.8	± 0.4	± 0.9	± 0.9	± 1.0	± 1.2	± 3.8
Stat.	± 6.9	± 4.2	± 3.9	± 4.1	± 3.7	± 4.4	± 4.4	± 4.7	± 4.9	± 5.5
Total Syst.	± 38.8	± 16.1	± 13.6	± 8.7	± 10.2	± 8.4	± 8.2	± 12.1	± 11.6	± 23.2
Total	± 39.4	± 16.7	± 14.2	± 9.6	± 10.8	± 9.5	± 9.3	± 13.0	± 12.5	± 23.9

Table B.14: (e +jets). Systematic and statistical uncertainties for the IP3D+SV1 tagger at a working point corresponding to a 70% b -tagging efficiency.

$p_T[GeV]$	25-30	30-40	40-50	50-60	60-75	75-90	90-110	110-140	140-200	200-300
ISR/FSR	± 2.3	± 2.0	± 3.2	± 3.3	± 2.5	± 2.5	± 3.3	± 1.9	± 2.9	± 7.5
Generator	± 3.9	± 1.4	± 0.3	± 1.8	± 5.7	± 0.6	± 5.7	± 2.0	± 2.7	± 1.2
Fragmentation	± 2.3	± 5.3	± 5.0	± 4.8	± 3.9	± 1.6	± 1.2	± 6.4	± 4.2	± 5.4
Diboson	± 0.5	± 0.5	± 0.1	± 0.1	± 0.1	± 0.6	± 0.5	± 0.9	± 0.9	± 0.1
single top	± 0.5	± 0.4	± 0.4	± 0.2	± 0.3	± 0.6	± 0.7	± 1.1	± 1.1	± 0.3
Z + jets	± 1.0	± 0.3	± 0.3	± 0.2	± 0.3	± 0.5	± 0.6	± 1.0	± 0.7	± 0.9
W + jets	± 1.1	± 0.3	± 0.3	± 0.3	± 0.2	± 0.6	± 0.5	± 0.8	± 0.9	± 1.2
Multijets	± 1.7	± 3.2	± 4.0	± 1.1	± 1.8	± 4.1	± 2.3	± 10.2	± 0.6	± 2.3
JES	± 2.6	± 4.9	± 1.9	± 2.0	± 3.2	± 6.6	± 5.2	± 7.2	± 8.5	± 18.1
JER	± 2.0	± 9.4	± 11.9	± 4.5	± 1.0	± 1.6	± 3.7	± 3.8	± 4.2	± 4.3
JRE	± 0.9	± 0.5	± 0.2	± 0.1	± 0.2	± 0.6	± 0.8	± 0.7	± 0.7	± 0.4
JVF	± 1.9	± 0.3	± 0.3	± 0.2	± 0.1	± 0.6	± 0.8	± 1.0	± 1.0	± 2.6
W+HF SF	± 0.9	± 0.7	± 0.4	± 0.2	± 0.4	± 0.8	± 0.9	± 1.4	± 1.3	± 0.6
ε_c	± 2.9	± 1.8	± 2.0	± 1.5	± 2.3	± 1.5	± 1.7	± 1.4	± 1.3	± 2.1
ε_{light}	± 1.3	± 0.9	± 0.6	± 0.2	± 0.4	± 0.5	± 0.8	± 0.9	± 0.9	± 1.4
E_T^{miss} cellout	± 0.4	± 0.4	± 0.5	± 0.3	± 0.1	± 0.6	± 0.6	± 0.7	± 0.9	± 0.2
E_T^{miss} pileup	± 0.5	± 0.4	± 0.3	± 0.1	± 0.3	± 0.5	± 0.4	± 0.7	± 0.9	± 0.3
e trigger	± 0.5	± 0.7	± 0.3	± 0.0	± 0.2	± 0.5	± 0.5	± 1.0	± 1.0	± 0.2
e smearing	± 0.5	± 0.5	± 0.3	± 0.1	± 0.1	± 0.7	± 0.5	± 1.1	± 0.7	± 0.5
e recID	± 1.1	± 0.4	± 0.4	± 0.3	± 0.2	± 0.5	± 0.6	± 0.8	± 0.8	± 1.0
MC e -energy scale	± 0.5	± 0.4	± 0.2	± 0.1	± 0.1	± 0.4	± 0.7	± 0.8	± 0.7	± 0.1
μ trigger	± 0.8	± 0.4	± 0.2	± 0.2	± 0.3	± 0.5	± 0.5	± 0.9	± 1.0	± 0.5
μ smearing	± 0.4	± 0.4	± 0.3	± 0.3	± 0.3	± 0.4	± 0.5	± 0.5	± 0.5	± 0.2
μ recID	± 0.5	± 0.5	± 0.3	± 0.1	± 0.2	± 0.5	± 0.5	± 0.8	± 0.8	± 0.2
MC μ -en. sc.	± 0.6	± 0.4	± 0.6	± 0.1	± 0.2	± 0.3	± 0.5	± 0.9	± 1.1	± 0.1
Lumi	± 3.5	± 1.2	± 0.8	± 1.0	± 0.5	± 1.0	± 1.4	± 1.3	± 1.9	± 3.6
Stat.	± 4.7	± 4.4	± 4.2	± 4.4	± 4.0	± 4.6	± 4.5	± 4.7	± 4.7	± 4.9
Total Syst.	± 8.5	± 12.9	± 14.3	± 8.1	± 8.6	± 9.0	± 10.1	± 15.4	± 11.9	± 21.3
Total	± 9.7	± 13.6	± 14.9	± 9.3	± 9.5	± 10.1	± 11.1	± 16.1	± 12.8	± 21.8

Table B.15: (e +jets). Systematic and statistical uncertainties for the IP3D+SV1 tagger at a working point corresponding to a 60% b -tagging efficiency.

$p_T[GeV]$	25-30	30-40	40-50	50-60	60-75	75-90	90-110	110-140	140-200	200-300
ISR/FSR	± 3.6	± 2.1	± 3.1	± 3.7	± 3.5	± 2.8	± 3.8	± 1.9	± 4.4	± 7.4
Generator	± 3.2	± 2.5	± 0.2	± 1.2	± 6.5	± 0.6	± 7.1	± 0.2	± 0.8	± 0.7
Fragmentation	± 4.3	± 6.8	± 3.5	± 4.0	± 2.4	± 5.3	± 2.2	± 3.3	± 3.2	± 4.0
Diboson	± 0.8	± 0.4	± 0.0	± 0.3	± 0.3	± 0.2	± 0.4	± 0.4	± 0.8	± 0.1
single top	± 1.1	± 0.4	± 0.2	± 0.3	± 0.3	± 0.5	± 0.3	± 0.6	± 1.0	± 0.3
Z + jets	± 1.0	± 0.3	± 0.3	± 0.2	± 0.5	± 0.5	± 0.3	± 0.4	± 0.9	± 0.6
W + jets	± 2.7	± 0.3	± 0.4	± 0.3	± 0.4	± 0.5	± 0.1	± 0.4	± 1.0	± 0.9
Multijets	± 9.2	± 2.0	± 4.2	± 3.4	± 1.0	± 4.6	± 3.7	± 6.0	± 0.7	± 4.4
JES	± 20.2	± 5.3	± 2.7	± 1.1	± 2.7	± 6.0	± 4.4	± 7.2	± 7.9	± 17.7
JER	± 7.4	± 10.2	± 11.4	± 4.0	± 1.8	± 1.9	± 3.2	± 4.2	± 4.4	± 4.2
JRE	± 1.5	± 0.5	± 0.0	± 0.2	± 0.3	± 0.0	± 0.2	± 0.2	± 0.7	± 0.1
JVF	± 16.0	± 0.3	± 0.1	± 0.1	± 0.2	± 0.4	± 0.3	± 0.5	± 0.8	± 2.4
W+HF SF	± 1.3	± 0.5	± 0.3	± 0.4	± 0.5	± 0.5	± 0.4	± 0.7	± 1.5	± 0.6
ε_c	± 3.0	± 1.8	± 2.0	± 1.6	± 1.8	± 1.5	± 2.1	± 1.2	± 1.4	± 2.1
ε_{light}	± 16.6	± 0.6	± 0.3	± 0.5	± 0.5	± 0.7	± 0.2	± 0.4	± 0.7	± 1.2
E_T^{miss} cellout	± 0.6	± 0.2	± 0.4	± 0.4	± 0.3	± 0.3	± 0.1	± 0.5	± 0.9	± 0.2
E_T^{miss} pileup	± 0.9	± 0.4	± 0.2	± 0.1	± 0.4	± 0.3	± 0.5	± 0.4	± 0.7	± 0.2
e trigger	± 1.0	± 0.3	± 0.2	± 0.4	± 0.3	± 0.4	± 0.2	± 0.5	± 0.9	± 0.2
e smearing	± 0.4	± 0.1	± 0.2	± 0.3	± 0.3	± 0.3	± 0.1	± 0.5	± 0.8	± 0.3
e recID	± 1.3	± 0.2	± 0.3	± 0.3	± 0.3	± 0.3	± 0.4	± 0.5	± 0.9	± 0.9
MC e -energy scale	± 0.5	± 0.3	± 0.1	± 0.3	± 0.2	± 0.2	± 0.1	± 0.6	± 1.0	± 0.2
μ trigger	± 0.8	± 0.4	± 0.1	± 0.2	± 0.3	± 0.3	± 0.3	± 0.7	± 1.0	± 0.7
μ smearing	± 0.6	± 0.3	± 0.3	± 0.2	± 0.2	± 0.3	± 0.3	± 0.4	± 0.5	± 0.4
μ recID	± 0.8	± 0.3	± 0.0	± 0.2	± 0.2	± 0.3	± 0.2	± 0.6	± 0.9	± 0.3
MC μ -en. sc.	± 1.0	± 0.2	± 0.0	± 0.2	± 0.3	± 0.2	± 0.3	± 0.4	± 0.9	± 0.1
Lumi	± 2.7	± 0.7	± 0.5	± 0.8	± 0.4	± 0.7	± 0.8	± 1.4	± 1.4	± 3.5
Stat.	± 6.5	± 4.1	± 4.2	± 4.3	± 3.7	± 4.4	± 4.6	± 4.7	± 4.8	± 5.2
Total Syst.	± 34.0	± 14.1	± 13.5	± 8.0	± 8.8	± 10.1	± 10.9	± 11.3	± 11.4	± 20.8
Total	± 34.6	± 14.7	± 14.1	± 9.1	± 9.5	± 11.0	± 11.9	± 12.2	± 12.4	± 21.4

Table B.16: (e +jets). Systematic and statistical uncertainties for the JetFitterCOMBNN tagger at a working point corresponding to a 70% b -tagging efficiency.

$p_T[GeV]$	25-30	30-40	40-50	50-60	60-75	75-90	90-110	110-140	140-200	200-300
ISR/FSR	± 3.9	± 2.9	± 3.2	± 3.5	± 3.1	± 1.7	± 3.0	± 1.9	± 4.5	± 6.0
Generator	± 5.2	± 3.5	± 0.1	± 0.1	± 6.7	± 0.3	± 5.6	± 1.3	± 0.3	± 1.2
Fragmentation	± 4.0	± 7.4	± 4.5	± 4.6	± 2.1	± 3.3	± 1.5	± 7.4	± 3.7	± 2.3
Diboson	± 0.1	± 0.3	± 0.1	± 0.2	± 0.0	± 0.9	± 0.4	± 0.9	± 0.0	± 0.1
single top	± 0.5	± 0.5	± 0.2	± 0.4	± 0.3	± 1.1	± 0.5	± 1.3	± 0.2	± 0.4
Z + jets	± 0.5	± 0.6	± 0.6	± 0.5	± 0.6	± 0.8	± 0.3	± 0.9	± 0.3	± 0.9
W + jets	± 1.6	± 1.1	± 0.7	± 0.6	± 0.7	± 1.1	± 0.5	± 0.9	± 0.3	± 1.4
Multijets	± 1.5	± 2.0	± 2.4	± 4.0	± 1.6	± 1.6	± 4.2	± 0.1	± 0.5	± 3.5
JES	± 13.4	± 4.5	± 4.2	± 1.3	± 2.4	± 4.4	± 4.2	± 5.2	± 6.5	± 16.6
JER	± 9.3	± 10.0	± 12.1	± 3.9	± 0.3	± 0.0	± 1.6	± 3.3	± 4.5	± 5.1
JRE	± 0.2	± 0.5	± 0.0	± 0.2	± 0.0	± 0.6	± 0.4	± 0.6	± 0.2	± 0.3
JVF	± 10.2	± 0.3	± 0.2	± 0.4	± 0.2	± 1.0	± 0.4	± 0.8	± 0.2	± 2.1
W+HF SF	± 0.6	± 0.7	± 0.3	± 0.6	± 0.2	± 1.5	± 0.7	± 1.3	± 0.3	± 0.3
ε_c	± 3.4	± 2.9	± 2.6	± 2.1	± 1.8	± 1.6	± 2.3	± 1.5	± 2.0	± 2.0
ε_{light}	± 11.7	± 2.3	± 1.7	± 1.1	± 0.7	± 1.0	± 0.6	± 1.0	± 0.4	± 2.7
E_T^{miss} cellout	± 0.2	± 0.3	± 0.2	± 0.4	± 0.1	± 0.9	± 0.4	± 1.0	± 0.3	± 0.2
E_T^{miss} pileup	± 0.2	± 0.5	± 0.1	± 0.3	± 0.1	± 0.9	± 0.4	± 0.9	± 0.1	± 0.3
e trigger	± 0.4	± 0.4	± 0.1	± 0.2	± 0.1	± 0.9	± 0.3	± 1.0	± 0.1	± 0.2
e smearing	± 0.4	± 0.3	± 0.1	± 0.3	± 0.1	± 1.0	± 0.6	± 0.9	± 0.2	± 0.5
e recID	± 0.8	± 0.5	± 0.2	± 0.3	± 0.0	± 1.0	± 0.4	± 1.0	± 0.3	± 0.9
MC e -energy scale	± 0.2	± 0.6	± 0.1	± 0.4	± 0.1	± 1.0	± 0.3	± 0.8	± 0.1	± 0.4
μ trigger	± 0.2	± 0.3	± 0.1	± 0.2	± 0.1	± 0.8	± 0.5	± 0.7	± 0.4	± 0.5
μ smearing	± 0.5	± 0.4	± 0.3	± 0.3	± 0.2	± 0.5	± 0.4	± 0.5	± 0.3	± 0.4
μ recID	± 0.2	± 0.6	± 0.2	± 0.3	± 0.1	± 0.7	± 0.5	± 0.8	± 0.1	± 0.2
MC μ -en. sc.	± 0.2	± 0.3	± 0.0	± 0.1	± 0.2	± 1.1	± 0.4	± 0.9	± 0.3	± 0.2
Lumi	± 2.1	± 0.4	± 0.4	± 0.4	± 0.1	± 0.8	± 0.5	± 0.9	± 1.1	± 3.1
Stat.	± 6.3	± 3.8	± 3.6	± 4.0	± 3.4	± 4.1	± 4.4	± 4.5	± 4.7	± 5.7
Total Syst.	± 24.2	± 14.7	± 14.5	± 8.7	± 8.5	± 7.4	± 9.5	± 10.8	± 10.2	± 19.0
Total	± 25.1	± 15.2	± 15.0	± 9.6	± 9.1	± 8.5	± 10.4	± 11.7	± 11.2	± 19.9

Table B.17: (e +jets). Systematic and statistical uncertainties for the JetFitterCOMBNN tagger at a working point corresponding to a 80% b -tagging efficiency.

$p_T[GeV]$	25-30	30-40	40-50	50-60	60-75	75-90	90-110	110-140	140-200	200-300
ISR/FSR	± 2.8	± 1.7	± 3.7	± 3.7	± 3.8	± 2.7	± 3.5	± 1.9	± 3.5	± 7.5
Generator	± 5.2	± 2.0	± 0.5	± 1.3	± 5.1	± 0.8	± 7.7	± 0.3	± 2.2	± 0.8
Fragmentation	± 1.9	± 3.8	± 4.3	± 5.0	± 1.9	± 2.9	± 3.5	± 4.3	± 3.4	± 3.2
Diboson	± 1.4	± 0.2	± 0.0	± 0.3	± 0.4	± 0.4	± 0.1	± 0.6	± 0.9	± 0.1
single top	± 1.7	± 0.2	± 0.2	± 0.5	± 0.4	± 0.5	± 0.4	± 0.9	± 1.2	± 0.4
Z + jets	± 1.6	± 0.1	± 0.0	± 0.3	± 0.4	± 0.7	± 0.2	± 0.5	± 1.0	± 0.8
W + jets	± 3.5	± 0.1	± 0.2	± 0.4	± 0.4	± 0.3	± 0.5	± 0.9	± 0.7	± 1.0
Multijets	± 17.3	± 1.9	± 3.1	± 0.1	± 0.9	± 6.2	± 4.1	± 10.3	± 0.2	± 5.4
JES	± 27.9	± 4.3	± 1.6	± 1.7	± 3.0	± 6.3	± 6.0	± 8.2	± 9.8	± 17.3
JER	± 22.8	± 9.3	± 10.2	± 3.5	± 1.1	± 2.1	± 4.0	± 4.8	± 4.0	± 3.3
JRE	± 1.7	± 0.2	± 0.2	± 0.5	± 0.2	± 0.4	± 0.3	± 0.4	± 1.0	± 0.2
JVF	± 22.2	± 0.5	± 0.1	± 0.3	± 0.3	± 0.6	± 0.4	± 0.8	± 0.9	± 3.1
W+HF SF	± 2.3	± 0.3	± 0.3	± 0.7	± 0.7	± 0.8	± 0.6	± 1.1	± 1.6	± 0.5
ε_c	± 2.6	± 1.5	± 1.8	± 1.4	± 1.9	± 1.4	± 2.0	± 1.3	± 1.5	± 2.4
ε_{light}	± 34.4	± 0.4	± 0.3	± 0.3	± 0.4	± 0.6	± 0.4	± 0.7	± 0.9	± 1.0
E_T^{miss} cellout	± 1.4	± 0.1	± 0.3	± 0.2	± 0.4	± 0.5	± 0.2	± 0.6	± 0.9	± 0.3
E_T^{miss} pileup	± 1.3	± 0.2	± 0.1	± 0.3	± 0.2	± 0.5	± 0.3	± 0.8	± 0.9	± 0.4
e trigger	± 1.5	± 0.1	± 0.0	± 0.5	± 0.4	± 0.4	± 0.3	± 0.5	± 0.8	± 0.3
e smearing	± 1.0	± 0.2	± 0.1	± 0.4	± 0.3	± 0.4	± 0.4	± 0.7	± 1.1	± 0.3
e recID	± 2.1	± 0.5	± 0.2	± 0.2	± 0.3	± 0.6	± 0.4	± 0.6	± 0.8	± 1.3
MC e -energy scale	± 1.2	± 0.1	± 0.1	± 0.4	± 0.5	± 0.3	± 0.3	± 0.6	± 0.9	± 0.1
μ trigger	± 1.6	± 0.4	± 0.2	± 0.3	± 0.5	± 0.4	± 0.3	± 0.5	± 0.9	± 0.6
μ smearing	± 0.6	± 0.4	± 0.2	± 0.4	± 0.3	± 0.4	± 0.4	± 0.4	± 0.5	± 0.3
μ recID	± 1.3	± 0.2	± 0.1	± 0.4	± 0.5	± 0.5	± 0.5	± 0.5	± 1.0	± 0.4
MC μ -en. sc.	± 1.3	± 0.1	± 0.0	± 0.5	± 0.3	± 0.5	± 0.2	± 0.8	± 1.0	± 0.1
Lumi	± 3.5	± 1.1	± 0.8	± 1.0	± 0.6	± 1.3	± 1.3	± 1.4	± 2.0	± 3.8
Stat.	± 7.3	± 4.4	± 4.3	± 4.4	± 4.0	± 4.5	± 4.6	± 4.7	± 5.0	± 4.8
Total Syst.	± 58.1	± 11.7	± 12.4	± 7.8	± 7.9	± 10.4	± 12.7	± 15.1	± 12.8	± 20.7
Total	± 58.6	± 12.4	± 13.1	± 9.0	± 8.9	± 11.3	± 13.5	± 15.8	± 13.8	± 21.3

Table B.18: (e +jets). Systematic and statistical uncertainties for the JetFitterCOMBNN tagger at a working point corresponding to a 60% b -tagging efficiency.

$p_T[GeV]$	25-30	30-40	40-50	50-60	60-75	75-90	90-110	110-140	140-200	200-300
ISR/FSR	± 2.7	± 2.3	± 4.0	± 3.6	± 3.6	± 2.6	± 3.8	± 2.0	± 3.5	± 7.2
Generator	± 5.7	± 3.0	± 1.3	± 1.3	± 4.7	± 0.8	± 7.8	± 0.2	± 1.8	± 0.5
Fragmentation	± 2.6	± 5.1	± 5.6	± 4.5	± 2.8	± 3.0	± 2.8	± 4.7	± 4.0	± 3.5
Diboson	± 1.6	± 0.5	± 0.1	± 0.3	± 0.1	± 0.3	± 0.5	± 0.5	± 0.9	± 0.1
single top	± 1.7	± 0.5	± 0.1	± 0.2	± 0.2	± 0.3	± 0.5	± 0.5	± 1.2	± 0.4
Z + jets	± 1.6	± 0.4	± 0.1	± 0.2	± 0.2	± 0.1	± 0.4	± 0.6	± 0.9	± 0.8
W + jets	± 3.7	± 0.3	± 0.2	± 0.4	± 0.2	± 0.1	± 0.3	± 0.2	± 1.1	± 0.9
Multijets	± 15.7	± 5.0	± 5.7	± 3.4	± 1.8	± 7.1	± 5.7	± 13.2	± 0.7	± 3.6
JES	± 29.0	± 4.2	± 1.4	± 2.0	± 3.6	± 6.8	± 6.6	± 8.4	± 10.0	± 17.5
JER	± 24.5	± 10.4	± 10.7	± 3.5	± 1.0	± 3.1	± 3.9	± 4.7	± 3.9	± 2.9
JRE	± 1.5	± 0.3	± 0.3	± 0.2	± 0.1	± 0.1	± 0.6	± 0.0	± 1.0	± 0.2
JVF	± 23.5	± 0.4	± 0.1	± 0.3	± 0.2	± 0.3	± 0.4	± 0.7	± 0.8	± 3.4
W+HF SF	± 2.5	± 0.5	± 0.3	± 0.5	± 0.3	± 0.4	± 0.7	± 0.7	± 1.6	± 0.4
ε_c	± 2.3	± 1.7	± 1.8	± 1.4	± 2.0	± 1.5	± 2.2	± 1.5	± 1.6	± 2.3
ε_{light}	± 41.6	± 0.3	± 0.1	± 0.2	± 0.2	± 0.1	± 0.1	± 0.4	± 0.8	± 1.5
E_T^{miss} cellout	± 1.6	± 0.3	± 0.2	± 0.2	± 0.2	± 0.2	± 0.3	± 0.5	± 1.0	± 0.3
E_T^{miss} pileup	± 1.3	± 0.3	± 0.1	± 0.3	± 0.1	± 0.3	± 0.3	± 0.6	± 0.9	± 0.3
e trigger	± 1.4	± 0.3	± 0.2	± 0.2	± 0.2	± 0.2	± 0.5	± 0.4	± 1.1	± 0.3
e smearing	± 1.7	± 0.3	± 0.2	± 0.5	± 0.2	± 0.1	± 0.5	± 0.3	± 1.1	± 0.6
e recID	± 1.6	± 0.5	± 0.3	± 0.3	± 0.1	± 0.3	± 0.5	± 0.7	± 1.0	± 1.2
MC e -energy scale	± 1.7	± 0.5	± 0.1	± 0.3	± 0.1	± 0.2	± 0.3	± 0.5	± 1.0	± 0.3
μ trigger	± 1.3	± 0.3	± 0.1	± 0.2	± 0.3	± 0.1	± 0.3	± 0.5	± 1.0	± 0.9
μ smearing	± 0.6	± 0.4	± 0.4	± 0.3	± 0.2	± 0.2	± 0.3	± 0.3	± 0.5	± 0.3
μ recID	± 1.5	± 0.5	± 0.3	± 0.0	± 0.2	± 0.2	± 0.4	± 0.4	± 1.0	± 0.3
MC μ -en. sc.	± 1.6	± 0.4	± 0.0	± 0.2	± 0.1	± 0.2	± 0.3	± 0.3	± 0.9	± 0.2
Lumi	± 3.6	± 1.1	± 0.8	± 1.1	± 0.7	± 1.3	± 1.5	± 1.7	± 2.0	± 3.8
Stat.	± 7.3	± 4.4	± 4.2	± 4.5	± 4.0	± 4.5	± 4.7	± 4.6	± 4.8	± 4.7
Total Syst.	± 63.9	± 14.1	± 14.2	± 8.2	± 8.1	± 11.3	± 13.6	± 17.4	± 13.1	± 20.6
Total	± 64.3	± 14.7	± 14.8	± 9.4	± 9.0	± 12.2	± 14.4	± 18.0	± 13.9	± 21.1

Table B.19: (e +jets). Systematic and statistical uncertainties for the JetFitterCOMBNN tagger at a working point corresponding to a 57% b -tagging efficiency.

$p_T[GeV]$	25-30	30-40	40-50	50-60	60-75	75-90	90-110	110-140	140-200	200-300
ISR/FSR	± 4.4	± 3.3	± 2.5	± 3.4	± 2.3	± 1.8	± 2.5	± 1.5	± 3.4	± 3.5
Generator	± 0.9	± 4.6	± 0.1	± 0.3	± 6.1	± 0.4	± 4.8	± 0.6	± 0.8	± 0.1
Fragmentation	± 6.4	± 7.3	± 3.2	± 5.6	± 1.4	± 4.3	± 1.3	± 5.5	± 2.8	± 2.6
Diboson	± 1.2	± 0.7	± 0.2	± 0.2	± 0.3	± 0.4	± 0.4	± 1.0	± 0.3	± 0.1
single top	± 1.6	± 0.9	± 0.3	± 0.2	± 0.5	± 0.4	± 0.4	± 1.3	± 0.4	± 0.6
Z + jets	± 1.1	± 1.2	± 1.0	± 0.8	± 1.0	± 0.3	± 0.7	± 1.0	± 0.3	± 1.1
W + jets	± 1.4	± 1.1	± 1.4	± 0.9	± 1.1	± 0.8	± 0.9	± 1.1	± 0.8	± 1.2
Multijets	± 13.7	± 1.5	± 2.0	± 8.4	± 2.8	± 2.1	± 4.7	± 6.7	± 4.8	± 7.4
JES	± 8.7	± 4.3	± 5.5	± 1.9	± 1.4	± 3.9	± 3.0	± 4.5	± 5.0	± 11.2
JER	± 13.6	± 6.3	± 12.2	± 4.6	± 0.6	± 0.9	± 1.3	± 2.7	± 3.8	± 5.3
JRE	± 0.4	± 0.4	± 0.3	± 0.1	± 0.3	± 0.1	± 0.2	± 0.9	± 0.1	± 0.1
JVF	± 7.1	± 1.8	± 0.7	± 0.2	± 0.3	± 0.6	± 0.3	± 1.0	± 0.2	± 1.2
W+HF SF	± 1.9	± 1.3	± 0.5	± 0.3	± 0.6	± 0.5	± 0.6	± 1.7	± 0.6	± 0.3
ε_c	± 3.1	± 2.6	± 2.4	± 1.8	± 2.2	± 2.0	± 2.0	± 1.9	± 2.3	± 2.9
ε_{light}	± 10.7	± 4.4	± 1.5	± 1.4	± 1.0	± 1.1	± 0.8	± 1.0	± 0.9	± 3.7
E_T^{miss} cellout	± 1.2	± 0.7	± 0.3	± 0.2	± 0.2	± 0.2	± 0.4	± 1.0	± 0.2	± 0.2
E_T^{miss} pileup	± 1.1	± 0.8	± 0.3	± 0.2	± 0.2	± 0.2	± 0.4	± 0.9	± 0.1	± 0.3
e trigger	± 1.2	± 0.8	± 0.2	± 0.1	± 0.5	± 0.1	± 0.3	± 0.9	± 0.2	± 0.4
e smearing	± 1.5	± 0.7	± 0.3	± 0.1	± 0.3	± 0.2	± 0.3	± 0.9	± 0.2	± 0.2
e recID	± 1.2	± 0.7	± 0.1	± 0.1	± 0.4	± 0.2	± 0.2	± 1.0	± 0.2	± 0.5
MC e -energy scale	± 1.3	± 0.7	± 0.3	± 0.0	± 0.4	± 0.3	± 0.4	± 1.0	± 0.2	± 0.2
μ trigger	± 1.1	± 0.9	± 0.3	± 0.1	± 0.4	± 0.1	± 0.4	± 0.8	± 0.3	± 0.4
μ smearing	± 0.6	± 0.5	± 0.3	± 0.4	± 0.4	± 0.3	± 0.3	± 0.5	± 0.3	± 0.4
μ recID	± 1.2	± 0.7	± 0.1	± 0.1	± 0.4	± 0.2	± 0.3	± 0.9	± 0.3	± 0.1
MC μ -en. sc.	± 0.9	± 0.6	± 0.2	± 0.0	± 0.2	± 0.1	± 0.4	± 1.0	± 0.1	± 0.3
Lumi	± 1.9	± 0.9	± 0.2	± 0.1	± 0.3	± 0.3	± 0.2	± 1.2	± 0.7	± 2.9
Stat.	± 6.5	± 3.7	± 3.6	± 3.9	± 3.3	± 4.0	± 4.3	± 4.4	± 4.6	± 5.7
Total Syst.	± 26.7	± 13.7	± 14.6	± 12.0	± 8.1	± 7.1	± 8.4	± 11.3	± 9.5	± 15.3
Total	± 27.4	± 14.2	± 15.0	± 12.6	± 8.7	± 8.1	± 9.5	± 12.2	± 10.6	± 16.3

Table B.20: (e +jets). Systematic and statistical uncertainties for the MV1 tagger at a working point corresponding to a 85% b -tagging efficiency.

$p_T[GeV]$	25-30	30-40	40-50	50-60	60-75	75-90	90-110	110-140	140-200	200-300
ISR/FSR	± 3.6	± 2.8	± 2.8	± 3.3	± 2.9	± 2.2	± 3.6	± 1.7	± 4.4	± 6.9
Generator	± 3.5	± 2.8	± 0.8	± 0.9	± 6.1	± 0.2	± 6.2	± 1.3	± 0.4	± 1.2
Fragmentation	± 3.6	± 9.0	± 3.1	± 3.3	± 2.0	± 3.0	± 3.1	± 5.0	± 4.2	± 4.4
Diboson	± 0.2	± 0.4	± 0.4	± 0.1	± 0.2	± 0.9	± 0.1	± 0.6	± 0.7	± 0.2
single top	± 0.5	± 0.5	± 0.5	± 0.1	± 0.2	± 0.9	± 0.2	± 0.8	± 0.8	± 0.4
Z + jets	± 0.5	± 0.5	± 0.4	± 0.3	± 0.5	± 1.0	± 0.2	± 0.7	± 0.6	± 0.7
W + jets	± 2.2	± 0.5	± 0.4	± 0.3	± 0.5	± 0.9	± 0.2	± 0.7	± 0.3	± 0.8
Multijets	± 14.5	± 2.1	± 3.9	± 3.5	± 3.5	± 4.4	± 0.8	± 5.3	± 2.1	± 6.9
JES	± 17.8	± 5.8	± 3.5	± 0.6	± 2.3	± 5.9	± 4.0	± 6.2	± 6.8	± 16.9
JER	± 9.0	± 12.3	± 11.2	± 4.0	± 0.7	± 0.0	± 3.1	± 4.0	± 4.2	± 4.6
JRE	± 0.4	± 0.5	± 0.5	± 0.1	± 0.3	± 0.7	± 0.3	± 0.4	± 0.3	± 0.2
JVF	± 14.2	± 0.4	± 0.3	± 0.1	± 0.2	± 0.7	± 0.2	± 0.7	± 0.6	± 2.0
W+HF SF	± 0.8	± 0.7	± 0.6	± 0.3	± 0.3	± 1.4	± 0.3	± 1.0	± 0.9	± 0.4
ε_c	± 3.4	± 2.3	± 1.9	± 1.7	± 1.8	± 1.5	± 1.9	± 1.4	± 1.5	± 2.4
ε_{light}	± 12.2	± 1.5	± 0.8	± 0.7	± 0.7	± 0.8	± 0.5	± 0.7	± 0.7	± 1.3
E_T^{miss} cellout	± 0.3	± 0.4	± 0.4	± 0.1	± 0.1	± 0.7	± 0.1	± 0.4	± 0.4	± 0.2
E_T^{miss} pileup	± 0.7	± 0.5	± 0.2	± 0.0	± 0.2	± 0.8	± 0.2	± 0.8	± 0.5	± 0.4
e trigger	± 0.3	± 0.4	± 0.3	± 0.2	± 0.2	± 0.7	± 0.2	± 0.8	± 0.5	± 0.1
e smearing	± 0.6	± 0.3	± 0.2	± 0.2	± 0.1	± 0.8	± 0.1	± 0.9	± 0.5	± 0.2
e recID	± 1.1	± 0.4	± 0.3	± 0.1	± 0.2	± 0.7	± 0.2	± 0.7	± 0.6	± 1.1
MC e -energy scale	± 0.4	± 0.4	± 0.3	± 0.2	± 0.1	± 0.7	± 0.1	± 0.6	± 0.5	± 0.2
μ trigger	± 0.3	± 0.5	± 0.4	± 0.2	± 0.1	± 0.5	± 0.2	± 0.8	± 0.4	± 0.6
μ smearing	± 0.8	± 0.4	± 0.3	± 0.3	± 0.3	± 0.5	± 0.4	± 0.5	± 0.5	± 0.3
μ recID	± 0.2	± 0.5	± 0.3	± 0.1	± 0.0	± 0.9	± 0.3	± 0.7	± 0.6	± 0.1
MC μ -en. sc.	± 0.1	± 0.7	± 0.2	± 0.0	± 0.0	± 0.7	± 0.0	± 0.6	± 0.6	± 0.3
Lumi	± 2.4	± 0.6	± 0.4	± 0.4	± 0.3	± 0.7	± 0.8	± 1.0	± 1.2	± 3.4
Stat.	± 6.3	± 4.0	± 3.8	± 4.0	± 3.5	± 4.1	± 4.4	± 4.6	± 4.9	± 5.2
Total Syst.	± 31.9	± 17.3	± 13.3	± 7.4	± 8.5	± 9.1	± 9.6	± 11.2	± 10.7	± 20.8
Total	± 32.6	± 17.7	± 13.9	± 8.4	± 9.2	± 10.0	± 10.5	± 12.1	± 11.8	± 21.4

Table B.21: (e +jets). Systematic and statistical uncertainties for the MV1 tagger at a working point corresponding to a 75% b -tagging efficiency.

$p_T[GeV]$	25-30	30-40	40-50	50-60	60-75	75-90	90-110	110-140	140-200	200-300
ISR/FSR	± 4.0	± 2.5	± 2.8	± 3.1	± 2.9	± 2.1	± 3.5	± 2.1	± 4.2	± 7.9
Generator	± 3.7	± 2.7	± 0.1	± 0.6	± 5.9	± 0.6	± 6.4	± 1.6	± 0.6	± 1.0
Fragmentation	± 2.3	± 8.0	± 2.9	± 3.7	± 2.9	± 3.4	± 2.4	± 4.1	± 3.5	± 4.4
Diboson	± 0.7	± 0.4	± 0.0	± 0.1	± 0.2	± 0.3	± 0.3	± 0.7	± 0.7	± 0.1
single top	± 0.7	± 0.5	± 0.1	± 0.3	± 0.1	± 0.2	± 0.3	± 0.8	± 0.9	± 0.4
Z + jets	± 1.3	± 0.3	± 0.3	± 0.2	± 0.3	± 0.2	± 0.2	± 0.6	± 0.6	± 0.6
W + jets	± 2.5	± 0.4	± 0.3	± 0.3	± 0.2	± 0.5	± 0.3	± 0.7	± 0.5	± 1.1
Multijets	± 9.9	± 1.4	± 4.3	± 2.9	± 1.2	± 6.7	± 3.3	± 4.0	± 1.3	± 4.1
JES	± 21.0	± 6.2	± 3.3	± 1.0	± 2.3	± 6.3	± 4.8	± 7.0	± 7.4	± 17.3
JER	± 14.1	± 9.8	± 11.1	± 3.8	± 0.8	± 1.4	± 3.2	± 4.0	± 4.8	± 4.2
JRE	± 0.8	± 0.5	± 0.1	± 0.2	± 0.2	± 0.0	± 0.2	± 0.3	± 0.2	± 0.1
JVF	± 16.6	± 0.4	± 0.2	± 0.1	± 0.3	± 0.3	± 0.3	± 0.8	± 0.7	± 2.2
W+HF SF	± 0.9	± 0.7	± 0.2	± 0.4	± 0.3	± 0.5	± 0.4	± 1.1	± 1.0	± 0.4
ε_c	± 3.5	± 1.8	± 1.9	± 1.7	± 1.6	± 1.4	± 2.0	± 1.2	± 1.3	± 2.1
ε_{light}	± 14.4	± 1.1	± 0.6	± 0.5	± 0.8	± 0.6	± 0.3	± 0.8	± 0.6	± 1.1
E_T^{miss} cellout	± 0.6	± 0.3	± 0.1	± 0.3	± 0.2	± 0.4	± 0.2	± 0.7	± 0.6	± 0.0
E_T^{miss} pileup	± 0.6	± 0.5	± 0.2	± 0.2	± 0.2	± 0.2	± 0.1	± 0.7	± 0.6	± 0.1
e trigger	± 0.6	± 0.5	± 0.1	± 0.2	± 0.1	± 0.2	± 0.1	± 0.7	± 0.6	± 0.3
e smearing	± 0.4	± 0.3	± 0.2	± 0.2	± 0.0	± 0.2	± 0.3	± 0.7	± 0.9	± 0.3
e recID	± 1.3	± 0.2	± 0.2	± 0.4	± 0.3	± 0.3	± 0.3	± 0.7	± 0.7	± 1.0
MC e -energy scale	± 0.6	± 0.4	± 0.1	± 0.1	± 0.1	± 0.2	± 0.3	± 0.6	± 0.6	± 0.2
μ trigger	± 0.8	± 0.7	± 0.2	± 0.3	± 0.1	± 0.2	± 0.1	± 0.6	± 0.8	± 0.6
μ smearing	± 0.5	± 0.4	± 0.2	± 0.4	± 0.3	± 0.3	± 0.3	± 0.5	± 0.5	± 0.4
μ recID	± 1.0	± 0.2	± 0.1	± 0.2	± 0.1	± 0.2	± 0.2	± 0.8	± 0.8	± 0.1
MC μ -en. sc.	± 0.8	± 0.4	± 0.1	± 0.2	± 0.2	± 0.6	± 0.0	± 0.7	± 0.8	± 0.1
Lumi	± 2.9	± 0.8	± 0.7	± 0.6	± 0.4	± 0.7	± 0.9	± 1.0	± 1.4	± 3.4
Stat.	± 6.4	± 4.0	± 4.0	± 4.0	± 3.7	± 4.4	± 4.3	± 4.6	± 4.9	± 5.4
Total Syst.	± 35.9	± 15.0	± 13.2	± 7.2	± 8.0	± 10.3	± 10.4	± 10.8	± 11.1	± 20.6
Total	± 36.5	± 15.5	± 13.8	± 8.2	± 8.8	± 11.2	± 11.3	± 11.7	± 12.1	± 21.3

Table B.22: (e +jets). Systematic and statistical uncertainties for the MV1 tagger at a working point corresponding to a 70% b -tagging efficiency.

$p_T[GeV]$	25-30	30-40	40-50	50-60	60-75	75-90	90-110	110-140	140-200	200-300
ISR/FSR	± 2.3	± 1.9	± 3.5	± 3.3	± 2.9	± 2.5	± 3.7	± 1.7	± 3.6	± 7.4
Generator	± 4.3	± 2.8	± 0.8	± 1.0	± 6.0	± 0.2	± 6.9	± 1.1	± 2.8	± 1.4
Fragmentation	± 2.5	± 5.0	± 3.8	± 4.0	± 2.6	± 2.3	± 1.0	± 5.0	± 3.7	± 3.9
Diboson	± 0.5	± 0.3	± 0.1	± 0.2	± 0.5	± 0.5	± 0.4	± 1.0	± 1.1	± 0.1
single top	± 0.7	± 0.5	± 0.2	± 0.1	± 0.6	± 0.6	± 0.5	± 1.0	± 1.4	± 0.5
Z + jets	± 0.9	± 0.3	± 0.1	± 0.1	± 0.5	± 0.5	± 0.4	± 0.9	± 1.2	± 0.5
W + jets	± 0.9	± 0.5	± 0.4	± 0.2	± 0.3	± 0.5	± 0.4	± 0.8	± 1.0	± 1.0
Multijets	± 6.3	± 2.0	± 6.2	± 0.4	± 1.6	± 2.9	± 0.8	± 12.1	± 2.9	± 2.9
JES	± 2.2	± 5.2	± 1.9	± 1.8	± 3.2	± 7.4	± 5.7	± 8.1	± 9.1	± 17.5
JER	± 4.1	± 10.4	± 10.9	± 3.7	± 1.5	± 1.9	± 4.1	± 4.1	± 3.7	± 3.2
JRE	± 1.0	± 0.2	± 0.0	± 0.2	± 0.5	± 0.3	± 0.5	± 0.5	± 1.0	± 0.1
JVF	± 1.8	± 0.3	± 0.1	± 0.0	± 0.3	± 0.8	± 0.6	± 0.9	± 1.2	± 2.9
W+HF SF	± 0.9	± 0.6	± 0.2	± 0.4	± 0.6	± 0.8	± 0.6	± 1.3	± 1.8	± 0.4
ε_c	± 2.7	± 1.6	± 1.6	± 1.4	± 1.9	± 1.4	± 1.6	± 1.0	± 1.2	± 1.9
ε_{light}	± 0.5	± 0.7	± 0.3	± 0.1	± 0.4	± 0.6	± 0.2	± 0.8	± 1.3	± 1.1
E_T^{miss} cellout	± 0.7	± 0.5	± 0.2	± 0.4	± 0.2	± 0.5	± 0.3	± 0.9	± 1.1	± 0.2
E_T^{miss} pileup	± 0.6	± 0.3	± 0.0	± 0.2	± 0.6	± 0.5	± 0.4	± 0.9	± 1.0	± 0.2
e trigger	± 0.5	± 0.4	± 0.1	± 0.2	± 0.3	± 0.4	± 0.4	± 0.8	± 1.2	± 0.1
e smearing	± 0.4	± 0.6	± 0.2	± 0.2	± 0.3	± 0.4	± 0.5	± 0.8	± 1.2	± 0.0
e recID	± 0.8	± 0.5	± 0.3	± 0.2	± 0.6	± 0.5	± 0.3	± 0.6	± 1.2	± 1.2
MC e -energy scale	± 0.5	± 0.4	± 0.1	± 0.1	± 0.4	± 0.3	± 0.2	± 0.8	± 1.3	± 0.1
μ trigger	± 0.6	± 0.4	± 0.3	± 0.3	± 0.4	± 0.4	± 0.4	± 0.9	± 1.0	± 0.5
μ smearing	± 0.4	± 0.4	± 0.3	± 0.4	± 0.4	± 0.3	± 0.4	± 0.5	± 0.6	± 0.1
μ recID	± 0.5	± 0.5	± 0.2	± 0.1	± 0.5	± 0.4	± 0.4	± 0.7	± 1.1	± 0.1
MC μ -en. sc.	± 0.5	± 0.3	± 0.1	± 0.0	± 0.6	± 0.3	± 0.4	± 0.9	± 1.2	± 0.1
Lumi	± 3.1	± 1.3	± 1.0	± 1.0	± 0.5	± 1.0	± 1.3	± 1.3	± 1.7	± 3.6
Stat.	± 4.5	± 4.3	± 4.0	± 4.3	± 3.8	± 4.7	± 4.7	± 4.5	± 4.9	± 4.8
Total Syst.	± 10.9	± 13.5	± 13.9	± 7.0	± 8.6	± 9.3	± 11.0	± 16.5	± 13.0	± 20.4
Total	± 11.8	± 14.2	± 14.4	± 8.2	± 9.4	± 10.4	± 11.9	± 17.1	± 13.9	± 21.0

Table B.23: (e +jets). Systematic and statistical uncertainties for the MV1 tagger at a working point corresponding to a 60% b -tagging efficiency.

$p_T[GeV]$	25-30	30-40	40-50	50-60	60-75	75-90	90-110	110-140	140-200	200-300
ISR/FSR	± 2.6	± 1.6	± 3.1	± 2.5	± 2.7	± 3.0	± 3.4	± 2.2	± 3.3	± 8.4
Generator	± 4.0	± 1.9	± 0.9	± 1.5	± 5.3	± 0.6	± 5.4	± 1.8	± 2.9	± 2.0
Fragmentation	± 1.8	± 3.7	± 3.3	± 1.4	± 1.8	± 1.0	± 0.6	± 5.1	± 3.2	± 7.9
Diboson	± 0.3	± 0.9	± 0.5	± 0.8	± 0.1	± 0.5	± 0.1	± 0.2	± 0.3	± 0.3
single top	± 0.6	± 0.9	± 0.9	± 0.8	± 0.3	± 0.6	± 0.5	± 0.3	± 0.9	± 0.5
Z + jets	± 1.0	± 0.7	± 0.6	± 0.7	± 0.1	± 0.4	± 0.2	± 0.4	± 0.7	± 1.0
W + jets	± 1.2	± 0.8	± 0.7	± 0.8	± 0.2	± 0.6	± 0.4	± 0.5	± 0.8	± 1.3
Multijets	± 3.1	± 3.9	± 7.6	± 8.2	± 0.9	± 0.3	± 4.1	± 4.8	± 2.5	± 3.0
JES	± 3.0	± 4.3	± 1.0	± 2.4	± 4.2	± 8.3	± 5.6	± 7.9	± 9.5	± 19.3
JER	± 3.8	± 12.0	± 12.6	± 5.2	± 1.9	± 2.7	± 4.1	± 4.9	± 5.2	± 4.3
JRE	± 0.9	± 0.8	± 0.5	± 0.9	± 0.1	± 0.3	± 0.6	± 0.2	± 0.7	± 0.7
JVF	± 2.5	± 0.7	± 0.8	± 0.5	± 0.2	± 0.5	± 0.6	± 0.8	± 0.9	± 3.3
W+HF SF	± 0.8	± 1.2	± 1.0	± 1.2	± 0.3	± 1.0	± 0.6	± 0.6	± 1.0	± 0.4
ε_c	± 2.4	± 2.1	± 1.9	± 1.9	± 1.9	± 1.6	± 1.6	± 1.4	± 1.6	± 2.9
ε_{light}	± 1.8	± 0.7	± 0.7	± 0.7	± 0.3	± 0.4	± 0.4	± 0.7	± 0.5	± 1.6
E_T^{miss} cellout	± 0.4	± 0.6	± 0.8	± 0.9	± 0.3	± 0.6	± 0.1	± 0.4	± 0.9	± 0.3
E_T^{miss} pileup	± 0.7	± 0.8	± 0.6	± 0.7	± 0.1	± 0.4	± 0.2	± 0.3	± 0.6	± 0.4
e trigger	± 0.2	± 0.8	± 0.6	± 0.8	± 0.0	± 0.5	± 0.2	± 0.4	± 0.7	± 0.2
e smearing	± 0.4	± 0.8	± 0.7	± 0.6	± 0.1	± 0.5	± 0.4	± 0.3	± 0.4	± 0.7
e recID	± 1.1	± 0.7	± 0.6	± 0.5	± 0.1	± 0.6	± 0.5	± 0.6	± 0.7	± 1.4
MC e -energy scale	± 0.4	± 0.8	± 0.7	± 0.6	± 0.3	± 0.6	± 0.3	± 0.3	± 0.6	± 0.2
μ trigger	± 0.6	± 0.7	± 0.6	± 0.8	± 0.2	± 0.5	± 0.3	± 0.4	± 0.3	± 0.9
μ smearing	± 0.4	± 0.5	± 0.5	± 0.5	± 0.3	± 0.4	± 0.4	± 0.4	± 0.5	± 0.3
μ recID	± 0.3	± 0.6	± 0.6	± 0.7	± 0.2	± 0.5	± 0.5	± 0.3	± 0.7	± 0.4
MC μ -en. sc.	± 0.5	± 0.5	± 0.5	± 1.0	± 0.1	± 0.3	± 0.3	± 0.3	± 0.6	± 0.2
Lumi	± 3.6	± 1.8	± 1.6	± 1.2	± 0.9	± 1.3	± 1.5	± 1.6	± 2.3	± 3.9
Stat.	± 4.0	± 4.9	± 4.5	± 4.7	± 4.4	± 4.9	± 5.0	± 5.2	± 5.2	± 5.2
Total Syst.	± 9.7	± 14.7	± 15.9	± 11.2	± 8.1	± 9.8	± 10.7	± 12.3	± 13.0	± 23.8
Total	± 10.5	± 15.5	± 16.5	± 12.2	± 9.2	± 10.9	± 11.8	± 13.4	± 14.0	± 24.3

Table B.24: (e +jets). Systematic and statistical uncertainties for the SV0 tagger at a working point corresponding to a 50% b -tagging efficiency.

$p_T[GeV]$	25-30	30-40	40-50	50-60	60-75	75-90	90-110	110-140	140-200	200-300
ISR/FSR	± 3.9	± 2.7	± 2.7	± 3.6	± 3.2	± 1.4	± 3.2	± 2.5	± 4.4	± 6.3
Generator	± 0.7	± 5.5	± 0.4	± 0.4	± 5.3	± 1.4	± 4.0	± 0.5	± 0.6	± 2.3
Fragmentation	± 6.4	± 8.1	± 5.4	± 4.9	± 4.4	± 0.5	± 1.0	± 6.9	± 4.8	± 4.5
Diboson	± 2.3	± 2.0	± 0.4	± 0.3	± 0.1	± 0.5	± 0.3	± 0.8	± 0.2	± 0.2
single top	± 3.2	± 2.2	± 0.5	± 0.4	± 0.2	± 0.7	± 0.6	± 1.1	± 0.3	± 0.4
Z + jets	± 2.7	± 1.8	± 0.9	± 0.7	± 1.1	± 0.6	± 0.8	± 0.8	± 0.4	± 1.3
W + jets	± 2.2	± 1.8	± 1.0	± 0.8	± 1.0	± 0.5	± 0.6	± 0.7	± 0.7	± 1.6
Multijets	± 4.2	± 1.3	± 4.8	± 8.8	± 6.6	± 17.9	± 1.3	± 3.3	± 1.5	± 19.1
JES	± 10.7	± 6.6	± 4.9	± 2.5	± 0.9	± 1.2	± 3.4	± 4.7	± 6.0	± 15.7
JER	± 11.2	± 12.2	± 13.5	± 3.2	± 0.5	± 2.6	± 2.4	± 3.2	± 5.3	± 7.2
JRE	± 2.5	± 1.9	± 0.4	± 0.0	± 0.2	± 0.2	± 0.3	± 0.9	± 0.1	± 0.4
JVF	± 10.0	± 1.8	± 0.4	± 0.3	± 0.3	± 8.9	± 0.2	± 0.9	± 0.1	± 1.7
W+HF SF	± 4.0	± 2.9	± 0.6	± 0.6	± 0.3	± 0.9	± 0.5	± 1.4	± 0.5	± 0.5
ε_c	± 4.2	± 2.6	± 2.5	± 2.0	± 2.1	± 1.4	± 2.3	± 2.0	± 2.2	± 2.7
ε_{light}	± 13.6	± 3.5	± 2.2	± 1.8	± 1.4	± 5.5	± 0.8	± 0.9	± 1.1	± 3.2
E_T^{miss} cellout	± 2.6	± 1.8	± 0.6	± 0.3	± 0.2	± 0.8	± 0.1	± 0.8	± 0.2	± 0.8
E_T^{miss} pileup	± 2.9	± 2.0	± 0.7	± 0.3	± 0.1	± 0.6	± 0.4	± 0.9	± 0.1	± 0.5
e trigger	± 2.5	± 2.0	± 0.4	± 0.2	± 0.2	± 0.6	± 0.3	± 1.0	± 0.2	± 0.3
e smearing	± 2.9	± 2.1	± 0.5	± 0.3	± 0.1	± 0.6	± 0.3	± 0.9	± 0.1	± 0.2
e recID	± 2.6	± 1.9	± 0.5	± 0.5	± 0.1	± 0.5	± 0.5	± 0.8	± 0.4	± 0.9
MC e -energy scale	± 2.5	± 1.9	± 0.3	± 0.3	± 0.0	± 0.6	± 0.3	± 0.9	± 0.2	± 0.2
μ trigger	± 2.2	± 1.9	± 0.4	± 0.2	± 0.2	± 0.4	± 0.4	± 0.9	± 0.0	± 0.7
μ smearing	± 0.8	± 0.7	± 0.4	± 0.3	± 0.3	± 0.4	± 0.4	± 0.5	± 0.2	± 0.4
μ recID	± 2.6	± 2.0	± 0.3	± 0.3	± 0.0	± 0.6	± 0.3	± 0.9	± 0.0	± 0.3
MC μ -en. sc.	± 2.2	± 1.7	± 0.5	± 0.3	± 0.1	± 0.5	± 0.0	± 1.0	± 0.3	± 0.2
Lumi	± 2.4	± 1.9	± 0.4	± 0.3	± 0.2	± 0.6	± 0.5	± 0.8	± 1.1	± 3.7
Stat.	± 6.7	± 4.0	± 4.0	± 4.2	± 3.4	± 3.5	± 4.5	± 4.7	± 4.9	± 6.5
Total Syst.	± 27.1	± 19.6	± 16.8	± 11.9	± 10.5	± 21.2	± 7.4	± 10.8	± 10.9	± 26.8
Total	± 27.9	± 20.0	± 17.2	± 12.6	± 11.1	± 21.5	± 8.7	± 11.8	± 12.0	± 27.5

Table B.25: (μ +jets). Systematic and statistical uncertainties for the IP3D+SV1 tagger at a working point corresponding to a 80% b -tagging efficiency.

$p_T[GeV]$	25-30	30-40	40-50	50-60	60-75	75-90	90-110	110-140	140-200	200-300
ISR/FSR	± 3.6	± 2.4	± 3.3	± 3.4	± 3.0	± 2.1	± 3.4	± 1.9	± 4.4	± 7.5
Generator	± 3.4	± 2.4	± 0.3	± 0.2	± 5.3	± 0.3	± 4.4	± 2.1	± 0.4	± 2.3
Fragmentation	± 0.2	± 8.6	± 4.5	± 3.7	± 2.7	± 3.4	± 0.7	± 6.2	± 4.1	± 5.0
Diboson	± 0.4	± 0.9	± 0.0	± 0.1	± 0.1	± 0.9	± 0.4	± 0.7	± 0.5	± 0.2
single top	± 0.3	± 1.0	± 0.2	± 0.3	± 0.2	± 1.2	± 0.4	± 1.1	± 0.6	± 0.4
Z + jets	± 1.0	± 0.7	± 0.3	± 0.1	± 0.5	± 1.0	± 0.4	± 0.9	± 0.3	± 0.7
W + jets	± 2.6	± 0.7	± 0.3	± 0.6	± 0.3	± 1.0	± 0.2	± 1.0	± 0.5	± 1.2
Multijets	± 13.4	± 1.7	± 4.0	± 4.7	± 6.8	± 0.6	± 1.5	± 5.3	± 1.7	± 14.0
JES	± 21.6	± 6.6	± 2.7	± 1.2	± 2.7	± 5.4	± 4.2	± 6.3	± 7.6	± 14.9
JER	± 16.4	± 10.3	± 11.1	± 4.7	± 0.3	± 1.1	± 3.1	± 3.9	± 5.3	± 5.9
JRE	± 0.0	± 1.0	± 0.0	± 0.0	± 0.1	± 1.0	± 0.3	± 0.7	± 0.4	± 0.5
JVF	± 17.4	± 0.8	± 0.2	± 0.4	± 0.2	± 1.1	± 0.4	± 0.9	± 0.5	± 2.4
W+HF SF	± 0.7	± 1.3	± 0.3	± 0.3	± 0.2	± 1.7	± 0.6	± 1.4	± 0.7	± 0.5
ε_c	± 3.5	± 2.1	± 1.9	± 1.8	± 2.0	± 1.8	± 1.9	± 1.5	± 1.5	± 2.5
ε_{light}	± 15.2	± 1.6	± 1.6	± 0.8	± 0.6	± 1.0	± 0.6	± 1.0	± 0.6	± 1.9
E_T^{miss} cellout	± 0.3	± 0.8	± 0.2	± 0.2	± 0.1	± 1.2	± 0.2	± 0.9	± 0.4	± 0.3
E_T^{miss} pileup	± 0.4	± 0.9	± 0.1	± 0.3	± 0.1	± 1.0	± 0.3	± 0.8	± 0.6	± 0.3
e trigger	± 0.4	± 1.0	± 0.1	± 0.1	± 0.0	± 1.0	± 0.3	± 0.9	± 0.5	± 0.3
e smearing	± 0.2	± 0.8	± 0.1	± 0.2	± 0.1	± 0.9	± 0.4	± 0.8	± 0.5	± 0.5
e recID	± 1.4	± 1.0	± 0.3	± 0.2	± 0.0	± 0.9	± 0.3	± 0.6	± 0.5	± 0.9
MC e -energy scale	± 0.1	± 0.9	± 0.1	± 0.2	± 0.2	± 1.0	± 0.1	± 0.7	± 0.4	± 0.1
μ trigger	± 0.3	± 0.8	± 0.1	± 0.2	± 0.1	± 1.0	± 0.5	± 0.7	± 0.6	± 0.6
μ smearing	± 0.4	± 0.5	± 0.4	± 0.2	± 0.3	± 0.6	± 0.4	± 0.5	± 0.4	± 0.3
μ recID	± 0.5	± 0.8	± 0.1	± 0.2	± 0.1	± 1.0	± 0.4	± 0.9	± 0.5	± 0.2
MC μ -en. sc.	± 0.9	± 0.8	± 0.1	± 0.1	± 0.1	± 0.8	± 0.3	± 1.0	± 0.8	± 0.3
Lumi	± 3.1	± 1.0	± 0.5	± 0.8	± 0.4	± 0.9	± 0.9	± 1.0	± 1.2	± 3.8
Stat.	± 6.9	± 4.2	± 3.9	± 4.1	± 3.7	± 4.4	± 4.4	± 4.7	± 4.9	± 5.5
Total Syst.	± 38.8	± 16.1	± 13.6	± 8.7	± 10.2	± 8.4	± 8.2	± 12.1	± 11.6	± 23.2
Total	± 39.4	± 16.7	± 14.2	± 9.6	± 10.8	± 9.5	± 9.3	± 13.0	± 12.5	± 23.9

Table B.26: (μ +jets). Systematic and statistical uncertainties for the IP3D+SV1 tagger at a working point corresponding to a 70% b -tagging efficiency.

$p_T[GeV]$	25-30	30-40	40-50	50-60	60-75	75-90	90-110	110-140	140-200	200-300
ISR/FSR	± 2.3	± 2.0	± 3.2	± 3.3	± 2.5	± 2.5	± 3.3	± 1.9	± 2.9	± 7.5
Generator	± 3.9	± 1.4	± 0.3	± 1.8	± 5.7	± 0.6	± 5.7	± 2.0	± 2.7	± 1.2
Fragmentation	± 2.3	± 5.3	± 5.0	± 4.8	± 3.9	± 1.6	± 1.2	± 6.4	± 4.2	± 5.4
Diboson	± 0.5	± 0.5	± 0.1	± 0.1	± 0.1	± 0.6	± 0.5	± 0.9	± 0.9	± 0.1
single top	± 0.5	± 0.4	± 0.4	± 0.2	± 0.3	± 0.6	± 0.7	± 1.1	± 1.1	± 0.3
Z + jets	± 1.0	± 0.3	± 0.3	± 0.2	± 0.3	± 0.5	± 0.6	± 1.0	± 0.7	± 0.9
W + jets	± 1.1	± 0.3	± 0.3	± 0.3	± 0.2	± 0.6	± 0.5	± 0.8	± 0.9	± 1.2
Multijets	± 1.7	± 3.2	± 4.0	± 1.1	± 1.8	± 4.1	± 2.3	± 10.2	± 0.6	± 2.3
JES	± 2.6	± 4.9	± 1.9	± 2.0	± 3.2	± 6.6	± 5.2	± 7.2	± 8.5	± 18.1
JER	± 2.0	± 9.4	± 11.9	± 4.5	± 1.0	± 1.6	± 3.7	± 3.8	± 4.2	± 4.3
JRE	± 0.9	± 0.5	± 0.2	± 0.1	± 0.2	± 0.6	± 0.8	± 0.7	± 0.7	± 0.4
JVF	± 1.9	± 0.3	± 0.3	± 0.2	± 0.1	± 0.6	± 0.8	± 1.0	± 1.0	± 2.6
W+HF SF	± 0.9	± 0.7	± 0.4	± 0.2	± 0.4	± 0.8	± 0.9	± 1.4	± 1.3	± 0.6
ε_c	± 2.9	± 1.8	± 2.0	± 1.5	± 2.3	± 1.5	± 1.7	± 1.4	± 1.3	± 2.1
ε_{light}	± 1.3	± 0.9	± 0.6	± 0.2	± 0.4	± 0.5	± 0.8	± 0.9	± 0.9	± 1.4
E_T^{miss} cellout	± 0.4	± 0.4	± 0.5	± 0.3	± 0.1	± 0.6	± 0.6	± 0.7	± 0.9	± 0.2
E_T^{miss} pileup	± 0.5	± 0.4	± 0.3	± 0.1	± 0.3	± 0.5	± 0.4	± 0.7	± 0.9	± 0.3
e trigger	± 0.5	± 0.7	± 0.3	± 0.0	± 0.2	± 0.5	± 0.5	± 1.0	± 1.0	± 0.2
e smearing	± 0.5	± 0.5	± 0.3	± 0.1	± 0.1	± 0.7	± 0.5	± 1.1	± 0.7	± 0.5
e recID	± 1.1	± 0.4	± 0.4	± 0.3	± 0.2	± 0.5	± 0.6	± 0.8	± 0.8	± 1.0
MC e -energy scale	± 0.5	± 0.4	± 0.2	± 0.1	± 0.1	± 0.4	± 0.7	± 0.8	± 0.7	± 0.1
μ trigger	± 0.8	± 0.4	± 0.2	± 0.2	± 0.3	± 0.5	± 0.5	± 0.9	± 1.0	± 0.5
μ smearing	± 0.4	± 0.4	± 0.3	± 0.3	± 0.3	± 0.4	± 0.5	± 0.5	± 0.5	± 0.2
μ recID	± 0.5	± 0.5	± 0.3	± 0.1	± 0.2	± 0.5	± 0.5	± 0.8	± 0.8	± 0.2
MC μ -en. sc.	± 0.6	± 0.4	± 0.6	± 0.1	± 0.2	± 0.3	± 0.5	± 0.9	± 1.1	± 0.1
Lumi	± 3.5	± 1.2	± 0.8	± 1.0	± 0.5	± 1.0	± 1.4	± 1.3	± 1.9	± 3.6
Stat.	± 4.7	± 4.4	± 4.2	± 4.4	± 4.0	± 4.6	± 4.5	± 4.7	± 4.7	± 4.9
Total Syst.	± 8.5	± 12.9	± 14.3	± 8.1	± 8.6	± 9.0	± 10.1	± 15.4	± 11.9	± 21.3
Total	± 9.7	± 13.6	± 14.9	± 9.3	± 9.5	± 10.1	± 11.1	± 16.1	± 12.8	± 21.8

Table B.27: (μ +jets). Systematic and statistical uncertainties for the IP3D+SV1 tagger at a working point corresponding to a 60% b -tagging efficiency.

$p_T[GeV]$	25-30	30-40	40-50	50-60	60-75	75-90	90-110	110-140	140-200	200-300
ISR/FSR	± 3.6	± 2.1	± 3.1	± 3.7	± 3.5	± 2.8	± 3.8	± 1.9	± 4.4	± 7.4
Generator	± 3.2	± 2.5	± 0.2	± 1.2	± 6.5	± 0.6	± 7.1	± 0.2	± 0.8	± 0.7
Fragmentation	± 4.3	± 6.8	± 3.5	± 4.0	± 2.4	± 5.3	± 2.2	± 3.3	± 3.2	± 4.0
Diboson	± 0.8	± 0.4	± 0.0	± 0.3	± 0.3	± 0.2	± 0.4	± 0.4	± 0.8	± 0.1
single top	± 1.1	± 0.4	± 0.2	± 0.3	± 0.3	± 0.5	± 0.3	± 0.6	± 1.0	± 0.3
Z + jets	± 1.0	± 0.3	± 0.3	± 0.2	± 0.5	± 0.5	± 0.3	± 0.4	± 0.9	± 0.6
W + jets	± 2.7	± 0.3	± 0.4	± 0.3	± 0.4	± 0.5	± 0.1	± 0.4	± 1.0	± 0.9
Multijets	± 9.2	± 2.0	± 4.2	± 3.4	± 1.0	± 4.6	± 3.7	± 6.0	± 0.7	± 4.4
JES	± 20.2	± 5.3	± 2.7	± 1.1	± 2.7	± 6.0	± 4.4	± 7.2	± 7.9	± 17.7
JER	± 7.4	± 10.2	± 11.4	± 4.0	± 1.8	± 1.9	± 3.2	± 4.2	± 4.4	± 4.2
JRE	± 1.5	± 0.5	± 0.0	± 0.2	± 0.3	± 0.0	± 0.2	± 0.2	± 0.7	± 0.1
JVF	± 16.0	± 0.3	± 0.1	± 0.1	± 0.2	± 0.4	± 0.3	± 0.5	± 0.8	± 2.4
W+HF SF	± 1.3	± 0.5	± 0.3	± 0.4	± 0.5	± 0.5	± 0.4	± 0.7	± 1.5	± 0.6
ε_c	± 3.0	± 1.8	± 2.0	± 1.6	± 1.8	± 1.5	± 2.1	± 1.2	± 1.4	± 2.1
ε_{light}	± 16.6	± 0.6	± 0.3	± 0.5	± 0.5	± 0.7	± 0.2	± 0.4	± 0.7	± 1.2
E_T^{miss} cellout	± 0.6	± 0.2	± 0.4	± 0.4	± 0.3	± 0.3	± 0.1	± 0.5	± 0.9	± 0.2
E_T^{miss} pileup	± 0.9	± 0.4	± 0.2	± 0.1	± 0.4	± 0.3	± 0.5	± 0.4	± 0.7	± 0.2
e trigger	± 1.0	± 0.3	± 0.2	± 0.4	± 0.3	± 0.4	± 0.2	± 0.5	± 0.9	± 0.2
e smearing	± 0.4	± 0.1	± 0.2	± 0.3	± 0.3	± 0.3	± 0.1	± 0.5	± 0.8	± 0.3
e recID	± 1.3	± 0.2	± 0.3	± 0.3	± 0.3	± 0.3	± 0.4	± 0.5	± 0.9	± 0.9
MC e -energy scale	± 0.5	± 0.3	± 0.1	± 0.3	± 0.2	± 0.2	± 0.1	± 0.6	± 1.0	± 0.2
μ trigger	± 0.8	± 0.4	± 0.1	± 0.2	± 0.3	± 0.3	± 0.3	± 0.7	± 1.0	± 0.7
μ smearing	± 0.6	± 0.3	± 0.3	± 0.2	± 0.2	± 0.3	± 0.3	± 0.4	± 0.5	± 0.4
μ recID	± 0.8	± 0.3	± 0.0	± 0.2	± 0.2	± 0.3	± 0.2	± 0.6	± 0.9	± 0.3
MC μ -en. sc.	± 1.0	± 0.2	± 0.0	± 0.2	± 0.3	± 0.2	± 0.3	± 0.4	± 0.9	± 0.1
Lumi	± 2.7	± 0.7	± 0.5	± 0.8	± 0.4	± 0.7	± 0.8	± 1.4	± 1.4	± 3.5
Stat.	± 6.5	± 4.1	± 4.2	± 4.3	± 3.7	± 4.4	± 4.6	± 4.7	± 4.8	± 5.2
Total Syst.	± 34.0	± 14.1	± 13.5	± 8.0	± 8.8	± 10.1	± 10.9	± 11.3	± 11.4	± 20.8
Total	± 34.6	± 14.7	± 14.1	± 9.1	± 9.5	± 11.0	± 11.9	± 12.2	± 12.4	± 21.4

Table B.28: (μ +jets). Systematic and statistical uncertainties for the JetFitterCOMBNN tagger at a working point corresponding to a 70% b -tagging efficiency.

$p_T[GeV]$	25-30	30-40	40-50	50-60	60-75	75-90	90-110	110-140	140-200	200-300
ISR/FSR	± 3.9	± 2.9	± 3.2	± 3.5	± 3.1	± 1.7	± 3.0	± 1.9	± 4.5	± 6.0
Generator	± 5.2	± 3.5	± 0.1	± 0.1	± 6.7	± 0.3	± 5.6	± 1.3	± 0.3	± 1.2
Fragmentation	± 4.0	± 7.4	± 4.5	± 4.6	± 2.1	± 3.3	± 1.5	± 7.4	± 3.7	± 2.3
Diboson	± 0.1	± 0.3	± 0.1	± 0.2	± 0.0	± 0.9	± 0.4	± 0.9	± 0.0	± 0.1
single top	± 0.5	± 0.5	± 0.2	± 0.4	± 0.3	± 1.1	± 0.5	± 1.3	± 0.2	± 0.4
Z + jets	± 0.5	± 0.6	± 0.6	± 0.5	± 0.6	± 0.8	± 0.3	± 0.9	± 0.3	± 0.9
W + jets	± 1.6	± 1.1	± 0.7	± 0.6	± 0.7	± 1.1	± 0.5	± 0.9	± 0.3	± 1.4
Multijets	± 1.5	± 2.0	± 2.4	± 4.0	± 1.6	± 1.6	± 4.2	± 0.1	± 0.5	± 3.5
JES	± 13.4	± 4.5	± 4.2	± 1.3	± 2.4	± 4.4	± 4.2	± 5.2	± 6.5	± 16.6
JER	± 9.3	± 10.0	± 12.1	± 3.9	± 0.3	± 0.0	± 1.6	± 3.3	± 4.5	± 5.1
JRE	± 0.2	± 0.5	± 0.0	± 0.2	± 0.0	± 0.6	± 0.4	± 0.6	± 0.2	± 0.3
JVF	± 10.2	± 0.3	± 0.2	± 0.4	± 0.2	± 1.0	± 0.4	± 0.8	± 0.2	± 2.1
W+HF SF	± 0.6	± 0.7	± 0.3	± 0.6	± 0.2	± 1.5	± 0.7	± 1.3	± 0.3	± 0.3
ε_c	± 3.4	± 2.9	± 2.6	± 2.1	± 1.8	± 1.6	± 2.3	± 1.5	± 2.0	± 2.0
ε_{light}	± 11.7	± 2.3	± 1.7	± 1.1	± 0.7	± 1.0	± 0.6	± 1.0	± 0.4	± 2.7
E_T^{miss} cellout	± 0.2	± 0.3	± 0.2	± 0.4	± 0.1	± 0.9	± 0.4	± 1.0	± 0.3	± 0.2
E_T^{miss} pileup	± 0.2	± 0.5	± 0.1	± 0.3	± 0.1	± 0.9	± 0.4	± 0.9	± 0.1	± 0.3
e trigger	± 0.4	± 0.4	± 0.1	± 0.2	± 0.1	± 0.9	± 0.3	± 1.0	± 0.1	± 0.2
e smearing	± 0.4	± 0.3	± 0.1	± 0.3	± 0.1	± 1.0	± 0.6	± 0.9	± 0.2	± 0.5
e recID	± 0.8	± 0.5	± 0.2	± 0.3	± 0.0	± 1.0	± 0.4	± 1.0	± 0.3	± 0.9
MC e -energy scale	± 0.2	± 0.6	± 0.1	± 0.4	± 0.1	± 1.0	± 0.3	± 0.8	± 0.1	± 0.4
μ trigger	± 0.2	± 0.3	± 0.1	± 0.2	± 0.1	± 0.8	± 0.5	± 0.7	± 0.4	± 0.5
μ smearing	± 0.5	± 0.4	± 0.3	± 0.3	± 0.2	± 0.5	± 0.4	± 0.5	± 0.3	± 0.4
μ recID	± 0.2	± 0.6	± 0.2	± 0.3	± 0.1	± 0.7	± 0.5	± 0.8	± 0.1	± 0.2
MC μ -en. sc.	± 0.2	± 0.3	± 0.0	± 0.1	± 0.2	± 1.1	± 0.4	± 0.9	± 0.3	± 0.2
Lumi	± 2.1	± 0.4	± 0.4	± 0.4	± 0.1	± 0.8	± 0.5	± 0.9	± 1.1	± 3.1
Stat.	± 6.3	± 3.8	± 3.6	± 4.0	± 3.4	± 4.1	± 4.4	± 4.5	± 4.7	± 5.7
Total Syst.	± 24.2	± 14.7	± 14.5	± 8.7	± 8.5	± 7.4	± 9.5	± 10.8	± 10.2	± 19.0
Total	± 25.1	± 15.2	± 15.0	± 9.6	± 9.1	± 8.5	± 10.4	± 11.7	± 11.2	± 19.9

Table B.29: (μ +jets). Systematic and statistical uncertainties for the JetFitterCOMBNN tagger at a working point corresponding to a 80% b -tagging efficiency.

$p_T[GeV]$	25-30	30-40	40-50	50-60	60-75	75-90	90-110	110-140	140-200	200-300
ISR/FSR	± 2.8	± 1.7	± 3.7	± 3.7	± 3.8	± 2.7	± 3.5	± 1.9	± 3.5	± 7.5
Generator	± 5.2	± 2.0	± 0.5	± 1.3	± 5.1	± 0.8	± 7.7	± 0.3	± 2.2	± 0.8
Fragmentation	± 1.9	± 3.8	± 4.3	± 5.0	± 1.9	± 2.9	± 3.5	± 4.3	± 3.4	± 3.2
Diboson	± 1.4	± 0.2	± 0.0	± 0.3	± 0.4	± 0.4	± 0.1	± 0.6	± 0.9	± 0.1
single top	± 1.7	± 0.2	± 0.2	± 0.5	± 0.4	± 0.5	± 0.4	± 0.9	± 1.2	± 0.4
Z + jets	± 1.6	± 0.1	± 0.0	± 0.3	± 0.4	± 0.7	± 0.2	± 0.5	± 1.0	± 0.8
W + jets	± 3.5	± 0.1	± 0.2	± 0.4	± 0.4	± 0.3	± 0.5	± 0.9	± 0.7	± 1.0
Multijets	± 17.3	± 1.9	± 3.1	± 0.1	± 0.9	± 6.2	± 4.1	± 10.3	± 0.2	± 5.4
JES	± 27.9	± 4.3	± 1.6	± 1.7	± 3.0	± 6.3	± 6.0	± 8.2	± 9.8	± 17.3
JER	± 22.8	± 9.3	± 10.2	± 3.5	± 1.1	± 2.1	± 4.0	± 4.8	± 4.0	± 3.3
JRE	± 1.7	± 0.2	± 0.2	± 0.5	± 0.2	± 0.4	± 0.3	± 0.4	± 1.0	± 0.2
JVF	± 22.2	± 0.5	± 0.1	± 0.3	± 0.3	± 0.6	± 0.4	± 0.8	± 0.9	± 3.1
W+HF SF	± 2.3	± 0.3	± 0.3	± 0.7	± 0.7	± 0.8	± 0.6	± 1.1	± 1.6	± 0.5
ε_c	± 2.6	± 1.5	± 1.8	± 1.4	± 1.9	± 1.4	± 2.0	± 1.3	± 1.5	± 2.4
ε_{light}	± 34.4	± 0.4	± 0.3	± 0.3	± 0.4	± 0.6	± 0.4	± 0.7	± 0.9	± 1.0
E_T^{miss} cellout	± 1.4	± 0.1	± 0.3	± 0.2	± 0.4	± 0.5	± 0.2	± 0.6	± 0.9	± 0.3
E_T^{miss} pileup	± 1.3	± 0.2	± 0.1	± 0.3	± 0.2	± 0.5	± 0.3	± 0.8	± 0.9	± 0.4
e trigger	± 1.5	± 0.1	± 0.0	± 0.5	± 0.4	± 0.4	± 0.3	± 0.5	± 0.8	± 0.3
e smearing	± 1.0	± 0.2	± 0.1	± 0.4	± 0.3	± 0.4	± 0.4	± 0.7	± 1.1	± 0.3
e recID	± 2.1	± 0.5	± 0.2	± 0.2	± 0.3	± 0.6	± 0.4	± 0.6	± 0.8	± 1.3
MC e -energy scale	± 1.2	± 0.1	± 0.1	± 0.4	± 0.5	± 0.3	± 0.3	± 0.6	± 0.9	± 0.1
μ trigger	± 1.6	± 0.4	± 0.2	± 0.3	± 0.5	± 0.4	± 0.3	± 0.5	± 0.9	± 0.6
μ smearing	± 0.6	± 0.4	± 0.2	± 0.4	± 0.3	± 0.4	± 0.4	± 0.4	± 0.5	± 0.3
μ recID	± 1.3	± 0.2	± 0.1	± 0.4	± 0.5	± 0.5	± 0.5	± 0.5	± 1.0	± 0.4
MC μ -en. sc.	± 1.3	± 0.1	± 0.0	± 0.5	± 0.3	± 0.5	± 0.2	± 0.8	± 1.0	± 0.1
Lumi	± 3.5	± 1.1	± 0.8	± 1.0	± 0.6	± 1.3	± 1.3	± 1.4	± 2.0	± 3.8
Stat.	± 7.3	± 4.4	± 4.3	± 4.4	± 4.0	± 4.5	± 4.6	± 4.7	± 5.0	± 4.8
Total Syst.	± 58.1	± 11.7	± 12.4	± 7.8	± 7.9	± 10.4	± 12.7	± 15.1	± 12.8	± 20.7
Total	± 58.6	± 12.4	± 13.1	± 9.0	± 8.9	± 11.3	± 13.5	± 15.8	± 13.8	± 21.3

Table B.30: (μ +jets). Systematic and statistical uncertainties for the JetFitterCOMBNN tagger at a working point corresponding to a 60% b -tagging efficiency.

$p_T[GeV]$	25-30	30-40	40-50	50-60	60-75	75-90	90-110	110-140	140-200	200-300
ISR/FSR	± 2.7	± 2.3	± 4.0	± 3.6	± 3.6	± 2.6	± 3.8	± 2.0	± 3.5	± 7.2
Generator	± 5.7	± 3.0	± 1.3	± 1.3	± 4.7	± 0.8	± 7.8	± 0.2	± 1.8	± 0.5
Fragmentation	± 2.6	± 5.1	± 5.6	± 4.5	± 2.8	± 3.0	± 2.8	± 4.7	± 4.0	± 3.5
Diboson	± 1.6	± 0.5	± 0.1	± 0.3	± 0.1	± 0.3	± 0.5	± 0.5	± 0.9	± 0.1
single top	± 1.7	± 0.5	± 0.1	± 0.2	± 0.2	± 0.3	± 0.5	± 0.5	± 1.2	± 0.4
Z + jets	± 1.6	± 0.4	± 0.1	± 0.2	± 0.2	± 0.1	± 0.4	± 0.6	± 0.9	± 0.8
W + jets	± 3.7	± 0.3	± 0.2	± 0.4	± 0.2	± 0.1	± 0.3	± 0.2	± 1.1	± 0.9
Multijets	± 15.7	± 5.0	± 5.7	± 3.4	± 1.8	± 7.1	± 5.7	± 13.2	± 0.7	± 3.6
JES	± 29.0	± 4.2	± 1.4	± 2.0	± 3.6	± 6.8	± 6.6	± 8.4	± 10.0	± 17.5
JER	± 24.5	± 10.4	± 10.7	± 3.5	± 1.0	± 3.1	± 3.9	± 4.7	± 3.9	± 2.9
JRE	± 1.5	± 0.3	± 0.3	± 0.2	± 0.1	± 0.1	± 0.6	± 0.0	± 1.0	± 0.2
JVF	± 23.5	± 0.4	± 0.1	± 0.3	± 0.2	± 0.3	± 0.4	± 0.7	± 0.8	± 3.4
W+HF SF	± 2.5	± 0.5	± 0.3	± 0.5	± 0.3	± 0.4	± 0.7	± 0.7	± 1.6	± 0.4
ε_c	± 2.3	± 1.7	± 1.8	± 1.4	± 2.0	± 1.5	± 2.2	± 1.5	± 1.6	± 2.3
ε_{light}	± 41.6	± 0.3	± 0.1	± 0.2	± 0.2	± 0.1	± 0.1	± 0.4	± 0.8	± 1.5
E_T^{miss} cellout	± 1.6	± 0.3	± 0.2	± 0.2	± 0.2	± 0.2	± 0.3	± 0.5	± 1.0	± 0.3
E_T^{miss} pileup	± 1.3	± 0.3	± 0.1	± 0.3	± 0.1	± 0.3	± 0.3	± 0.6	± 0.9	± 0.3
e trigger	± 1.4	± 0.3	± 0.2	± 0.2	± 0.2	± 0.2	± 0.5	± 0.4	± 1.1	± 0.3
e smearing	± 1.7	± 0.3	± 0.2	± 0.5	± 0.2	± 0.1	± 0.5	± 0.3	± 1.1	± 0.6
e recID	± 1.6	± 0.5	± 0.3	± 0.3	± 0.1	± 0.3	± 0.5	± 0.7	± 1.0	± 1.2
MC e -energy scale	± 1.7	± 0.5	± 0.1	± 0.3	± 0.1	± 0.2	± 0.3	± 0.5	± 1.0	± 0.3
μ trigger	± 1.3	± 0.3	± 0.1	± 0.2	± 0.3	± 0.1	± 0.3	± 0.5	± 1.0	± 0.9
μ smearing	± 0.6	± 0.4	± 0.4	± 0.3	± 0.2	± 0.2	± 0.3	± 0.3	± 0.5	± 0.3
μ recID	± 1.5	± 0.5	± 0.3	± 0.0	± 0.2	± 0.2	± 0.4	± 0.4	± 1.0	± 0.3
MC μ -en. sc.	± 1.6	± 0.4	± 0.0	± 0.2	± 0.1	± 0.2	± 0.3	± 0.3	± 0.9	± 0.2
Lumi	± 3.6	± 1.1	± 0.8	± 1.1	± 0.7	± 1.3	± 1.5	± 1.7	± 2.0	± 3.8
Stat.	± 7.3	± 4.4	± 4.2	± 4.5	± 4.0	± 4.5	± 4.7	± 4.6	± 4.8	± 4.7
Total Syst.	± 63.9	± 14.1	± 14.2	± 8.2	± 8.1	± 11.3	± 13.6	± 17.4	± 13.1	± 20.6
Total	± 64.3	± 14.7	± 14.8	± 9.4	± 9.0	± 12.2	± 14.4	± 18.0	± 13.9	± 21.1

Table B.31: (μ +jets). Systematic and statistical uncertainties for the JetFitterCOMBNN tagger at a working point corresponding to a 57% b -tagging efficiency.

$p_T[GeV]$	25-30	30-40	40-50	50-60	60-75	75-90	90-110	110-140	140-200	200-300
ISR/FSR	± 4.4	± 3.3	± 2.5	± 3.4	± 2.3	± 1.8	± 2.5	± 1.5	± 3.4	± 3.5
Generator	± 0.9	± 4.6	± 0.1	± 0.3	± 6.1	± 0.4	± 4.8	± 0.6	± 0.8	± 0.1
Fragmentation	± 6.4	± 7.3	± 3.2	± 5.6	± 1.4	± 4.3	± 1.3	± 5.5	± 2.8	± 2.6
Diboson	± 1.2	± 0.7	± 0.2	± 0.2	± 0.3	± 0.4	± 0.4	± 1.0	± 0.3	± 0.1
single top	± 1.6	± 0.9	± 0.3	± 0.2	± 0.5	± 0.4	± 0.4	± 1.3	± 0.4	± 0.6
Z + jets	± 1.1	± 1.2	± 1.0	± 0.8	± 1.0	± 0.3	± 0.7	± 1.0	± 0.3	± 1.1
W + jets	± 1.4	± 1.1	± 1.4	± 0.9	± 1.1	± 0.8	± 0.9	± 1.1	± 0.8	± 1.2
Multijets	± 13.7	± 1.5	± 2.0	± 8.4	± 2.8	± 2.1	± 4.7	± 6.7	± 4.8	± 7.4
JES	± 8.7	± 4.3	± 5.5	± 1.9	± 1.4	± 3.9	± 3.0	± 4.5	± 5.0	± 11.2
JER	± 13.6	± 6.3	± 12.2	± 4.6	± 0.6	± 0.9	± 1.3	± 2.7	± 3.8	± 5.3
JRE	± 0.4	± 0.4	± 0.3	± 0.1	± 0.3	± 0.1	± 0.2	± 0.9	± 0.1	± 0.1
JVF	± 7.1	± 1.8	± 0.7	± 0.2	± 0.3	± 0.6	± 0.3	± 1.0	± 0.2	± 1.2
W+HF SF	± 1.9	± 1.3	± 0.5	± 0.3	± 0.6	± 0.5	± 0.6	± 1.7	± 0.6	± 0.3
ε_c	± 3.1	± 2.6	± 2.4	± 1.8	± 2.2	± 2.0	± 2.0	± 1.9	± 2.3	± 2.9
ε_{light}	± 10.7	± 4.4	± 1.5	± 1.4	± 1.0	± 1.1	± 0.8	± 1.0	± 0.9	± 3.7
E_T^{miss} cellout	± 1.2	± 0.7	± 0.3	± 0.2	± 0.2	± 0.2	± 0.4	± 1.0	± 0.2	± 0.2
E_T^{miss} pileup	± 1.1	± 0.8	± 0.3	± 0.2	± 0.2	± 0.2	± 0.4	± 0.9	± 0.1	± 0.3
e trigger	± 1.2	± 0.8	± 0.2	± 0.1	± 0.5	± 0.1	± 0.3	± 0.9	± 0.2	± 0.4
e smearing	± 1.5	± 0.7	± 0.3	± 0.1	± 0.3	± 0.2	± 0.3	± 0.9	± 0.2	± 0.2
e recID	± 1.2	± 0.7	± 0.1	± 0.1	± 0.4	± 0.2	± 0.2	± 1.0	± 0.2	± 0.5
MC e -energy scale	± 1.3	± 0.7	± 0.3	± 0.0	± 0.4	± 0.3	± 0.4	± 1.0	± 0.2	± 0.2
μ trigger	± 1.1	± 0.9	± 0.3	± 0.1	± 0.4	± 0.1	± 0.4	± 0.8	± 0.3	± 0.4
μ smearing	± 0.6	± 0.5	± 0.3	± 0.4	± 0.4	± 0.3	± 0.3	± 0.5	± 0.3	± 0.4
μ recID	± 1.2	± 0.7	± 0.1	± 0.1	± 0.4	± 0.2	± 0.3	± 0.9	± 0.3	± 0.1
MC μ -en. sc.	± 0.9	± 0.6	± 0.2	± 0.0	± 0.2	± 0.1	± 0.4	± 1.0	± 0.1	± 0.3
Lumi	± 1.9	± 0.9	± 0.2	± 0.1	± 0.3	± 0.3	± 0.2	± 1.2	± 0.7	± 2.9
Stat.	± 6.5	± 3.7	± 3.6	± 3.9	± 3.3	± 4.0	± 4.3	± 4.4	± 4.6	± 5.7
Total Syst.	± 26.7	± 13.7	± 14.6	± 12.0	± 8.1	± 7.1	± 8.4	± 11.3	± 9.5	± 15.3
Total	± 27.4	± 14.2	± 15.0	± 12.6	± 8.7	± 8.1	± 9.5	± 12.2	± 10.6	± 16.3

Table B.32: (μ +jets). Systematic and statistical uncertainties for the MV1 tagger at a working point corresponding to a 85% b -tagging efficiency.

$p_T[GeV]$	25-30	30-40	40-50	50-60	60-75	75-90	90-110	110-140	140-200	200-300
ISR/FSR	± 3.6	± 2.8	± 2.8	± 3.3	± 2.9	± 2.2	± 3.6	± 1.7	± 4.4	± 6.9
Generator	± 3.5	± 2.8	± 0.8	± 0.9	± 6.1	± 0.2	± 6.2	± 1.3	± 0.4	± 1.2
Fragmentation	± 3.6	± 9.0	± 3.1	± 3.3	± 2.0	± 3.0	± 3.1	± 5.0	± 4.2	± 4.4
Diboson	± 0.2	± 0.4	± 0.4	± 0.1	± 0.2	± 0.9	± 0.1	± 0.6	± 0.7	± 0.2
single top	± 0.5	± 0.5	± 0.5	± 0.1	± 0.2	± 0.9	± 0.2	± 0.8	± 0.8	± 0.4
Z + jets	± 0.5	± 0.5	± 0.4	± 0.3	± 0.5	± 1.0	± 0.2	± 0.7	± 0.6	± 0.7
W + jets	± 2.2	± 0.5	± 0.4	± 0.3	± 0.5	± 0.9	± 0.2	± 0.7	± 0.3	± 0.8
Multijets	± 14.5	± 2.1	± 3.9	± 3.5	± 3.5	± 4.4	± 0.8	± 5.3	± 2.1	± 6.9
JES	± 17.8	± 5.8	± 3.5	± 0.6	± 2.3	± 5.9	± 4.0	± 6.2	± 6.8	± 16.9
JER	± 9.0	± 12.3	± 11.2	± 4.0	± 0.7	± 0.0	± 3.1	± 4.0	± 4.2	± 4.6
JRE	± 0.4	± 0.5	± 0.5	± 0.1	± 0.3	± 0.7	± 0.3	± 0.4	± 0.3	± 0.2
JVF	± 14.2	± 0.4	± 0.3	± 0.1	± 0.2	± 0.7	± 0.2	± 0.7	± 0.6	± 2.0
W+HF SF	± 0.8	± 0.7	± 0.6	± 0.3	± 0.3	± 1.4	± 0.3	± 1.0	± 0.9	± 0.4
ε_c	± 3.4	± 2.3	± 1.9	± 1.7	± 1.8	± 1.5	± 1.9	± 1.4	± 1.5	± 2.4
ε_{light}	± 12.2	± 1.5	± 0.8	± 0.7	± 0.7	± 0.8	± 0.5	± 0.7	± 0.7	± 1.3
E_T^{miss} cellout	± 0.3	± 0.4	± 0.4	± 0.1	± 0.1	± 0.7	± 0.1	± 0.4	± 0.4	± 0.2
E_T^{miss} pileup	± 0.7	± 0.5	± 0.2	± 0.0	± 0.2	± 0.8	± 0.2	± 0.8	± 0.5	± 0.4
e trigger	± 0.3	± 0.4	± 0.3	± 0.2	± 0.2	± 0.7	± 0.2	± 0.8	± 0.5	± 0.1
e smearing	± 0.6	± 0.3	± 0.2	± 0.2	± 0.1	± 0.8	± 0.1	± 0.9	± 0.5	± 0.2
e recID	± 1.1	± 0.4	± 0.3	± 0.1	± 0.2	± 0.7	± 0.2	± 0.7	± 0.6	± 1.1
MC e -energy scale	± 0.4	± 0.4	± 0.3	± 0.2	± 0.1	± 0.7	± 0.1	± 0.6	± 0.5	± 0.2
μ trigger	± 0.3	± 0.5	± 0.4	± 0.2	± 0.1	± 0.5	± 0.2	± 0.8	± 0.4	± 0.6
μ smearing	± 0.8	± 0.4	± 0.3	± 0.3	± 0.3	± 0.5	± 0.4	± 0.5	± 0.5	± 0.3
μ recID	± 0.2	± 0.5	± 0.3	± 0.1	± 0.0	± 0.9	± 0.3	± 0.7	± 0.6	± 0.1
MC μ -en. sc.	± 0.1	± 0.7	± 0.2	± 0.0	± 0.0	± 0.7	± 0.0	± 0.6	± 0.6	± 0.3
Lumi	± 2.4	± 0.6	± 0.4	± 0.4	± 0.3	± 0.7	± 0.8	± 1.0	± 1.2	± 3.4
Stat.	± 6.3	± 4.0	± 3.8	± 4.0	± 3.5	± 4.1	± 4.4	± 4.6	± 4.9	± 5.2
Total Syst.	± 31.9	± 17.3	± 13.3	± 7.4	± 8.5	± 9.1	± 9.6	± 11.2	± 10.7	± 20.8
Total	± 32.6	± 17.7	± 13.9	± 8.4	± 9.2	± 10.0	± 10.5	± 12.1	± 11.8	± 21.4

Table B.33: (μ +jets). Systematic and statistical uncertainties for the MV1 tagger at a working point corresponding to a 75% b -tagging efficiency.

$p_T[GeV]$	25-30	30-40	40-50	50-60	60-75	75-90	90-110	110-140	140-200	200-300
ISR/FSR	± 4.0	± 2.5	± 2.8	± 3.1	± 2.9	± 2.1	± 3.5	± 2.1	± 4.2	± 7.9
Generator	± 3.7	± 2.7	± 0.1	± 0.6	± 5.9	± 0.6	± 6.4	± 1.6	± 0.6	± 1.0
Fragmentation	± 2.3	± 8.0	± 2.9	± 3.7	± 2.9	± 3.4	± 2.4	± 4.1	± 3.5	± 4.4
Diboson	± 0.7	± 0.4	± 0.0	± 0.1	± 0.2	± 0.3	± 0.3	± 0.7	± 0.7	± 0.1
single top	± 0.7	± 0.5	± 0.1	± 0.3	± 0.1	± 0.2	± 0.3	± 0.8	± 0.9	± 0.4
Z + jets	± 1.3	± 0.3	± 0.3	± 0.2	± 0.3	± 0.2	± 0.2	± 0.6	± 0.6	± 0.6
W + jets	± 2.5	± 0.4	± 0.3	± 0.3	± 0.2	± 0.5	± 0.3	± 0.7	± 0.5	± 1.1
Multijets	± 9.9	± 1.4	± 4.3	± 2.9	± 1.2	± 6.7	± 3.3	± 4.0	± 1.3	± 4.1
JES	± 21.0	± 6.2	± 3.3	± 1.0	± 2.3	± 6.3	± 4.8	± 7.0	± 7.4	± 17.3
JER	± 14.1	± 9.8	± 11.1	± 3.8	± 0.8	± 1.4	± 3.2	± 4.0	± 4.8	± 4.2
JRE	± 0.8	± 0.5	± 0.1	± 0.2	± 0.2	± 0.0	± 0.2	± 0.3	± 0.2	± 0.1
JVF	± 16.6	± 0.4	± 0.2	± 0.1	± 0.3	± 0.3	± 0.3	± 0.8	± 0.7	± 2.2
W+HF SF	± 0.9	± 0.7	± 0.2	± 0.4	± 0.3	± 0.5	± 0.4	± 1.1	± 1.0	± 0.4
ε_c	± 3.5	± 1.8	± 1.9	± 1.7	± 1.6	± 1.4	± 2.0	± 1.2	± 1.3	± 2.1
ε_{light}	± 14.4	± 1.1	± 0.6	± 0.5	± 0.8	± 0.6	± 0.3	± 0.8	± 0.6	± 1.1
E_T^{miss} cellout	± 0.6	± 0.3	± 0.1	± 0.3	± 0.2	± 0.4	± 0.2	± 0.7	± 0.6	± 0.0
E_T^{miss} pileup	± 0.6	± 0.5	± 0.2	± 0.2	± 0.2	± 0.2	± 0.1	± 0.7	± 0.6	± 0.1
e trigger	± 0.6	± 0.5	± 0.1	± 0.2	± 0.1	± 0.2	± 0.1	± 0.7	± 0.6	± 0.3
e smearing	± 0.4	± 0.3	± 0.2	± 0.2	± 0.0	± 0.2	± 0.3	± 0.7	± 0.9	± 0.3
e recID	± 1.3	± 0.2	± 0.2	± 0.4	± 0.3	± 0.3	± 0.3	± 0.7	± 0.7	± 1.0
MC e -energy scale	± 0.6	± 0.4	± 0.1	± 0.1	± 0.1	± 0.2	± 0.3	± 0.6	± 0.6	± 0.2
μ trigger	± 0.8	± 0.7	± 0.2	± 0.3	± 0.1	± 0.2	± 0.1	± 0.6	± 0.8	± 0.6
μ smearing	± 0.5	± 0.4	± 0.2	± 0.4	± 0.3	± 0.3	± 0.3	± 0.5	± 0.5	± 0.4
μ recID	± 1.0	± 0.2	± 0.1	± 0.2	± 0.1	± 0.2	± 0.2	± 0.8	± 0.8	± 0.1
MC μ -en. sc.	± 0.8	± 0.4	± 0.1	± 0.2	± 0.2	± 0.6	± 0.0	± 0.7	± 0.8	± 0.1
Lumi	± 2.9	± 0.8	± 0.7	± 0.6	± 0.4	± 0.7	± 0.9	± 1.0	± 1.4	± 3.4
Stat.	± 6.4	± 4.0	± 4.0	± 4.0	± 3.7	± 4.4	± 4.3	± 4.6	± 4.9	± 5.4
Total Syst.	± 35.9	± 15.0	± 13.2	± 7.2	± 8.0	± 10.3	± 10.4	± 10.8	± 11.1	± 20.6
Total	± 36.5	± 15.5	± 13.8	± 8.2	± 8.8	± 11.2	± 11.3	± 11.7	± 12.1	± 21.3

Table B.34: (μ +jets). Systematic and statistical uncertainties for the MV1 tagger at a working point corresponding to a 70% b -tagging efficiency.

$p_T[GeV]$	25-30	30-40	40-50	50-60	60-75	75-90	90-110	110-140	140-200	200-300
ISR/FSR	± 2.3	± 1.9	± 3.5	± 3.3	± 2.9	± 2.5	± 3.7	± 1.7	± 3.6	± 7.4
Generator	± 4.3	± 2.8	± 0.8	± 1.0	± 6.0	± 0.2	± 6.9	± 1.1	± 2.8	± 1.4
Fragmentation	± 2.5	± 5.0	± 3.8	± 4.0	± 2.6	± 2.3	± 1.0	± 5.0	± 3.7	± 3.9
Diboson	± 0.5	± 0.3	± 0.1	± 0.2	± 0.5	± 0.5	± 0.4	± 1.0	± 1.1	± 0.1
single top	± 0.7	± 0.5	± 0.2	± 0.1	± 0.6	± 0.6	± 0.5	± 1.0	± 1.4	± 0.5
Z + jets	± 0.9	± 0.3	± 0.1	± 0.1	± 0.5	± 0.5	± 0.4	± 0.9	± 1.2	± 0.5
W + jets	± 0.9	± 0.5	± 0.4	± 0.2	± 0.3	± 0.5	± 0.4	± 0.8	± 1.0	± 1.0
Multijets	± 6.3	± 2.0	± 6.2	± 0.4	± 1.6	± 2.9	± 0.8	± 12.1	± 2.9	± 2.9
JES	± 2.2	± 5.2	± 1.9	± 1.8	± 3.2	± 7.4	± 5.7	± 8.1	± 9.1	± 17.5
JER	± 4.1	± 10.4	± 10.9	± 3.7	± 1.5	± 1.9	± 4.1	± 4.1	± 3.7	± 3.2
JRE	± 1.0	± 0.2	± 0.0	± 0.2	± 0.5	± 0.3	± 0.5	± 0.5	± 1.0	± 0.1
JVF	± 1.8	± 0.3	± 0.1	± 0.0	± 0.3	± 0.8	± 0.6	± 0.9	± 1.2	± 2.9
W+HF SF	± 0.9	± 0.6	± 0.2	± 0.4	± 0.6	± 0.8	± 0.6	± 1.3	± 1.8	± 0.4
ε_c	± 2.7	± 1.6	± 1.6	± 1.4	± 1.9	± 1.4	± 1.6	± 1.0	± 1.2	± 1.9
ε_{light}	± 0.5	± 0.7	± 0.3	± 0.1	± 0.4	± 0.6	± 0.2	± 0.8	± 1.3	± 1.1
E_T^{miss} cellout	± 0.7	± 0.5	± 0.2	± 0.4	± 0.2	± 0.5	± 0.3	± 0.9	± 1.1	± 0.2
E_T^{miss} pileup	± 0.6	± 0.3	± 0.0	± 0.2	± 0.6	± 0.5	± 0.4	± 0.9	± 1.0	± 0.2
e trigger	± 0.5	± 0.4	± 0.1	± 0.2	± 0.3	± 0.4	± 0.4	± 0.8	± 1.2	± 0.1
e smearing	± 0.4	± 0.6	± 0.2	± 0.2	± 0.3	± 0.4	± 0.5	± 0.8	± 1.2	± 0.0
e recID	± 0.8	± 0.5	± 0.3	± 0.2	± 0.6	± 0.5	± 0.3	± 0.6	± 1.2	± 1.2
MC e -energy scale	± 0.5	± 0.4	± 0.1	± 0.1	± 0.4	± 0.3	± 0.2	± 0.8	± 1.3	± 0.1
μ trigger	± 0.6	± 0.4	± 0.3	± 0.3	± 0.4	± 0.4	± 0.4	± 0.9	± 1.0	± 0.5
μ smearing	± 0.4	± 0.4	± 0.3	± 0.4	± 0.4	± 0.3	± 0.4	± 0.5	± 0.6	± 0.1
μ recID	± 0.5	± 0.5	± 0.2	± 0.1	± 0.5	± 0.4	± 0.4	± 0.7	± 1.1	± 0.1
MC μ -en. sc.	± 0.5	± 0.3	± 0.1	± 0.0	± 0.6	± 0.3	± 0.4	± 0.9	± 1.2	± 0.1
Lumi	± 3.1	± 1.3	± 1.0	± 1.0	± 0.5	± 1.0	± 1.3	± 1.3	± 1.7	± 3.6
Stat.	± 4.5	± 4.3	± 4.0	± 4.3	± 3.8	± 4.7	± 4.7	± 4.5	± 4.9	± 4.8
Total Syst.	± 10.9	± 13.5	± 13.9	± 7.0	± 8.6	± 9.3	± 11.0	± 16.5	± 13.0	± 20.4
Total	± 11.8	± 14.2	± 14.4	± 8.2	± 9.4	± 10.4	± 11.9	± 17.1	± 13.9	± 21.0

Table B.35: (μ +jets). Systematic and statistical uncertainties for the MV1 tagger at a working point corresponding to a 60% b -tagging efficiency.

$p_T[GeV]$	25-30	30-40	40-50	50-60	60-75	75-90	90-110	110-140	140-200	200-300
ISR/FSR	± 2.6	± 1.6	± 3.1	± 2.5	± 2.7	± 3.0	± 3.4	± 2.2	± 3.3	± 8.4
Generator	± 4.0	± 1.9	± 0.9	± 1.5	± 5.3	± 0.6	± 5.4	± 1.8	± 2.9	± 2.0
Fragmentation	± 1.8	± 3.7	± 3.3	± 1.4	± 1.8	± 1.0	± 0.6	± 5.1	± 3.2	± 7.9
Diboson	± 0.3	± 0.9	± 0.5	± 0.8	± 0.1	± 0.5	± 0.1	± 0.2	± 0.3	± 0.3
single top	± 0.6	± 0.9	± 0.9	± 0.8	± 0.3	± 0.6	± 0.5	± 0.3	± 0.9	± 0.5
Z + jets	± 1.0	± 0.7	± 0.6	± 0.7	± 0.1	± 0.4	± 0.2	± 0.4	± 0.7	± 1.0
W + jets	± 1.2	± 0.8	± 0.7	± 0.8	± 0.2	± 0.6	± 0.4	± 0.5	± 0.8	± 1.3
Multijets	± 3.1	± 3.9	± 7.6	± 8.2	± 0.9	± 0.3	± 4.1	± 4.8	± 2.5	± 3.0
JES	± 3.0	± 4.3	± 1.0	± 2.4	± 4.2	± 8.3	± 5.6	± 7.9	± 9.5	± 19.3
JER	± 3.8	± 12.0	± 12.6	± 5.2	± 1.9	± 2.7	± 4.1	± 4.9	± 5.2	± 4.3
JRE	± 0.9	± 0.8	± 0.5	± 0.9	± 0.1	± 0.3	± 0.6	± 0.2	± 0.7	± 0.7
JVF	± 2.5	± 0.7	± 0.8	± 0.5	± 0.2	± 0.5	± 0.6	± 0.8	± 0.9	± 3.3
W+HF SF	± 0.8	± 1.2	± 1.0	± 1.2	± 0.3	± 1.0	± 0.6	± 0.6	± 1.0	± 0.4
ε_c	± 2.4	± 2.1	± 1.9	± 1.9	± 1.9	± 1.6	± 1.6	± 1.4	± 1.6	± 2.9
ε_{light}	± 1.8	± 0.7	± 0.7	± 0.7	± 0.3	± 0.4	± 0.4	± 0.7	± 0.5	± 1.6
E_T^{miss} cellout	± 0.4	± 0.6	± 0.8	± 0.9	± 0.3	± 0.6	± 0.1	± 0.4	± 0.9	± 0.3
E_T^{miss} pileup	± 0.7	± 0.8	± 0.6	± 0.7	± 0.1	± 0.4	± 0.2	± 0.3	± 0.6	± 0.4
e trigger	± 0.2	± 0.8	± 0.6	± 0.8	± 0.0	± 0.5	± 0.2	± 0.4	± 0.7	± 0.2
e smearing	± 0.4	± 0.8	± 0.7	± 0.6	± 0.1	± 0.5	± 0.4	± 0.3	± 0.4	± 0.7
e recID	± 1.1	± 0.7	± 0.6	± 0.5	± 0.1	± 0.6	± 0.5	± 0.6	± 0.7	± 1.4
MC e -energy scale	± 0.4	± 0.8	± 0.7	± 0.6	± 0.3	± 0.6	± 0.3	± 0.3	± 0.6	± 0.2
μ trigger	± 0.6	± 0.7	± 0.6	± 0.8	± 0.2	± 0.5	± 0.3	± 0.4	± 0.3	± 0.9
μ smearing	± 0.4	± 0.5	± 0.5	± 0.5	± 0.3	± 0.4	± 0.4	± 0.4	± 0.5	± 0.3
μ recID	± 0.3	± 0.6	± 0.6	± 0.7	± 0.2	± 0.5	± 0.5	± 0.3	± 0.7	± 0.4
MC μ -en. sc.	± 0.5	± 0.5	± 0.5	± 1.0	± 0.1	± 0.3	± 0.3	± 0.3	± 0.6	± 0.2
Lumi	± 3.6	± 1.8	± 1.6	± 1.2	± 0.9	± 1.3	± 1.5	± 1.6	± 2.3	± 3.9
Stat.	± 4.0	± 4.9	± 4.5	± 4.7	± 4.4	± 4.9	± 5.0	± 5.2	± 5.2	± 5.2
Total Syst.	± 9.7	± 14.7	± 15.9	± 11.2	± 8.1	± 9.8	± 10.7	± 12.3	± 13.0	± 23.8
Total	± 10.5	± 15.5	± 16.5	± 12.2	± 9.2	± 10.9	± 11.8	± 13.4	± 14.0	± 24.3

Table B.36: (μ +jets). Systematic and statistical uncertainties for the SV0 tagger at a working point corresponding to a 50% b -tagging efficiency.

APPENDIX C

TWO DIMENSIONAL LIKELIHOOD FIT TO EXTRACT *R*

It is possible to extend the procedure outline in Chapter 7 by adding additional constraints to better measure the $t\bar{t}$ content in the sample of events. The dilepton channel has relatively good purity but the lepton+jets channel suffers from large contributions from background processes. The complicated final states in lepton+jets makes it more sensitive to systematic effects, including predictions of background rates. Many $t\bar{t}$ cross section measurements exploit kinematic differences between $t\bar{t}$ and backgrounds to constrain the $t\bar{t}$ production rate and similar techniques can be applied to this analysis.

The first measurement of the $t\bar{t}$ cross section performed by ATLAS [15] used three variables to extract the $t\bar{t}$ content in the data sample. The variables chosen were charge of the lepton, η of the lepton, and $\exp(-8 \times \text{Aplanarity}(\text{jets}, \text{lepton}))$. Lepton η tends to be more central for $t\bar{t}$ events than for the backgrounds, which tend to have a flat distribution. Since the LHC is a proton-proton collider, there are more positively charged valence quarks which affect the rates of W^+ to W^- rates as well as single top production meaning the charge of the lepton from these processes tends to be positive. Since $t\bar{t}$ is produced through gluon-gluon fusion or quark-antiquark annihilation, it is charge symmetric. This charge asymmetry can be exploited to constrain the non- $t\bar{t}$ backgrounds in the lepton+jets channel.

Rather than examining all three variables listed in [15], only the lepton charge and η are used here. Lepton η is symmetric around zero so it's absolute magnitude is used to define a new variable, $|\eta_l| \times \text{Charge}$, which contains information about both the charge asymmetry and the η_l distribution. The distributions before any tagging (to illustrate the signal-background separation) are shown in Fig. C.1.

Events are binned in two dimensional histograms (Figure C.2) based on number of b -tagged jets and $|\eta_l| \times \text{Charge}$. The extraction of R and $\sigma_{t\bar{t}}$ is performed similarly

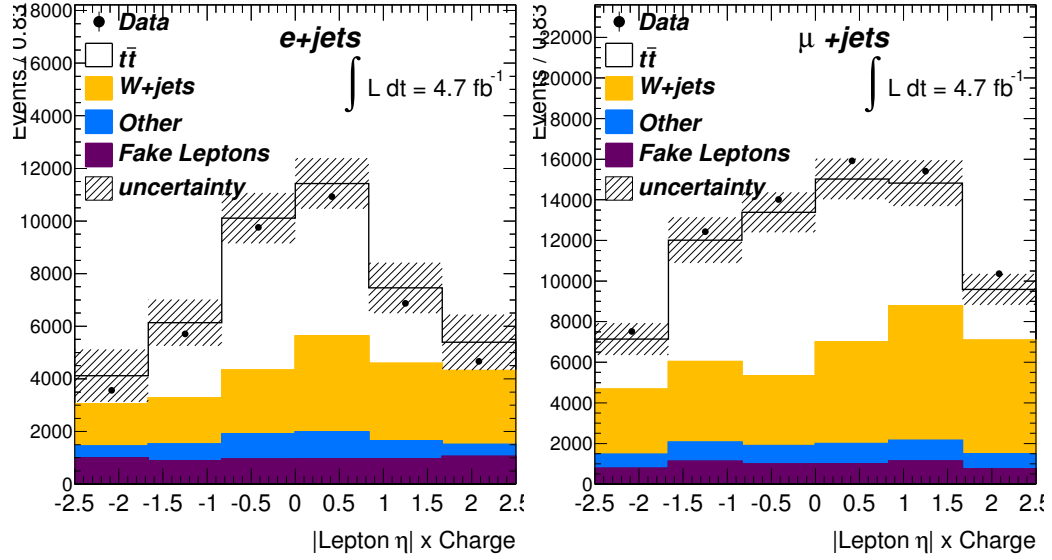


Figure C.1: The distributions of $|\eta_l| \times \text{Charge}$ for the electron (left) and muon (right) channel before any tagging requirement is applied.

to the 1-D case but the likelihood is also performed along the $|\eta_l| \times \text{Charge}$ dimension as shown in Eq. C.1.

$$L = \prod_{\text{channel}} \left(\prod_{n\text{-tag}, |\eta_l| \times \text{charge bin}} \text{Poisson}(N_{\text{channel},n} | < N_{\text{channel},n} >) \right) \quad (\text{C.1})$$

For the dilepton channel, nothing changes with respect to the one dimensional analysis and the 1 dimensional histograms are used.

The full set of systematic uncertainties is shown in Table C.1. In comparison to the 1-D systematic uncertainties (Table 7.1), the improvements are marginal relative to the added complexity. One systematic effect that is missing is due to modeling uncertainties for the η_l distributions. From the **ALPGEN** parameter variations shown in Chapter 4, it is expected that this contribution will be small since this variable is resilient against variations (see Figure 6.15) but should be included for completeness.

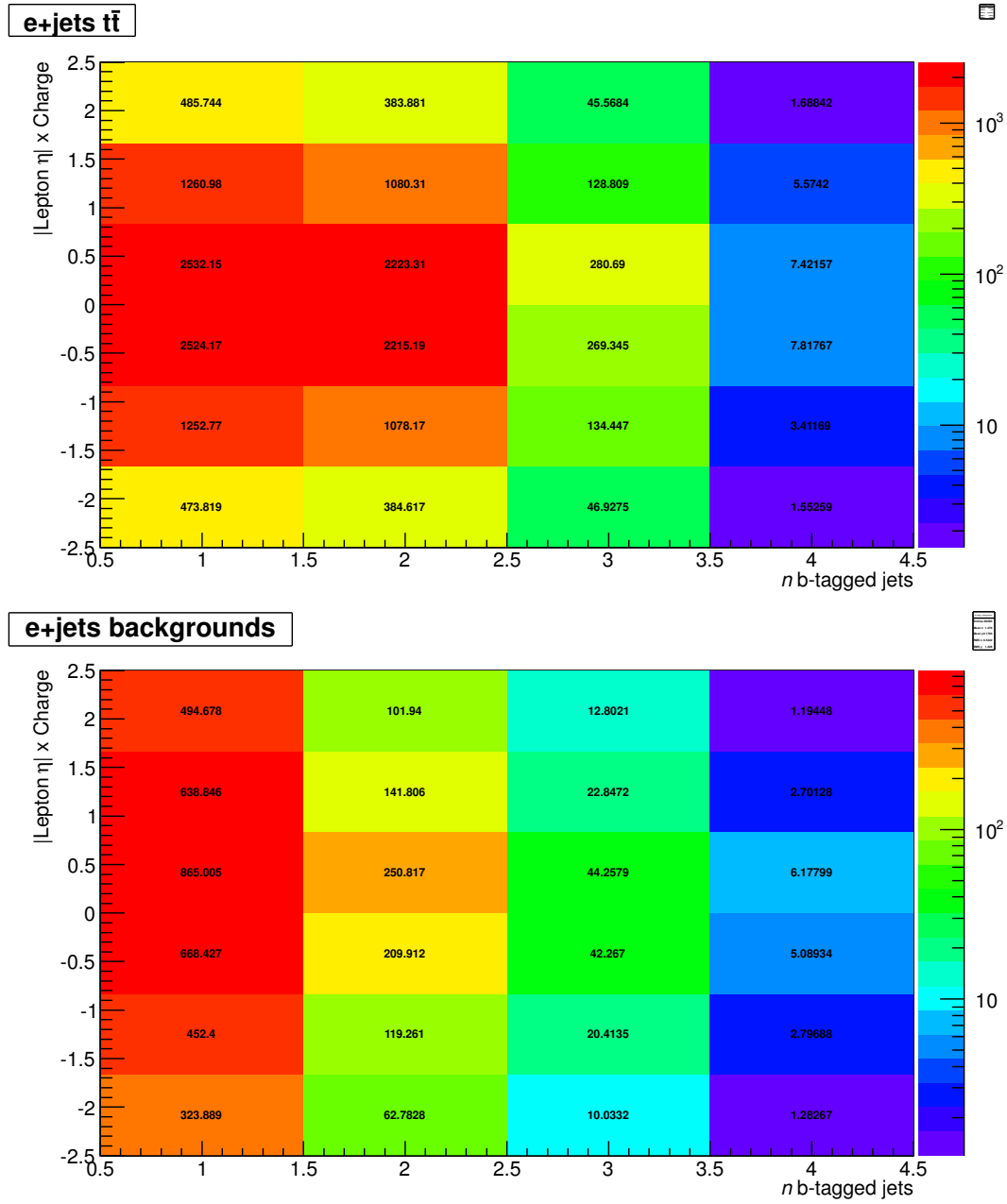


Figure C.2: The 2-dimensional templates for the electron channel for $t\bar{t}$ (top) and the backgrounds(bottom).

	R MV1 60%	R MV1 70%	$\sigma_{t\bar{t}}$ MV1 60%	$\sigma_{t\bar{t}}$ MV1 70%
ISR/FSR	± 6.9	± 5.7	± 7.7	± 7.9
Generator	± 0.5	± 0.3	± 2.5	± 2.7
Fragmentation	± 0.8	± 0.0	± 2.0	± 2.2
Diboson	± 0.1	± 0.1	± 0.1	± 0.1
single top	$^{+0.1}_{-0.1}$	$^{+0.1}_{-0.1}$	$^{+0.3}_{-0.3}$	$^{+0.3}_{-0.3}$
Z + jets	± 0.9	± 0.9	± 1.3	± 1.4
W + jets	± 0.3	± 0.6	± 0.9	± 1.2
Multijets	± 1.2	± 1.4	± 2.7	± 2.9
JES	$^{+1.0}_{-2.1}$	$^{+1.7}_{-2.5}$	$^{+11.9}_{-10.0}$	$^{+13.0}_{-10.9}$
JER	± 2.5	± 2.0	± 3.0	± 2.9
JRE	± 0.0	± 0.0	± 0.1	± 0.1
JVF	± 0.0	± 0.1	± 1.4	± 1.5
W+HF SF	$^{+0.2}_{-0.2}$	$^{+0.2}_{-0.2}$	$^{+0.5}_{-0.5}$	$^{+0.4}_{-0.5}$
ε_b	± 8.4	± 7.5	± 2.5	± 2.3
ε_c	± 0.8	± 0.7	± 1.0	± 1.1
ε_{light}	± 0.5	± 0.5	± 0.5	± 0.1
E_T^{miss} cellout	$^{+0.1}_{-0.1}$	$^{+0.0}_{-0.1}$	$^{+0.2}_{-0.1}$	$^{+0.1}_{-0.1}$
E_T^{miss} pileup	$^{+0.0}_{-0.0}$	$^{+0.0}_{-0.1}$	$^{+0.2}_{-0.0}$	$^{+0.1}_{-0.0}$
e trigger	± 0.1	± 0.0	± 0.3	± 0.3
e smearing	± 0.0	± 0.0	± 0.0	± 0.0
e recID	± 0.1	± 0.1	± 0.5	± 0.5
MC e -energy scale	$^{+0.0}_{-0.1}$	$^{+0.1}_{-0.0}$	$^{+0.2}_{-0.2}$	$^{+0.2}_{-0.2}$
μ trigger	$^{+0.0}_{-0.0}$	$^{+0.0}_{-0.0}$	$^{+0.0}_{-0.0}$	$^{+0.0}_{-0.0}$
μ smearing	$^{+0.1}_{-0.1}$	$^{+0.1}_{-0.1}$	$^{+0.7}_{-0.7}$	$^{+0.7}_{-0.7}$
μ recID	± 0.1	± 0.0	± 0.2	± 0.2
MC μ energy scale	± 0.0	± 0.0	± 0.0	± 0.0
Luminosity	± 0.4	± 0.5	± 5.1	± 5.2
Statistical	± 0.5	± 0.4	± 0.5	± 0.5
Total Systematic	$^{+11.4}_{-11.5}$	$^{+10.0}_{-10.2}$	$^{+16.3}_{-15.0}$	$^{+17.4}_{-15.9}$
Total	$^{+11.4}_{-11.5}$	$^{+10.0}_{-10.2}$	$^{+16.4}_{-15.0}$	$^{+17.4}_{-15.9}$

Table C.1: Table of relative uncertainties in % for the measurement of R and $\sigma_{t\bar{t}}$ using the 2-D method.

APPENDIX D

EVENT YIELDS AND CONTROL PLOTS

The event yields and control plots for the five decay channels are presented in this section. Table D.1 shows the event yields for all five channels for signal and background contributions with full normalization uncertainties. Figure D.1 shows the W transverse mass distribution for the lepton+jets channels which is sensitive to the QCD multijet background. Figure D.2 shows the E_T^{miss} distribution which is also sensitive to the QCD multijet normalization but also detector modeling effects. Figure D.3 shows the dilepton invariant mass around the Z peak, which shows the effectiveness of the Z window cut at reducing the Z +jets contribution to the same flavor lepton sample. Figure D.4 shows the H_T distribution for $e\mu$ events and illustrates the excellent $t\bar{t}$ purity in this particular channel.

	e +jets	μ +jets	ee	$e\mu$	$\mu\mu$
$t\bar{t}$	19400 $^{+4200}_{-2700}$	31900 $^{+5400}_{-4300}$	590 $^{+103}_{-76}$	4400 $^{+520}_{-510}$	1700 $^{+200}_{-200}$
W +jets	13500 $^{+3500}_{-2800}$	26700 $^{+6700}_{-5400}$	-	-	-
Z +jets	2800 $^{+1600}_{-1500}$	2600 $^{+1500}_{-1400}$	40 $^{+21}_{-17}$	200 $^{+80}_{-80}$	140 $^{+66}_{-60}$
single top	990 $^{+170}_{-150}$	1660 $^{+270}_{-240}$	30 $^{+6}_{-7}$	210 $^{+25}_{-25}$	80 $^{+12}_{-13}$
dibosons	240 $^{+70}_{-150}$	380 $^{+110}_{-90}$	9 $^{+4}_{-3}$	68 $^{+14}_{-12}$	23 $^{+7}_{-6}$
non-prompt leptons	5000 ± 2500	5000 ± 970	177 ± 89	117 ± 50	12 ± 4
Total	41900 $^{+7500}_{-5900}$	68200 $^{+11000}_{-9000}$	850 $^{+130}_{-100}$	5000 $^{+300}_{-290}$	1960 $^{+150}_{-160}$
Observed	39004	71515	707	5083	2062

Table D.1: Event yields for the five analysis channels. Uncertainties include both systematic and statistical uncertainties. Total uncertainties account for correlated systematics across samples such as jet energy scale and fragmentation.

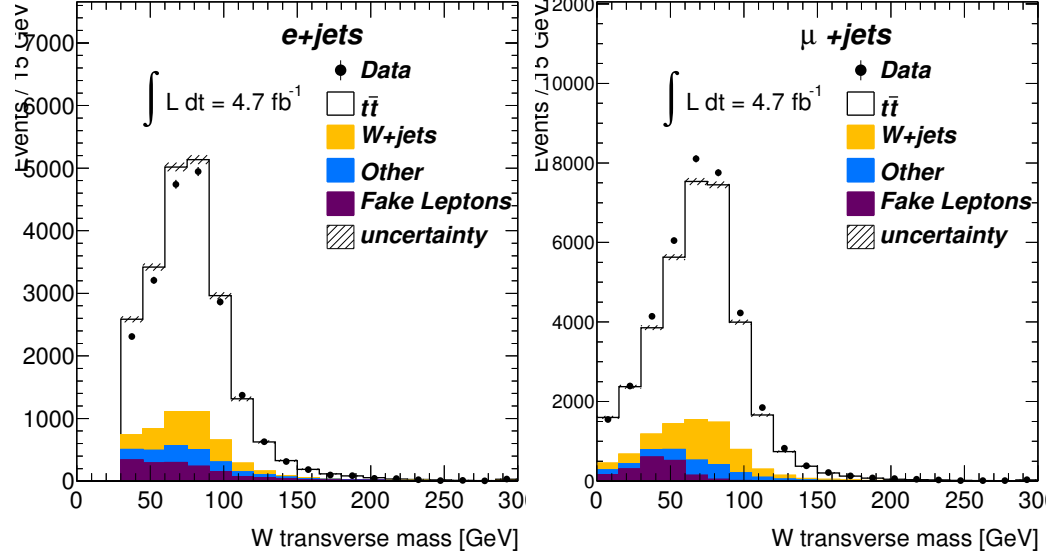


Figure D.1: The W transverse mass distributions for the electron + jets and muon+ jets channels.

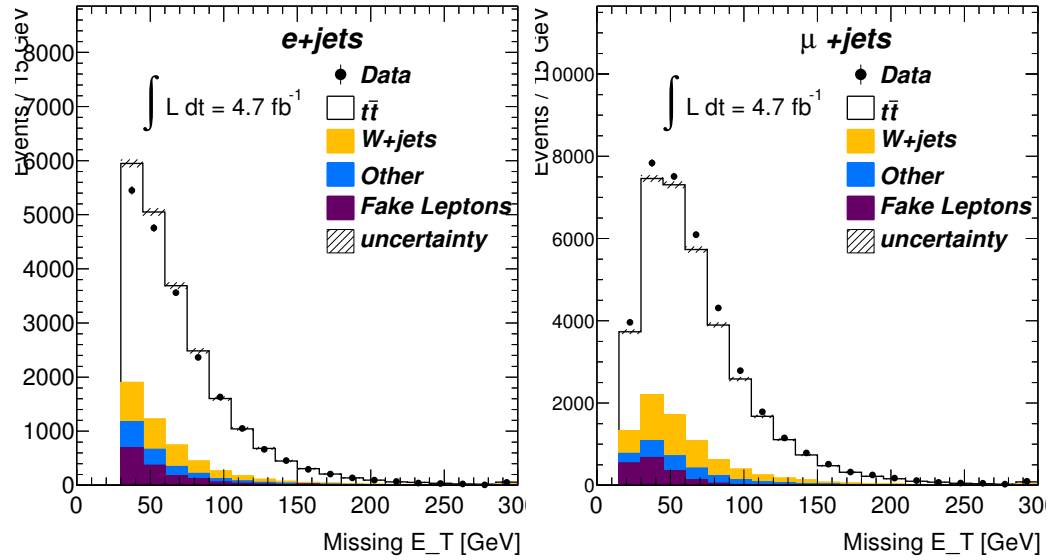


Figure D.2: The E_T^{miss} distributions for the electron + jets and muon+ jets channels.

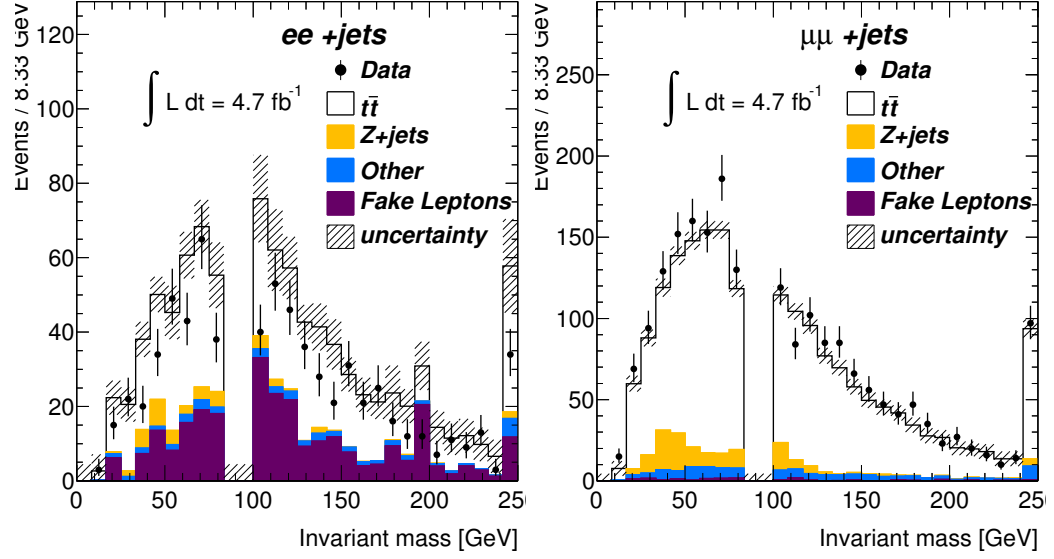


Figure D.3: The dilepton invariant mass distributions for the electron-electron and muon-muon channels.

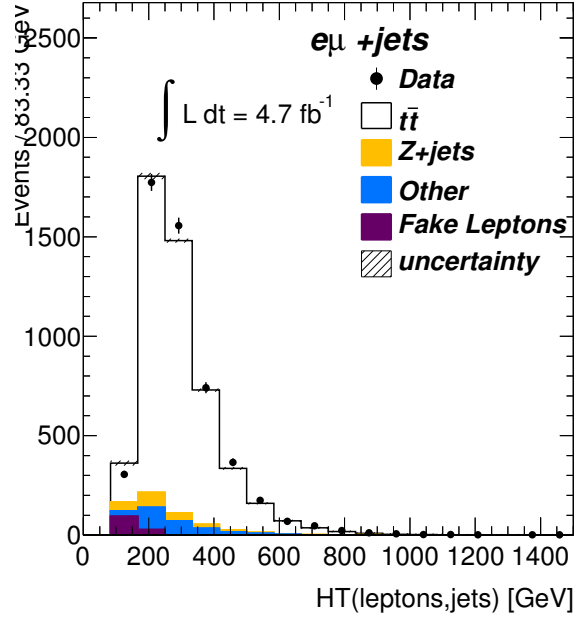


Figure D.4: The H_T distribution for the electron-muon channel.

APPENDIX E

MEASUREMENTS OF R AND THE TOP PAIR CROSS SECTION IN THE INDIVIDUAL CHANNELS

Tables E.1 through E.7 contain the uncertainties for the measurements in individual channels, as well as uncertainties for the combined single lepton and dilepton channels separately. Figure E.1 shows the likelihood distributions ($-2\ln(L/L_{\max})$) for the individual channel fits to data along with the combined likelihood. Table E.8 summarizes the results for the individual fits.

	R MV1 60%	R MV1 70%	$\sigma_{t\bar{t}}$ MV1 60%	$\sigma_{t\bar{t}}$ MV1 70%
ISR/FSR	± 8.4	± 6.7	± 11.2	± 11.9
Generator	± 0.8	± 0.3	± 3.4	± 3.7
Fragmentation	± 1.3	± 0.3	± 2.1	± 2.5
Diboson	± 0.0	± 0.0	± 0.0	± 0.0
single top	$+0.1$ -0.1	$+0.1$ -0.1	$+0.2$ -0.2	$+0.1$ -0.2
Z + jets	± 0.6	± 0.9	± 1.3	± 1.7
W + jets	± 0.6	± 0.9	± 1.3	± 1.8
Multijets	± 1.5	± 1.9	± 5.1	± 5.8
JES	$+2.1$ -2.3	$+2.7$ -2.9	$+13.6$ -12.0	$+15.2$ -13.1
JER	± 1.0	± 1.2	± 2.0	± 2.5
JRE	± 0.0	± 0.0	± 0.0	± 0.0
JVF	± 0.1	± 0.2	± 1.8	± 1.8
W+HF SF	$+0.3$ -0.3	$+0.3$ -0.3	$+0.7$ -0.8	$+0.8$ -0.8
ε_b	± 9.7	± 8.5	± 0.6	± 0.5
ε_c	± 1.2	± 1.0	± 0.8	± 0.9
ε_{light}	± 0.7	± 0.6	± 0.7	± 0.1
E_T^{miss} cellout	$+0.2$ -0.0	$+0.1$ -0.0	$+0.1$ -0.1	$+0.0$ -0.1
E_T^{miss} pileup	$+0.0$ -0.1	$+0.0$ -0.1	$+0.2$ -0.0	$+0.3$ -0.0
e trigger	± 0.0	± 0.1	± 0.7	± 0.8
e smearing	± 0.1	± 0.0	± 0.1	± 0.0
e recID	± 0.1	± 0.1	± 1.1	± 1.1
MC e -energy scale	$+0.1$ -0.1	$+0.0$ -0.0	$+0.5$ -0.4	$+0.5$ -0.4
μ trigger	$+0.0$ -0.0	$+0.0$ -0.0	$+0.0$ -0.0	$+0.0$ -0.0
μ smearing	$+0.0$ -0.0	$+0.0$ -0.1	$+0.1$ -0.1	$+0.1$ -0.0
μ recID	± 0.0	± 0.0	± 0.0	± 0.0
MC μ energy scale	± 0.1	± 0.0	± 0.1	± 0.0
Luminosity	± 0.3	± 0.5	± 5.1	± 5.4
Statistical	± 1.1	± 0.8	± 1.1	± 1.0
Total Systematic	$+13.3$ -13.3	$+11.5$ -11.6	$+19.9$ -18.8	$+21.8$ -20.3
Total	$+13.3$ -13.4	$+11.6$ -11.6	$+19.9$ -18.8	$+21.8$ -20.4

Table E.1: Table of relative uncertainties in % for the measurement of R and $\sigma_{t\bar{t}}$ in the electron channel.

	R MV1 60%	R MV1 70%	$\sigma_{t\bar{t}}$ MV1 60%	$\sigma_{t\bar{t}}$ MV1 70%
ISR/FSR	± 8.8	± 7.1	± 8.2	± 7.8
Generator	± 0.0	± 0.3	± 1.7	± 1.4
Fragmentation	± 0.5	± 0.2	± 1.8	± 2.0
Diboson	± 0.1	± 0.1	± 0.0	± 0.1
single top	$^{+0.0}_{-0.2}$	$^{+0.0}_{-0.3}$	$^{+0.3}_{-0.3}$	$^{+0.2}_{-0.4}$
Z + jets	± 0.4	± 0.6	± 0.8	± 1.1
W + jets	± 0.7	± 1.0	± 1.4	± 1.9
Multijets	± 0.7	± 0.8	± 1.5	± 1.7
JES	$^{+2.7}_{-2.5}$	$^{+3.4}_{-3.3}$	$^{+13.3}_{-12.7}$	$^{+15.0}_{-13.9}$
JER	± 0.8	± 1.0	± 1.2	± 1.6
JRE	± 0.1	± 0.1	± 0.1	± 0.1
JVF	± 0.2	± 0.2	± 1.8	± 1.9
W+HF SF	$^{+0.2}_{-0.4}$	$^{+0.2}_{-0.5}$	$^{+0.6}_{-0.7}$	$^{+0.6}_{-0.8}$
ε_b	± 10.0	± 9.0	± 0.6	± 0.4
ε_c	± 1.0	± 0.8	± 1.1	± 1.3
ε_{light}	± 0.8	± 0.8	± 1.3	± 0.4
E_T^{miss} cellout	$^{+0.0}_{-0.1}$	$^{+0.0}_{-0.2}$	$^{+0.1}_{-0.0}$	$^{+0.0}_{-0.1}$
E_T^{miss} pileup	$^{+0.0}_{-0.2}$	$^{+0.0}_{-0.2}$	$^{+0.2}_{-0.0}$	$^{+0.1}_{-0.0}$
e trigger	± 0.1	± 0.1	± 0.1	± 0.0
e smearing	± 0.1	± 0.1	± 0.1	± 0.1
e recID	± 0.1	± 0.1	± 0.1	± 0.1
MC e -energy scale	$^{+0.0}_{-0.1}$	$^{+0.0}_{-0.1}$	$^{+0.1}_{-0.0}$	$^{+0.0}_{-0.1}$
μ trigger	$^{+0.0}_{-0.0}$	$^{+0.0}_{-0.0}$	$^{+0.0}_{-0.0}$	$^{+0.0}_{-0.0}$
μ smearing	$^{+0.0}_{-0.1}$	$^{+0.0}_{-0.3}$	$^{+0.9}_{-0.9}$	$^{+0.9}_{-1.0}$
μ recID	± 0.1	± 0.1	± 0.3	± 0.2
MC μ energy scale	± 0.0	± 0.1	± 0.0	± 0.0
Luminosity	± 0.4	± 0.5	± 5.2	± 5.5
Statistical	± 0.9	± 0.7	± 0.9	± 0.8
Total Systematic	$^{+13.7}_{-13.7}$	$^{+12.2}_{-12.2}$	$^{+17.1}_{-16.6}$	$^{+18.4}_{-17.6}$
Total	$^{+13.8}_{-13.7}$	$^{+12.2}_{-12.2}$	$^{+17.2}_{-16.7}$	$^{+18.4}_{-17.6}$

Table E.2: Table of relative uncertainties in % for the measurement of R and $\sigma_{t\bar{t}}$ in the muon channel.

	R MV1 60%	R MV1 70%	$\sigma_{t\bar{t}}$ MV1 60%	$\sigma_{t\bar{t}}$ MV1 70%
ISR/FSR	± 8.5	± 6.9	± 8.9	± 8.7
Generator	± 0.4	± 0.3	± 2.4	± 2.4
Fragmentation	± 0.9	± 0.0	± 1.8	± 2.2
Diboson	± 0.0	± 0.0	± 0.0	± 0.0
single top	$+0.0$ -0.1	$+0.1$ -0.1	$+0.2$ -0.2	$+0.2$ -0.2
Z + jets	± 0.4	± 0.7	± 1.0	± 1.4
W + jets	± 0.6	± 0.9	± 1.4	± 1.8
Multijets	± 1.1	± 1.2	± 2.8	± 3.0
JES	$+2.4$ -2.5	$+3.1$ -3.1	$+13.5$ -12.4	$+15.1$ -13.5
JER	± 0.9	± 1.1	± 1.5	± 2.0
JRE	± 0.0	± 0.0	± 0.1	± 0.1
JVF	± 0.2	± 0.2	± 1.8	± 1.9
W+HF SF	$+0.3$ -0.3	$+0.3$ -0.3	$+0.7$ -0.7	$+0.7$ -0.7
ε_b	± 9.8	± 8.8	± 0.1	± 0.0
ε_c	± 1.1	± 0.9	± 1.0	± 1.1
ε_{light}	± 0.8	± 0.7	± 1.1	± 0.2
E_T^{miss} cellout	$+0.0$ -0.0	$+0.0$ -0.0	$+0.0$ -0.0	$+0.0$ -0.0
E_T^{miss} pileup	$+0.0$ -0.1	$+0.0$ -0.1	$+0.2$ -0.0	$+0.2$ -0.0
e trigger	± 0.0	± 0.0	± 0.3	± 0.3
e smearing	± 0.0	± 0.0	± 0.0	± 0.0
e recID	± 0.0	± 0.1	± 0.4	± 0.4
MC e -energy scale	$+0.0$ -0.0	$+0.0$ -0.0	$+0.2$ -0.1	$+0.2$ -0.1
μ trigger	$+0.0$ -0.0	$+0.0$ -0.0	$+0.0$ -0.0	$+0.0$ -0.0
μ smearing	$+0.1$ -0.0	$+0.0$ -0.0	$+0.5$ -0.6	$+0.6$ -0.6
μ recID	± 0.0	± 0.0	± 0.1	± 0.1
MC μ energy scale	± 0.0	± 0.0	± 0.0	± 0.0
Luminosity	± 0.4	± 0.5	± 5.2	± 5.4
Statistical	± 0.7	± 0.5	± 0.7	± 0.6
Total Systematic	$+13.4$ -13.4	$+11.8$ -11.8	$+17.8$ -17.0	$+19.2$ -18.0
Total	$+13.5$ -13.5	$+11.8$ -11.8	$+17.8$ -17.0	$+19.2$ -18.0

Table E.3: Table of relative uncertainties in % for the measurement of R and $\sigma_{t\bar{t}}$ in the lepton+jets channel.

	R MV1 60%	R MV1 70%	$\sigma_{t\bar{t}}$ MV1 60%	$\sigma_{t\bar{t}}$ MV1 70%
ISR/FSR	± 7.0	± 5.9	± 10.7	± 11.2
Generator	± 0.3	± 1.0	± 1.2	± 1.5
Fragmentation	± 0.5	± 0.8	± 2.8	± 3.3
Diboson	± 0.0	± 0.1	± 0.1	± 0.1
single top	$+0.1$ -0.2	$+0.2$ -0.3	$+0.4$ -0.4	$+0.5$ -0.3
Z + jets	± 2.2	± 2.1	± 2.2	± 2.0
W + jets	± 0.0	± 0.1	± 0.2	± 0.2
Multijets	± 9.2	± 11.0	± 17.8	± 18.3
JES	$+1.3$ -1.6	$+1.2$ -1.7	$+7.4$ -6.5	$+6.9$ -6.4
JER	± 1.9	± 1.4	± 1.8	± 1.7
JRE	± 0.1	± 0.0	± 0.0	± 0.0
JVF	± 0.1	± 0.1	± 0.8	± 0.9
W+HF SF	$+0.3$ -0.2	$+0.2$ -0.0	$+0.3$ -0.1	$+0.4$ -0.1
ε_b	± 8.1	± 7.4	± 1.9	± 2.0
ε_c	± 0.1	± 0.1	± 0.1	± 0.1
ε_{light}	± 0.1	± 0.1	± 0.0	± 0.2
E_T^{miss} cellout	$+0.0$ -0.1	$+0.1$ -0.0	$+0.2$ -0.3	$+0.4$ -0.2
E_T^{miss} pileup	$+0.3$ -0.1	$+0.0$ -0.0	$+0.0$ -0.2	$+0.1$ -0.2
e trigger	± 0.2	± 0.1	± 1.3	± 1.4
e smearing	± 0.1	± 0.1	± 0.2	± 0.4
e recID	± 0.1	± 0.2	± 2.1	± 2.0
MC e -energy scale	$+0.2$ -0.0	$+0.4$ -0.0	$+0.4$ -0.5	$+0.3$ -0.5
μ trigger	$+0.0$ -0.0	$+0.0$ -0.0	$+0.0$ -0.0	$+0.0$ -0.0
μ smearing	$+0.1$ -0.2	$+0.0$ -0.0	$+0.2$ -0.2	$+0.3$ -0.2
μ recID	± 0.1	± 0.1	± 0.2	± 0.1
MC μ energy scale	± 0.0	± 0.1	± 0.1	± 0.1
Luminosity	± 0.3	± 0.3	± 4.8	± 4.6
Statistical	± 3.1	± 2.7	± 4.1	± 4.6
Total Systematic	$+14.5$ -14.5	$+14.8$ -14.9	$+23.2$ -22.9	$+23.7$ -23.6
Total	$+14.8$ -14.8	$+15.1$ -15.1	$+23.5$ -23.3	$+24.1$ -24.0

Table E.4: Table of relative uncertainties in % for the measurement of R and $\sigma_{t\bar{t}}$ in the ee channel.

	R MV1 60%	R MV1 70%	$\sigma_{t\bar{t}}$ MV1 60%	$\sigma_{t\bar{t}}$ MV1 70%
ISR/FSR	± 7.4	± 6.1	± 3.4	± 3.8
Generator	± 0.7	± 0.6	± 2.1	± 2.2
Fragmentation	± 0.9	± 0.1	± 0.4	± 0.3
Diboson	± 0.1	± 0.0	± 0.1	± 0.1
single top	$^{+0.1}_{-0.1}$	$^{+0.1}_{-0.1}$	$^{+0.3}_{-0.3}$	$^{+0.2}_{-0.4}$
Z + jets	± 1.5	± 1.5	± 1.5	± 1.6
W + jets	± 0.0	± 0.0	± 0.0	± 0.0
Multijets	± 0.8	± 0.9	± 0.8	± 0.8
JES	$^{+0.8}_{-1.0}$	$^{+0.6}_{-0.8}$	$^{+2.9}_{-3.0}$	$^{+2.8}_{-2.9}$
JER	± 0.5	± 0.4	± 0.5	± 0.5
JRE	± 0.0	± 0.0	± 0.0	± 0.0
JVF	± 0.1	± 0.1	± 0.9	± 0.9
W+HF SF	$^{+0.1}_{-0.1}$	$^{+0.0}_{-0.1}$	$^{+0.1}_{-0.1}$	$^{+0.1}_{-0.1}$
ε_b	± 8.2	± 7.3	± 1.1	± 1.2
ε_c	± 0.1	± 0.1	± 0.0	± 0.0
ε_{light}	± 0.1	± 0.2	± 0.0	± 0.1
E_T^{miss} cellout	$^{+0.0}_{-0.1}$	$^{+0.0}_{-0.0}$	$^{+0.0}_{-0.0}$	$^{+0.1}_{-0.0}$
E_T^{miss} pileup	$^{+0.0}_{-0.0}$	$^{+0.0}_{-0.0}$	$^{+0.0}_{-0.1}$	$^{+0.0}_{-0.1}$
e trigger	± 0.0	± 0.0	± 0.6	± 0.6
e smearing	± 0.0	± 0.0	± 0.1	± 0.0
e recID	± 0.1	± 0.1	± 1.0	± 1.0
MC e -energy scale	$^{+0.0}_{-0.0}$	$^{+0.0}_{-0.0}$	$^{+0.3}_{-0.1}$	$^{+0.2}_{-0.0}$
μ trigger	$^{+0.0}_{-0.0}$	$^{+0.0}_{-0.0}$	$^{+0.0}_{-0.0}$	$^{+0.0}_{-0.0}$
μ smearing	$^{+0.1}_{-0.1}$	$^{+0.0}_{-0.1}$	$^{+0.8}_{-0.9}$	$^{+0.8}_{-0.8}$
μ recID	± 0.0	± 0.0	± 0.2	± 0.2
MC μ energy scale	± 0.0	± 0.0	± 0.1	± 0.0
Luminosity	± 0.3	± 0.3	± 4.5	± 4.5
Statistical	± 1.1	± 1.0	± 1.6	± 1.5
Total Systematic	$^{+11.3}_{-11.3}$	$^{+9.7}_{-9.7}$	$^{+7.3}_{-7.3}$	$^{+7.4}_{-7.5}$
Total	$^{+11.3}_{-11.3}$	$^{+9.7}_{-9.7}$	$^{+7.5}_{-7.5}$	$^{+7.6}_{-7.6}$

Table E.5: Table of relative uncertainties in % for the measurement of R and $\sigma_{t\bar{t}}$ in the $e\mu$ channel.

	R MV1 60%	R MV1 70%	$\sigma_{t\bar{t}}$ MV1 60%	$\sigma_{t\bar{t}}$ MV1 70%
ISR/FSR	± 7.1	± 6.1	± 2.5	± 2.5
Generator	± 0.1	± 0.9	± 3.4	± 3.4
Fragmentation	± 0.0	± 0.8	± 1.1	± 1.0
Diboson	± 0.1	± 0.0	± 0.1	± 0.1
single top	$+0.2$ -0.2	$+0.1$ -0.1	$+0.2$ -0.3	$+0.4$ -0.4
Z + jets	± 2.8	± 2.6	± 2.8	± 2.5
W + jets	± 0.0	± 0.1	± 0.1	± 0.1
Multijets	± 0.1	± 0.0	± 0.2	± 0.2
JES	$+1.3$ -1.7	$+1.0$ -1.5	$+5.5$ -5.5	$+5.3$ -5.4
JER	± 1.6	± 1.5	± 1.5	± 1.4
JRE	± 0.0	± 0.0	± 0.0	± 0.0
JVF	± 0.1	± 0.1	± 1.1	± 1.0
W+HF SF	$+0.1$ -0.2	$+0.0$ -0.2	$+0.2$ -0.1	$+0.1$ -0.1
ε_b	± 8.1	± 7.2	± 2.0	± 1.8
ε_c	± 0.1	± 0.1	± 0.1	± 0.1
ε_{light}	± 0.1	± 0.2	± 0.0	± 0.1
E_T^{miss} cellout	$+0.0$ -0.1	$+0.1$ -0.2	$+0.4$ -0.3	$+0.6$ -0.2
E_T^{miss} pileup	$+0.0$ -0.1	$+0.0$ -0.2	$+0.3$ -0.0	$+0.2$ -0.0
e trigger	± 0.0	± 0.0	± 0.1	± 0.1
e smearing	± 0.0	± 0.1	± 0.1	± 0.0
e recID	± 0.0	± 0.0	± 0.0	± 0.1
MC e -energy scale	$+0.0$ -0.2	$+0.0$ -0.1	$+0.0$ -0.1	$+0.1$ -0.0
μ trigger	$+0.0$ -0.0	$+0.0$ -0.0	$+0.0$ -0.0	$+0.0$ -0.0
μ smearing	$+0.2$ -0.2	$+0.2$ -0.1	$+1.8$ -1.6	$+1.7$ -1.4
μ recID	± 0.3	± 0.2	± 2.2	± 2.2
MC μ energy scale	± 0.0	± 0.0	± 0.1	± 0.1
Luminosity	± 0.4	± 0.4	± 4.7	± 4.6
Statistical	± 1.9	± 1.6	± 2.6	± 2.7
Total Systematic	$+11.3$ -11.4	$+10.0$ -10.1	$+9.7$ -9.7	$+9.4$ -9.5
Total	$+11.5$ -11.5	$+10.2$ -10.2	$+10.1$ -10.0	$+9.8$ -9.8

Table E.6: Table of relative uncertainties in % for the measurement of R and $\sigma_{t\bar{t}}$ in the $\mu\mu$ channel.

	R MV1 60%	R MV1 70%	$\sigma_{t\bar{t}}$ MV1 60%	$\sigma_{t\bar{t}}$ MV1 70%
ISR/FSR	± 7.3	± 6.1	± 3.4	± 3.6
Generator	± 0.4	± 0.0	± 2.2	± 2.2
Fragmentation	± 0.6	± 0.2	± 0.3	± 0.2
Diboson	± 0.1	± 0.1	± 0.1	± 0.1
single top	$^{+0.1}_{-0.1}$	$^{+0.1}_{-0.1}$	$^{+0.3}_{-0.3}$	$^{+0.3}_{-0.3}$
Z + jets	± 1.9	± 1.8	± 2.0	± 1.8
W + jets	± 0.1	± 0.0	± 0.1	± 0.0
Multijets	± 0.9	± 1.0	± 1.4	± 1.3
JES	$^{+1.0}_{-1.3}$	$^{+0.8}_{-1.1}$	$^{+3.8}_{-3.9}$	$^{+3.8}_{-3.8}$
JER	± 0.9	± 0.8	± 0.2	± 0.1
JRE	± 0.0	± 0.0	± 0.0	± 0.0
JVF	± 0.1	± 0.1	± 1.0	± 0.9
W+HF SF	$^{+0.0}_{-0.1}$	$^{+0.0}_{-0.0}$	$^{+0.1}_{-0.1}$	$^{+0.1}_{-0.1}$
ε_b	± 8.2	± 7.3	± 1.4	± 1.4
ε_c	± 0.1	± 0.1	± 0.1	± 0.0
ε_{light}	± 0.1	± 0.2	± 0.1	± 0.1
E_T^{miss} cellout	$^{+0.0}_{-0.1}$	$^{+0.0}_{-0.1}$	$^{+0.2}_{-0.1}$	$^{+0.1}_{-0.1}$
E_T^{miss} pileup	$^{+0.0}_{-0.1}$	$^{+0.0}_{-0.0}$	$^{+0.1}_{-0.0}$	$^{+0.1}_{-0.0}$
e trigger	± 0.0	± 0.0	± 0.5	± 0.5
e smearing	± 0.0	± 0.0	± 0.0	± 0.0
e recID	± 0.0	± 0.1	± 0.8	± 0.8
MC e -energy scale	$^{+0.1}_{-0.0}$	$^{+0.0}_{-0.0}$	$^{+0.2}_{-0.1}$	$^{+0.1}_{-0.1}$
μ trigger	$^{+0.0}_{-0.0}$	$^{+0.0}_{-0.0}$	$^{+0.0}_{-0.0}$	$^{+0.0}_{-0.0}$
μ smearing	$^{+0.1}_{-0.0}$	$^{+0.1}_{-0.1}$	$^{+1.0}_{-1.0}$	$^{+0.9}_{-1.0}$
μ recID	± 0.1	± 0.1	± 0.6	± 0.7
MC μ energy scale	± 0.0	± 0.0	± 0.1	± 0.1
Luminosity	± 0.3	± 0.3	± 4.6	± 4.6
Statistical	± 0.9	± 0.8	± 1.3	± 1.3
Total Systematic	$^{+11.3}_{-11.3}$	$^{+9.7}_{-9.8}$	$^{+7.9}_{-8.0}$	$^{+8.0}_{-8.0}$
Total	$^{+11.3}_{-11.4}$	$^{+9.8}_{-9.8}$	$^{+8.1}_{-8.1}$	$^{+8.1}_{-8.1}$

Table E.7: Table of relative uncertainties in % for the measurement of R and $\sigma_{t\bar{t}}$ in the dilepton channel.

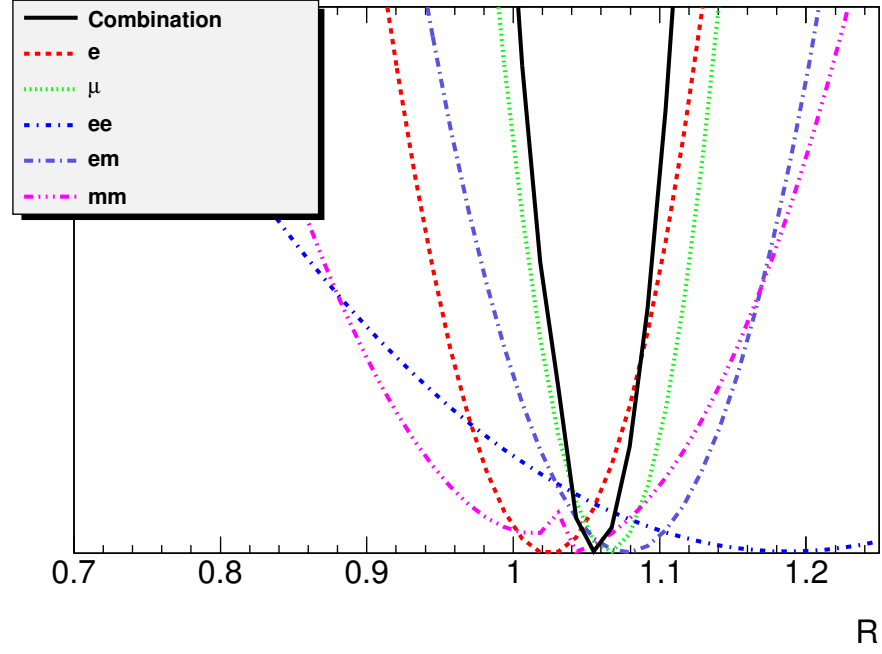


Figure E.1: The likelihood function for each of the channels evaluated at the combined fitted value for the $t\bar{t}$ cross section.

	R MV1 60%	R MV1 70%	$\sigma_{t\bar{t}}$ MV1 60% [pb]	$\sigma_{t\bar{t}}$ MV1 70% [pb]
Electron	1.12 ± 0.13	1.06 ± 0.12	153 ± 31	152 ± 32
Muon	1.11 ± 0.14	1.05 ± 0.12	175 ± 30	175 ± 32
EE	1.22 ± 0.15	1.24 ± 0.15	140 ± 32	130 ± 31
EM	1.12 ± 0.11	1.08 ± 0.10	181 ± 15	170 ± 14
MM	1.08 ± 0.12	1.03 ± 0.10	185 ± 19	182 ± 18
Combined	1.11 ± 0.12	1.06 ± 0.11	167^{+25}_{-24}	167^{+27}_{-26}

Table E.8: Table of results for all of the channels.